Computational Component Analysis Techniques for High Temperature Power Plant Applications

JAMES PAUL ROUSE, MENG. (HONS)

THESIS SUBMITTED TO THE UNIVERSITY OF NOTTINGHAM FOR THE DEGREE OF DOCTOR OF PHILOSOPHY

SUPERVISORS:
DR. WEI SUN
PROF. THOMAS H. HYDE
DR. CHRISTOPHER J. HYDE

February 2014

Abstract

There is a trend in the power industry for high temperature components (such as steam pipe work) to be operated in an increasingly arduous fashion. This would involve the use of elevated steam temperatures/pressures and a greater frequency of start up/shut down cycles. Such generation strategies are being adopted due to the need for thermally efficient power supply that can match fluctuating market demands. If these generation strategies are to be implemented safely it is critical that careful analysis of the system components is conducted in order to ensure that premature failure does not occur. The advanced material models and techniques that are used in academia to simulate these components are often out of reach of the engineers working in industry.

The present work describes the development of an analysis "toolbox" that takes several advanced material models (which can accommodate complex loading conditions) and applies them in numerical (finite element analysis, FEA) and approximate life estimation methods. The toolbox comprises several modules, each of which relates to a specific aspect of component analysis. In this thesis, the fundamental procedures behind these modules are developed in novel ways in addition to the development of the toolbox as a whole. The toolbox modules may be roughly divided into the definition of a component's material, geometry and loading condition, followed by some form of analysis procedure and a report of the key results.

A material's behaviour is commonly determined from mechanical tests. For in service components, scoop sampling is an exciting new method to extract small amounts of material which may then be tested using several novel small specimen techniques. An investigation has been conduced in the present work that verifies the safety of this method and allows the localised stress behaviour around an excavation to be estimated. Material constants in material behaviour models are usually determined by fitting the outputs of the model to experimental data in an optimisation procedure. A great deal of work has been completed on this topic using the complex Chaboche unified visco-plasticity model. This has led to the formation of the combined parallel optimisation strategy and the development of data cleaning for the determination of material constants in any model.

Due to the high temperature conditions power plant components operate in, creep is a major concern. Several damage material models have been compared which can represent failure due to creep. Generally, these models can be divided into power law

and hyperbolic sine functions. Through a comparative investigation using multiple component geometries, it has been found that the hyperbolic sine function creep law gives lower predictions of failure time than the power law models at realistic stress levels. Hyperbolic sine function failure lives were also more representative of reality. It is therefore critical when performing component analysis to consider the form of a material model as well as the loading range its material constants are applicable to. The Chaboche unified visco-plasticity model has also been discussed. Using this model, both hardening due to the accumulation of plastic strain and viscous effects (such as creep stress relaxation) may be described. Models like this will play an important role in the analysis of high temperature components as they experience fluctuations in both load and temperature.

Although it appears simple, the geometry of a high temperature pipe bend in a power plant is actually complex due to the manufacturing process employed (a straight pipe section is heated through induction coils and bent using a fixed radius arm). The pipe's wall thickness not only varies circumferentially around the pipe's cross section but also around the bend itself. Through the analysis of industrial data (collected by ultrasonic measurement of components during outage inspections) several novel geometry factors have been developed that quantify this dimension variation. A new method to analyse such pipe bends has also been created that interpolates the stress states between two dimensional (2D) models that represent the cross section of a pipe bend at several key locations.

Once a geometry, loading condition and material has been defined, an analysis procedure may be employed in order to assess the condition of the component. As creep is a key concern under high temperature conditions, most of the analysis procedures discussed in the present work are focused on the prediction of peak rupture stresses ($\hat{\sigma}_R$) which may be used to estimate failure lives due to creep. Several approximate (errors are typically less than 5%) parametric relationships have been developed that allow peak rupture stresses to be determined based on, for example, pipe bend geometry factors. In addition, to aid in bespoke FEA analyses, a collection of routines with a graphical user interface (GUI) have been created that can write input files for a commercial FEA code (ABAQUS), run the job and post process the results. This can save a great amount of user effort when attempting to analyse components. Finally, an original neural network (that uses a partially connected, multiple input node architecture) has been proposed that predicts $\hat{\sigma}_R$ in pipe bends operating under steady-state creep conditions. Both internal pressure and system loads have been incorporated as inputs for this neural network. This has required the definition of several new load factors that describe the system loads acting on a component.

Recommendations for future developments based on this research have also been given. Future developments may look to include fatigue effects in parametric equations, as well as considering the effect of varying loading conditions (possibly through a

damage fraction approach). The Chaboche model (or similar unified model) may be modified to include temperature dependency and damage effects (allowing for a wider application to component analysis). The effect of geometry variation may be included in the neural network, again extending its applicability, and stresses due to temperature distributions in the piping components may be incorporated (at present, these have not been considered, however system loads may be thermally driven).

The work presented in this thesis addresses a complete analysis procedure, from collecting material information from a component through scoop sampling, to determining material constants for this material by an optimisation procedure and analysing the component using either numerical or approximate methods. Although pipe bends have been considered for the significant part of this work due to the relatively small amount of research reported in literature, similar methodologies may be applied to other power plant components of interest, such as welds, steam headers or branch pipes.

Acknowledgements

I would like to take this opportunity to express my sincere gratitude to several people who, without their support and guidance, I would not be writing this thesis.

Firstly, I would like to thank my principal supervisor, Dr. Wei Sun. It is because of his encouragement that I first considered undertaking a Ph.D., and it is because of his dedication to his students that I have completed it. The same encouragement and dedication has also been extended to me by my additional supervisors, Professor Thomas H. Hyde and Dr. Christopher J. Hyde, and by Professor Andrew Morris (who provided a great deal of information on power plant operating conditions and assisted tremendously in securing funding for the research). My research would not have come to fruition if not for my supervisors' scientific guidance and general support. My Ph.D. was partly funded through an Engineering and Physical Sciences Research Council (EPSRC) industrial case study award (EP/J50211X/1, awarded through E.On UK), therefore I would like to give a special word of thanks to the EPSRC.

I have shared my time at the University of Nottingham with some wonderful colleges, particularly those from the Structural Integrity and Dynamics (SID) and the University Technology Centre (UTC) research divisions, who have made this experience a pleasure. In particular, I would like to thank Mr. Francesco Cortellino, who provided a great deal of assistance in producing a publication on small punch sampling and continues research in this fascinating area. A special mention should also be given to members of the technical staff at the University of Nottingham, notably Mr. Shane Maskill, Mr. Thomas Buss, Mr. Keith Dinsdale and Dr. Nigel Neate, who were always willing to advise and help with experimental matters.

Finally, I would like to thank my friends and family. The love and support from my mother, father and brother has not only helped me through my Ph.D. but continues to drive me forward. To them and everyone else who has contributed to my research in so many different ways, I am truly grateful.

Nomenclature

To aid the reader's understanding a nomenclature of commonly used symbols and abbreviations is presented here. In several cases, particularly with reference to material model coefficients, the definition of a symbol is context dependent. Symbol definitions are given in the text to avoid confusion and have been divided into subject areas to make context recognition easier over the wide range of research fields considered in this thesis. Note that, in general, symbols in a bold typeface are vectors or tensors.

Symbols

General

A, A_s	Area (Normal, Shear)
b	Burger's Vector
E	Young's Modulus
$\boldsymbol{F}$, F, F_s	Force (Vector, Normal, Shear)
f_k	Surface Element
G	Shear Modulus
i, j, k	Indices
K	Bulk Modulus
L, L_0, L_f, ΔL	Length (Instantaneous, Initial, Final, Change in)
$\boldsymbol{S}$, S_{ij}	Deviatoric Stress (Tensor, Component)
$\boldsymbol{u}$, u_i	Displacement (Vector, Component)
V	Volume
γ	Shear Strain
Δ	Volumetric Strain
δ_{ij}	Kronecker Delta
$\boldsymbol{\epsilon}$, ϵ_{ij}	Engineering Strain (Tensor, Component)
$\boldsymbol{\varepsilon}$, ε_{ij}	True Strain (Tensor, Component)
ε_e	Elastic Strain Component
$\boldsymbol{\varepsilon_p}$, $\varepsilon_{p\,ij}$, ε_p	Plastic Strain (Tensor, Component, Uniaxial)
ϕ, ϕ_0	Lateral Dimension (Instantaneous, Initial)
$d\lambda$	Plastic Multiplier

ν	Poisson's Ratio
σ, σ_{ij}	Stress (Tensor, Component)
σ_1, σ_2, σ_3	Principal Stresses (Maximum, Intermediate, Minimum)
σ_{EQ}	Equivalent (von Mises) Stress
σ_m	Hydrostatic (Mean) Stress
σ_{UTS}	Ultimate Tensile Strength
σ_Y	Yield Stress
τ	Shear Stress

Creep Material Models

A, B	Dyson Model Strain Rate Material Constants
A, n, m	Norton's Model Material Constants (Multiplier, Stress Exponent, Time Exponent)
A, n, m	Kachanov Model Strain Rate Material Constants
A, n, c, B', n'	Liu-Murakami Model Strain Rate Material Constants
a, b, c, d, e, t_a, T_a	Orr's Equation Coefficients
B, q_2, p	Liu-Murakami Model Damage Rate Material Constants
B, χ, ϕ	Kachanov Model Damage Rate Material Constants
D, N, v	Dyson Model Cavitation Damage Rate Material Constants
H	Strain Hardening Internal Variable (Dyson Model)
h, H'	Dyson Model Strain Hardening Rate Material Constants
K_c	Dyson Model Precipitate Coarsening Damage Rate Material Constants
Q_c	Activation Energy
R	Universal Gas Constant
T, T_m	Temperature (Operating, Melting)
t, t_f	Time (Instant, Failure)
$\bar{t}$	Fictitious Time (Liu-Murakami Model)
$t_{f\,i}^{exp}$	i^{th} Experimental Creep Time to Failure
$t_{f\,i}^{pre}(\boldsymbol{x})$	i^{th} Creep Time to Failure Predicted by the Constant set $\boldsymbol{x}$
α	Multiaxial Material Constant (Kachanov and Liu-Murakami Models)
ε_0	Initial/Instantaneous Strain
$\boldsymbol{\varepsilon_c}$, $\varepsilon_{c\,ij}$, ε_c	Creep Strain (Tensor, Component, Uniaxial)
$\dot{\boldsymbol{\varepsilon}}_{\boldsymbol{c}}$, $\dot{\varepsilon}_{c\,ij}$, $\dot{\varepsilon}_{c\,min}$	Creep Strain Rate (Tensor, Component, Minimum Uniaxial)
$\varepsilon_{c\,EQ}$	Equivalent (von Mises) Creep Strain
$\varepsilon_{c\,f}$	Failure Creep Strain in a Uniaxial Creep Test
$\varepsilon_{c\,p}$	Creep Strain at the end of the Primary Creep Region in a Uniaxial Test
ε_j^{exp}	j^{th} Experimental Creep Strain
$\varepsilon_j^{pre}(\boldsymbol{x})$	j^{th} Creep Strain Predicted by the Constant set $\boldsymbol{x}$
σ_{APP}	Applied Stress
σ_R	Rupture Stress

ϕ	Precipitate Coarsening Damage Internal Variable (Dyson Model)
ω	Creep Damage (Kachanov and Liu-Murakami Models)
ω_2	Cavitation Damage Internal Variable (Dyson Model)

Chaboche Unified Visco Plasticity Model

a_i, C_i	Armstrong-Frederick Coefficients (i^{th} Back Stress Component)
b, Q, H	Drag Stress Material Constants
f	Yield Function
k	Initial Yield Surface Size
N	Loading Cycle Number
p	Accumulated Plastic Strain
R	Drag Stress
Z, n	Viscous Stress Material Constants
ε_v	Viscous Strain Component
ε_T	Total Strain
$\frac{\Delta\sigma}{2}$	Stress Range
$\frac{\Delta\sigma_i^{exp}}{2}$	Stress Range from Cyclic Experiments used to Optimise the Chaboche Model Constant Set $\boldsymbol{x}$
$\frac{\Delta\sigma(\boldsymbol{x})_i^{pre}}{2}$	Stress Range Predicted by the Chaboche Model (Using the Constant Set $\boldsymbol{x}$)
σ_0, n_0	Ramberg-Osgood Law Material Constants
σ_i^{exp}	Stress from Cyclic Experiments used to Optimise the Chaboche Model Constant Set $\boldsymbol{x}$
$\sigma(\boldsymbol{x})_i^{pre}$	Stress Predicted by the Chaboche Model (Using the Constant Set $\boldsymbol{x}$)
$\sigma_{\text{RELAX}\,i}^{exp}$	Relaxation Stress (During Strain Hold Loading) from Cyclic Experiments used to Optimise the Chaboche Model Constant Set $\boldsymbol{x}$
$\sigma(\boldsymbol{x})_{\text{RELAX}\,i}^{pre}$	Relaxation Stress (During Strain Hold Loading) Predicted by the Chaboche Model (Using the Constant Set $\boldsymbol{x}$)
$\boldsymbol{\chi}$	Back Stress Tensor
$\boldsymbol{\chi}'$, χ'_{ij}	Deviatoric Back Stress (Tensor, Component)
χ_i	i^{th} Uniaxial Back Stress Component

Component Modelling and Analysis

A, B, C, D, E, F, G, H, I	Fitting Coefficients (Parametric Equations)
D_O	External Pipe Diameter

Ex	Extrados Factor
$e_{In/Ex}$	Wall Thickness Variation (BS EN 13480)
h	Scoop Sample Cut Depth
In	Intrados Factor
I_Z	Second Moment of Area about the Z Axis
k	Loading Factor
M_Z	Bending Moment about the Z Axis
P_i	Internal Pressure
R_M	Mean Bend Radius
R_O, R_I	Pipe Cross Section Radii (Outer, Inner)
R_x, R_y, R_z	Rotational Displacement System Load Factors
r	Radial Position
Th	Wall Thickness
Th_{AV}	Average Wall Thickness
Th_{Ex}	Extrados Wall Thickness
Th_{In}	Intrados Wall Thickness
Th_{NOM}	Nominal Wall Thickness
$t_{f\,o}$	Reference Time to Failure
U_r, U_Z, U_θ	Displacement Components (Radial, Axial, Hoop)
U_x, U_y, U_z	Displacement Components (X, Y, Z)
X, Y, Z	Displacement System Load Factors
θ	Pipe Bend Circumferential Position Angle
σ_{APP}	Applied Stress
σ_{AX}	Closed End Axial Pressure
$\sigma_{AX\,A}$	Additional Axial Stress
$\sigma_{AX\,MAX}$	Maximum Allowable Axial Stress
$\sigma_{AX\,T}$	Total Axial Stress
σ_{MDH}	Mean Diameter Hoop Stress
$\hat{\sigma}_R$	Peak Steady State Rupture Stress
σ_r	Radial Stress
σ_{SS}	Steady-State Creep Stress
σ_z	Axial Stress
σ_θ	Circumferential Stress
φ	Pipe Bend Angle
$\hat{\omega}$	Peak Damage

Optimisation and Neural Networks

$E(\boldsymbol{x})$	Error Function in an Optimisation Algorithm
$\nabla E(\boldsymbol{x})$, $\nabla^2 E(\boldsymbol{x})$, $J(\boldsymbol{x})$	Gradient, Hessian and Jacobian Matrices in an Optimisation Algorithms

EXP_i	i^{th} Experimental Value
$F_i(\boldsymbol{x})$	i^{th} Objective Function
M_i	Number of Data Points Considered by the i^{th} Objective Function
$\max \left\lvert A_{ij}^{exp} \right\rvert$	Maximum Experimental Value of the j^{th} Type
$PRED_i$	i^{th} Predicted Value
r^2	Coefficient of Determination
W_i	i^{th} Weight for a Neuron in a Neural Network
w_j	Weighting Value for the j^{th} Objective Function
$\boldsymbol{X}$, X_i	Inputs to a Neural Network (Vector, Component)
$\boldsymbol{x}$	Vector of Parameters to be Optimised
Y	Local (Neuron) Output in a Neural Network
$\hat{Y}$	Output from a Neural Network
θ	Bias for a Neuron in a Neural Network
σ_{EXP}	Standard Deviation of Experimental Results

Abbreviations

2D	Two Dimensional
3D	Three Dimensional
AC	Alternating Current
ANN	Artificial Neural Network
BC	Boundary Condition
BCC	Body Centre Cubic
BPNN	Back Propagated Neural Network
BS	British Standard
CAE	Computer Aided Engineering
CDM	Continuum Damage Mechanics
CP	Combined Parallel Optimisation
CPH	Close Packed Hexagonal
DC	Direct Current
ECCC	European Creep Collaborative Committee
FCC	Face Centre Cubic
FEA	Finite Element Analysis
GL	Geometric Linear
GNL	Geometric Non-Linearity
GUI	Graphical User Interface
HAZ	Heat Affected Zone
LVDT	Linear Variable Differential Transformer
NDT	Non-Destructive Testing
NN	Neural Network

RBF	Radial Basis Function
RF	Radio Frequency
S	Series Optimisation
SEM	Scanning Electron Microscopy
SP	Separated Parallel Optimisation
SPCT	Small Punch Creep Test
TMF	Thermo-Mechanical Fatigue

List of Publications

Peer Reviewed Journal Publications

J. P. Rouse, M. Z. Leom, W. Sun, T. H. Hyde, A. Morris, "Steady-State Creep Peak Rupture Stresses in 90° Pipe Bends with Manufacture Induced Cross Section Dimension Variations" *International Journal of Pressure Vessels and Piping*, Volumes 105 - 106, May - June 2013, Pages 1 - 11.

J. P. Rouse, C.J.Hyde, W. Sun, T. H. Hyde, "Effective Determination of Cyclic-Visco-Plasticity Material Properties Using an Optimisation Procedure and Experimental Data Exhibiting Scatter" *Materials at High Temperatures*, Volume 12, July 2013, Pages 117 - 128.

J. P. Rouse, C.J.Hyde, W. Sun, T. H. Hyde, "Comparison of Several Optimisation Strategies for the Determination of Material Constants in the Chaboche Visco-Plasticity Model" *Journal of Strain Analysis*, Volume 48, August 2013, Pages 347 - 363.

J. P. Rouse, W. Sun, T. H. Hyde, A. Morris, "Comparative Assessment of Several Creep Damage Models" *International Journal of Pressure Vessels and Piping*, Volumes 108 - 109, August - September 2013, Pages 81 - 87.

J. P. Rouse, F. Cortellino, W. Sun, T. H. Hyde, J. Shingledecker, "Small Punch Creep Testing: A Review on Modelling and Data Interpretation" *Materials Science and Technology*, Volume 29, November 2013, Pages 1326 - 1345.

J. P. Rouse, W. Sun, T. H. Hyde, "The Effects of Scoop Sampling on the Creep Behaviour of Power Plant Straight Pipes" *Journal of Strain Analysis*, Volume 48, November 2013, Pages 494 - 511.

J. P. Rouse, C. J. Hyde, W. Sun, T. H. Hyde, "Pragmatic Optimisation Methods for Determining the Material Constants of a Visco-Plasticity Model from Isothermal Experimental Data" *Materials Science and Technology*, DOI–10.1179/1743284713Y.0000000277 (Available On-line 20th May 2013).

J. P. Rouse, W. Sun, T. H. Hyde, A. Morris, W. Montgomery, "A Method to Approximate the Steady-State Creep Response of 3D Pipe Bend FE (Finite Element) Models Under Internal Pressure Loading Using 2D Axi-Symmetric Models" *Journal of Pressure Vessel Technology*, DOI–10.1115/1.4025720 (Available On-line 10th September 2013).

N. O'Dowd, T. H. Hyde, W. Sun, S. B. Leen, T. P. Farragher, C. J. Hyde, J. P. Rouse, "Cyclic Visco-plasticity Testing and Modelling of a Service-aged P91 Steel" *Journal of Pressure Vessel Technology*, Under Review).

Peer Reviewed Conference Publications

J. P. Rouse, W. Sun, T. H. Hyde, A. Morris, "Comparative Assessment of Several Creep Damage Models" *13th International Conference on Pressure Vessel Technology (ICPVT-13)*, London, U.K., 20–23 May 2012.

C. J. Hyde, W. Sun, T. H. Hyde, J. P. Rouse, T. Farragher, S. Lean, N. O'Dowd, "Cyclic Visco-Plasticity Testing and Modelling of a Service-Aged P91 Steel" *2012 ASME Pressure Vessels and Piping Conference (PVP2012)*, Toronto, Canada, 15–19 July, 2012.

J. P. Rouse, C. J. Hyde, W. Sun, T. H. Hyde, "Optimisation Methods and Procedures for Determining the Chaboche Unified Visco-plasticity Model Material Constants from Experimental Data" *9th International Conference on Creep and Fatigue at Elevated Temperatures (ICCFET-9)*, London, U.K., 25–27 September 2012.

T. H. Hyde, F. Cortellino, J. P. Rouse, W. Sun, "Small Punch Creep Testing and Data Analysis of a P91 Steel at 650°C" *2nd International Conference on Small Specimen Testing Techniques*, Ostrava, Czech Republic, 2–4 October 2012.

Other

J. P. Rouse, W. Sun, T. H. Hyde, A. Morris, "A Framework for a Life Assessment "Toolbox" used to Evaluate Critical Power Plant Components" *Energy Materials Conference 2012: High Temperature Materials*, Poster Presentation, Loughborough, U.K., 16–17 October 2012.

F. Cortellino, J. P. Rouse, T. H. Hyde, W. Sun, J. Shingledecker, "Comparison of Interpretation Techniques for the Small Punch Creep Test Method for a High Temperature Steel" *Energy Materials Conference 2012: High Temperature Materials*, Verbal Presentation, Loughborough, U.K., 16–17 October 2012.

Contents

Chapter 1

Introduction

1.1 Background

The operating conditions of high temperature power plant components are complex. Often, systems will be cycled from full load, high temperature conditions to periods of inactivity (depending on market demands for power generation). Cycles will commonly not be periodic in nature. Furthermore, components within the system may be replaced as part of retrofit activities, giving rise to a range of materials with different deformation properties being used across the plant. Discontinuities are also present in piping runs in the form of weldments or bend sections. While necessary due to the space envelope constraints, material and geometric discontinuities are often regions of localised material degradation, potentially leading to failure. The above effects will only be exacerbated by the present trend in the power industry for existing plant to be operated at higher temperatures for longer periods and with a higher stop/start frequency. Clearly, if these more arduous generation patterns are to be adopted safely, careful analysis of what is already an intricate and detailed structure is critical.

While several design codes are available to practising engineers (such as, in the UK, PD5500 and the R5/R6 procedures) they are often over conservative and greatly simplify the analysis problem. While this is completely justified for these codes (their scope is often so large that close scrutiny would make them difficult to implement), the concern for the safety of components under new operating patterns remains. Power station operators will conduct regular inspections (known as outages, often taking place every 4 years). These may include material characterisation and ranking studies on "at risk" components or the inspection of specific components for any signs of degradation (such as surface micro-cracking through replica testing) or dimension change. This wealth of information is often archived and could be exploited fully with the use of more advanced analysis techniques.

1.2 Objectives

The objectives of the present research fall into four main categories. Firstly, the development of a piece of software acting as an analysis "toolbox". This will give a methodology for engineers to implement more advanced analysis techniques. Furthermore, the presence of bespoke piece of analysis software encourages inspection information to be collated between various departments. Secondly, advanced material models, capable of being used to predict a component's response under the complex loading conditions described above, will be compared and developed. In particular, methods to determine material constants for these models from experimental data will be analysed. Thirdly, novel material characterisation techniques that could be applied to high temperature power plant will be considered. Both advanced material models and novel characterisation techniques can be implemented in the analysis toolbox described previously. Finally, by way of examples, the procedures developed and compared in the previous three objectives will be applied to steam pipe bends. Weldments and pipe bends are the two most common discontinuities encountered in piping systems. While welds have received much research attention, bends, particularly exhibiting manufacture induced dimensional variation, have not been analysed to the same degree. Investigations in pipe bends will provide both novel information on these components as well as a vehicle to demonstrate the use of the analysis toolbox.

1.3 Thesis Layout

A literature review is presented at the beginning of this thesis (chapter 2) that details the present understanding of high temperature material behaviour and power plant component analysis. This will provide the reader with a background so the novelty of the research can be appreciated.

The research presented in this thesis is divided into three main sections, each dealing with the development of a different aspect of the analysis toolbox (material, geometry and loading/analysis).

The analysis of a component will depend on the determination of material properties for a suitably complex material model. This determination procedure will often require some form of optimisation, where initial estimates of material constant values are "fine tuned" so that the output of the material model matches the results of experiments as close as possible (note that the fitting quality may be limited due to, for example, experimental scatter in the optimisation data). Chapter 3 discusses several developments for the effective implementation of an optimisation procedure, particularly when a single set of material constants should be able to predict the results of multiple experiments. The optimisation procedure is developed for the Chaboche unified visco-plasticity model. The inclusion of this model in chapter 3 is also significant as a model similar to it will most likely be used in the future to predict the behaviour of high temperature

components which are cycled, and will therefore experience hardening due to plastic strain accumulation as well as creep effects. Operators may well want to determine material parameters for specific components as these can vary substantially between heats of material and due to different service histories. In such cases, novel small specimen techniques may be used to analyse a component's material (removal of a full size specimen would potentially compromise structural integrity). Scoop sampling is a method to remove small amounts of material from the surface of a component, however little research has been done to analyse the stress state in the vicinity of the scoop excavation. An investigation to this end is carried out in chapter 5 for high temperature pipe sections (deforming due to creep) that are subjected to internal pressure and system loading. Given that creep is a significant concern for materials operating at high temperatures, a comparison of several creep damage models is presented in chapter 4. Particular attention is paid to the differences in predicted failure times for a stress range lower than that used to determine a model's material constants. This is particularly relevant to component analysis, as it is common for accelerated high stress tests to be used to estimate material constants which are then applied to realistic low stress problems.

Pipe bend sections have not received as much attention as weld sections in research literature. Both however are discontinuities in the steam pipe system of a power plant and potential locations of failure. Pipe bend sections have been analysed in great detail in the present work (notably chapter 6) to demonstrate the applicability of the analysis methodology and to generate novel characterisation and analysis techniques for these specific components. Although the geometry of a pipe bend may seem simplistic, the manufacturing process used to create bends leads to variations in the wall thickness and cross section around the pipe bend. A method has been developed to characterise these dimension variations using industry data. In addition, a novel modelling procedure has been presented that allows for the estimation of the stress state in a three dimensional (3D) pipe FEA model from two dimensional (2D) cross section models.

Once a geometry, material and load condition have been defined for a component (such as a pipe bend section), some form of analysis is required in order to determine the stress state in the component and the potential for a reduction in remnant life. Several approximate parametric equations have been developed based on finite element analysis (FEA) studies that allow users to estimate peak rupture stresses for specific loading conditions. To extend the analysis capability of the methodology, a neural network (NN) has also been created that can estimate peak rupture stresses in a pipe bend due to the application of a complex system load condition. Subroutines have also been written that allow users to produce, run, and post process FEA models of power plant components. Several of the creep damage models discussed in chapter 4 have been incorporated into this feature. This work is detailed in chapter 7.

The foundation for an advanced analysis methodology has been established in this

thesis. Advances have been made in several key areas of the methodology and novel characterisation/analysis techniques have been developed. The developed methodology can be extended further (for example, to include alternative component types such as steam headers) in future research, which is summarised in chapter 8.

Chapter 2

Literature Review

2.1 Introduction

The analysis of high temperature components used for power generation requires an understanding of several key areas in engineering science. Materials will deform due to complex loading patterns with varying operating temperatures and applied forces. As a result, controlling deformation mechanisms will potentially change, compete or interact over a component's life. Prolonged exposure will often cause a structural change to the material, ultimately resulting in the degradation of the material, loss of load carrying capability and failure. Clearly, the application of advanced analysis methods requires the knowledge of materials, solid mechanics and characterisation methods. Additionally, to make any procedures developed relevant to practising engineers, an appreciation of the codes and methods currently adopted by industry is necessary. The following chapter discusses the present standing of these topics so that the novelty of the work included in this thesis may be appreciated.

2.2 The Structure of Materials and Deformation/Failure Mechanisms

2.2.1 Material Structure and the Solidification of Metals

Matter, in any state, is the formation of atoms that are bonded together. As atoms are brought into proximity with each other, bonding forces develop between the atoms. The distance between atoms is dependent on their relative species and is due to the equilibrium between the general attractive force between atoms and the repulsive force experienced at small distances. This inter atomic spacing and the type of bond formed has a direct influence on the structure of the material, and therefore its physical properties. The behaviour of a material will depend on its structure and how this structure changes with exposure to various external factors[1].

Although the understanding of ceramics and plastics has been greatly enhanced in recent years and their use is common in many areas, metals are still the predominant engineering material and will be for the foreseeable future. This is especially true in the design of high temperature components for power industry, where cost (for manufacture, instillation and maintenance) and resistance to deformation are the driving factors. For this reason, only metallic materials will be considered in the current review.

Metals are characterised by metallic bonds (as opposed to ionic or covalent primary bonds), whereby valence electrons are no longer localised to a particular atom, but rather form an "electron gas" which randomly circulates between atoms. Most metals used by engineers for component design are polycrystalline. A crystal is a periodic and repeating three dimensional assembly of atoms (this is distinct from an amorphous solid where no repeating order is observable[2]). This was originally described by von Laue in 1912[3] by observing the diffraction of x-rays in metallic crystals. In polycrystalline materials, several crystals (or grains as they are more commonly known) nucleate and grow during a metal's solidification. For metals, three main assemblies are considered (see figure 2.1), namely the face centred cubic (FCC), body centred cubic (BCC) and the close packed hexagonal (CPH)[1,4]. These structures dictate the location of lattice points, which should not be confused with the centre of an atom. Lattice points will indicate the location of a base (this may be a combination of several atoms of different species).

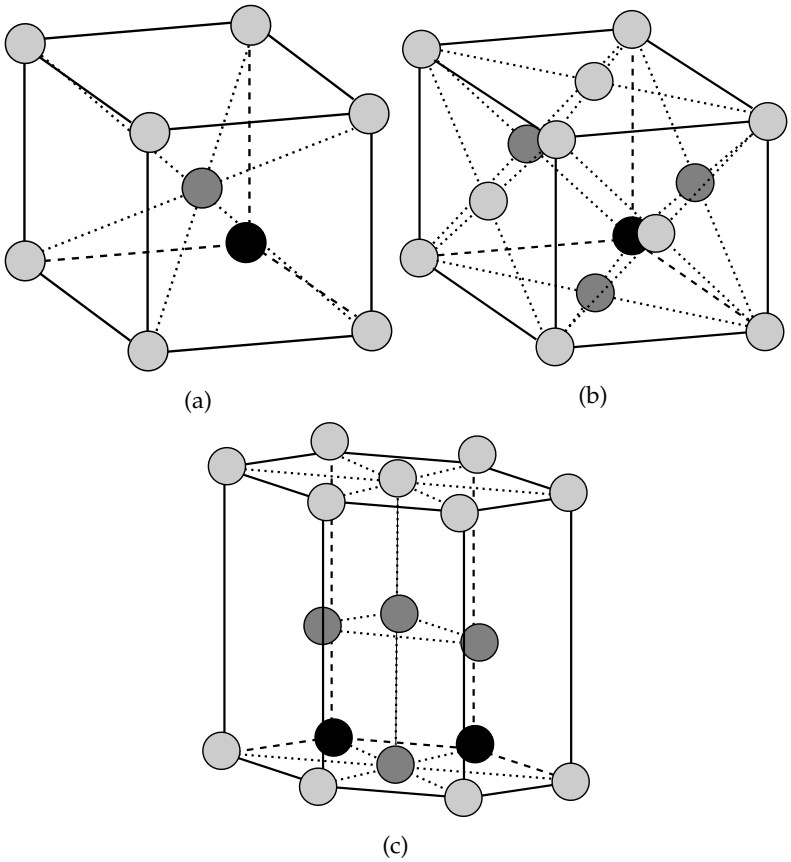

Figure 2.1: Common lattice patterns for metals. Structures shown are (a) the body centred cubic (BCC), (b) the face centred cubic (FCC) and (c) the close packed hexagonal (CPH) arrangements[1].

Solidification of molten metals is a key stage in the formation of a material's structure and physical properties of the material will be strongly dependent on this process. As the temperature of a melt is reduced the latent heat of solidification is released as thermal energy. In the disordered liquid metal, small crystals will nucleate at random points. Due to the remainder of the melt still being at a relatively high temperature, the smaller of these nucleation crystals will be destroyed. Only nucleation crystals above a critical size will survive and grow (the addition of atoms to the crystals at the expense of the melt). This homogeneous (random) nucleation is not commonly experienced in foundries however. Heterogeneous nucleation, where suspended impurities or foreign particles in the melt act as nucleation points, is more common for larger industrial melts. Heterogeneous nucleation results in smaller grains due to there generally being a greater number of nucleation points. It is very common in crystal development for growth to be preferential in certain directions (depending on the lattice structure). This causes crystals to develop in tree like "branches" called dendrites[4]. These dendrite structures will in turn grow by transferring latent heat into the surrounding melt (new dendrite limbs are therefore not formed in the immediate vicinity of one another, giving a regular dendrite shape). Eventually, the crystals will impinge on one another and, if a supply

of melt is unavailable, voids at the grain boundaries will be present. There is usually a misorientation between the atoms in adjacent grains (see figure 2.2). High (greater than 10°) angles of misorientation may be the result of the fine grain structure due to heterogeneous nucleation. These high angle grains will have high energy levels are likely to melt first should the metal be reheated. Lower angle ($5^{\circ} - 10^{\circ}$) misalignments can be caused by convection currents in the melt disturbing the dendrite structures[1].

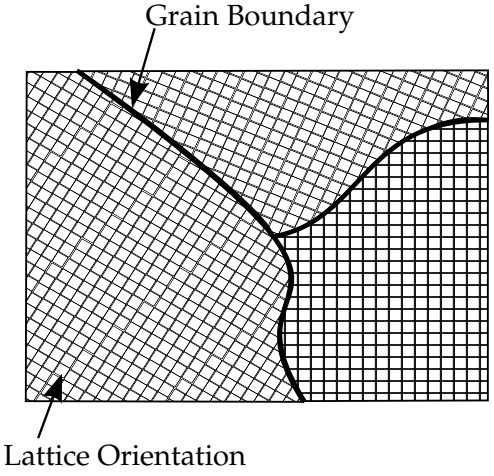

Figure 2.2: Illustration of grain boundaries showing lattice misalignment[1].

2.2.2 Defects, Deformation and Fracture

It has been identified already that most metals used for high temperature applications are polycrystalline. The presence of grain boundaries can be viewed as an imperfection in the structure as it leads to heterogeneous behaviour on the microscopic scale (however the randomised orientation of grain boundaries suggests homogeneous behaviour on the macroscopic level). Similar larger scale discontinuities in the material are cracks or the inclusion of gas bubbles and foreign matter. Although these defects tend to be the result of material processing it is important to recognise that defects are also present within the crystals themselves[1]. The deformation kinetics and characteristics of a material will be strongly dependent on both the formation of grains and the structure (including defects) of the crystals[1]. The inclusion of a defect in a material's structure may not result in an adverse effect, depending on the intended application of the material. Generally, defects in the crystal structure may be considered as one of four categories: point, line, planar (or wall[5]) and volume defects[1,4]. The most relevant defects (namely point, dislocation and void defects) will be briefly described, however it is worth pointing out that in many deformation situations a material's physical behaviour will be due to the complex interaction between several types of defects[5].

Although point defects are commonly small and their distortion effects are heavily localised in the lattice structure; vacancies, interstitial and substitutional atoms may play

a significant role due to their control of various other processes, such as the diffusion of atoms in the lattice or the motion of dislocations[4]. A vacancy is an empty space in the lattice structure where an atom would normally be expected (see figure 2.3). Similarly, an interstitial atom occurs when an atom is displaced from its normal location into an interstitial site (between normal locations, see figure 2.3). While interstitial atoms may be located at a multitude of potential locations within the structure and their analysis is therefore complex[2]; vacancies are generally much simpler to appreciate (it is simply the lack of a atom in a lattice location that may affect the placement of atoms around the vacancy) and play an important role in the motion of dislocations.

Vacancies tend to be created at certain locations within the crystal structure (when a sufficient amount of energy is available to break an atom's normal bonds, displace it, and reform the bonds at an interstitial location[5]). These preferred locations are known as vacancy sources and include the free surfaces of a crystal, a grain boundary or the half plane of atoms in an edge dislocation (discussed later in this section[1]). The production of vacancy in a material operating in high temperature conditions is an attempt to return the material back to an equilibrium condition[1]. When a heat source is removed, vacancies will tend to migrate to the vacancy source locations to be annihilated (these locations are now deemed vacancy sinks), again returning the material to equilibrium. It is worth noting that vacancies may be "frozen in" a material if the temperature is too low (meaning that there is not enough energy or time for vacancies to migrate) or if the material is rapidly cooled ("quenched"). More detail on the creation/annihilation of vacancies, particularly at edge dislocations, is given later in this section.

Substitution atoms are impurities (atoms of a different specie) that become part of the crystal structure. This may be due to remnants or previous melt in a foundry's crucible or a secondary metal that has been added intentionally as an alloying element. Substitutional atoms may be physically larger or smaller than "regular" atoms and will affect many physical properties of a material (for example, the doping of semiconductors to affect a material's electrical resistivity[5]). From a mechanical perspective, substitutional atoms may affect a material by solid solution or precipitate hardening[5].

Solid solution hardening is similar to the substitutional atom shown in figure 2.3, whereby an atom of a different specie takes the place of a regular atom. This is at least the case for a metallic substitutional atom in a metallic matrix (where both atoms are of a similar size[2]). Interstitial substitution may also occur if a significantly smaller substitution atom takes a location between lattice points[2]. These substitutional atoms will create "friction" that limits the migration of, say, dislocations. The solid solution structure may be developed further through precipitate hardening.

Precipitate hardening (or ageing) involves the production of a secondary "impurity" phase within the material that is soluble at high temperatures but exhibits decreasing solubility with decreasing temperature[3]. Generally, a solid material will be heat treated at an elevated temperature in order for a structure to develop with a homogeneous

spread of the impurity atoms. The material is then quenched, freezing this structure in place. An ageing process occurs (possibly during component operation) at a temperature lower than the heat treatment temperature, allowing the secondary phase particles to coalesce (forming "islands" of the impurity in the material matrix), as well as aiding in the removal of any frozen in vacancies. The secondary phase will impede the motion of defects such as dislocations and will significantly alter the characteristics of the material.

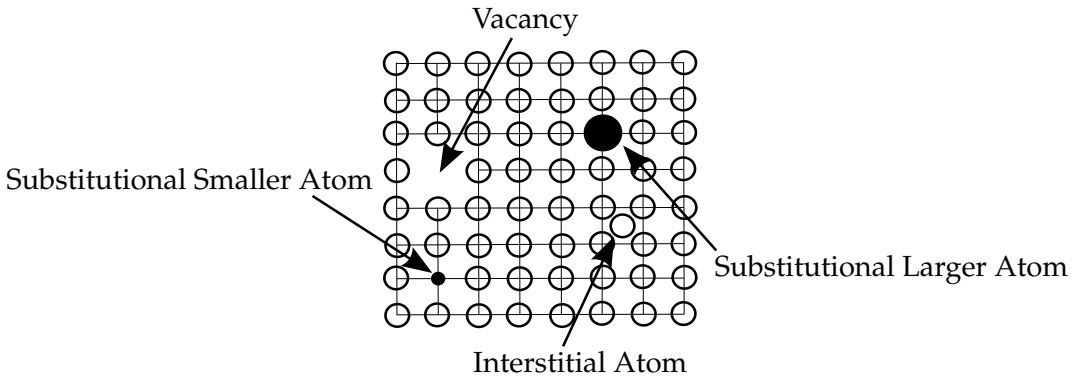

Figure 2.3: Illustration of point defects, such as vacancy, substitutional and interstitial atom defects in a material structure[1].

A crystal will typically not only include point defects but also a line of discontinuities running through the grain. These are known as dislocations and occur when a full plane of atoms in the lattice structure cannot form, therefore a "half plane" is wedged between two other lattice planes. Dislocations are critical for deformation processes as they allow a crystal structure to alter under the application of a load without destroying the crystal structure. The presence of dislocations is the main reason for the large discrepancy between Frenkel's theoretical approximation (published in 1926) of the slip of a crystal (whereby a plane on atoms acts as a rigid body, predicting that a crystal should be difficult to deform) and the observed reality (where crystal planes may slip on a localised or "half plane" scale)[1].

Dislocations may occur in many directions but can be resolved into two components, namely edge (see figure 2.4(a)) and screw components (see figure 2.4(b)). The difference between these dislocation types can be explained by considering the direction of the slip movement (known as the Burgers vector, characterised by b in figure 2.4) with respect to the dislocation line. If the Burgers vector is perpendicular to the dislocation line the component is an edge dislocation and if the Burgers vector is parallel it is a screw type dislocation[1,2].

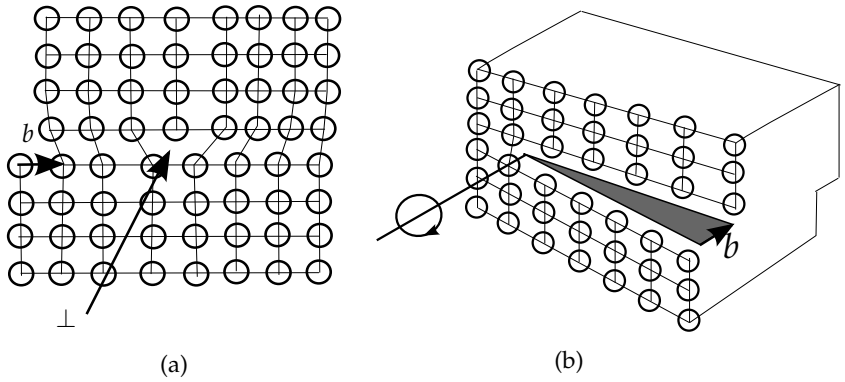

Figure 2.4: Dislocation structural defects, showing (a) an edge type and (b) a screw type.

The motion of dislocations (both individually and interacting with other dislocations) is a fundamental aspect of plastic deformation[5]. Attention will be paid to the glide or slip of an edge dislocation, however similar ideas may be translated to the case of a screw dislocation. Atoms away from the dislocation are generally in their minimum energy position (the lattice is relatively undisturbed from the defect free case), however the distortion caused by dislocation means that even small movements will allow the half plane to shift and line up with a corresponding half plane below the slip line (note here the extra half plane is assumed to be above the slip line, therefore the dislocation is said to be positive[1]). This can occur even under the application of relatively small shear loads. Of course, this leaves a half plane of atoms that are no longer aligned, therefore the dislocation has moved an atomic spacing[3]. When the half plane reaches a free surface a slip step of size b (the Burgers vector) is created. This dislocation motion is illustrated in figure 2.5. Note that prior to glide (figure 2.5 (a)) the half plane is between the atom planes 3 and 4 and after glide (figure 2.5 (b)) the half plane of atoms is between planes 4 and 5.

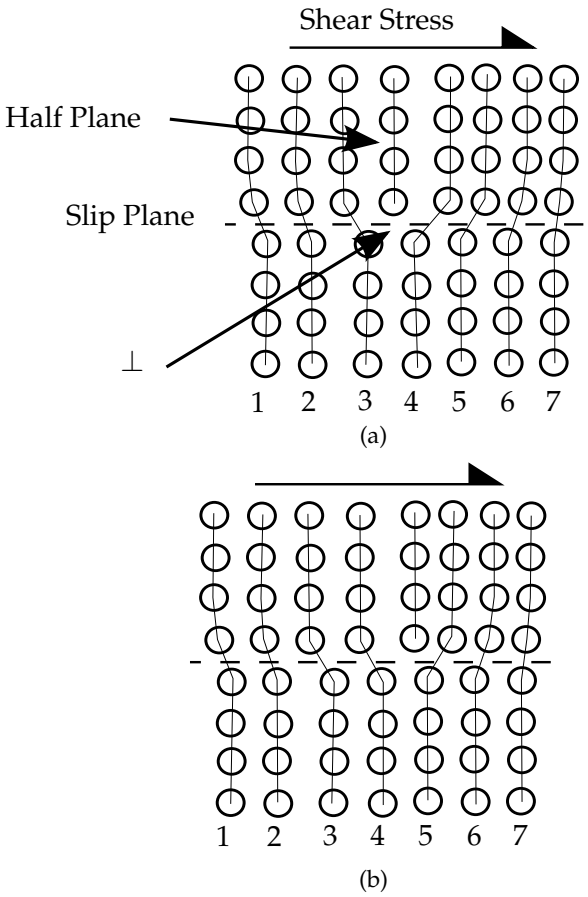

Figure 2.5: Movement of an edge dislocation by glide, showing (a) the lattice prior to the application of a shear stress and (b) after glide has occurred[1].

While the above description of the motion of a dislocation is valid for motion in the direction of a slip plane there are occasions when the half plane meets some obstruction, such as a secondary phase region or vacancy. To overcome this obstacle the dislocation will climb, resulting in a change in the number of atoms in the half plane (either a reduction or increase, depending on the obstacle encountered)[1]. It has been mentioned before that edge dislocations may act as vacancy sources or sinks. This is achieved through climb (shown in figure 2.6). A vacancy may be annihilated for example by a dislocation's half plane loosing an atom to fill the vacancy during motion (figure 2.6 (a)). Alternatively, a vacancy may be created if a dislocation's half plane gains an atom (figure 2.6 (b)).

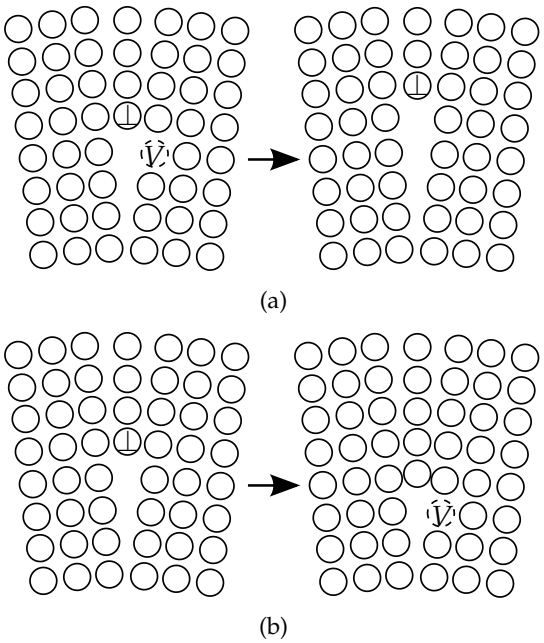

Figure 2.6: The climb of a dislocation (signified by $\perp$) to (a) annihilate a vacancy (signified by V, the dislocation acts as a vacancy sink) and (b) to create a vacancy (the dislocation acts as a vacancy source)[1].

Dislocations will commonly exist in annealed (heat treated) metals in low density networks. When a material is deformed by an increasing load these dislocations will multiply causing plastic (irrecoverable) deformation[6]. The increased dislocation density means that dislocation motion is increasingly difficult, resulting in the hardening of the material and a resistance to deformation. Some high temperature processes will enable recovery, where by diffusion through the crystal lattice or dislocation climb (see figure 2.6 (b)) annihilates a dislocation by emitting a vacancy and makes subsequent motion easier[7]. Dislocation entanglement and recovery are important physical mechanisms in the deformation of high temperature components.

The formation of voids (open areas in the material) is a noted feature in the failure (and fracture) of ductile materials[1]. These defects are required to nucleate as cavities (holes), grow and finally coalesce by localised necking in the intervoid ligaments[8] for the characteristic fibrous ductile failure (see figure 2.7 for an example of a ductile failure surface for a P91 steel tested at an elevated temperature) to be achieved[9]. Ductile fracture (which is the concern of this review due to the scope of the present work) is characterised by a slow moving crack in a specimen accumulating large amounts of plastic deformation[6]. This is in stark contrast to brittle failure, where little plastic deformation is observed and crack growth is often quick, leaving a smooth failure surface[10]. The presence of voids can be used as an indication of damage (a reduction in the ability of a material to carry a load) and, as a consequence of nucleation (there is a redistribution of stress and strain after de-bonding), a reduction in the hardening capability of the material[9]. The nucleation of a cavity can be achieved by several

mechanisms depending on the dominant deformation mechanism. In creep conditions (described in section 2.3.3) for example, cavities may nucleate by the following:

- The relative sliding of grain boundaries leading to cavities at compressive/tensile ledges and grain boundary triple-points (W type voids, see figure 2.8)[11].
- The condensation of vacancies in high stress regions such as grain boundaries (R type voids, see figure 2.8)[11].
- Dislocation "pile up" (known as the Zener-Stroh[12–14] mechanism), whereby dislocations stack up at an obstacle such as a grain boundary or secondary phase interface. The high amounts of energy released when dislocations coalesce generally results in the formation of a Zener-Stroh crack.
- Any of the above mechanisms acting in conjunction with a particle obstacle.

Creep cavities may then grow due to plastic straining, causing the diffusion of material (at low stresses) or the motion of dislocations[11]. If voids are distributed along grain boundaries, crack growth may be constrained by the creep of the rest of the material. High concentrations of voids along the grain boundaries could potentially lead to the unconstrained growth of an intergranular crack[15] (following the shape of grain boundaries and leaving a faceted failure surface, see figure 2.9), when the remaining ligaments of material cannot support the applied load and coalescence of voids occurs quickly[11].

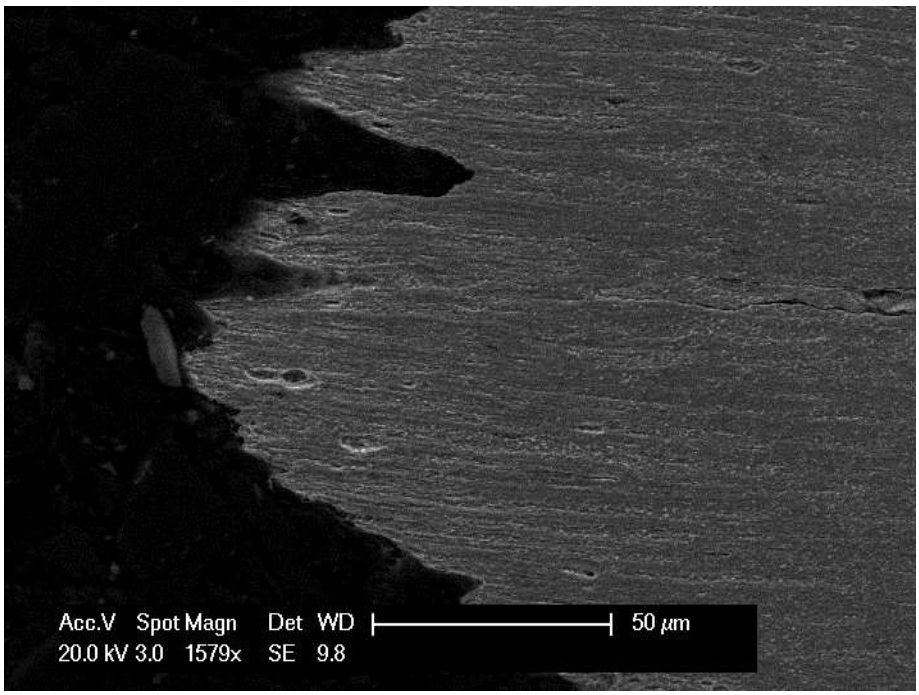

Figure 2.7: A scanning electron microscopy (SEM) image of the failed surface of a P91 steel loaded in tension at 600°C. Note the rough and fibrous failure surface and the voids that have not coalesced beneath the failure surface.

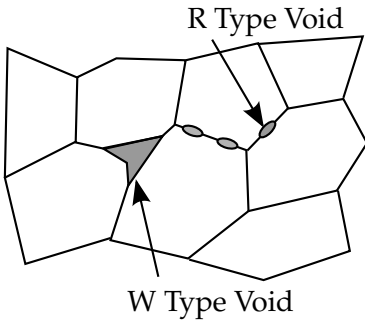

Figure 2.8: R and W type intergranular cavitations.

The fracture of a metal loaded cyclically (fatigue loading) is distinctly different to that of a material loaded monotonically and is mainly dependent on the nucleation of fatigue cracks[3,16]. These cracks may initiate at microscopic defects, such as particle inclusions in the material structure or processing induced voids[6], however a mechanism also exists for fatigue crack initiation in a defect free sample. Dislocation glide will cause staircase like structures at the surface of a material. Under cyclic loading, these structures become notch like[17]. The material around these notched areas will be damaged due to dislocation motion and micro-cracks initiate in these areas. Cracks will propagate in a transgranular direction (across grains, see figure 2.9) even if the initiated crack is intergranular[16]. The direction of crack propagation was originally described by Forsyth and is typically in the direction of the maximum shear stress. This initial crack growth can represent 40-99% of the fatigue life. Secondary crack growth is generally quick and occurs in the direction of maximum tensile stress (due to the remaining un-cracked specimen section being unable to support the applied load)[16].

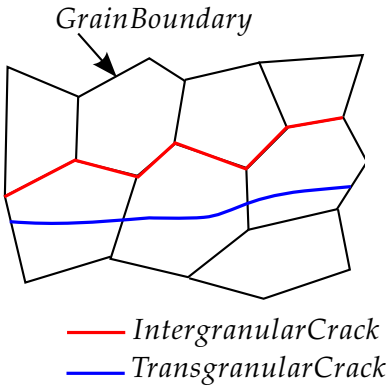

Figure 2.9: An illustration of intergranular and transgranular cracking.

2.3 Deformation Mechanisms

2.3.1 Elasticity and Concepts of Stress and Strain

When a body is loaded, it will initially deform in a fashion which is said to be elastic. This involves the stretching of inter atomic bonds and is recoverable. Providing that the yield stress of the material is not exceeded and loads are not cycled to a high amount or at a high frequency, an elastically deformed body will return to its original shape and size when a load is removed. Elasticity is said to be instantaneous as there is no time dependence to observed deformations. Before a detailed account of elasticity in materials can be given, it is necessary to define the fundamental quantities of interest in solid mechanics, namely stress and strain.

Fundamentally, normal strain may be considered a ratio of the change in dimensions of an element of material to a length value[18]. Engineering strain (ϵ, also known as average strain) normalises a change in length (ΔL) to the initial length of the element (L_0), see figure 2.10 and equation (2.1). For large deformation problems it is inconvenient to refer a change in length to the initial "gauge" length of an element. Normalising the change to an instantaneous dimension value (L) is commonly more useful and defines true strain (ε, see equation (2.2)). A true strain increment $d\varepsilon$ is found by dividing an instantaneous change in length (dL) by the instantaneous length of the element (L). The actual value of ε is found by integrating this incremental expression between limits (where L_0 is the initial length of the element and L_f is the final length), as shown in equation (2.2). For small deformations, ϵ and ε are identical.

$$\epsilon = \frac{\Delta L}{L_0} \tag{2.1}$$

$$\varepsilon = \int_{L_0}^{L_f} \frac{dL}{L} = \ln \frac{L_f}{L_0} \tag{2.2}$$

When a material is extended in one longitudinal direction it will contract in the other perpendicular lateral directions. Similarly, a compressive displacement will result in an increase in the lateral thickness of the element. In figure 2.10, the lateral strain is given by equation (2.3), where ϕ and ϕ_0 are instantaneous and initial lateral dimension values, respectively. S. D. Poisson[19] discovered that in the elastic region of deformation, ϵ_{long} (the longitudinal strain) and ϵ_{lat} (the lateral strain) could be related by the constant ν (Poisson's ratio, see equation (2.4)). This constant can take any value in the range $0 \leq \nu \leq 0.5$. A theoretical material may have no lateral deformation when it is axially loaded, giving the lower limit of $\nu = 0$. The upper limit of ν (0.5) is enforced by the definition of the bulk modulus (discussed later in section 2.3.1). No volume change will occur during plastic yielding, therefore $\nu = 0.5$ is assumed for plastic deformation (discussed later in section 2.3.2).

Deformation may not only result in a change in dimension but also a change in the

angle between two lines that were initially perpendicular. This is known as shear strain (γ), described by equation (2.5). Figure 2.11 shows the shear strain for a 2D square element of side length h. It is displaced by the force F_s a distance of a, resulting in a parallelogram deformed element.

$$\epsilon_{lat} = \frac{\phi_0 - \phi}{\phi_0} \tag{2.3}$$

$$\nu = -\frac{\epsilon_{lat}}{\epsilon_{long}} \tag{2.4}$$

$$\gamma \approx \tan\theta = \frac{a}{h} \tag{2.5}$$

Stress is a measure of force per unit area. Using SI units, it is defined in terms of Newtons (N) per meter squared (m^2), or more commonly known as Pascals (Pa). As with strain, stress may act in a normal or shear direction, see figures 2.10 and 2.11, respectively. A force F may be applied in a direction that is perpendicular to an area A, giving rise to the normal stress σ (defined by equation (2.6)). For a shear stress τ, a force (F_s) is applied parallel to a surface (of area A_s), see equation (2.7).

$$\sigma = \frac{F}{A} \tag{2.6}$$

$$\tau = \frac{F_s}{A_s} \tag{2.7}$$

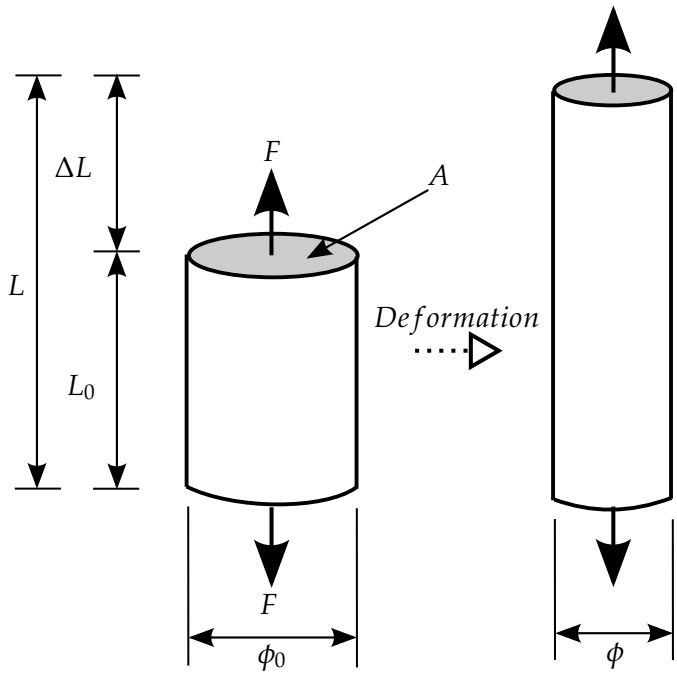

Figure 2.10: A cylindrical element undergoing deformation due to the application of a normal load.

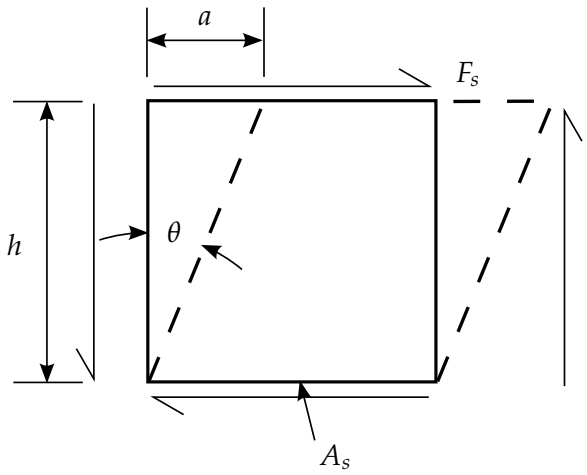

Figure 2.11: The shear loading of a rectangular element[3].

Often, it is necessary to define the stresses and strains which act on a body in multiple directions. This is done through the use of tensors, which will be derived for strain and stress in the following sections.

The Strain Tensor

A body is said to be deformed if there has been some change in its shape or volume due to the application of a load. A body will deform to some extent with the application of any load. In general, every point in a body experiences some translation in space when

the body is deformed. Consider a point in a body defined by the Cartesian coordinates $x = x_1$, $y = x_2$ and $z = x_3$. After the deformation, the same point has the coordinates $x = \acute{x_1}$, $y = \acute{x_2}$ and $z = \acute{x_3}$. The displacement vector ($\boldsymbol{u}$) of the point may be given by equation (2.8) in the direction i, where $i = 1, 2, 3$. Clearly, $\acute{\boldsymbol{x}}$ is a function of $\boldsymbol{x}$, and therefore $\boldsymbol{u}$ is also a function of $\boldsymbol{x}$.

$$u_i = x_i - \acute{x_i} \tag{2.8}$$

Suppose that two points in the body are now considered. The scalar distance between these two points before and after deformation (dl and $d\acute{l}$) would be given by the difference in the point vectors $d\boldsymbol{x}$ and $d\acute{\boldsymbol{x}}$, respectively (see equation (2.9)).

$$\begin{aligned} dl &= \sqrt{\left(dx_1^2 + dx_2^2 + dx_3^2\right)} \\ d\acute{l} &= \sqrt{\left(d\acute{x}_1^2 + d\acute{x}_2^2 + d\acute{x}_3^2\right)} \end{aligned} \tag{2.9}$$

The deformed vector $d\acute{\boldsymbol{x}}$ is a function of $d\boldsymbol{x}$, therefore $d\acute{l}^2 = \sum_{i=1}^{3} \left(dx_i + du_i\right)^2$. The deformation gradient in the direction i (du_i) is found by summing the contributions to u_i in the directions x_1, x_2 and x_3, i.e. $du_i = \sum_{j=1}^{3} \left(\delta u_i / \delta x_j\right) dx_j$. Equation (2.10) is found by substituting this into the expression for $d\acute{l}^2$ and expanding. Note that when using Einstein notation, a summation ($\sum$) is implied when an index is used twice in the same term[20]. Equation (2.10) may therefore be written in a more compact form (see equation (2.11)).

$$d\acute{l}^2 = \sum_{i=1}^{3} \left(dx_i^2 + \sum_{j=1}^{3} \left(2\frac{\delta u_i}{\delta u_j} dx_i dx_j + \sum_{k=1}^{3} \frac{\delta u_i}{\delta x_j} \frac{\delta u_i}{\delta x_k} dx_j dx_k \right) \right) \tag{2.10}$$

$$d\acute{l}^2 = dl^2 + 2\frac{\delta u_i}{\delta x_j} dx_i dx_j + \frac{\delta u_i}{\delta x_j} \frac{\delta u_i}{\delta x_k} dx_j dx_k \tag{2.11}$$

The second term in equation (2.11) is summed over two dimensions (i and j), is symmetric and may be written in the form shown in equation (2.12). Equation (2.11) may be written as equation (2.13) if this substitution is made, where u_{ij} is given by equation (2.14). The tensor u_{ij} represents a normalised change in length (i.e. the change in an element length) and is known as the strain tensor. It is more commonly given by the symbol ε_{ij}.

$$\left(\frac{\delta u_i}{\delta x_j} + \frac{\delta u_j}{\delta x_i} \right) dx_i dx_j \tag{2.12}$$

$$d\acute{l}^2 = dl^2 + 2u_{ij} dx_i dx_j \tag{2.13}$$

$$u_{ij} = \varepsilon_{ij} = \frac{1}{2} \left(\frac{\delta u_i}{\delta x_j} + \frac{\delta u_j}{\delta x_i} + \frac{\delta u_k}{\delta x_i} \frac{\delta u_k}{\delta x_j} \right) \tag{2.14}$$

In most engineering situations, displacements are small in comparison to a component's dimensions, meaning the last term in equation (2.14) becomes small and is negligible. The strain tensor can therefore be written as equation (2.15). The fully expanded strain matrix may also be seen in equation (2.15). A generalised co-ordinate system has been used here (directions 1, 2 and 3), however it may be transposed to any system notation (such as x, y, z). Note that the shear strain components of the tensor $\boldsymbol{\varepsilon}$ are those where $i \neq j$, equivalent to γ in section 2.3.1. For shear strains, deformation is said to act on the i^{th} plane in the j^{th} direction. A co-ordinate system may be chosen for the strain tensor such that all shear components are zero. In this case, only the diagonal components (ε_{11}, ε_{22} and ε_{33}) have the potential to be non-zero. These are known as the principal strains (acting in the principal directions 1, 2 and 3).

$$\boldsymbol{\varepsilon} = \frac{1}{2}\left(\frac{\delta u_i}{\delta x_j} + \frac{\delta u_j}{\delta x_i}\right) = \begin{vmatrix} \varepsilon_{11} & \varepsilon_{12} & \varepsilon_{13} \\ \varepsilon_{21} & \varepsilon_{22} & \varepsilon_{23} \\ \varepsilon_{31} & \varepsilon_{32} & \varepsilon_{33} \end{vmatrix} \tag{2.15}$$

The Stress Tensor

Consider the forces acting on the deformed body described in figures 2.10 and 2.11. The presence of external loads (forces or temperature changes that would cause deformation) acting on the body to deform it will mean that the atoms in the body cease to be in a state of thermal equilibrium. Internal forces are generated in order to restore this equilibrium[21]. The pressures caused by these internal forces applied over finite areas are called stresses.

Forces may be split into two categories. Body forces act on a volume or mass (examples of these are gravitational or electromagnetic effects), whereas surface forces act over an area (for example, pressure). The total force applied to a body may therefore be given by the volume integral (over the volume dV) of the vector $\boldsymbol{F}$ (the force per unit volume) shown in equation (2.16). In order for continuity to be maintained, the forces on an element of material can be considered to be applied on that elements surfaces by the neighbouring elements. In short, the required resultant force may be given as a surface integral[21].

$$\int \boldsymbol{F} dV \tag{2.16}$$

Each component of $\boldsymbol{F}$ may be integrated over a volume in the i^{th} direction by $\int F_i dV$. In the same way that the integral of a scalar over an arbitrary volume can be transformed into a surface integral if the scalar is the divergence of a vector, a vector integrated over a volume may be transformed into a surface integral if the vector is the divergence of a second order tensor (see equation (2.17), where σ_{ik} is a second order tensor known as the stress tensor). A resultant force component may therefore be written as equation (2.18), where the stress tensor σ_{ik} is integrated over the surface element df_k[21].

$$F_i = \sum_{i=1}^{3} \frac{\delta \sigma_{ik}}{\delta x_k} \tag{2.17}$$

$$\int F_i dV = \oint \sigma_{ik} df_k \tag{2.18}$$

As discussed briefly in the introduction to section 2.3.1, stresses may be considered to act in normal (perpendicular) or shear (tangential) directions. Components of stress acting on a body are shown in figure 2.12, where a generalised co-ordinate system is used (directions 1, 2 and 3). Note that the first of the indices in each stress component will denote which surface the stress acts on and the second index defines the direction. Elements of σ_{ik} where $i = k$ are therefore normal stresses. The stress tensor is expressed by equation (2.19). A co-ordinate system may be chosen such that only the diagonal components of the stress tensor are non-zero. Theses are known as principal stresses[3]. The angular moment on the element shown in figure 2.12 should be equal to 0 for small deformations (the body is in equilibrium). For this to be the case, shear stresses are considered to act in complementary pairs, i.e. $\sigma_{ij} = \sigma_{ji}$ when $i \neq j$. The stress tensor is therefore diagonally symmetric with six independent real values.

$$\boldsymbol{\sigma} = \begin{vmatrix} \sigma_{11} & \sigma_{12} & \sigma_{13} \\ \sigma_{21} & \sigma_{22} & \sigma_{23} \\ \sigma_{31} & \sigma_{32} & \sigma_{33} \end{vmatrix} \tag{2.19}$$

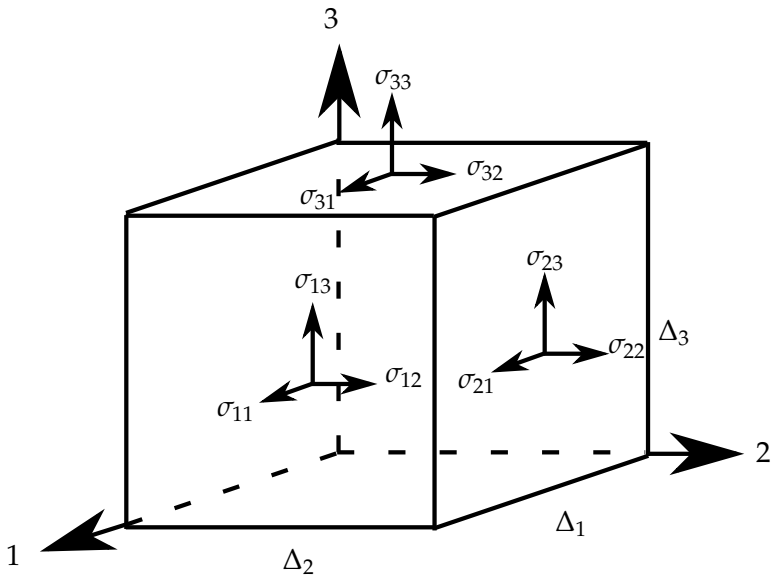

Figure 2.12: The resolved stresses acting on a cubic element[3].

The stress tensor itself may be divided into a hydrostatic (or mean) and deviatoric tensors. Hydrostatic stresses represent the tensile or compressive state of a loaded body, giving rise to a change in its volume. Deviatoric stresses represent the shear stress state causing a distortion of the body (a change in its shape). The mean stress (σ_m) is given by the average of the normal stresses (equation (2.20)). All non-diagonal components of the hydrostatic stress tensor are zero and the diagonal components are equal to σ_m (the hydrostatic stress tensor is isotropic). The deviatoric stress tensor (S_{ij}) is found by subtracting σ_m from the normal components of $\boldsymbol{\sigma}$, as shown in equation (2.21). Note that the symbol δ_{ij} is known as the Kronecker delta and is defined by equation (2.22)[3].

$$\sigma_m = \frac{\sigma_{11} + \sigma_{22} + \sigma_{33}}{3} \tag{2.20}$$

$$S_{ij} = \sigma_{ij} - \sigma_m \delta_{ij} \tag{2.21}$$

$$\delta_{ij} = \begin{cases} 1, & \text{if } i = j. \\ 0, & \text{if } i \neq j. \end{cases} \tag{2.22}$$

Elasticity

Stresses and strains have been defined in the previous sections based purely on static and geometric relationships, however they may be related to one another by a material behaviour model. These material models are known as constitutive equations[3]. For small displacements, deformations are recoverable (i.e. the body will return to its original shape and size upon the removal of the load) and is said to be elastic. Larger deformations may result in yielding of a material. This permanently alters the structure of the material, meaning that after the load is removed there will be some residual (unrecovered) deformation. This type of deformation is said to be plastic (see section 2.3.2).

For elastic deformations (which are dependent on the stretching of inter-atomic bonds[21]), Hooke's law (named in honour of its originator Robert Hooke[22]) may be used to relate stress and strain. In a one dimensional case, a stress (σ) may be found from a corresponding elastic strain (ε) by a material dependent constant (E). This material constant is known as the modulus of elasticity or Young's modulus (named after Thomas Young who investigated this phenomenon extensively). The proportional relationship between σ and ε is shown in equation (2.23). Young's modulus can be determined from tensile material tests. A material sample will initially deform with a linear relationship between stress and strain (provided stresses are less than the yield stress σ_Y are considered). The gradient of this linear deformation is equal to E (see figure 2.13).

$$\sigma = E\varepsilon \tag{2.23}$$

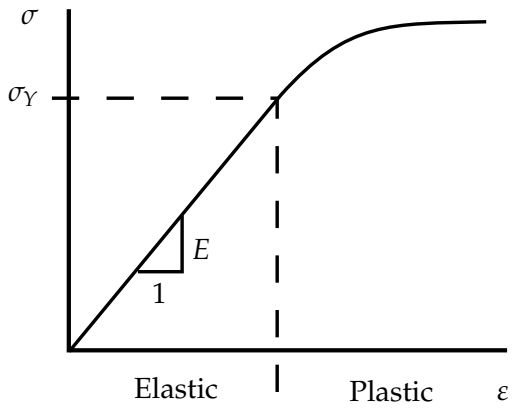

Figure 2.13: A typical elastic/plastic behaviour of a metallic material in stress/strain space[18].

Poisson's ratio has been introduced earlier to relate strains in the normal and transverse directions. Therefore, using the one-dimensional definition of Hooke's law and Poissons ratio, a generalised three dimensional version of Hooke's law can be derived (see equation (2.24)). This allows for the calculation of the elastic strain in one of the normal directions (1, 2 or 3) using the three stresses in the normal directions (or vice versa). It is assumed here that the material is isotropic (the material has the same properties in all directions) and homogeneous (there is no variation in material properties over the body). While some degree of anisotropy and inhomogeneity is common in metallic materials, these assumptions are often applied to analysis problems and are used in the present work[3].

$$\varepsilon_{11} = \frac{1}{E}\left[\sigma_{11} - \nu\left(\sigma_{22} + \sigma_{33}\right)\right]$$

$$\varepsilon_{22} = \frac{1}{E}\left[\sigma_{22} - \nu\left(\sigma_{11} + \sigma_{33}\right)\right] \tag{2.24}$$

$$\varepsilon_{33} = \frac{1}{E}\left[\sigma_{33} - \nu\left(\sigma_{11} + \sigma_{22}\right)\right]$$

An elastic shear strain can be related to a shear stress by the modulus of elasticity in shear (G, determined from torsion tests[3]). The linear relationship between shear stress and strain can be seen in equation (2.25). If an element under pure shear is considered (i.e. the normal stresses are equal to 0) it can be shown (by orientating the material element correctly) that the maximum and minimum principal stresses are $\pm\sigma_{ij}$ (where σ_{ij} is the pure shear stress that was originally applied, therefore $i \neq j$), with an intermediate principal stress equal to zero. Substituting these values into Hooke's law (equation (2.24)), the maximum strain is found to be equation (2.26). Through rearrangement of this expression, a relationship between E, ν and G can be derived as

shown in equation (2.27)[18].

$$\sigma_{12} = G\varepsilon_{12}$$

$$\sigma_{23} = G\varepsilon_{23} \tag{2.25}$$

$$\sigma_{13} = G\varepsilon_{13}$$

$$\varepsilon_{max} = \frac{\sigma_{ij}}{E}(1+\nu) = \frac{\varepsilon_{ij}}{2} \tag{2.26}$$

$$G = \frac{E}{2(1+\nu)} \tag{2.27}$$

Another important quantity that describes elastic deformation is the bulk modulus K. If the principal strains in Hooke's law are summed, the change in volume or volumetric strain (Δ, also known as the hydrostatic dilation), may be determined. K is a ratio between the hydrostatic stress and the volumetric strain. Noting equation (2.28) and recalling the definition of σ_m (equation (2.20)), an expression for K can be derived in terms of E and ν, see equation (2.29)[3]. Most metals have a Poisson's ratio of approximately a third, therefore $K \approx E$. If a material experiences no volume change under hydrostatic loading it will have a K value equal to infinity. A theoretical maximum for ν therefore exists at 0.5[18].

$$\Delta = \frac{1-2\nu}{E}(\sigma_{11} + \sigma_{22} + \sigma_{33}) \tag{2.28}$$

$$K = \frac{E}{3(1-2\nu)} \tag{2.29}$$

2.3.2 Plasticity

If the yield stress of a material (σ_Y) is exceeded during loading, inter atomic bonds will be broken and reformed[21,23]. This causes a permanent change to the structure of the material. If the load is removed, elastic deformation will be recovered however there will be some un-recovered "plastic" deformation (as shown in figure 2.14). When the load is removed after elastic/plastic deformation, the stress in the material element will linearly approach zero with a gradient equal to the linear elastic deformation gradient (Young's modulus E, see figure 2.14)[23].

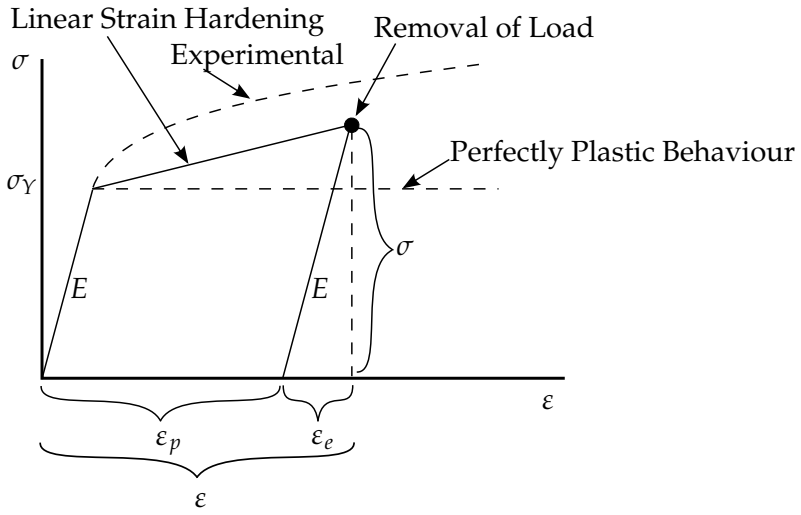

Figure 2.14: Representations of elastic/plastic behaviour and the effect of unloading after plastic deformation[23].

Several models have been proposed to approximate this behaviour, the simplest being the elastic-perfectly-plastic model shown in figure 2.14 where no hardening behaviour is assumed and prolonged elongation of the specimen accumulates plastic strain with no increase in stress (defined mathematically by Melan[24,25] and based on the work of Prandtl[25,26]). Potentially large errors in plastic stresses and strains are noticed however if these simple models are applied, therefore some form of hardening is required. The modelling of hardening is often dependent on the concept of a yield surface, which will now be introduced.

It is a relatively easy matter to estimate at what stress a material begins to yield from a uniaxial tensile test by observing the point the stress versus strain curve begins to become non-linear. In many situations however, loads will act in several directions simultaneously. Generalised criteria are therefore required to estimate when multiaxial yielding will occur. These are known as yield criteria. It is important to note that yielding will occur due to shear loading as plasticity is controlled by the motion of dislocations (recall the crystallographic slip described in section 2.2.2). As plasticity is a shearing process, it will not be dependent on the hydrostatic stress σ_m (see the definition of the deviatoric stress in equation (2.20)). As only hydrostatic stress alters a body's volume, plasticity can be regarded as a constant volume process[23].

Two yield criteria are presented here which are applicable to ductile materials, namely the Tresca and von Mises yield criteria, shown in figure 2.15[27]. The Tresca criterion (also known as the maximum shear stress criterion) assumes that yielding will occur when the maximum shear stress reaches a critical value (σ_Y). In short, yielding will occur if one of the conditions shown in equation (2.30) are met, where σ_1, σ_2 and σ_3 are the principal stresses. Alternatively, the von Mises criterion is determined by assuming that yielding will occur when a maximum shear strain energy is exceeded,

see equation (2.31)[27]. This work was based on the total strain energy components proposed by Huber and the observation of Maxwell that plasticity is not dependent on the hydrostatic component of this strain energy[27]. There is a great deal of experimental evidence, collected by observing yielding under multiaxial conditions, that supports the von Mises yield criterion, particularly in metals[3,27].

Given that yielding is not dependent on the hydrostatic stress yield criterion, when plotted in principal stress space (i.e. with axis directions σ_1, σ_2 and σ_3), will be prismatic with the hydrostatic axis ($\sigma_1 = \sigma_2 = \sigma_3$) along its centre (see figure 2.15 (a)). A yield surface may be considered if the prism is viewed down the hydrostatic axis, known as the deviatoric plane (see figure 2.15 (b))[28]. It is common to view the yield criterion on the deviatoric plane so that critical deviatoric components of stress can be easily observed, along with any changes to the yield surfaces as a result of hardening .

$$\begin{aligned} |\sigma_1 - \sigma_2| &> \sigma_Y \\ |\sigma_2 - \sigma_3| &> \sigma_Y \\ |\sigma_3 - \sigma_1| &> \sigma_Y \end{aligned} \tag{2.30}$$

$$\sigma_Y = \frac{1}{\sqrt{2}}\sqrt{(\sigma_{11} - \sigma_{22})^2 + (\sigma_{22} - \sigma_{33})^2 + (\sigma_{33} - \sigma_{11})^2 + 6\left(\sigma_{12}^2 + \sigma_{23}^2 + \sigma_{31}^2\right)} \tag{2.31}$$

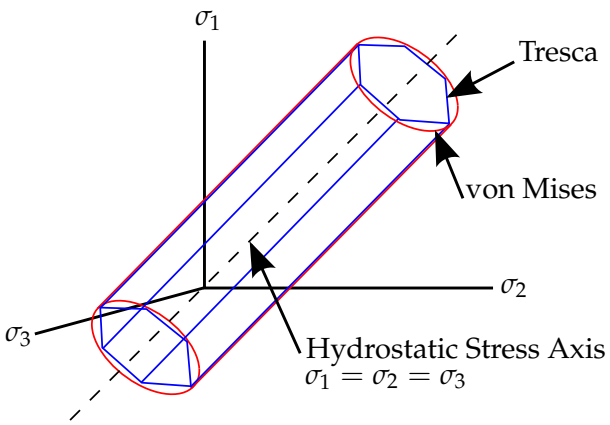

(a)

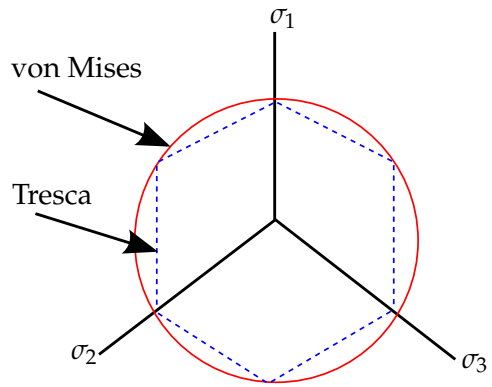

(b)

Figure 2.15: The Tresca and von Mises yield criteria in principal stress space, showing (a) the yield prisms and (b) the yield surfaces viewed from a deviatoric (π) plane (the hydrostatic axis points out of the page).

The effect of the hydrostatic stress on the yield criterion can be verified by considering figure 2.16. The von Mises criterion is shown here for a body with an arbitrary stress B applied (represented by the vector $\vec{OB}$). It is clear that the vector $\vec{OA}$ is the hydrostatic component of $\vec{OB}$ and $\vec{AB}$ is the deviatoric component. Note that every point on the deviatoric plane has the same hydrostatic stress. If a second stress (D) is considered, it is evident that $\vec{AB} = \vec{CD}$. In other words, although the stress D is greater than B, no yielding has occurred as the deviatoric components of the stresses are the same in both cases. To consider yielding, a single deviatoric plane is therefore required. This reference plane is known as the π plane and has a zero hydrostatic stress ($\sigma_m = 0$, see figure 2.15) (b)[28].

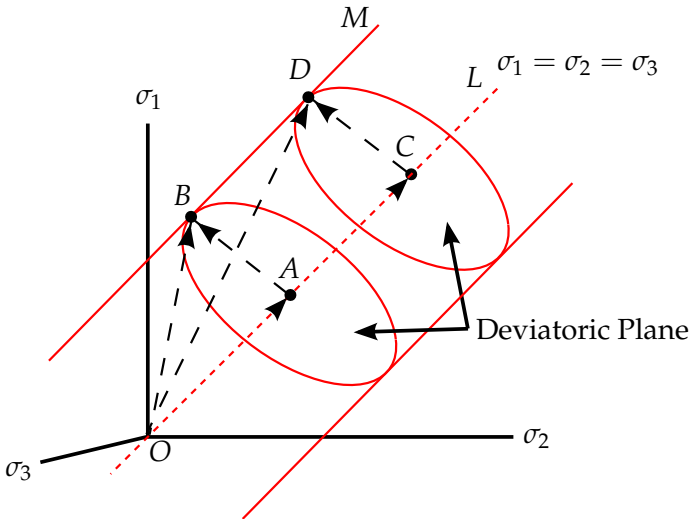

Figure 2.16: An illustration of the effect of hydrostatic stress on the von Mises yield criterion[28].

When a material hardens (note that harden is used as a general term and could involve the physical softening of a material) the yield surface undergoes some form of change. How this change is represented is dependent on the material model applied and is defined by the yield function. Two distinct forms of yield surface alteration are observed, the effects of which can be seen in principal stress space in figure 2.17. Given some initial yield condition, isotropic hardening (figure 2.17 (a)) will cause the uniform expansion of the yield surface[29–31]. Kinematic hardening on the other hand will not affect the size of the yield surface but rather its orientation[29–31], causing an offset in some direction (figure 2.17 (b)). It has been remarked that in the initial stages of plasticity, kinematic effects will be the dominant hardening mechanism, however isotropic effects will become more pronounced under cyclic conditions (see section 2.3.4)[32,33]. The models presented here for the description of hardening under a monotonic plastic load are therefore largely concerned with describing the translation of a yield surface (kinematic hardening).

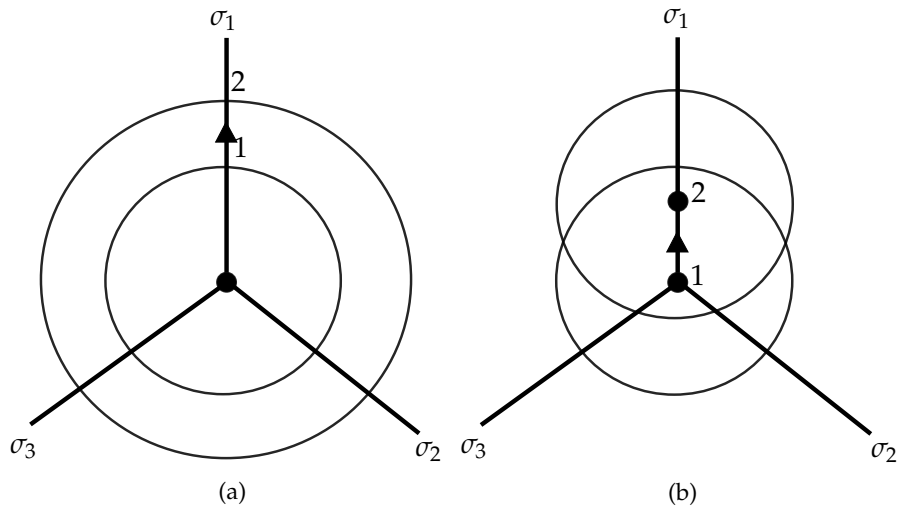

Figure 2.17: Types of yield surface alteration (hardening) due to the application of plastic strain, showing (a) isotropic hardening and (b) kinematic hardening.

Considering the scenario where combined isotropic and kinematic hardening behaviour takes place, equation (2.32) can be derived for a limiting case[32,34]. Note that, so long as f is less than or equal to zero, no hardening takes place and the deformation is assumed to be elastic.

$$f = \phi\left(\sigma_{ij} - \alpha_{ij}\right) - F\left(\beta\right) - k = 0 \tag{2.32}$$

where α_{ij} represents a translation in the yield surface (due to kinematic hardening) and β is a scalar quantity that defines the size of the yield surface (that may be altered due to isotropic hardening). The quantity k represents the initial size of the yield surface. The function ϕ determines a scalar equivalent for the difference between the centre of the yield surface (defined by α_{ij}) and the applied stress (σ_{ij})[35]. Clearly, if α_{ij} is equal to 0, pure isotropic hardening will be predicted, and if β remains constant, pure kinematic work hardening is modelled[32]. In the short term, kinematic work hardening is the more realistic as it accounts for the Baushinger effect (where a variation in yield stress is observed when plastic loads are cycled) and anisotropy due to plastic deformation[32], however its predictive capability can be compromised if more complex loading histories are considered. Prager suggested equation (2.33) for the yield surface translation increment ($d\alpha_{ij}$)[36].

$$d\alpha_{ij} = c d\varepsilon_{p\,ij} \tag{2.33}$$

The translation increment is dependent on a material constant c, known as the hardening modulus[32], and the increment of plastic strain ($d\varepsilon_{p\,ij}$). The yield surface is taken to translate in the direction on the outward unit normal to the yield surface[32] (see figure 2.18). Note this direction is distinctly different to the modification proposed by Ziegler, where the yield surface translation increment is dependent on a multiplier ($d\mu$)

that is greater than zero and will move in the direction of a vector between the centre of the yield surface and the stress point[37], see equation (2.34). Note that a Tresca yield criterion is used in figure 2.18 to highlight the difference between an increment normal to the yield surface (known as the normality rule, as used in Prager's model) and an increment in the direction of the stress vector (as it is in Ziegler's model).

$$d\alpha_{ij} = d\mu \left(\sigma_{ij} - \alpha_{ij}\right) \tag{2.34}$$

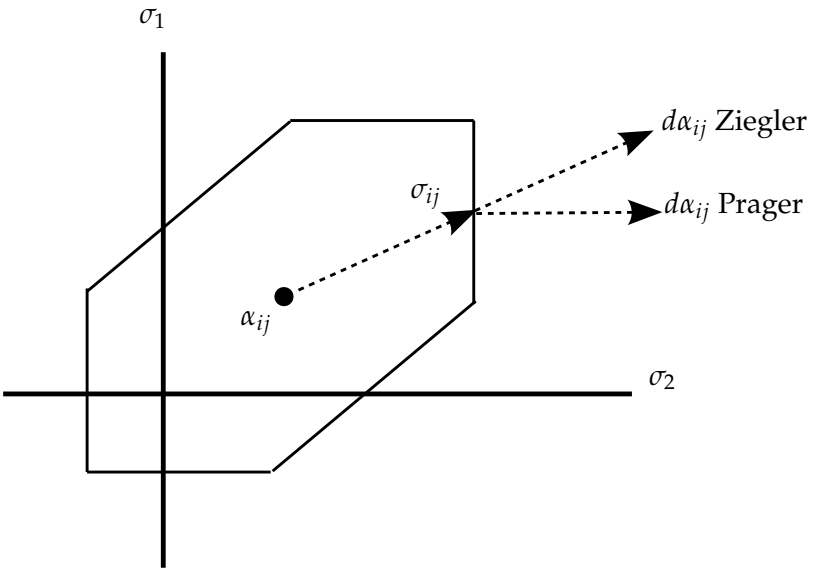

Figure 2.18: An illustration of the differences in the Prager and Ziegler hardening models when applied to a Tresca yield surface.

According to the classical normality rule (which has been shown to be a good approximation of plasticity in metals), plastic strain increments will accumulate in the direction of the normal to the yield surface[3], and can be determined by equation (2.35)[34]. The direction of the plastic strain increment ($d\boldsymbol{\varepsilon_p}$) is given by $\frac{\delta f}{\delta \boldsymbol{\sigma}}$, with plastic strain magnitudes dependent on the plastic multiplier ($d\lambda$).

$$d\boldsymbol{\varepsilon_p} = d\lambda \frac{\delta f}{\delta \boldsymbol{\sigma}} \tag{2.35}$$

For conformity to other models, the translation of the yield surface is redefined as the kinematic stress tensor $\boldsymbol{\chi}$, or back stress as it is more commonly called ($\boldsymbol{\alpha} = \boldsymbol{\chi}$). Returning attention to the Prager model and considering the normality rule, an expression for the plastic strain increment can be derived. To reiterate with the new notation, the Prager model for kinematic hardening can be expressed by equation (2.36)[36].

$$\begin{aligned} f = \phi\left(\sigma - c\boldsymbol{\varepsilon_p}\right) - k = 0 \\ \boldsymbol{\chi} = c\boldsymbol{\varepsilon_p} \\ \therefore d\boldsymbol{\chi} = cd\boldsymbol{\varepsilon_p} \end{aligned} \tag{2.36}$$

By noting the limiting condition of ($df = f = 0$), the plastic multiplier can be determined from the normality rule[34], shown in equation (2.37) (note the : operator is the double dot product).

$$df = \frac{\delta f}{\delta \boldsymbol{\sigma}} : d\boldsymbol{\sigma} - \frac{\delta f}{\delta \boldsymbol{\sigma}} : d\boldsymbol{\chi} = \frac{\delta f}{\delta \boldsymbol{\sigma}} : d\boldsymbol{\sigma} - \frac{\delta f}{\delta \boldsymbol{\sigma}} : cd\boldsymbol{\varepsilon_p} = 0 \tag{2.37}$$

Replacing the expression for plastic strain increment with that is defined by the normality rule[34], equation (2.38) can be found.

$$\begin{aligned} \frac{\delta f}{\delta \boldsymbol{\sigma}} : d\boldsymbol{\sigma} - \frac{\delta f}{\delta \boldsymbol{\sigma}} : \frac{\delta f}{\delta \boldsymbol{\sigma}} d\lambda c = 0 \\ \therefore d\lambda c = H(f) \frac{\left\langle \frac{\delta f}{\delta \boldsymbol{\sigma}} : d\boldsymbol{\sigma} \right\rangle}{c\left(\frac{\delta f}{\delta \boldsymbol{\sigma}} : \frac{\delta f}{\delta \boldsymbol{\sigma}}\right)} \end{aligned} \tag{2.38}$$

Note the Heaviside step (H) function in equation (2.38) has a value of 0 if its argument is negative and unity if the argument is greater than or equal to 0. Through the use of this function, plastic strain is ensured to only accumulate when a 0 value of the yield function is realised (i.e. there is no plastic flow in the elastic domain). The McCauley brackets can be defined for an argument u by equation (2.39).

$$\langle u \rangle = uH(u) \tag{2.39}$$

Prager's model exhibits linearity in stress strain predictive behaviour, and as such encounters problems when used in connection with complex loading patterns, particularly when loading and subsequent unloading actions are applied along different stress paths[34]. A Prager kinematic hardening behaviour law will predict, in the case of alternating plastic strain, that steady-state behaviour will be realised after a single loading cycle[32]. This is clearly at odds with experimentally observed results (see figure 2.19).

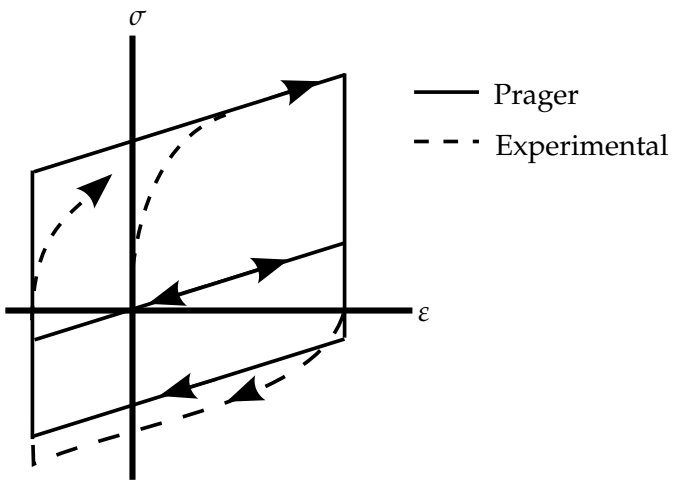

Figure 2.19: A comparison of Prager's model and experimental data for a uniaxial specimen under a reversed plastic load[34].

Armstrong and Frederick proposed a non linear model that addressed this discrepancy (see equation (2.40)). The yield surface increment will be normal to the yield surface and contains both a linear term ($\frac{2}{3}C_1 d\varepsilon_{p\,ij}$ which is similar to Prager's model shown in equation (2.33)) and a non linear feedback term[38].

$$d\chi_{ij} = \frac{2}{3}C_1 d\varepsilon_{p\,ij} - C_2 \chi_{ij} dp \tag{2.40}$$

2.3.3 Creep

While elastic and plastic deformations are instantaneous, some deformation mechanisms are time dependent. At elevated temperatures metals, even when loaded below the yield stress, can deform inelastically (that is to say, a deformation that is not recovered upon the removal of the load). This mechanism is termed creep and is a major concern for operators of high temperature components.

Creep is usually said to initiate at approximately 40% of the melting temperature of a material (T_m)[11,20]. The most fundamental method in characterising this behaviour is the constant temperature, constant stress (below the material's yield stress) uniaxial creep curve[11,15,20], found by testing a specimen to rupture (failure). Generally, it is the mathematical properties of this curve and the related physical phenomenon that allow material constants to be derived for constitutive models, paying particular attention to the local strain rates. A typical uniaxial creep curve, originally described by Andrade in 1910[39] is given in figure 2.20.

After an initial instantaneous recoverable (elastic) deformation (ε_0), the uniaxial creep curve can be considered to comprise of three distinct regions, with a different physical mechanisms controlling creep strain evolution in each zone[11,15,20]. Primary creep is characterised by a monotonic decrease in creep strain rate, shown in figure 2.20 as region

I. This is caused by the hardening of the material[11]. Various hardening mechanisms have been described in section 2.2.2, however the exact mechanism depends on the particular operating environment of the material. During secondary or steady-state creep (marked as *II* in figure 2.20), the rate of strain hardening is balanced by the rate of recovery, hence causing a constant minimum creep strain rate ($\dot{\varepsilon}_{c\ min}$). Tertiary creep (region *III* in figure 2.20) represents the finial zone where creep strain increases to failure. It is commonly associated with the formation of microscopic voids and cracks and thus most damage accumulation takes place in this period[20]. Although it may be assumed on first glance that the acceleration of strain rates in the tertiary creep region is due to the localised necking of a specimen (the reduction in area in a constant load test would give rise to an increase in stress), a tertiary region is still noted in tests where loads are adjusted to keep the stress constant. The formation of creep voids would give rise to a reduction in cross section area that is not related to a constant volume necking process, hence a loss in load carrying capability and the tertiary region still being observed.

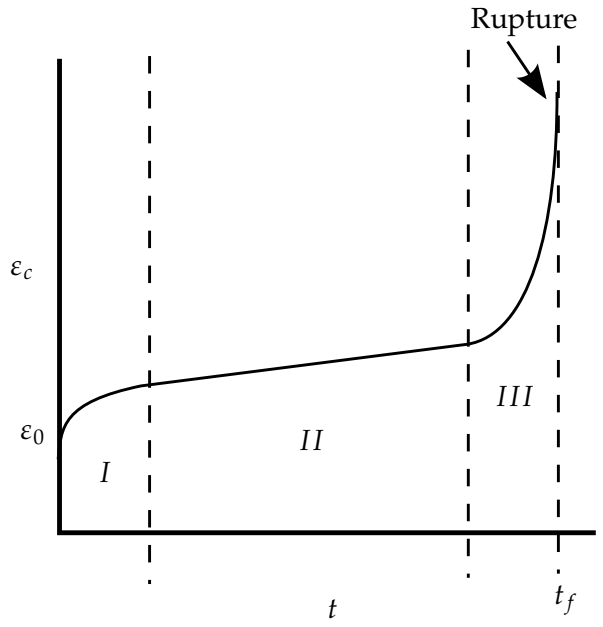

Figure 2.20: A typical constant temperature and load uniaxial creep curve, as identified by Andrade, showing primary, secondary and tertiary creep regions[11,20].

Creep behaviour has a strong dependency on stress (although it is not agreed that creep occurs at all stresses, including very low stress cases). Generally, an increase in stress results in a reduction in the time it takes for a specimen to fail (t_f, see figure 2.21 (a)) and an increase in the amount of creep strain (ε_c) required for the specimen to fail. Similarly, steady-state or minimum creep strain rates ($\dot{\varepsilon}_{c\ min}$) are reduced with a reduction in stress (see figure 2.21 (b))[20].

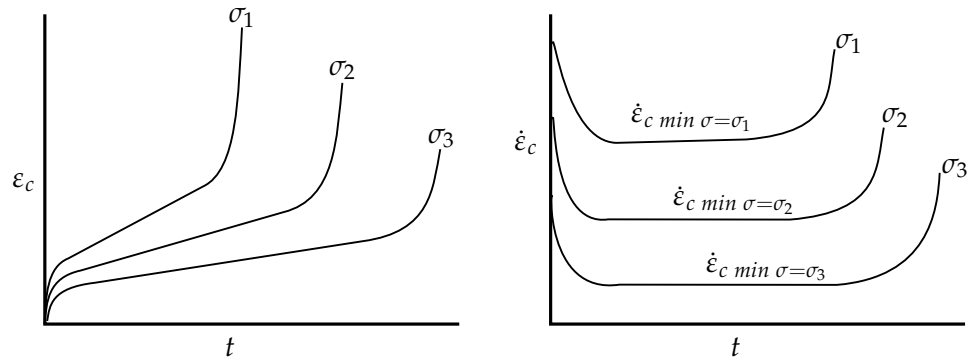

(a) (b)

Figure 2.21: The effect of stress on uniaxial creep behaviour in constant temperature specimens, showing (a) the effect on creep strain (ε_c) and (b) the effect on creep strain rate ($\dot{\varepsilon}_c$). Note that $\sigma_1 > \sigma_2 > \sigma_3$.

The physical mechanisms that control creep are greatly dependent on the operating environment that the material is subjected to. The effects of both stress and temperature were described by Ashby and co-workers[40] through the development of the deformation mechanism map. While the exact boundary locations in this map are material dependent, some general comments may be made based on the example schematic shown in figure 2.22. Note that in these diagrams stresses are commonly normalised to the material's shear modulus (G) and operating temperatures (T) are normalised to the material's melting temperature (T_m). A detailed explanation of several deformation mechanisms on an atomistic level is given in section 2.2.2. Above a certain stress threshold, "instantaneous" plastic behaviour is assumed to take place through dislocation glide. Below this threshold, creep occurs either by diffusion of matter or, as is more common in industrial cases, by the motion of dislocations (see section 2.2.2)[29]. Diffusion creep generally takes place a very low stresses and can be broadly described for a polycrystalline material as the atomic diffusion of matter, directed by stress, acting to elongate the material's grains in the loading direction. Several mechanisms exist for diffusion creep. For example, the Coble creep mechanism[41] describes the diffusion of matter or vacancies at the grain boundaries only. At higher temperatures, Naberro-Herring[42,43] creep may initiate, whereby matter and vacancies diffuse through the lattice. A third mechanism, known as the Harper-Dorn[42,43] mechanism has also been observed in some cases and predicts the viscous flow of a metal at rates far greater than those suggested by the Naberro-Herring mechanism.

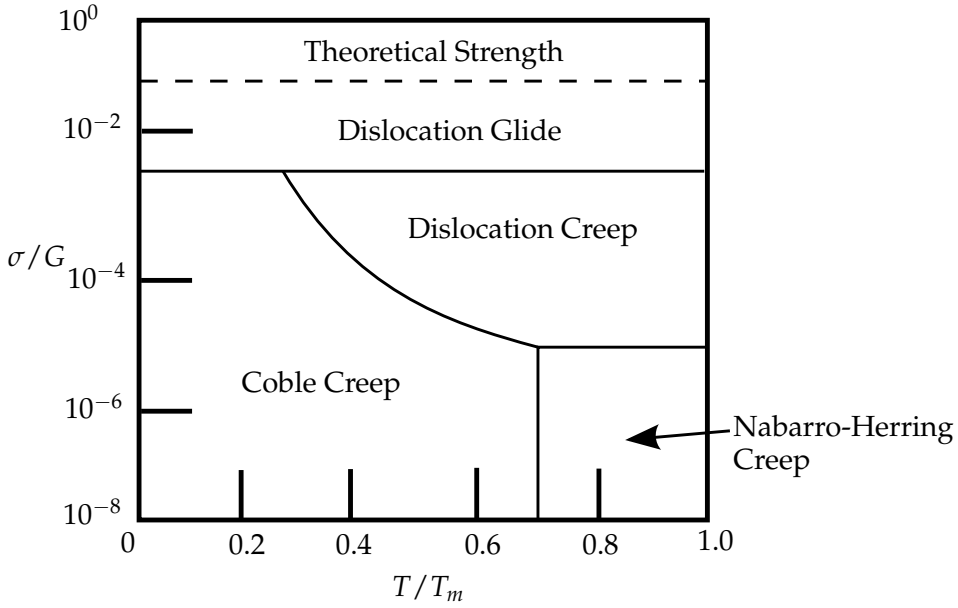

Figure 2.22: A simplified defamation mechanism map for creep behaviour, established by Ashby[3,40,44].

Primary creep strains may be described by equation (2.41)[20], where A, n and m are material dependent constants. This formulation may be used to highlight two different approaches for cases where the applied stress changes during creep. Equation (2.41) may be differentiated with respect to time (t) to give an expression for the creep strain rate ($\dot{\varepsilon}_c$), see equation (2.42). This is the time hardening approach, which can be seen graphically in figure 2.23 (a). When the creep stress changes, the metal's creep strain rate is assumed to be the same as the creep strain rate of a sample that has undergone no variable stress creep deformation at the same time instant. In figure 2.23 (a), the lines $A\vec{A}'$ and $B\vec{B}'$ would be equivalent. Equation (2.41) may be rearranged to give equation (2.43). This term for time may be substituted into equation (2.42) to give equation (2.44); an expression for the strain hardening approach (see figure 2.23 (b)). Creep strain rates here are not compared at a time instant but rather at creep strain values. Again, $A\vec{A}'$ and $B\vec{B}'$ would be equivalent[20]. In practice, strain hardening tends to give a better prediction of short term "step up" or "step down" effects than the time hardening mechanism. In some cases, an average of both approaches has been proven to give the best predictions (this is known as combined hardening).

$$\varepsilon_c = A\sigma^n t^m \tag{2.41}$$

$$\dot{\varepsilon}_c = Am\sigma^n t^{m-1} \tag{2.42}$$

$$t = \left(\frac{\varepsilon_c}{A\sigma^n}\right)^{\frac{1}{m}} \tag{2.43}$$

$$\dot{\varepsilon}_c = mA^{1/m}\sigma^{n/m}\varepsilon_c^{(m-1)/m} \tag{2.44}$$

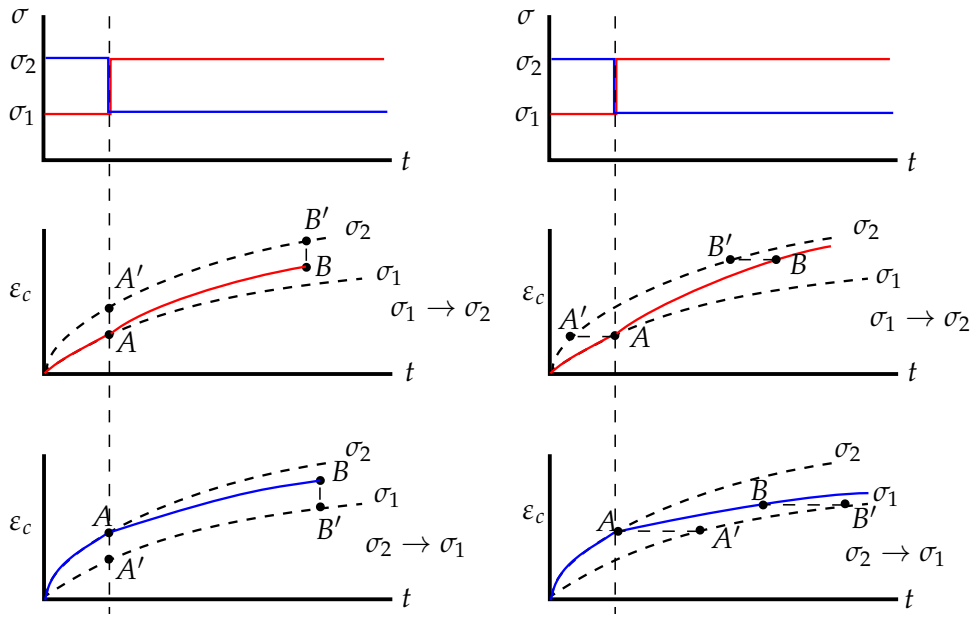

Figure 2.23: Representations of (a) time hardening and (b) strain hardening behaviour in variable stress creep deformations.

Several parametric procedures have also been applied to creep phenomenon. For example, the Monkman-Grant[45] relationship can be used relate the minimum creep strain rate of a uniaxial creep test ($\dot{\varepsilon}_{c\,min}$) to the time to failure (t_f), as shown in equation (2.45), where m and C are material constants.

$$C = \log t_f + m \log \dot{\varepsilon}_{c\,min} \tag{2.45}$$

Alternatively, the Larson-Miller parameter[46] allows for the characterisation of creep rupture times without defining load or stress. Generally, the Larson-Miller parameter can be calculated using equation (2.46), where t_f is the time to failure (in hours), T is the temperature of the specimen (in Kelvin), C is a material constant and LMP is the Larsson-Miller parameter.

$$\text{LMP} = \frac{T\left(C + \log t_f\right)}{1000} \tag{2.46}$$

While parametric descriptions of creep are useful for determining overall trends in data, constitutive material models (particularly those that can represent multiaxial stress states) can be applied to component analysis problems in order to approximate a response to a loading condition. Building on the work of Bailey[47,48] and assuming that high temperature creep takes place with a constant material volume[49], Norton[50] proposed equation (2.47) to represent the primary and secondary creep strain rates observed in uniaxial creep tests. This was later generalised to the multiaxial case by Odqvist[51] using the flow rule (see equation (2.48)). Note that σ_{EQ} and S_{ij} are the von Mises equivalent stress (see equation (2.31)) and the deviatoric stress component, respectively. The material constants A, n and m are known as the stress multiplier, stress exponent and time exponent, respectively. This type of expression is known as a power law due to the use of exponents. Temperature dependency may be estimated by the implementation of an Arrhenius type function[3] shown in equation (2.49), where Q_c is the material dependent creep activation energy, R is the universal gas constant and T is the temperature[11].

$$\dot{\varepsilon}_c = A\sigma^n t^m \tag{2.47}$$

$$\dot{\varepsilon}_{c\,ij} = \frac{3}{2} A\sigma_{EQ}^{n-1} S_{ij} t^m \tag{2.48}$$

$$\dot{\varepsilon}_c = A\sigma^n t^m e^{-\frac{Q_c}{RT}} \tag{2.49}$$

Due to the degenerative action of tertiary creep, the perdition of the full creep curve often requires the concept of "damage" to be introduced. Models that incorporate damage have been shown to be highly useful not only in the field of creep strain prediction but also in creep crack growth problems[52]. The constitutive equations proposed by Kachanov[53] and later modified by Robotnov[54,55] (for simplicity hereafter referred to as the Kachanov model, expressed in equations (2.50) and (2.51)) provide a relatively simple introduction to the field of creep damage evolution as a method of life estimation. Multiaxial forms of the Kachanov model were later suggested by Leckie and Hayhurst[56].

$$\frac{d\varepsilon_{c\,ij}}{dt} = \dot{\varepsilon}_{c\,ij} = \frac{3}{2} A \left(\frac{\sigma_{EQ}}{1-\omega} \right)^n \frac{S_{ij}}{\sigma_{EQ}} t^m \tag{2.50}$$

$$\frac{d\omega}{dt} = \dot{\omega} = B \frac{\sigma_R^{\chi}}{(1-\omega)^{\phi}} \tag{2.51}$$

where $\varepsilon_{c\,ij}$, S_{ij}, σ_{EQ} are the multiaxial creep strain component, deviatoric stress component and the von Mises equivalent stress, respectively. The damage parameter, ω (initially proposed by Kachanov[53] but reconfigured to the form shown by Robotnov[54]), represents the condition of the specimen, and can most readily be considered as a

measurement of micro-cracks and micro-voids[57–59]. In the presented form, this damage parameter will take the value of 0 for a virgin, undamaged material element and 1 for a completely failed element[54]. As shown above, the evolution of this parameter is dependent on the rupture stress, σ_R , which is defined in equation (2.52).

$$\sigma_R = \alpha\sigma_1 + (1-\alpha)\sigma_{EQ} \tag{2.52}$$

The triaxial material constant, α (which lies between 0 and 1), determines the value of the rupture stress by quantifying the contributions from σ_1 and σ_{EQ}, the maximum principal stress and equivalent von Mises stress, respectively. The material constants A, m and n control primary and secondary creep, and are similar to the Norton's law material constants, whereas the remaining constants (namely B, χ and ϕ) control failure through an accelerating tertiary creep strain rate[53].

As can be clearly seen in the constitutive equations (equations (2.50) and (2.51)), there is an inverse dependency of $(1-\omega)$ for the creep strain and damage rates. Therefore, as the damage parameter ω approaches unity, the strain/damage rate will increase, approaching infinity[60,61]. If this is taken to its logical conclusion in terms of FE analyses, commercially available programs will limit the time steps taken as the rate quantities increase, thus greatly increasing computing time (in effect, analyses will cease only when some minimum limit on step duration is surpassed, not because the damage parameter has achieved unity). This effect can be reduced by applying some limit to damage, say 0.99, implying that should the damage values at the Gauss points of an element reach such a high value the load carrying capability will be critically impaired for that element and load will be shed onto lower damage sections and ligaments[61]. This process however can make failure criterion subjective and, while not infinite, damage rates will still be high as damage approaches the imposed limit, greatly increasing computing time.

The Liu-Murakami creep damage model attempted to address the issue of high strain/damage rates as the damage parameter approaches unity. It can be used to represent primary, steady-state and tertiary multiaxial creep, characterised by equations (2.53) and (2.54)[62].

$$\dot{\varepsilon}_{c\,ij} = c\acute{B}\sigma_{EQ}^{\acute{n}-1}S_{ij}e^{-c\bar{t}} + \frac{3}{2}A\sigma_{EQ}^{n-1}S_{ij}\exp\left[\frac{2(n+1)}{\pi\sqrt{1+(3/n)}}\left(\frac{\sigma_1}{\sigma_{EQ}}\right)^2\omega^{3/2}\right] \tag{2.53}$$

$$\dot{\omega} = \frac{B\left[1-e^{-q_2}\right]}{q_2}\sigma_R^p e^{(q_2\omega)} \tag{2.54}$$

where c, $\acute{B}$ and $\acute{n}$ are material constants representing primary creep and A, n, q_2 and p are material constants describing secondary and tertiary creep[62]. While $\bar{t}$, the so called fictitious time, can de ambiguous in nature, it is true that for constant stress

conditions, $t = \bar{t}$[63]. Due to its small contribution to total creep strain however, primary creep is usually neglected by removing the addition term dependent on fictitious time (equation (2.55)), hence giving a more simplified version of the Liu-Murakami strain rate equations[64].

$$\dot{\varepsilon}_{c\,ij} = \frac{3}{2} A \sigma_{EQ}^{n-1} S_{ij} \exp\left[\frac{2(n+1)}{\pi\sqrt{1+(3/n)}}\left(\frac{\sigma_1}{\sigma_{EQ}}\right)^2 \omega^{3/2}\right] \tag{2.55}$$

The use of an exponential damage term in the Liu-Murakami model means that damage rates at failure are far less than those observed in Kachanov's model (an example of this difference can be seen in figure 2.24). This greatly aids in reducing computing time when attempting to perform damage analyses. Note that rupture stress, σ_R, takes the same form as in the Kachanov model (equation (2.52)), with multiaxial behaviour being represented again by the material constant α.

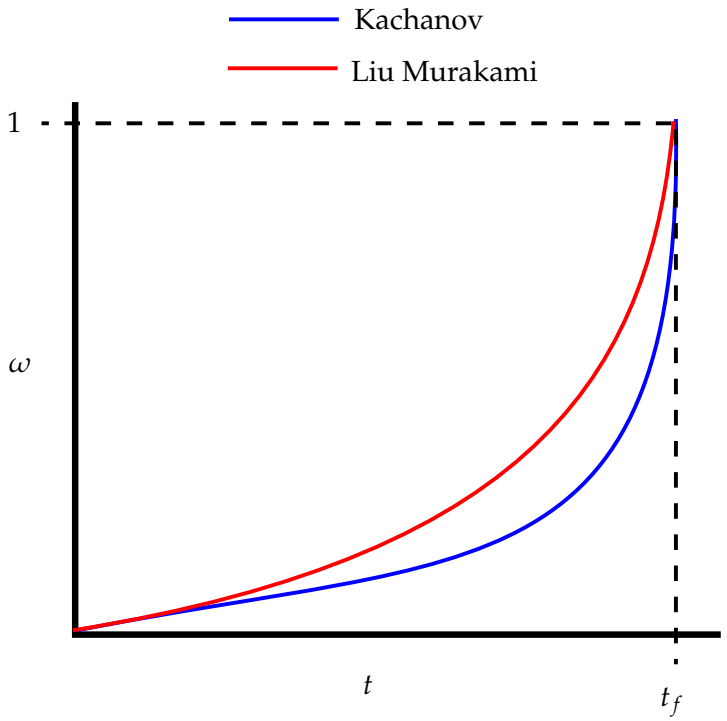

Figure 2.24: A comparison of damage accumulation rates in the Kachanov and Liu-Murakami creep damage models.

Unlike the Kachanov-Robotnov and Liu-Murakami models, Dyson's model uses a hyperbolic sine function (as opposed to a power law)[65–67]. Based on the model proposed by Othman, Hayhurst and Dyson, this revised model attempted to address a discrepancy observed between experimental and predicted failure times if minimum strain rates are fitted to with good accuracy (or vice versa)[65–67], and provides a method of representing primary, secondary and tertiary creep regions through the use of several

internal variables (see equations (2.56) to (2.59)).

$$\dot{\varepsilon}_{c\,ij} = \frac{3}{2} A \left(\frac{S_{ij}}{\sigma_{EQ}} \right) \sinh \left(\frac{B\sigma(1-H)}{(1-\omega_2)(1-\phi)} \right) \tag{2.56}$$

$$\frac{dH}{dt} = \dot{H} = \frac{h}{\sigma_{EQ}} \varepsilon_{c\,EQ} \left(1 - \frac{H}{\acute{H}} \right) \tag{2.57}$$

$$\frac{d\phi}{dt} = \dot{\phi} = \frac{K_c}{3} (1-\phi)^4 \tag{2.58}$$

$$\frac{d\omega_2}{dt} = \dot{\omega}_2 = DN\varepsilon_{c\,EQ} \left(\frac{\sigma_1}{\sigma_{EQ}} \right)^{\nu} \tag{2.59}$$

In this model, a total of three state variables are employed. Note the variable N is included to be equal to 1 in a tensile loading condition and 0 at all other times, thus ensuring damage accumulates only in tensile loading. The parameter H represents strain hardening during primary creep, and evolves from 0 at the beginning of loading to a saturation value of $\acute{H}$ at the end of primary creep. This value is then maintained throughout the rest of the creep life. The remaining state variables represent carbide precipitate spacing, or ageing, (ϕ, taking some value in the range $0 < \phi < 1$) and intergranular cavitation damage (ω_2). It is worth noting that the failure value for this second damage variable is dependent on the loading condition, taking a value of $1/3$ in uniaxial cases and 1 in multiaxial stress states. Multiaxial behaviour is not accounted for by a rupture stress and instead by the quantity ν in the cavitation damage equation (equation (2.59)). Note that this can take any positive value, and is not limited to a range of 0 to 1 (as is the case for α)[65–67]. An equivalent creep strain, $\varepsilon_{c\,EQ}$, can be found using the von Mises equation (equation (2.31)) and substituting stress values for strain components. By using a sinh function (as opposed to a power law), Dyson's model has the potential to give a better estimation of creep behaviour over a wide stress range[65]. This topic is discussed in greater detail in chapter 4.

An alternative material model was proposed by Evans and Wilshire and is known as the θ projection method[68]. This has been used in many analysis problems, including stochastic cases where small variations in material properties may be observed[69–72]. The model can be described by equations (2.60) and (2.61). Note that σ_{EQ} and $\varepsilon_{c\,EQ}$ are the von Mises equivalent stress and strain, respectively, t is time, T is temperature. The quantities θ_1, θ_2, θ_3 and θ_4 are defined by a total of 16 material constants, generally signified by a_{ij}, where $i = 1, 2, 3, 4$ and $j = 1, 2, 3, 4$. This model has been shown to be particularly adept at predicting full uniaxial creep strain curves and including stress and temperature dependencies. In a damage model described by Evans and Evans, internal variables representing hardening, damage and thermal softening were be related to the quantities θ_1, θ_2, θ_3 and θ_4[72]. Empirical relationships have been developed for uniaxial and biaxial stress conditions that would potentially allow for the direct evaluation of

the θ projection parameters. Despite this, extensive testing programs are still required to estimate all material constants.

$$\varepsilon_{c\,EQ} = \theta_1 \left[1 - \exp\left(-\theta_2 t\right)\right] + \theta_3 \left[\exp\left(-\theta_4 t\right) - 1\right] \tag{2.60}$$

$$\ln \theta_i = a_{i1} + a_{i2}\sigma_{EQ} + a_{i3}T + a_{i4}\sigma_{EQ}T \tag{2.61}$$

2.3.4 Fatigue

Until now only monotonic loads have been considered, that is to say a load which only increases (such as in a tensile plasticity test) or maintains a steady value (such as in a creep test). In many cases however, loads will fluctuate and cycle through a component's life. The potential for plastic strain accumulation during this loading can result in degradation of a material (i.e. a loss in load carrying capability) and ultimately failure. This mechanism is known as fatigue (in particular, low cycle fatigue, which is most relevant to the present work). It has been discussed already that this mechanism is dependent on the initiation and propagation of transgranular cracks (see section 2.2.2). Several material models will be presented in this section that can represent the complex hardening behaviour that may be witnessed in fatigue load cases.

A typical fluctuating load (stress) that could cause fatigue in a material is presented in figure 2.25. The critical parameters in this figure are defined in equation (2.62), namely the stress range ($\Delta\sigma$), the stress amplitude (σ_a) and the mean stress (σ_{mean}). Additionally the fatigue stress ratio (R_σ) is defined in equation (2.62).

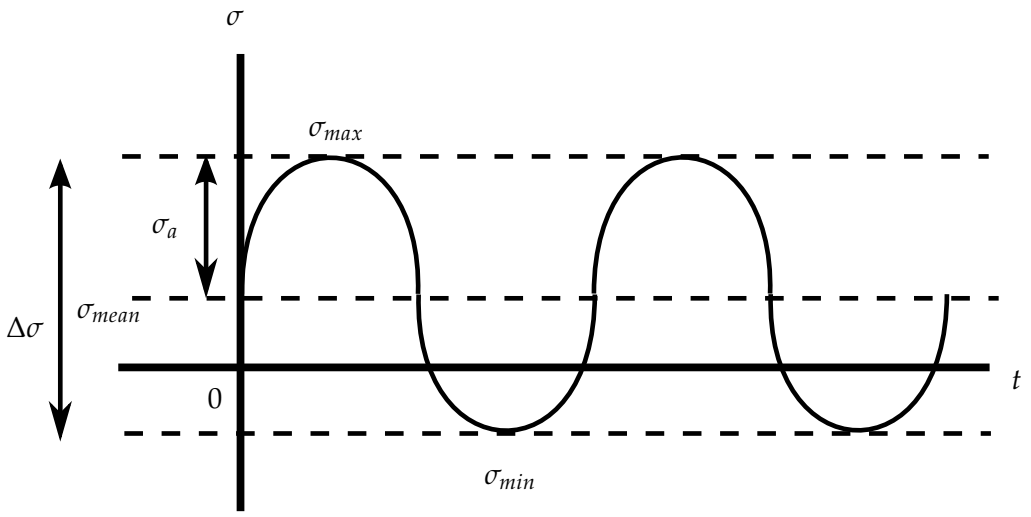

Figure 2.25: A stress waveform that may give rise to fatigue behaviour.

$$\begin{aligned} \Delta\sigma &= \sigma_{max} - \sigma_{min} \\ \sigma_a &= \frac{\sigma_{max} + \sigma_{min}}{2} \\ \sigma_{mean} &= \frac{\Delta\sigma}{2} \\ R_\sigma &= \frac{\sigma_{min}}{\sigma_{max}} \end{aligned} \tag{2.62}$$

Building on the work of Albert[73], Rankine[74] and Hodgkinson[75] in the 19^{th} century, Wohler[16,76] established the well known S-N diagram and the concept of a fatigue limit. Here, a fully reversed ($\sigma_{mean} = 0$, $R_\sigma = -1$) fatigue test is conducted for a particular σ_a, with the number of cycles to failure (or crack initiation) recorded. This procedure is repeated for an alternative σ_a value. An example S-N diagram is presented in figure 2.26. The relationship drawn from this diagram, which was verified experientially by Bauschinger, is that a reduction in $\Delta\sigma$ leads to an increase in the number of cycles that can be applied to the material before failure by fatigue occurs (N_f)[77]. The endurance limit for some materials suggests that, below a certain stress range, failure by fatigue will either not occur or will require a very large number of cycles.

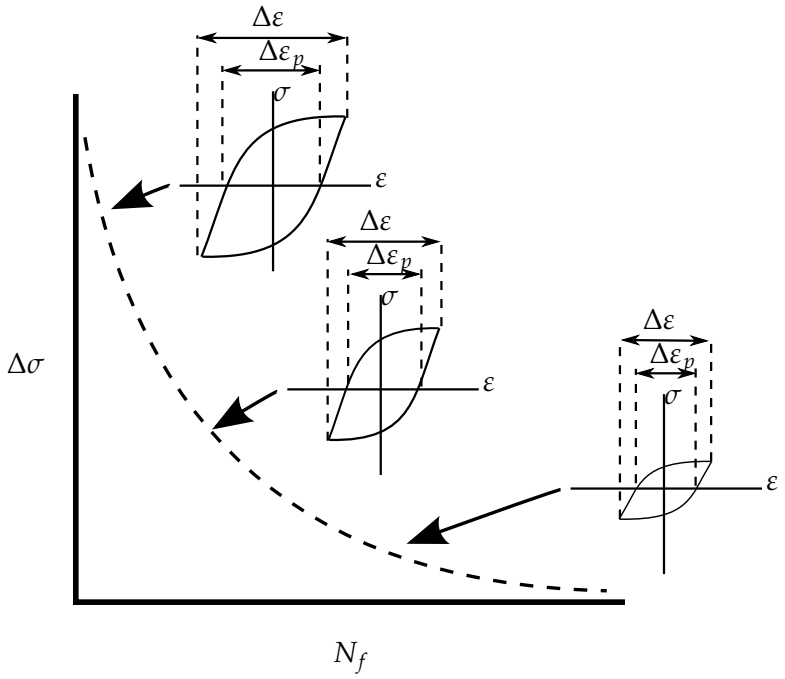

Figure 2.26: An example Wohler diagram[76].

Mean stress has a significant effect on the number of cycles a component can withstand before failing due to fatigue, therefore several relationships have been established between σ_a and σ_{mean}. Using these (or similar relationships), safe operating conditions can be estimated for a component that may be susceptible to the fatigue mechanism.

Graphical interpretations of three major relationships, namely the Gerber[78], Goodman[79] and Soderberg[80] models, can be seen in figure 2.27. The controlling equations of the Gerber, Goodman and Soderberg models are given in equations (2.63) to (2.65), respectively, and are generally dependent on the quantity $\sigma_{a\ R_\sigma=-1}$. $\sigma_{a\ R_\sigma=-1}$ is a reference stress amplitude and is equivalent to the fully reversed ($\sigma_{min} = -\sigma_{max}$) stress amplitude that would result in the same fatigue life as the $\sigma_a - \sigma_{mean}$ combination[81]. Alternative methods were suggested by Smith-Watson-Topper[82] and Walker[83] using the maximum stress (σ_{max}) in a loading profile, shown in equations (2.66) and (2.67), respectively. Note γ in Walker's model is a fitting constant (when $\gamma = 0.5$ Walker's model simplifies to the Smith-Watson-Topper model). A fatigue life (N_f) may in turn be estimated using Basquin's relationship[84], shown in equation (2.68), where $\acute{\sigma_f}$ and b are material dependent fitting constants. A similar relationship to Basquin's relationship was formulated by Coffin and Masson[85,86] in 1954 (see equation (2.69)) and relates a plastic strain range $\Delta\varepsilon_p$ (see figure 2.27) to the fatigue life (N_f) by the fitting constants $\acute{\varepsilon_f}$ and c.

$$\sigma_a = \sigma_{a\ R_\sigma=-1}\left(1 - \left(\frac{\sigma_{mean}}{\sigma_{UTS}}\right)^2\right) \tag{2.63}$$

$$\sigma_a = \sigma_{a\ R_\sigma=-1}\left(1 - \left(\frac{\sigma_{mean}}{\sigma_{UTS}}\right)\right) \tag{2.64}$$

$$\sigma_a = \sigma_{a\ R_\sigma=-1}\left(1 - \left(\frac{\sigma_{mean}}{\sigma_{Y}}\right)\right) \tag{2.65}$$

$$\begin{aligned} \sigma_{a\ R_\sigma=-1} &= \sqrt{\sigma_{max}\sigma_a} \\ \sigma_{a\ R_\sigma=-1} &= \sigma_{max}\sqrt{\frac{1-R}{2}} \\ \sigma_{a\ R_\sigma=-1} &= \sigma_a\sqrt{\frac{2}{1-R}} \end{aligned} \tag{2.66}$$

$$\begin{aligned} \sigma_{a\ R_\sigma=-1} &= \sigma_{max}^{1-\gamma}\sigma_a^{\gamma} \\ \sigma_{a\ R_\sigma=-1} &= \sigma_{max}\left(\frac{1-R}{2}\right)^{\gamma} \\ \sigma_{a\ R_\sigma=-1} &= \sigma_a\left(\frac{2}{1-R}\right)^{1-\gamma} \end{aligned} \tag{2.67}$$

$$\sigma_{a\ R_\sigma=-1} = \acute{\sigma_f}\left(2N_f\right)^b \tag{2.68}$$

$$\frac{\Delta\varepsilon_p}{2} = \acute{\varepsilon_f}\left(2N_f\right)^c \tag{2.69}$$

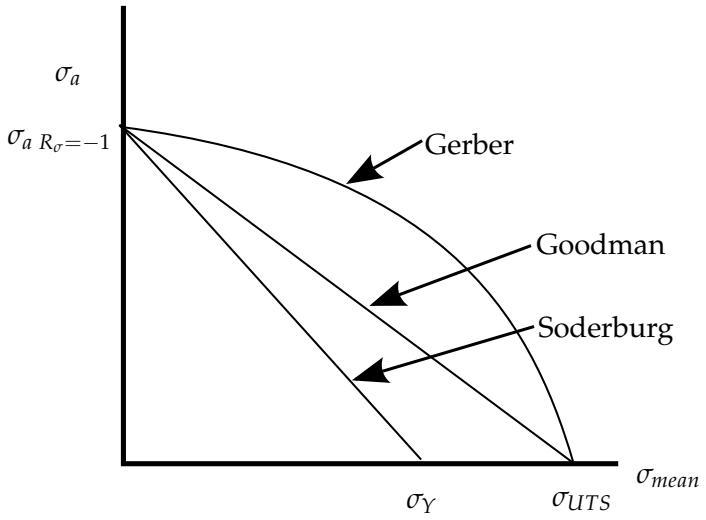

Figure 2.27: Example constant life design models for fatigue loading problems.

A drawback to the parametric and empirical methods described thus far is the large amount of experimental data that must be generated in order to define, say, the Wohler diagram. As with creep, constitutive models have greater applicability in component analysis problems, particularly in cases where load cycles are not uniform (for example, load amplitudes may change during a component's life). Building off the work of Prager (see section 2.3.2), Mroz proposed the concept of "field of work hardening moduli"[32]. Rather than a single effective plastic modulus being assumed (as with Prager's model), the hardening curve is approximated by several linear sections, each relating to a different plastic modulus (see figure 2.28 (a)). Mathematically, this can be represented in stress space by a collection of L circles (see figure 2.28 (b) and equation (2.70)), each defined by a yield function in the form of equation (2.36)[32].

$$\begin{aligned} f^{(0)} &= \phi\left(\sigma_{ij} - \chi_{ij}^{(0)}\right) - \left(k^{(0)}\right) = 0 \\ f^{(1)} &= \phi\left(\sigma_{ij} - \chi_{ij}^{(1)}\right) - \left(k^{(1)}\right) = 0 \\ &\vdots \\ f^{(L)} &= \phi\left(\sigma_{ij} - \chi_{ij}^{(L)}\right) - \left(k^{(L)}\right) = 0 \end{aligned} \tag{2.70}$$

Note that equation (2.71) is also true.

$$d\lambda_0 \frac{\delta f_0}{\delta \sigma} = d\lambda_1 \frac{\delta f_1}{\delta \sigma} = \cdots d\lambda_L \frac{\delta f_L}{\delta \sigma} = 0 \tag{2.71}$$

For an initially isotropic material, these surfaces are similar and share the same origin[32]. Surfaces are assumed to be unable to intersect and instead, if contact is made, multiple surfaces will consecutively connect with subsequent surfaces and move as one. As the stress point traverses stress space, it will come into contact with the first yield

surface ($f^{(0)}$) if the elastic domain limit is exceeded, indicating the onset of yielding and thus altering the gradient of the stress strain plot (see figure 2.28 (a)) to the first plastic modulus. This "active" surface will translate (by the amount df_m) along the vector connecting stress point considered and the corresponding stress point on the following surface. By using this condition, the outward normal on each surface will coincide with one another when surfaces come into contact (see figure 2.28 (b)). Such a translation can be shown mathematically using equation (2.72) (for surface m), based on the formulation by Zeigler.

$$d\chi_m = d\boldsymbol{\mu}_m \left(\boldsymbol{\sigma}_{m+1} - \boldsymbol{\sigma}\right) \tag{2.72}$$

Assuming only kinematic hardening and constant values for the initial size of the yield surface (k), equation (2.73) can be derived from the consistency condition (which prevents a stress point falling outside the active yield surface), allowing for derivation of the multiplier in the kinematic hardening expression (again for surface m).

$$df_m = \frac{\delta f_m}{\delta \boldsymbol{\sigma}} : d\boldsymbol{\sigma} - \frac{\delta f_m}{\delta \boldsymbol{\sigma}} : d\boldsymbol{\chi} = \frac{\delta f_m}{\delta \boldsymbol{\sigma}} : d\boldsymbol{\sigma} - \frac{\delta f_m}{\delta \boldsymbol{\sigma}} : d\mu_m \left(\boldsymbol{\sigma}_{m+1} - \boldsymbol{\sigma}\right) = 0 \tag{2.73}$$

$$d\mu_m = H\left(f_m\right) \frac{\left\langle \frac{\delta f_m}{\delta \boldsymbol{\sigma}} : d\boldsymbol{\sigma} \right\rangle}{\frac{\delta f_m}{\delta \boldsymbol{\sigma}} : \left(\boldsymbol{\sigma}_{m+1} - \boldsymbol{\sigma}\right)} = H\left(f_m\right) \frac{\langle n : d\boldsymbol{\sigma} \rangle}{n : \left(\boldsymbol{\sigma}_{m+1} - \boldsymbol{\sigma}\right)} \tag{2.74}$$

Note that equation (2.74) deviates from Mroz's original presentation, as now the Heaviside function (H) is incorporated to ensure yielding only occurs with a non-negative yield function value. Plastic strain increments may in turn be given by equation (2.75).

$$d\boldsymbol{\varepsilon_p} = \frac{1}{K} n (d\boldsymbol{\sigma} \cdot n) c \tag{2.75}$$

where K represents the plastic modulus (constant within a particular yield surface and akin to c in the Prager model) and n, which indicates the direction of the outward normal in stress space (the normality rule).

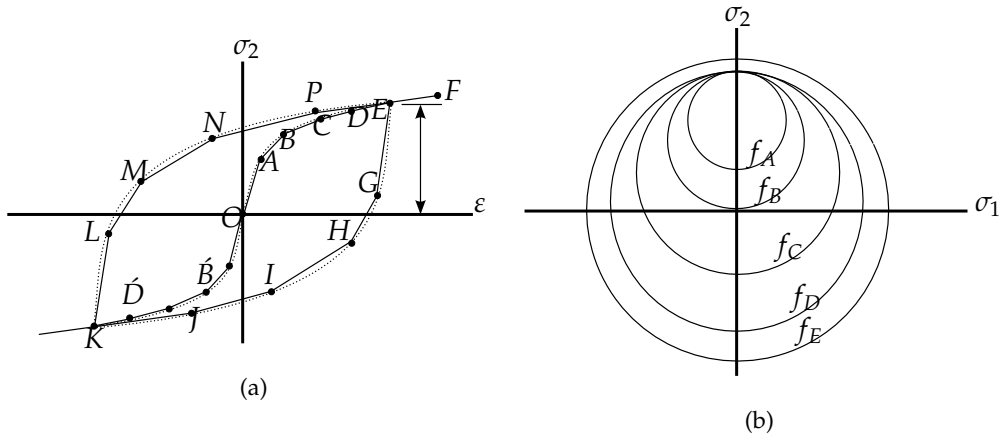

Figure 2.28: The Mroz multisurface model for the cyclic hardening of materials, showing (a) the effect of varying hardening moduli to approximate an experimental hysteresis loop and (b) the transition of Mroz's circular yield surfaces due to a load applied in the 2 direction.

The Mroz model has several advantages over the more simplistic models, such as its ability to predict the non-linear stress strain loops in a material's response and to describe the Bauschinger effect (where a reverse loaded material, that has previously yielded in tension, will generally yield at a stress prior to the compressive yield strength of the material)[29]. Under asymmetric loading conditions however, no ratchetting (where, in a stress limit test, the mean strain increases with cycles, which may reach an approximately steady value or continue to increase leading to failure[29]) is predicted due to a lack of isotropic hardening in cyclic stable conditions[34]. A clear practical drawback in terms of application however of the Mroz model is that, to describe the response of a material with sufficient accuracy, large numbers of surfaces may be required, each surface requiring the storage of a tensor (most commonly of six components, representing the centre of each surface) and scalar variable (indicating a surface's size)[34]. Potential solutions to this problem were proposed by envisaging a two surface model, consisting of a yielding surface and a bounding, limit surface. An example of such a formulation is the Dafalias-Popov model[87]. In this form, the plastic modulus becomes a function ($\hat{K}$, equation (2.76)) of two distances in stress space (see figures 2.29 and 2.30)[87].

$$K = \hat{K}\left(\delta, \delta_{in}\right) \tag{2.76}$$

where δ represents the stress distance between the stress point and the limit[87], and is quantified by comparing the stress point on the yield surface to the corresponding stress point on the bounding surface, shown in equation (2.77) (see figure 2.29).

$$\delta = \left[\left(\bar{\sigma}_{ij} - \sigma_{ij}\right)\left(\bar{\sigma}_{ij} - \sigma_{ij}\right)\right]^{1/2} \tag{2.77}$$

The use of this distance allows a continuously variable plastic modulus[87]. The initial value of this distance (i.e. the stress distance at the end of elastic deformation, the same

magnitude as line $\bar{A}B$ in figure 2.30, indicating the onset of yielding), δ_{in}, will change at each reversal but is constant during plastic flow[87]. Effectively, the yield surface takes the role of the "active" surface in the Mroz model, while the bounding surface represents the subsequent surface. Both the yield surface and the bounding surface will undergo kinematic and isotropic hardening behaviour. This can be represented by the yield functions shown in equations (2.78) and (2.79).

$$f = G\left(\boldsymbol{\sigma} - \boldsymbol{\chi}\right) - k(\lambda) = 0 \tag{2.78}$$

$$\bar{f} = \bar{G}\left(\bar{\boldsymbol{\sigma}} - \bar{\boldsymbol{\chi}}\right) - \bar{k}(\lambda) = 0 \tag{2.79}$$

where barred variables denote those relating to the bounding surface. Note the surfaces will be similar if $G = \bar{G}$. The centre of the surface will be defined by $\boldsymbol{\chi}$ as in the previous models, with the size of the surfaces is governed by an internal variable λ. As in the previously described Mroz model, when contact is made between the two surfaces, their outward unit normals will be coincidental. Note every stress-strain curve asymptotically approaches the bounding surface. The translation of the surfaces (the increment of $\boldsymbol{\chi}$), which occurs for both surfaces simultaneously, is therefore controlled by equations (2.80) and (2.81)[34,87].

$$d\boldsymbol{\chi} = \frac{K_\alpha}{K}\frac{\langle n : \nu \rangle}{n : \nu}\nu = K_\alpha \frac{d\lambda}{n : \nu}\nu \tag{2.80}$$

$$d\bar{\boldsymbol{\chi}} = d\boldsymbol{\chi} - d\mu\left(\bar{\boldsymbol{\sigma}} - \boldsymbol{\sigma}\right) \tag{2.81}$$

where $d\mu$ and $d\lambda$ are suitable multipliers. The direction of translation is governed by a unit vector ν, given along the direction of $d\boldsymbol{\chi}$. K_α is a generalisation of a plastic modulus E_α, found using equation (2.82).

$$d\chi_{11} = E_\alpha d\varepsilon_{p\,11} \tag{2.82}$$

From the limiting condition for the yield surface ($df = 0$), an expression for K_α can be derived (equation (2.83))[34].

$$K_\alpha = K - \frac{1}{\left(\dfrac{\delta f}{\delta \boldsymbol{\sigma}} : \dfrac{\delta f}{\delta \boldsymbol{\sigma}}\right)^{1/2}}\frac{\delta k}{\delta \lambda} \tag{2.83}$$

A similar modulus, E_β, generalised by K_β, also exists and is defined by equation (2.84).

$$d\bar{\chi}_{11} = E_\beta d\varepsilon_{p\,11} = d\chi_{11} - \left(E_\alpha - E_\beta d\varepsilon_{p\,11}\right) \tag{2.84}$$

In the case where the elastic domain's size does not change E_α will equal the plastic

modulus at a given point and, if parallel bounds are used in stress strain space (indicated by a constant $\bar{A}\bar{B}$ magnitude), E_β will be equal to the asymptotic value of the plastic modulus. The plastic strain increment, found by using the flow rule, can be given by equation (2.85).

$$d\boldsymbol{\varepsilon_p} = \frac{1}{K} \langle n : d\boldsymbol{\sigma} \rangle \, n \tag{2.85}$$

The multiplier terms can be found by applying the limiting condition as before. While the two surface model requirements for tensor storage are far less than for the multisurface models, several difficulties can arise, largely due to the need to update variables such as the tangent modulus K, which increases storage requirements and can cause over estimated responses in complex multidimensional loading[34]. It is worth pointing out that, if the surfaces are assumed to translate as they do in the Mroz model, the translation increments can be described by equations (2.86) and (2.87).

$$d\boldsymbol{\chi} = \frac{K_\alpha}{K} \frac{\langle n : d\boldsymbol{\sigma} \rangle}{n : (\bar{\boldsymbol{\sigma}} - \boldsymbol{\sigma})} (\bar{\boldsymbol{\sigma}} - \boldsymbol{\sigma}) \tag{2.86}$$

$$d\bar{\boldsymbol{\chi}} = \frac{K_\beta}{K} \frac{\langle n : d\boldsymbol{\sigma} \rangle}{n : (\bar{\boldsymbol{\sigma}} - \boldsymbol{\sigma})} (\bar{\boldsymbol{\sigma}} - \boldsymbol{\sigma}) \tag{2.87}$$

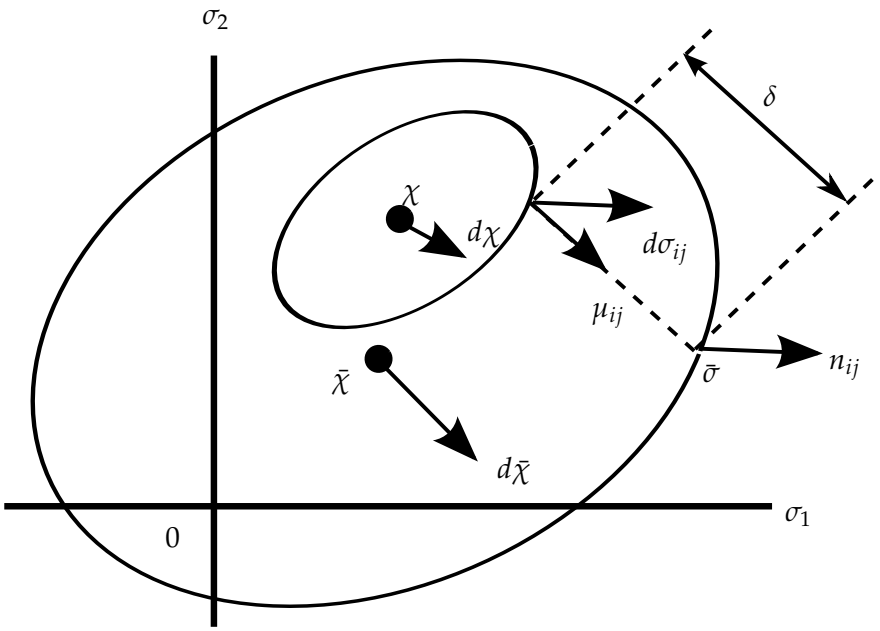

Figure 2.29: Representation of the Dafalias-Popov model in stress space[87].

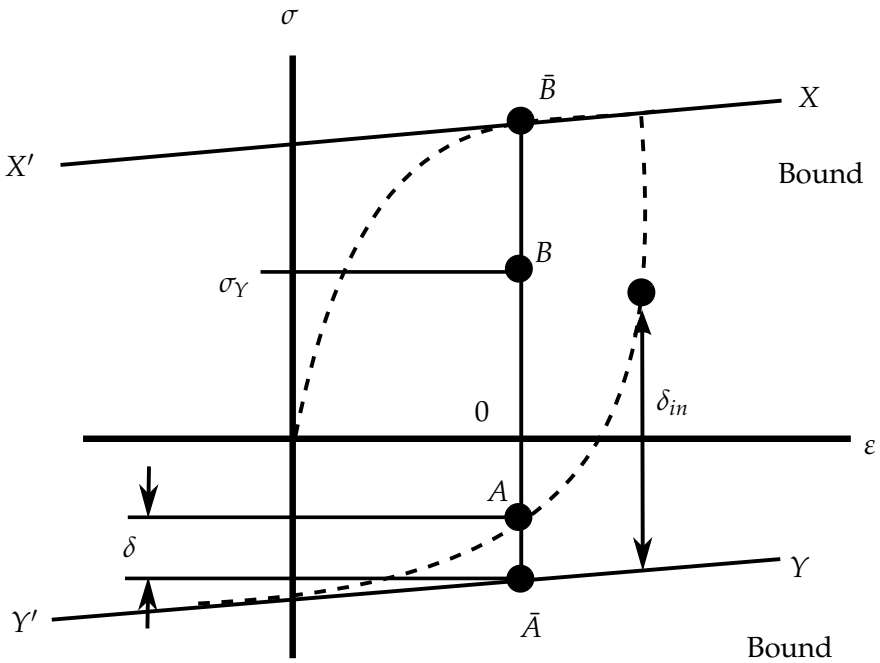

Figure 2.30: Representation of the Dafalias-Popov model in stress strain space, demonstrating the meaning of δ and δ_{in} [87].

2.3.5 Deformation Mechanism Interaction

In the area of high temperature component analysis there are many occasions where materials may operate in a high temperature environment and under a fluctuating load. In these cases, both creep and fatigue mechanisms may act to deform a material. The interaction between creep and fatigue is often considered through the application of interaction diagrams (figure 2.31). Damage fractions due to creep (where an exposure time t is referenced to t_f, the failure time due to pure creep) and fatigue (where the number of cycles a component experiences, N, is referenced to the number of cycles to give failure by pure fatigue, N_f) are compared in these diagrams. An idealised material assumes a linear relationship between these damage fractions, however real materials tend to diverge from this behaviour [88,89]. An alternative to constructing an interaction diagram is the strain partioning method [90], however both of these methods require extensive testing programs and are difficult to implement in real world analyses. Alternatively, the two layer model was proposed by Kichenin [91] (building on the work of Sweeney and Ward) and has been applied with success by Figiel and Gunther [92] and Leen et. al. [93]. Plastic and viscous effects are considered separately, however a total strain (ε) is calculated using elastic (ε_e), plastic (ε_p) and viscous (ε_v) contributions (see equation (2.88)). Inelastic contributions are controlled through a factor f (see equation (2.89)), which lies in the range $0 \geq f \geq 1$ and is dependent on two effective

moduli representing viscous and plastic behaviour (K_v and K_p, respectively). Any plasticity or creep material model may be used to define these moduli. While the two layer model can give good predictions of a material's behaviour in the short term, significant changes in the material over extended loading periods may cause the user defined f value to become inaccurate, thus compromising the model's predictive ability. A unified model is therefore the preferred option.

$$\varepsilon = \varepsilon_e + (1 - f)\varepsilon_p + f\varepsilon_v \tag{2.88}$$

$$f = \frac{K_v}{K_p + K_v} \tag{2.89}$$

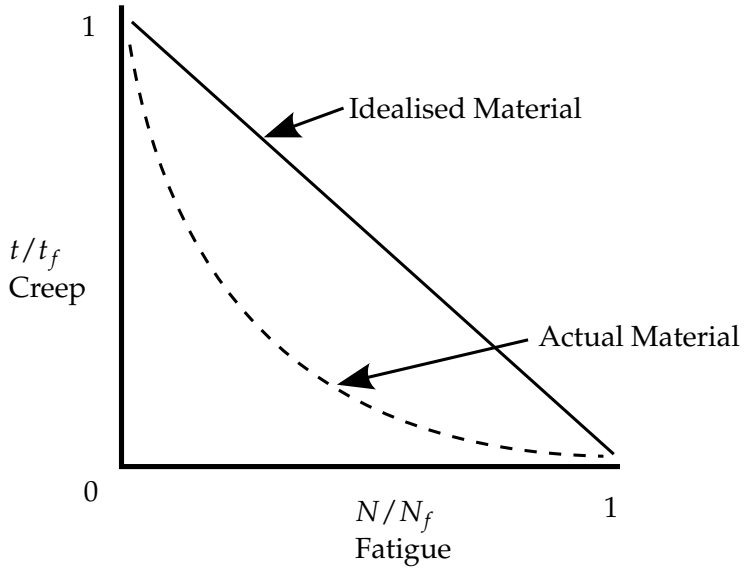

Figure 2.31: The interaction of creep and fatigue mechanisms[88].

The Chaboche unified visco-plasticity model is presented here as a constitutive equation that can represent the complex material hardening mechanisms observed in fatigue tests as well as the relaxation of a stress due to the accumulation of creep strain[94,95]. Several damage modifications to the Chaboche model have been proposed to model the failure aspect of creep and fatigue interactions[59,96–99], however these are considered outside the scope of the present review.

The Chaboche model decomposes total strain (ε_T) into elastic and plastic components ($\varepsilon_T = \varepsilon_e + \varepsilon_p$), and allows for the interpretation of both kinematic and isotropic hardening through the use of appropriate internal variable tensors. Nonlinear kinematic hardening is expressed through the use of several differential equations that update the relevant kinematic variables. In this way, only one surface definition is required (the yielding surface). For the Chaboche model, the yield function is defined by equation (2.90)[94,95].

$$f = J(\boldsymbol{\sigma} - \boldsymbol{\chi}) - R - k \tag{2.90}$$

where the back stress ($\boldsymbol{\chi}$) designates the centre of a yield surface and the drag stress (R) denotes the variation of its size (this can either act to increase or decrease the size of the yield surface, see figure 2.32). Through the use of these quantities, kinematic and isotropic hardening may be represented, respectively. The function $J(\boldsymbol{\sigma} - \boldsymbol{\chi})$ allows for the interpretation of a distance in stress space (the scalar equivalent in the deviatoric space[100]), which for a von Mises material can be characterised by equation (2.91).

$$J(\boldsymbol{\sigma} - \boldsymbol{\chi}) = \left[\frac{3}{2}\left(S_{ij} - \acute{\chi}_{ij}\right)\left(S_{ij} - \acute{\chi}_{ij}\right)\right]^{1/2} \tag{2.91}$$

where S_{ij} and $\acute{\chi}_{ij}$ are the deviatoric components of $\boldsymbol{\sigma}$ and $\boldsymbol{\chi}$, respectively. To provide a better approximation of the kinematic effects, the back stress can be decomposed into several components (by way of example, two back stress components will be used here)[30]. An Armstrong and Frederick type kinematic hardening law is used to define the increment for each component, taking the form of equation (2.92)[101].

$$d\boldsymbol{\chi}_i = C_i\left(a_i d\boldsymbol{\varepsilon_p} - \boldsymbol{\chi}_i dp\right) \tag{2.92}$$

where C_i and a_i are both material constants (a_i defines the stationary value and C_i dictates how quickly this value is achieved[102,103]). The accumulated plastic strain (p) is a monotonic quantity and is the summation of the modulus of the plastic strain values, described mathematically by equation (2.93).

$$dp = \left|d\boldsymbol{\varepsilon_p}\right| \tag{2.93}$$

By decomposing the back stress into multiple components, transient and long term behaviour may be accounted for, here with a_1 and C_1 describing initial non-linearity and a_2 and C_2 describing asymptotic behaviour. The total back stress is given as a summation of these components, therefore for N components, the total back stress ($\boldsymbol{\chi}$) is given by equation (2.94).

$$\boldsymbol{\chi} = \sum_{i=1}^{N} \boldsymbol{\chi}_i \tag{2.94}$$

Variations in the scalar drag stress (R) will represent the effects of isotropic hardening and, as such, will alter only the size of the yield surface. In the form originally presented by Chaboche, only primary behaviour (either hardening or softening) is represented. The drag stress will undergo some initial monotonic increment before reaching a stabilised asymptotic value. This saturated value is signified by Q, with the rate at which this stabilised value is reached being determined by b, see equation (2.95).

$$dR = b\,(Q - R)\,dp \tag{2.95}$$

Creep effects will be present when time or strain rate has an influence on inelastic behaviour[34]. Time dependent behaviour can be introduced through the definition of a viscous stress (σ_v), forming a component of total stress, summarised in equation (2.96).

$$\boldsymbol{\sigma} = \boldsymbol{\chi} + (R + k + \sigma_v)\, sgn\,(\boldsymbol{\sigma} - \boldsymbol{\chi}) \tag{2.96}$$

where the function $sgn(x)$ is specified by equation (2.97).

$$sgn(x) = \begin{cases} 1 & \text{if } x > 0 \\ 0 & \text{if } x = 0 \\ -1 & \text{if } x < 0 \end{cases} \tag{2.97}$$

The viscous stress takes the form of a power law (see equation (2.98)). Z and n are viscous material coefficients.

$$\sigma_v = Z\dot{p}^{1/n} \tag{2.98}$$

To find the plastic strain increment ($d\boldsymbol{\varepsilon_p}$) the flow rule with a normality condition is applied. To find the normal direction, the yield surface translation vector ($\boldsymbol{S} - \acute{\boldsymbol{\chi}}$) is normalised to produce a unit vector. The size of the yield surface is given by $R + k$, however for the limiting condition of yield surface (when $f = 0$), equation (2.99) is also true.

$$J\,(\boldsymbol{\sigma} - \boldsymbol{\chi}) = R + k \tag{2.99}$$

The flow rule can therefore be written as equation (2.100)[34].

$$\frac{d\boldsymbol{\varepsilon_p}}{dt} = \frac{3}{2} d\lambda \frac{\boldsymbol{S} - \acute{\boldsymbol{\chi}}}{J\,(\boldsymbol{\sigma} - \boldsymbol{\chi})} \tag{2.100}$$

where $d\lambda$ is the plastic multiplier, which is given by equation (2.101). The plastic strain increment ($d\boldsymbol{\varepsilon_p}$) may therefore be calculated from equation (2.102).

$$d\lambda = \left[\frac{\langle f \rangle}{Z}\right]^n \tag{2.101}$$

$$d\varepsilon_p = \frac{3}{2} \left\langle \frac{J\,(\boldsymbol{\sigma} - \boldsymbol{\chi}) - R - k}{Z} \right\rangle^n \frac{\boldsymbol{S} - \acute{\boldsymbol{\chi}}}{J\,(\boldsymbol{\sigma} - \boldsymbol{\chi})} dt \tag{2.102}$$

Note that the definition of the brackets used in equation (2.102) is given in equation (2.103).

$$\langle x \rangle = \begin{cases} x & \text{if } x \geq 0 \\ 0 & \text{if } x < 0 \end{cases} \tag{2.103}$$

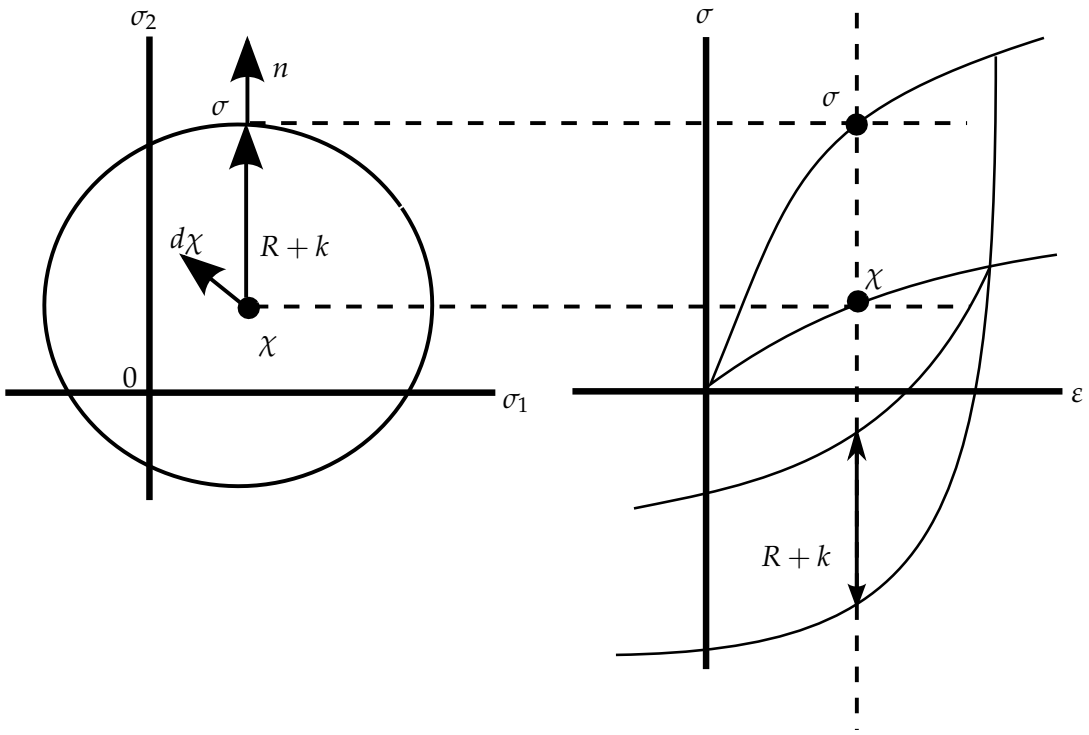

Figure 2.32: The Chaboche unified visco-plasticity model, showing the translation of a yield surface and the its effect on hardening behaviour in stress versus strain space.

2.4 Power Plant Components

A great deal has been said so far about common deformation mechanisms and analysis methodologies for high temperature components. One industry that has numerous examples of these components is the power industry, notably coal fired steam plant. Steam will be generated in a boiler and transported to steam chests and turbines (divided into high, intermediate and low pressure sections) via a pipework system. The turbine drives a generator to produce electricity while the steam from the turbine outlet is condensed and circulated. The piping system is required to navigate the power station and, due to space envelope and manufacturing considerations, weldments and bends are necessary inclusions. These features introduce geometric and material property discontinuities in the pipe system and are potential sources of weakness. Of the failures in pressurised pipe work recorded by the power industry, the majority have been localised around regions such as weldments or bends[104]. The understanding of the structural integrity of these pipework components is clearly paramount for the safe operation of a power stations[65,105,106]. Additionally, the accurate quantification of remaining life in a component is fundamental to maintenance and replacement strategies and therefore the economic running of a power plant. Present methods of analysis are often considered overly conservative as investigations of retired components have shown that many do not display significant damage[107].

A main steam pipe system (that is to say, the principal supply line of steam from the boiler to the steam chests) for a generation unit at full load may see steam at a temperature of $550^{\circ}C$ and a pressure of 150 bar (15 MPa), although in Europe new generation pulverised coal power plants will be designed for steam up to $700^{\circ}C$ and 300 bar[105]. These high temperature operating conditions indicate that creep failure is a major concern for the power industry. Furthermore, plant will often be cycled in order to match market demands and generate in an efficient manner. These start up and shut down cycles will become more frequent in the future as generation strategies are refined. Fatigue is therefore also a potential failure mechanism for these components, however it has not been studied in the literature to the same degree as creep. It is worth pointing out here that the loads imparted on a pipe system component (such as a weldment or bend) are not limited to the internal pressure generated by the steam supply. System loads in the structure due to thermal expansion or cold pull (whereby a pipe system is plastically strained at room temperature in an attempt to reduce the effects of thermal expansion) are also present[108]. Bearing in mind that a pipework system is often made up of several bends and straight sections (see figure 2.33 for an example), these loading patterns will be complex and strongly dependent on a particular power station's layout.

The characterisation of creep for weldments in pipe systems has received significant attention in literature from authors such as Hyde, Sun and Becker[64,109] and Hayhurst[110]. This has lead to the study of type IV creep cracking (a crack in the heat affected zone, or HAZ, region of a weld, near the parent material) in pipe welds[111] and an understanding of the residual stresses due to the welding process[112–114]. Relatively little work has been completed however for pipe bends, particularly for cases where there is manufacturing induced geometry variation. Much of the present work will therefore focus on the creep behaviour of pipe bends.

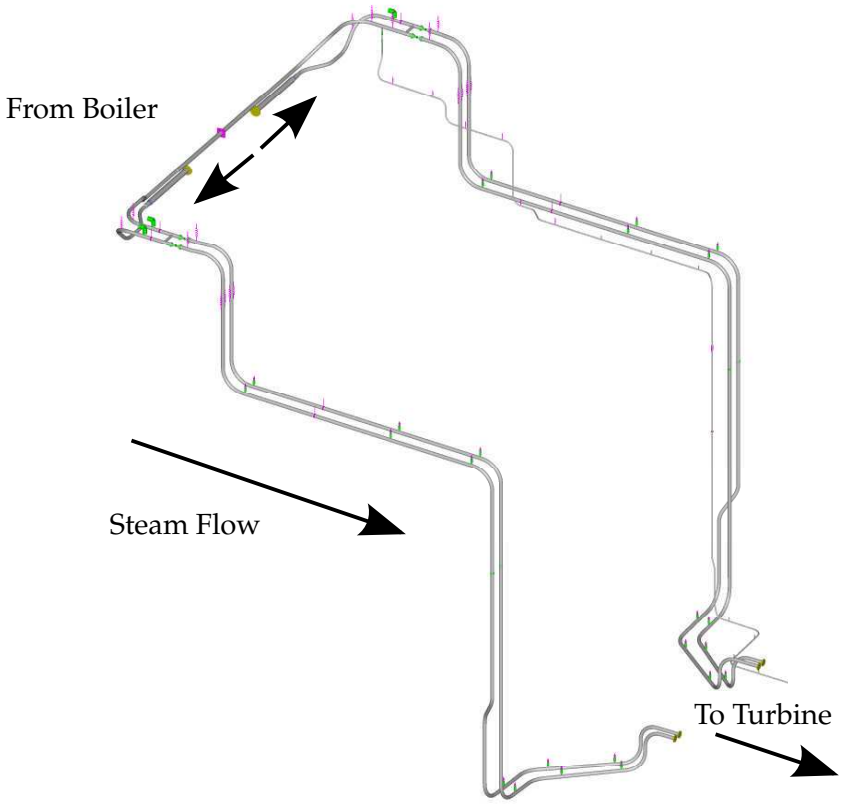

Figure 2.33: An example main steam pipe work system for a single unit in a coal fired power station. This image was generated using the commercial pipe load analysis software PSA5[115].

The large radius pipe bends used in the power industry are commonly manufactured by hot bending straight sections using a fixed radius arm and an induction heating ring assembly[116], see figure 2.34 (a). There are almost inevitable variations in the wall thickness for all but the largest of bend radii. The tensile stresses at the outside of the bend (the extrados) will cause a reduction in the wall thickness; whereas the compressive stress at the inside surfaces of the bend (the intrados) will cause an increase in wall thickness (see figure 2.34 (b))[117,118]. The degree of wall thickness variation (with respect to some nominal value such as the uniform wall thickness of the straight pipe section) will also differ around the pipe bend and may change due to service exposure. The definition of bend geometry is made more complex through the tendency of bends to become oval under a bending moment (the von Karman effect)[119]. Initial ovality in the pipe bend cross section will occur during manufacturing by bending as the pipe flattens in the vertical direction. Under internal pressure alone the pipe will attempt to inflate, regaining a more circular cross section[119,120]. Under additional system loading and the loading imposed by the pipe hanger support systems (both potentially causing torques or closing bending moments), the ovality of the pipe cross section may become more pronounced after a long term service at high temperature. Major pipe bend dimensions,

namely the mean bend radius (R_M), bend angle (φ) and internal/external pipe radius (R_I and R_O, respectively), are defined in figure 2.34 (b).

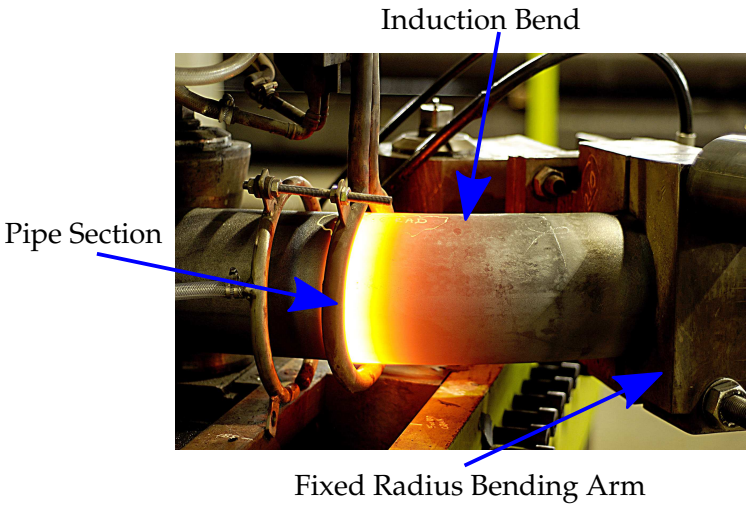

(a)

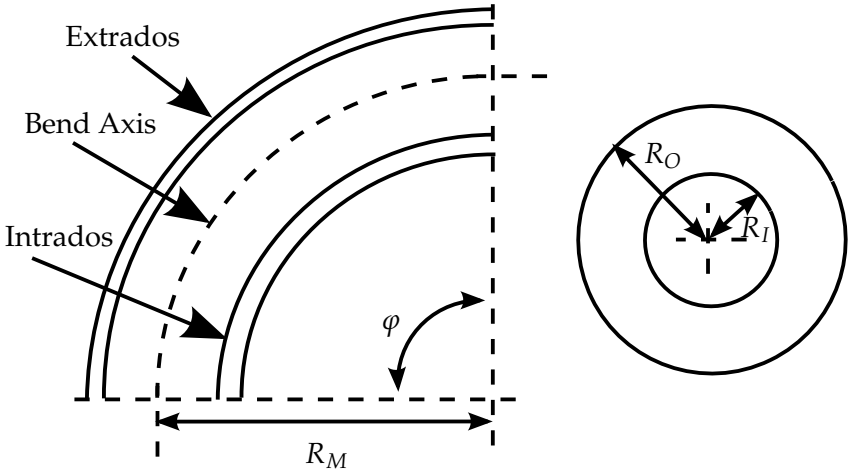

(b)

Figure 2.34: Images of power plant pipe bends, showing (a) the induction heating bending process[116] and (b) the major dimensions of a pipe bend and the definition of the intrados/extrados (viewed in the bending plane and the pipe cross section).

2.4.1 Power Plant Pipe Analysis

Given the high pressures and temperatures of the steam that power plant pipework must transport, it is of critical importance that a pipework system is safe and structurally sound. Many novel monitoring systems have been developed for assessing the "fitness" of power plant components. These include "on line" management systems that monitor power station load characteristics (such as main steam temperature and pressure) and estimate component degradation using generalised finite element models[121,122]. While these advances have shown some success, established design codes and analysis procedures are still by far the most commonly used tools in industry for component fitness

assessment, along with frequent inspection during outage periods[123]. In the UK, the R5[124,125] procedure is commonly used for high temperature assessment and the R6[126] procedure for low temperature fracture assessment of power plant components. These step by step methods usually involve decomposing a loading history into cycles. The likelihood of failure by various mechanisms, such as plastic collapse, creep and fatigue, is calculated by estimating damage accumulation and mechanisms interaction factors. Sensitivity analysis may also be conducted to take account of variations in material properties. Multiple design codes are also available for pressurised components, notably in the U.K. PD5500[127] for pressure vessels (this is similar to the American ASME VIII) and BS EN 13480[128] (succeeding BS 806[129]) for piping components specifically. Variations in the geometry of a component, loading and material properties are accounted for through safety factors. Codes tend to give conservative estimates of life spans for piping components due to wide range of potential applications/uncertainties and the paramount need for safety. The present work looks to perform more accurate analyses of piping components, therefore techniques that can analyse bespoke pipe sections are considered here.

In the interest of simplicity, creep in straight pipe sections will be considered first. For most situations in the power industry the well known thin walled assumption for pipes is not valid due to the wall thickness values having a similar order of magnitude to the outer diameter of a pipe[18]. Elastic solutions for the "thick walled" case have been developed, where radial stress components (σ_r, see figure 2.35) are assumed to vary through the wall thickness. A solution for the constant steady-state stresses (observed in a structure during the secondary creep region, see section 2.3.3) was proposed by Kraus[130] based on these elastic solutions for an internal pressure loading (P_i). Considering an element in a thick walled cylinder (as shown in figure 2.35) and applying Norton's law (see equation (2.47)), the steady-state stress components in the radial (σ_r), circumferential (σ_θ) and axial (σ_z) directions can be calculated, shown in equation (2.104). Note equation (2.104) simplifies to the elastic solution if the stress exponent n is set to 1. These solutions can be used to show the effect of stress redistribution in the transient creep period to achieve a steady-state value, with peak creep circumferential stresses located at the outside surface of a pipe section (see figure 2.36).

$$\begin{Bmatrix} \sigma_r \\ \sigma_\theta \\ \sigma_z \end{Bmatrix} = \frac{P_i}{\left(\left(\frac{R_O}{R_I}\right)^{2/n} - 1\right)} \begin{Bmatrix} 1 - \left(\frac{R_O}{r}\right)^{2/n} \\ 1 + \frac{(2-n)}{n}\left(\frac{R_O}{r}\right)^{2/n} \\ 1 + \frac{(1-n)}{n}\left(\frac{R_O}{r}\right)^{2/n} \end{Bmatrix} \tag{2.104}$$

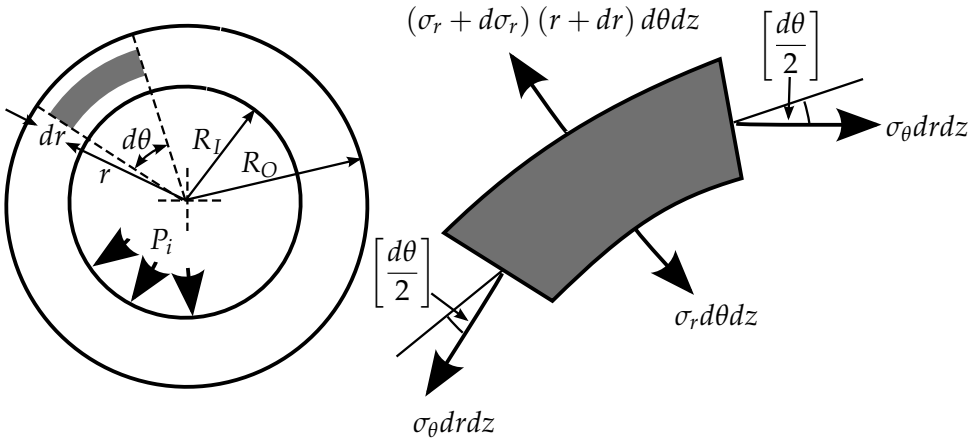

Figure 2.35: The solution for a thick walled pipe section under steady-state creep, after Kraus[130].

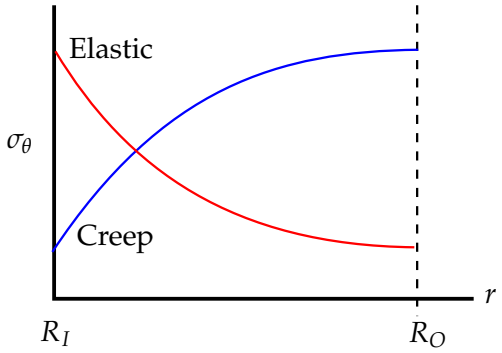

Figure 2.36: A comparison of the elastic and steady-state creep circumferential stress solutions for a thick walled pipe section[130].

Although estimates of the elastic stresses in pipe bends loaded by an internal pressure have been proposed by Hong et. al.[131], closed form creep solutions are yet to be developed. The analysis of pipe bends is made more complex by the geometry variation experienced at these locations due to the manufacturing processes employed and the complex load patterns imparted by the pipe system. FEA has been employed in several publications to simulate the stress state of pipe bends (both with and without geometry variation). For 3D pipe bend analysis, a large proportion of the published literature is concerned with the determination of plastic collapse loads for pipe bends[118,120,132–135]. Ovality in internally pressurised pipe bends has been considered by Yaghi et. al.[104] and Veerappan and Shanmugam[118] through the use of FEA to develop parametric equations to determine steady-state creep stresses and allowable internal pressures according to design codes, receptively. No system loads were included in either of these works and a constant oval cross section was assumed (i.e. for a particular circumferential position

on the pipe cross section, a constant wall thickness is assumed for all bend positions). Despite the limited relevance to advanced creep analyses, several common features are noted from the published literature that can be used to construct pipe bend FEA models.

A FEA mesh of a full 90° pipe bend can be seen in figure 2.37. If system loads are neglected a three dimensional (3D) quarter model can be used to represent the complexity of a full pipe bend (see figure 2.37 (b))[132,136]. This is achieved through the assumption of the planes of symmetry in the bending plane and at middle of the bend section. Straight sections of the pipe may be attached to the end of the bend section which should be long enough to ensure that the conditions at the straight/bend interface are modelled correctly while not unnecessarily increasing computing time[135,137]. Normally, it is difficult to specify a condition for this region that would reflect the realistic physical response. An incorrect constraint would drastically affect the behaviour of the bend, therefore it is more prudent to minimise the numerical effects of an unverified boundary condition by separating it from the region of interest (i.e. the bend section)[107]. At the free end of the straight section, all degrees of freedom may be constrained, effectively representing a connection to a substantial "anchor" (such as a land boiler or steam chest). In the straight pipe section, a uniform wall thickness is assumed. This is fair as in reality a straight section will usually be welded to the bend section, therefore the only dimension variation in the straight section is due to relatively small mill tolerances. Pipe bend models may be simplified further by using an axi-symmetric two dimensional (2D) approximation. Providing a constant cross section is defined around the bend section, reasonable approximations of the stress state in the bend section (i.e. away from bend/straight interface region) may be calculated[104,138,139]. An example 2D FEA pipe bend mesh can be seen in figure 2.37 (c). Again, the use of rotational symmetry limits the inclusion of geometry variation around the bend and the application of system loads in this type of approximation[139].

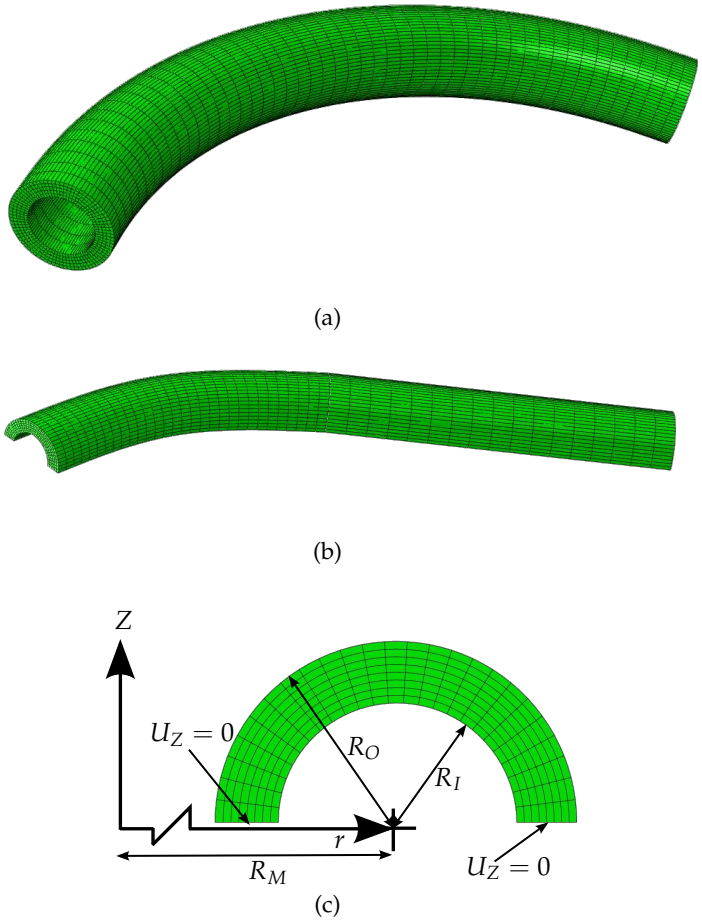

Figure 2.37: Illustrations of FEA meshes for pipe bends, showing (a) a full 90° pipe bend model, (b) a 3D quarter model approximation and (c) an axi-symmetric 2D approximation.

2.4.2 Power Plant Non Destructive Testing (NDT)

It is clear from the previous sections that some form monitoring of the condition of power plant components would be greatly beneficial in planning a power station's operation. The results of these investigations can be used to validate design or condition calculations, determine material properties for further analyses and provide information to formulate component maintenance/replacement strategies. Condition monitoring may take place during maintenance outages or during operation, depending on the type of component considered and the investigation procedure employed. Non-destructive testing (NDT) methods are designed so that there is no significant detrimental effect on a component's condition as a result of testing. Ultrasonic and acoustic pulses may be used for example to determine the location of cavities in a material by noticing an "echo" in reflected waves[140–142]. Both defects and component dimensions may be estimated by timing the periods between echoes and noting that larger amplitudes will be noticed at the internal and external surfaces. As the time it takes for a wave to propagate

through a specimen is usually very short visualisation may be difficult, therefore a pulse repetition frequency may be used. Echoes are measured numerous times per second to give an apparent steady display. Void fractions or changes in component dimensions may be used to infer any significant degradation that has taken place due to service exposure. The growth of defects such as cracks may alternatively be measured in situ using the potential drop method, where either a direct current (DC)[143] or alternating current (AC)[144] electrical supply is placed across the surface of a component and the presence/size of a defect is calculated by noting a voltage drop from a reference value. A.C. supplies have an advantage over D.C. supplies in that Eddy currents are generated in the centre of the material, forcing the currents to flow in a layer below the surface. The depth of this surface or "skin" may be controlled by the supply frequency, allowing for the depth of an internal defect to be estimated.

Several NDT methods are dependent on information determined from the surface of a component. For example, hardness readings (which may be taken using bespoke equipment) from the surface of in service components have been correlated to Larson-Miller parameter (see equation (2.46)) values to approximate the remnant life of a component operating in the creep regime[145]. Morris et. al. have also reported the development of an in situ digital image correlation machine for determining localised strain patterns on the surface of components[146,147]. A randomised speckled pattern is applied to the surface of the component along with large reference nodes. The relative motion between these points (determined by comparing before and after digital photos and performing digital image correlation) is used to estimate surface strains, which in turn can validate other analysis methods. Surface strains and the surface micro-structure of a component can be determined using the replica technique[148], where a negative of the surface is taken using acetyl-cellulose tape. A positive replica can be "developed" from this tape by electroplating it with, say, a thin layer of gold-palladium. This positive replica can then be subjected to microscopy, potentially highlighting the initiation of surface cracks or other defects.

An alternative to NDT is quasi non-destructive mechanical testing. Although small amounts of material are removed from an in service component, the surface defect that remains is deemed to have no significant effect on the future operation of the component. Scoop sampling is a novel method employed to extract sample material for the manufacture of small specimens from in service components (such as pipe work or reactors)[149,150]. Several in-situ scoop sampling machines have been developed for industrial use[151,152], such as the one produced by Rolls-Royce[151]. A hemispherical cutter is driven into the surface of the component, revolving about a feed axis (see figure 2.38 (a), note a cutter diameter of $50mm$ is often used). This causes a small scoop of material to be extracted, the depth of which can be controlled (see figure 2.38). In some cases, multiple small specimens may be machined from this scoop of material. Clearly therefore, a deeper cut will be more valuable for small specimen manufacture

than a shallow sample. The depth of cut however is limited by concerns over structural integrity (most notably the requirement to maintain a minimum design wall thickness). The amount of material needed to be removed to manufacture full size conventional specimens often compromises the structural integrity of a component, necessitating extensive repair or even complete replacement. Several novel small specimen samples have been proposed, examples of which are provided in figure 2.39 with some typical major dimensions for scale. Due to the specimen design, only secondary creep material properties can be determined from the impression[153,154] (where an indenter is forced into a sample and creep occurs in a compressive fashion, see figure 2.39 (b)) and small ring[155] (where a ring of material is stretched by two pins, see figure 2.39 (d)) tests. The two bar specimen (see figure 2.39 (a)) is a novel design that is still under development, however it has an advantage over the miniature tensile specimen proposed by EPRI[156] (see figure 2.39 (c)) in that end grips do not need to be attached (which in many cases can be difficult and may lead to load misalignment). Potentially, full creep curves could be characterised for a material from either of these test methods. Fracture is also allowed to occur in the small punch test (see figure 2.39 (e)), which may be used to determine plastic or creep material properties[157]. In this test, a ceramic indenter is forced through a thin disc of material, the deflections of which are recorded and converted by some method into strain values. The interpretation procedure to correlate the results of the small punch test is the subject of ongoing research, however the specimen's simplistic design and small size make it a potentially valuable test and analysis method.

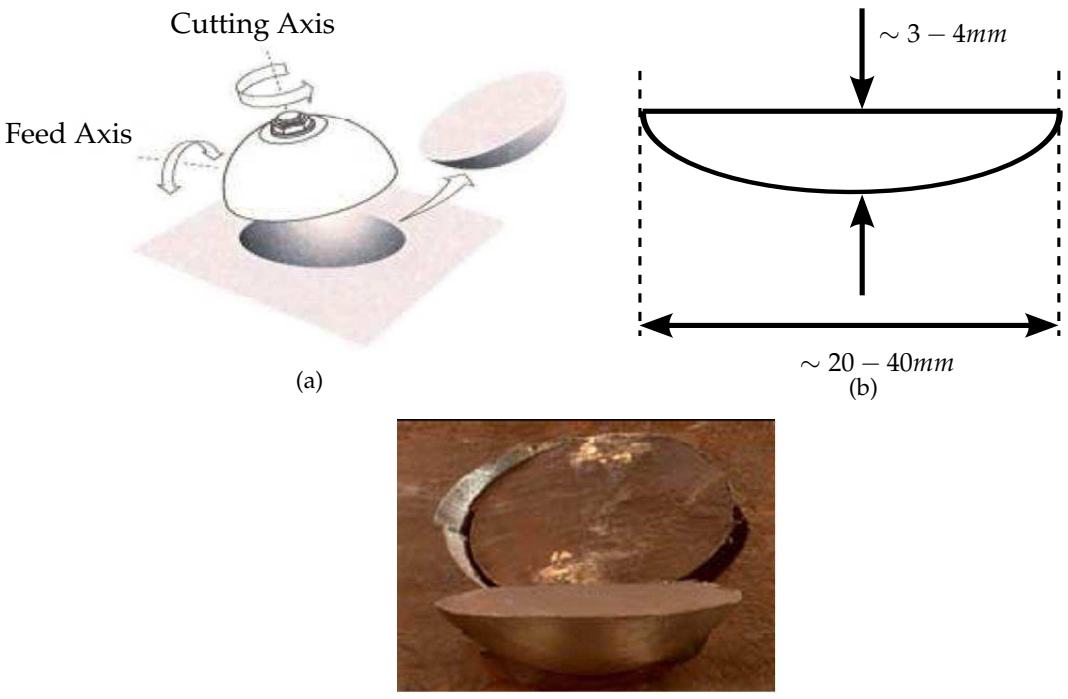

Figure 2.38: Illustrations of (a) the Rolls Royce scoop sampling procedure[151] and (b) typical dimensions of a scoop sample. A photo, (c), of a scoop sample is also included.

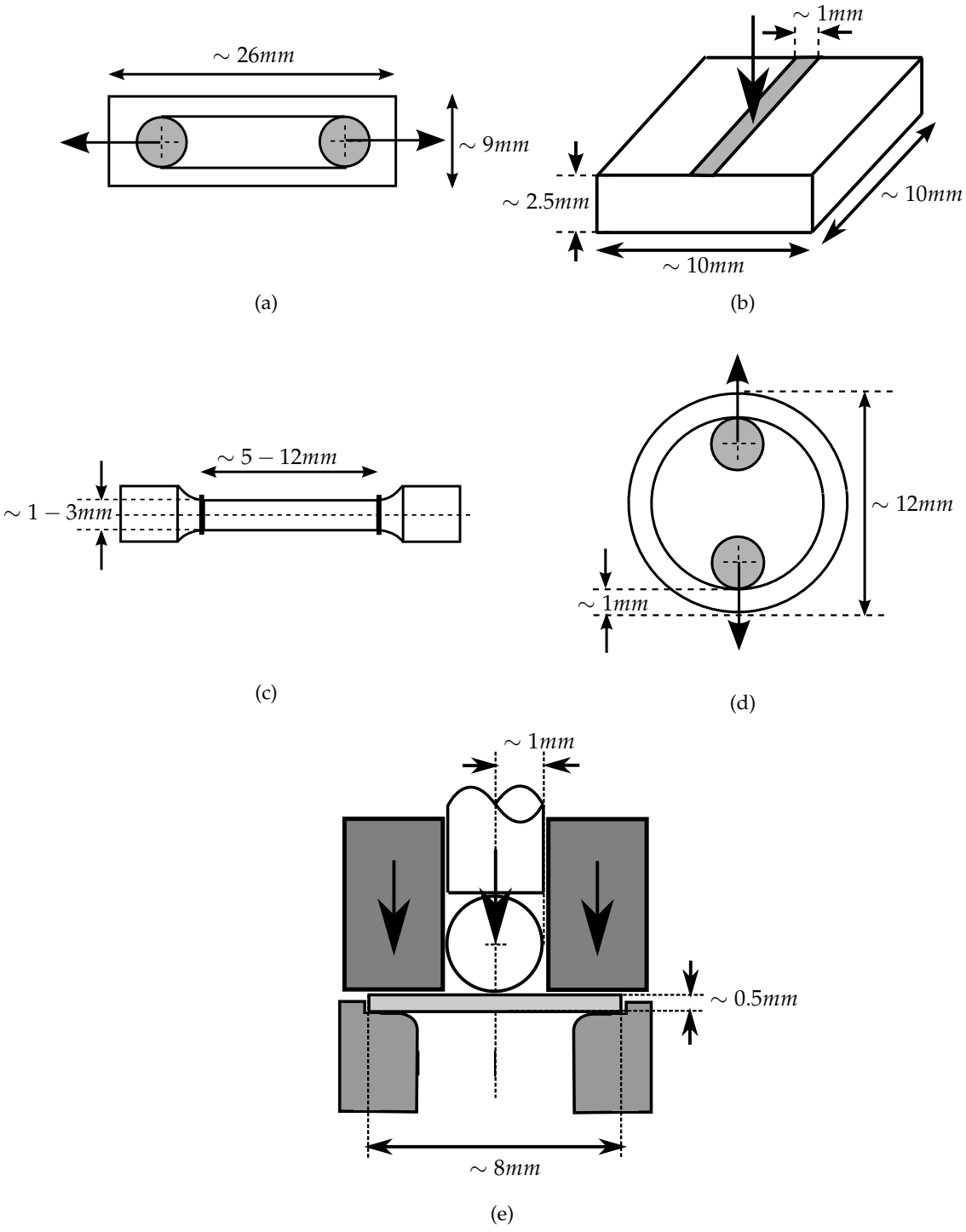

Figure 2.39: Examples of typical/novel small specimen samples, showing approximate dimensions. (a) Two bar specimen[158], (b) Impression specimen[153,154], (c) Miniature tensile specimen[156], (d) Small ring specimen[155] and (e) Small punch specimen[157].

2.5 Artificial Neural Networks

2.5.1 Relevance to the Present Work

Neural networks were first proposed by McCulloch and Pitts in 1943[159] and have been implemented in literature to determine patterns and trends in data where some correlation exists but controlling functions are either unknown or too complex to implement. As will be discussed in a later chapter, solutions for various problems (such as steady-state creep stress distributions) related to pipe bends are due to the systematic application of an internal pressure and system loads. Once trained, a neural network could be used as an analysis tool for a practising engineer. Approximate techniques are a module in the toolbox outline, and it is an objective in the present work that a neural network (NN) can be developed for steady-state creep peak rupture stresses in pipe bends subjected to internal pressure and system loads. If this is achieved, engineers could quickly and easily determine an approximate reference solution for a component, which could in turn be used to assess the risk for a reduction in remnant life for a particular operation strategy.

Due to the constant nature of the loading conditions considered for pipe bends in the present work (neural networks will be used to determine time independent steady-state stress solutions for pipe bends), this review will be limited to back propagated (BP), recurrent and radial basis function (RBF) architectures, as opposed to dynamic networks which are used for time dependent patterns[160].

2.5.2 Neural Network Fundamentals

Artificial Neural Networks (ANNs) are mathematical representations of biological central nervous systems[161]. Biological neurons consist of a nucleus surrounded by a membrane. Connections to other neurons are made through a network of fibrous dendrites. The axon extends from the nucleus and transmits electrical signals to the neurons. Signals are received through synapses located in the dendrites of the neuron (see figure 2.40). When signals surpass a certain threshold level in the neuron it triggers a constant magnitude and duration electrical signal through the axon[160,161].

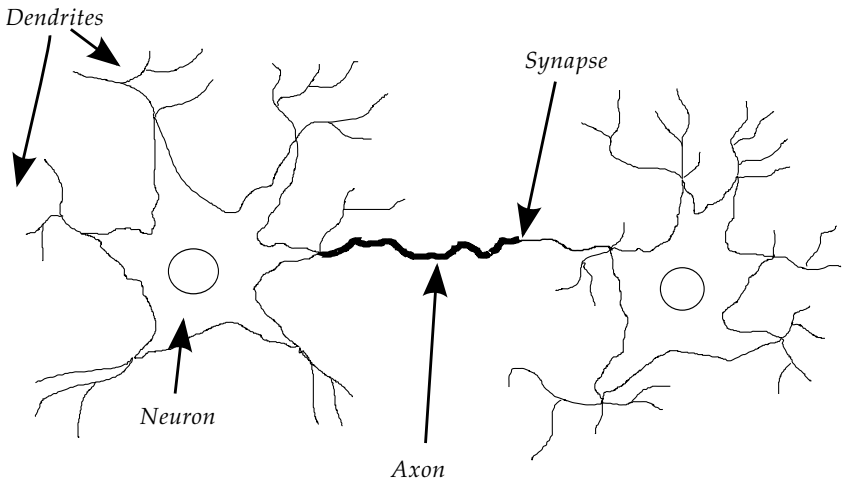

Figure 2.40: A biological neural network[160].

Fundamentally, an ANN neuron (see figure 2.41 (a)) takes a group of inputs (or signals in a vector $\boldsymbol{X}$), multiply them by weighting values (W_i) and pass them through mathematical functions ($S(X_i, W_i, \theta)$), giving rise to the effective input S. This function is known as the propagation rule and, while many variants exist, the most simple and applicable is the weighted summation rule in equation (2.105) (shown for a single neuron fed by i inputs). External inputs (or biases, θ) may be used to distinguish certain neurons in a network. The effective input is used in an activation function $F(S)$ (akin the natural neuron's threshold) to determine the neuron's output Y. In fully connected networks, this will be passed on to subsequent neurons as an input (along with the local outputs from other neurons on that layer.) The interaction between the inputs and outputs of neurons is dictated by the network's architecture.

Weights and biases (the network's characteristic values) used in a particular network are determined in a process called training. In effect, this is a form of optimisation and similar methods (such as a least squares evaluation of the Gauss-Newton method[162], see section 2.6.3) may be used for this purpose. A set of inputs with known outputs are collected and fed into the neural network. From a usually randomised starting position, the training algorithm will iteratively alter the network's characteristic values to minimise the difference between approximated outputs from the network (Y) and the corresponding true values. Typically, a validation sequence would also be required for the approval of a network. In some cases, ANNs can "overfit" the training data set. This means that while errors in the training set are small, predicted values outside the training set (where clearly a predictive ANN has the greatest value) show very large errors.

$$S = \sum_{i=1}^{n} X_i W_i + \theta \tag{2.105}$$

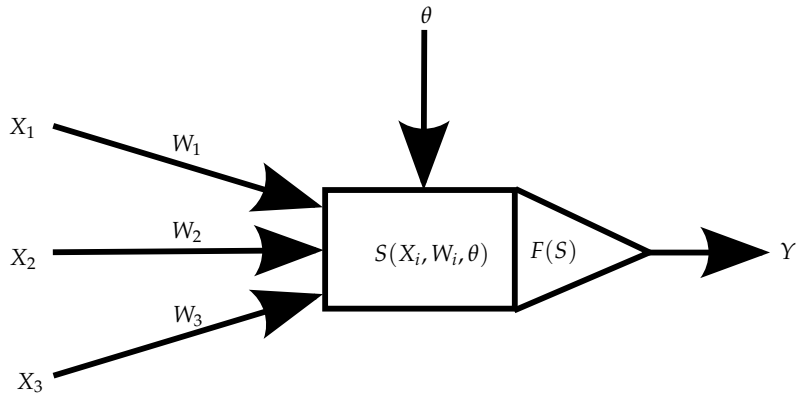

Figure 2.41: An individual ANN neuron[160].

2.5.3 Activation Functions

Multiple neurons will be implemented in an ANN to determine the patterns in a data set. Often, input arrays will comprise of different types of data, which should be considered in alternative ways for efficient ANNs. For example, an output value (Y) may have a linear dependence on some quantities in an input array $\boldsymbol{X}$, but sinusoidal dependencies on others. Multiple activation functions must therefore be considered for a good fitting (note these will be dependent on a neuron's effective inputs S, the activation function being signified by $F(S)$).

Activation functions are often (but not limited to) non-decreasing functions. Limiting functions are also generally used (these are directly analogous to the biological neuron's threshold). These can be hard-limiting functions (such as the sgn function, see figure 2.42 (a)) or softer transition functions (such as semi-linear or sigmoid dependencies, see figure 2.42 (b) and (c))[160]. The most common function used is the sigmoid function (see equation (2.106)), which approaches 1 for large positive values of S, has a value of 0.5 when $S = 0$ and approaches 0 when the effective input is negative. Stochastic activation functions may also be incorporated. In these cases, neuron outputs are not determined directly from the effective inputs, but the sum of effective inputs determines the probability that a certain neuron output value will be achieved.

$$F(S) = \frac{1}{1 + e^{-S}} \tag{2.106}$$

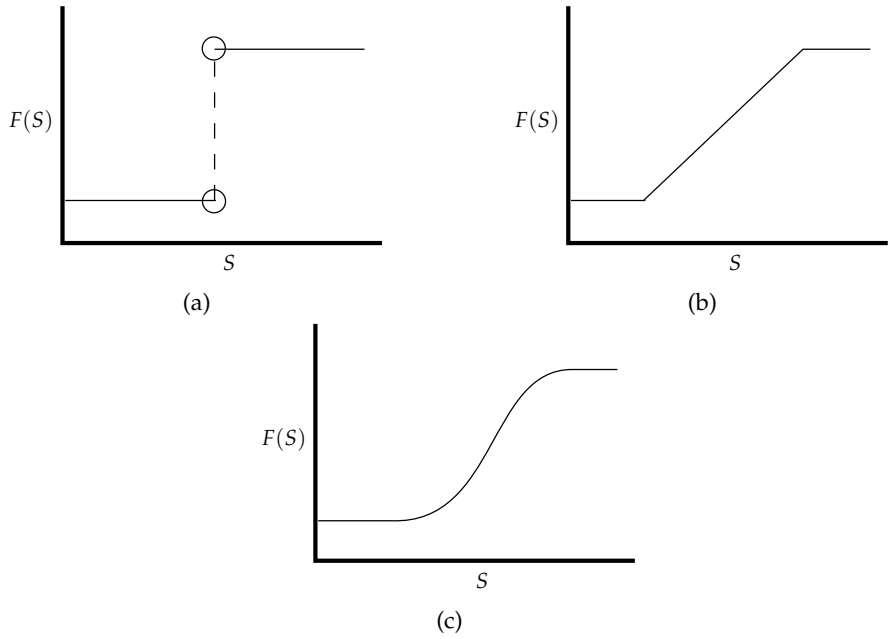

Figure 2.42: Common non-decreasing activation functions: (a) the *sgn* hard-limiting function, (b) a semi-linear limiting function and (c) a smoothly limiting sigmoid function.

In the present work, neural networks will be constructed using MATALB's Neural Network toolbox[163]. All three of the above activation functions are available within this toolbox.

2.5.4 Neural Network Architectures and Training Procedures

For all but the simplest systems, fully connected ANNs will comprise of many layers of neurons that are all linked together (see figure 2.43 (b)). Back propagated neural networks (BPNNs) are simple examples of these feed forward networks. An array of inputs $\boldsymbol{X}$ (length m) will form the input layer. These inputs are fed to the first "hidden" layer of neurons (in figure 2.43 (b) length n). Each neuron is fed by all of the inputs (weighted in some way, depending on the prorogation rule used) and the effective input is determined by the neuron's function S_{1j} ($1 \leq j \leq n$). An output for that neuron is determined from the effective input by the activation function. The outputs of the neurons from this first hidden layer are fed as inputs into the neurons of the next hidden layer. Commonly, local outputs from the last hidden layer of inputs are summed in an output neuron, giving rise to the network's output $\hat{Y}$[160]. Y is therefore the local output from a neuron and $\hat{Y}$ is the global output from the neural network.

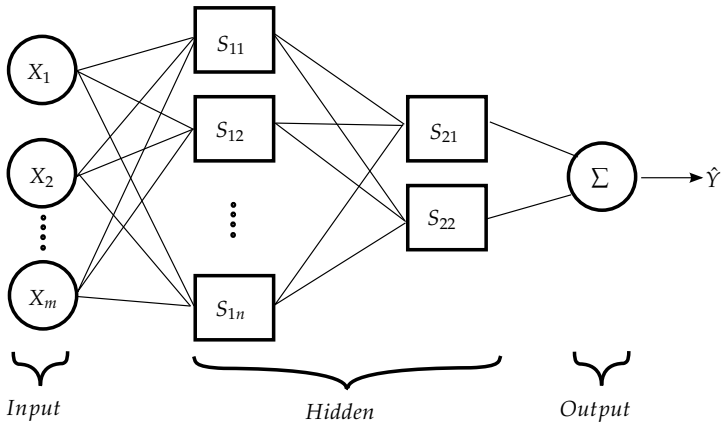

Figure 2.43: A 2 layer feed forward fully connected ANN[161].

Training is completed for a neural network in order to determine the magnitude of the weights and biases for each neuron. This is done for a sample training set of data. BPNNs are part of the family of feed forward ANNs (these are the type that have been described thus far). During calculations, data flows uni-directionally from the input nodes to the output. For training purposes in BPNNs, errors (E) between the outputs predicted for an ANN and the true training values are compared using the sum of squares approach. Using a gradient descent optimisation method, the change to a weight is determined by a multiplier term and the rate of change in E with respect to the weight W_i. Optimisation routines are discussed in detail later in the present chapter with regard to material constant optimisation. These same routines are also valid for ANNs. It is worth noting that, if training is undertaken for a specific data set only, it is termed supervised learning. Un-supervised learning results in weights and biases being continuously updated as new information is made available. Supervised learning is considered more relevant to the current project as the intended application demands a deterministic capability without continually performing FEA calculations to generate new data (see chapter 7).

$$\Delta W_i = -\eta \frac{\delta E}{\delta W_i} \tag{2.107}$$

Radial basis function (RBF) networks have the same data flow direction as BPNNs (data flows uni-directionally from the input nodes to the output), however the architectures and activation functions used differ greatly. BPNNs will usually contain several hidden layers of neurons, whereas RBFs will always contain a single hidden layer of neurons (in addition to the input and output layers). The RBF network accounts for greater complexity in a pattern by adding neurons to this single hidden layer (see figure 2.44). The radial basis function itself is a function whose argument is referenced to a "centre", a common form of which is the Gaussian (bell shaped) function given in first term of equation (2.108)[161]. Usually, linear terms are added to complement the Gaussian transfer functions (dependent on the quantity b_i in equation (2.108)). Each of

the m inputs in $\boldsymbol{X}$ are fed into each of the n RBF neurons. A Gaussian RBF neuron has two characteristic values associated with it: a centre c_i and the quantity λ_i, dictating the spread of the Gaussian bell curve. Unlike BPNNs using the summation propagation rule, weights are applied after the activation function. A bias θ may be applied to the output node, giving rise to the network's output $\hat{Y}$. Values of c_i and λ_i are found by various specialist methods (such as the sub-sampling and K-means algorithms) to reflect the natural clustering of the training data. Network training optimises weight values to fit the training data. As RBFs tend to have fewer neurons than BPNNs, weight values converge quickly, meaning that training and computation times are commonly greatly reduced for complex systems.

$$\hat{Y} = \sum_{i=1}^{n} \left(W_i e^{(\lambda_i^2 (X - c_i)^2)} \right) + \sum_{j=1}^{m} \left(b_j x_j \right) + \theta \tag{2.108}$$

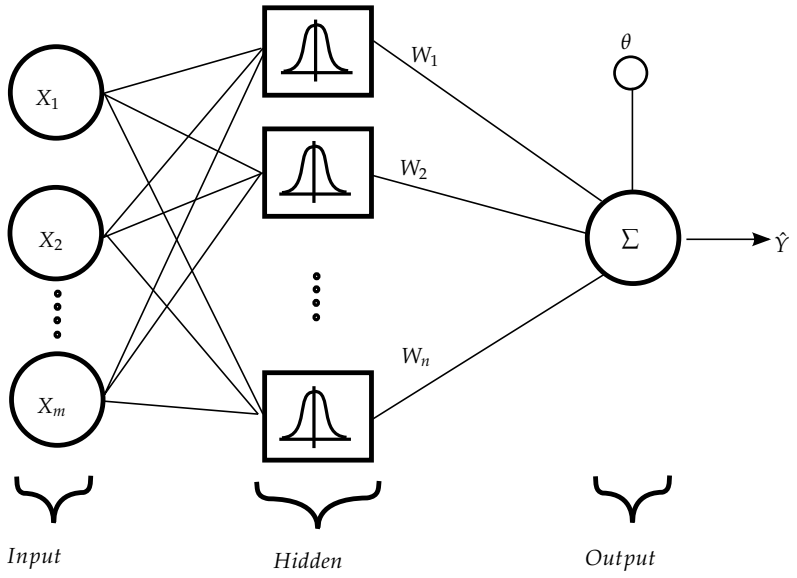

Figure 2.44: A RBF ANN structure[161].

Examples shown so far have been for fully connected networks. This is not an accurate representation of a biological neural network and tends to lead to significant redundancy in the network (i.e. storage, computation and training requirements are far greater for fully connected networks[164]). Customised networks can be developed that connect only specified neurons, meaning that the network can be more efficient. It is also worth noting that while only feed forward ANNs are described here, recurrent topologies have been used in literature[161], such as the Boltzmann and Hopfield networks. In these cases, information does flow in one direction only but can cycle on a local basis, potentially allowing for more complex functions to be analysed. These aspects are considered outside the scope of the present work.

2.6 Optimisation Methods

2.6.1 Relevance to the Present Work

A great deal of the present work focusses on the application of material models in component simulations. To make the results of these simulations relevant, material parameters for the models need to be accurately determined from experimental data. In many cases, procedures to determine these material constants directly from the experimental data demand the application of several assumptions, potentially impairing the predictive capability of the material model. Optimisation procedures are often implemented in order to "fine tune" material constants and restore the quality of fit (compared to experimental data[165]). In the present work, optimisation strategies are developed for a complex visco-plastic material model. This case requires a set of parameters to be optimised (which is common), therefore simple one dimension optimisation procedures are omitted from the present review. Focus will mainly be given to the gradient methods as these are generally straight forward to apply and can provide good results (coefficients of determination are typically above 0.97 after optimisation)[166]. Alternatives such as genetic or evolutionary algorithms[166–169] and pattern search methods[166] have been applied to similar problems, although these methods tend to be computational intensive. A brief overview of these methods is presented at the end of this section.

2.6.2 Multiple Dimension Optimisation Overview

Consider a function (f) that has several (n) real arguments that can be generally expressed as the vector $\boldsymbol{x}$, such that equation (2.109) is true[170].

$$\boldsymbol{x} = (x_1, x_2, ...x_n) = \mathbb{R}^n \tag{2.109}$$

Each argument in the function f is a degree of freedom (or dimension), therefore an optimisation procedure using f will be deemed multidimensional.

Now consider the situation where the function f is to be fitted to a set of data points, here signified by g. For a given $\boldsymbol{x}$ there may be an error (E) between the values predicted by f and the true values given by g. One of the most common methods to represent this error is the sum of squares approach[162]. For m values in g, the total error would be given by equation (2.110). This expression is known as the objective function.

$$E(\boldsymbol{x}) = \sum_{i=1}^{m} (g_i - f(\boldsymbol{x}))_i^2 \tag{2.110}$$

It is the goal of an optimisation procedure to minimise the error E by altering the values of $\boldsymbol{x}$ (note E is a function of $\boldsymbol{x}$). Often, due to physical constraints, limits may be placed on $\boldsymbol{x}$ meaning that optimised value must fall between a lower bound LB and an upper bound UB.

In the present work, a material model would be represented by the function f, with its related material constants forming $\boldsymbol{x}$. The data from experimental procedures populates g. The optimisation method attempts to minimise the difference between the predicted and experimental results by fine tuning the material constants.

2.6.3 Gradient Method Overview

The gradient optimisation method is an iterative approach. Several algorithms have been proposed, however there are underlying concepts that first must be considered. A set of real values can be used to define an starting point for $\boldsymbol{x}$. This starting point shall be called $\boldsymbol{x}^0$. The function E (the error function to be minimised) will decrease most rapidly in the direction $-\nabla E(\boldsymbol{x}^0)$ [171], where the ∇ operator determines the gradient of the function E at the point $\boldsymbol{x}^0$, as shown by equation (2.111) [162].

$$\nabla E(\boldsymbol{x}^0) = \left[\frac{\delta E(\boldsymbol{x}^0)}{\delta x_1} ... \frac{\delta E(\boldsymbol{x}^0)}{\delta x_n}\right]^T \tag{2.111}$$

where n is the dimension of $\boldsymbol{x}$. An iterative step will therefore take a direction of $-\nabla E(\boldsymbol{x}^0)$. The first iteration, resulting in $\boldsymbol{x}^1$, can therefore be found using equation (2.112).

$$\boldsymbol{x}^1 = \boldsymbol{x}^0 + \alpha^0 d(\boldsymbol{x}^0) \tag{2.112}$$

where α^0 is a step length scalar which can be found at each step by minimising the scalar function ϕ, as shown in equation (2.113) (this is known as a line search). The quantity $d(\boldsymbol{x}^0)$ is a direction search vector and takes the general form shown in equation (2.114), where M_0 is a nxn matrix [171]. The exact form of $d(\boldsymbol{x}^0)$ and M_0 relates to specific algorithms developed by numerous authors. Some examples of these are discussed in section 2.6.4.

$$\phi(\alpha^0) = E\left(\boldsymbol{x}^0 + \alpha^0 d(\boldsymbol{x}^0)\right) \tag{2.113}$$

$$d(\boldsymbol{x}^0) = -M_0 \nabla E\left(\boldsymbol{x}^0\right) \tag{2.114}$$

Note that the above example shows the first iteration in a gradient optimisation procedure. This procedure is repeated until some termination criteria are satisfied. This will commonly involve satisfying some minimum value for the error, gradient or step length values [170].

2.6.4 Gradient Method Optimisation Algorithms

Several algorithms have been developed that utilise the concept of gradient based optimisation. Perhaps the most simplest of these is the steepest descent algorithm. In

this case, the direction of descent equation ($d(\boldsymbol{x}^0)$) takes the form of equation (2.114) and M_0 is an identity matrix ($\boldsymbol{I}$), shown by equation (2.115)[171]. Although this algorithm is relatively simple to program, step sizes tend to be short and solutions may "zig-zag" in the optimisation space, causing computation times to be elongated[170].

$$\boldsymbol{I} = \begin{bmatrix} 1 & 0 & \cdots & 0 \\ 0 & 1 & \cdots & 0 \\ \vdots & \vdots & \ddots & \vdots \\ 0 & \cdots & 0 & 1 \end{bmatrix} \tag{2.115}$$

A more direct approach is the Newton method where $d(\boldsymbol{x}^0)$ is dependent on the second partial derivative of $E(\boldsymbol{x})$, known as the Hessian ($\nabla^2 E(\boldsymbol{x})$, see equation (2.116)), and is therefore deemed a second order method (as opposed to the first order steepest descent method). The step direction is given by equation (2.117). This effectively uses a quadratic expression to approximate the gradient at the point $\boldsymbol{x}^0$ and minimises it to calculate the next iterative point $\boldsymbol{x}^1$. A potential pitfall of this method is the inability of the algorithm to distinguish between points of minima and maxima. It is critical therefore that a good initial condition is provided so that solutions do not diverge. To aid in the understanding of Newton's method, a one dimensional example is shown in figure 2.45. It can be seen that from an initial estimate ($\boldsymbol{x}^0$) a revised estimate ($\boldsymbol{x}^1$) of the value of $\boldsymbol{x}$ to minimise the function $E(\boldsymbol{x})$ can be determined by minimising a quadratic function based on the gradient at $\boldsymbol{x}^0$. As with the steepest descent method, further iterations will be performed to refine the approximation of $\boldsymbol{x}$.

$$\nabla^2 E(\boldsymbol{x}) = \begin{bmatrix} \dfrac{\delta^2 E(\boldsymbol{x})}{\delta {x_1}^2} & \dfrac{\delta^2 E(\boldsymbol{x})}{\delta {x_1}^2 \delta {x_2}^2} & \cdots & \dfrac{\delta^2 E(\boldsymbol{x})}{\delta {x_1}^2 \delta {x_n}^2} \\ \dfrac{\delta^2 E(\boldsymbol{x})}{\delta {x_1}^2 \delta {x_2}^2} & \dfrac{\delta^2 E(\boldsymbol{x})}{\delta {x_2}^2} & \cdots & \dfrac{\delta^2 E(\boldsymbol{x})}{\delta {x_2}^2 \delta {x_n}^2} \\ \vdots & \vdots & \ddots & \vdots \\ \dfrac{\delta^2 E(\boldsymbol{x})}{\delta {x_1}^2 \delta {x_n}^2} & \dfrac{\delta^2 E(\boldsymbol{x})}{\delta {x_2}^2 \delta {x_n}^2} & \cdots & \dfrac{\delta^2 E(\boldsymbol{x})}{\delta {x_n}^2} \end{bmatrix} \tag{2.116}$$

$$d(\boldsymbol{x}^0) = -\left[\nabla^2 E(\boldsymbol{x})\right]^{-1} \left[\nabla E(\boldsymbol{x})\right] \tag{2.117}$$

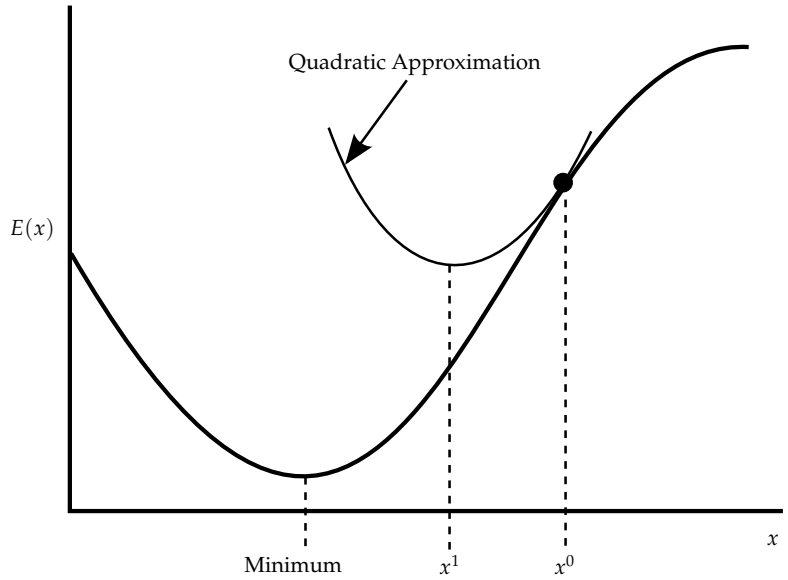

Figure 2.45: A one dimensional example of Newton's method for the first iteration of an optimisation procedure[172].

The Gauss-Newton method holds an advantage over the Newton method for least squares problems in that the Hessian matrix does not need to be calculated (which can be computationally expensive) but is rather conveniently approximated using the first order derivatives, see equation (2.118)[173,174]. The Hessian is approximated using the Jacobian (signified by the operator J_0 for the 0^{th} iteration). The multiplication of the Jacobian and its transpose (signified by the superscript T) provides a term which is a dominant component of the Hessian and is therefore a good approximation of it, particularly in the vicinity of the optimum value of $\boldsymbol{x}$. As this method is in effect the same as Newton's method in terms of step size, the convergence rate of the Gauss-Newton method is similar to that of Newton's method.

Calculation of J_0 (see equation (2.120)) is dependent on the error function $E(\boldsymbol{x})$ being made up of residual terms. A residual is the difference between a true value (g_i) and the value predicted by a function of $\boldsymbol{x}$ ($f(\boldsymbol{x})_i$), as shown in equation (2.119). The residuals are stored as a column vector of length m, where m is the number of data points in the set g. The Jacobian is calculated by taking the gradient of each of these residuals in turn, as shown in equation (2.120) where the ∇ operator is defined by equation (2.111)[173].

$$\nabla^2 E(\boldsymbol{x}) \approx J_0^T J_0 \tag{2.118}$$

$$\sum_{i=1}^{m} (g_i - f(\boldsymbol{x}))_i^2 = \sum_{i=1}^{m} r_i(\boldsymbol{x})^2 \tag{2.119}$$

$$J_0(\boldsymbol{x}_0) = \left[\frac{\delta E(\boldsymbol{x}^0)_j}{\delta x_i}\right]_{\substack{j=1,2,\ldots,m \\ i=1,2,\ldots,n}} = \begin{bmatrix} \nabla E(\boldsymbol{x}_0)^{1^T} \\ \nabla E(\boldsymbol{x}_0)^{2^T} \\ \vdots \\ \nabla E(\boldsymbol{x}_0)^{m^T} \end{bmatrix} \tag{2.120}$$

An additional improvement to the Newton method is available by application of the Levenberg-Marquardt algorithm[173,175,176]. This is in effect an interpolation of the steepest descent gradient method and the Gauss-Newton method, exploiting the latter's faster convergence rate in a more robust algorithm (solutions for the Gauss-Newton method may diverge from the local minima for some optimisation topographies). Levenberg originally proposed equation (2.121) as an increment in an optimisation routine[175]. A damping factor (λ) is introduced to determine the contributions of first order (i.e. the steepest gradient descent method, signified by the identity matrix I) and second order (i.e. the Gauss-Newton method, signified by the Hessian $\nabla^2 E(\boldsymbol{x}^0)$) methods. A reduction in the error function $E(\boldsymbol{x})$ would suggest that a reduction in λ (usually in factors of 10) would be prudent. This would mean that the Gauss-Newton method would become more dominant and the better convergence rate of this method could be exploited. An increase in $E(\boldsymbol{x})$ requires an increase of λ to promote the use of the steepest descent method to converge back into the local minima region[173]. Note that the Hessian term ($\nabla^2 E(\boldsymbol{x}^0)$) may be replaced by the Jacobian approximation shown in equation (2.118), however the full form is presented here.

$$\boldsymbol{x}^1 = \boldsymbol{x}^0 - \left(\nabla^2 E(\boldsymbol{x}^0) + \lambda I\right)^{-1} \nabla E(\boldsymbol{x}^0) \tag{2.121}$$

An improvement to Levenberg's method was suggested by Marquardt in 1963, giving rise to the increment method shown in equation (2.122)[176]. In this case the identity matrix I has been replaced with the diagonal components of the Hessian matrix. This alteration is particularly effective when λ is large and the iterate enters a low gradient region in the solution space. As the steepest descent method is dominant (λ is large) increments may be small with equation (2.121). The use of equation (2.122) however scales the gradient values ($\nabla E(\boldsymbol{x}^0)$) based on the curvature of $E(\boldsymbol{x})$, allowing for larger steps to be taken.

$$\boldsymbol{x}^1 = \boldsymbol{x}^0 - \left(\nabla^2 E(\boldsymbol{x}^0) + \lambda diag[\nabla^2 E(\boldsymbol{x}^0)]\right)^{-1} \nabla E(\boldsymbol{x}^0) \tag{2.122}$$

Historically the damping parameter λ in equation (2.122) was adjusted directly to minimise the function $E(\boldsymbol{x})$, however the concept of a "trust region" has provided an automated approach for this problem. A "trust region" is created (commonly through a Taylor series expansion[173]) in which it is expected a good approximation of $E(\boldsymbol{x})$ is possible. An iterative step is limited to this trust region, with both the direction and length of the iteration being determined from the trust region. The size of the trust

region is re-evaluated for each iteration. λ is determined from the size of the trust region and the iteration increment. This is distinctly different to the line search method shown in equation (2.113) in which a good approximation of the whole of $E(\boldsymbol{x})$ is assumed, potential leading to an iteration overshooting a local minimum and diverging from the optimum solution[173].

2.6.5 Genetic and Pattern Search Optimisation

Genetic evolutionary algorithms (such as NSGA-II implemented in MATLAB[169]) involve taking an initial population defined by the user (consisting of a group of individuals, each consisting of a unique set of the variables to be optimised) and generating new individuals from it by allowing for crossover and mutation[167,177]. Elitism may be applied, meaning that only a predefined number of individuals are permitted to survive to create the next generation. Such procedures hold an advantage over gradient methods as derivatives need not be evaluated, however analysis can be lengthy and global optimisation is not guaranteed[167,177]. Objective functions are required to allow for quantitative comparison of the individuals and to rate their performance at fitting to the experimental data. Analysis can be limited to a given number of generations to prevent lengthy mathematical search for a purely theoretical minimum. Optimum solutions can be suggested by higher population density zones in optimisation space after a given number of generations[171].

A pattern optimisation may alternatively be implemented[178]. From an initial condition, small aberrations in parameter values are introduced in the various dimensions. The iteration step then takes the direction of the point that gives the minimum objective function value. The limits of the variations in parameter values can then be reduced, converging on the minimum objective function value[179].

While both of the above methods have been applied to the determination of material constants they are generally more computationally expensive than gradient methods. It will be demonstrated in chapter 3 that the gradient method is suitable for material constant fine tuning and can provide excellent fitting qualities.

2.7 Summary

This literature review has attempted to condense a tremendous amount of research and investigation that has been conducted in a variety of fields and over several centuries. While not all the information presented here is directly quoted in the rest of this thesis, it has been the intention of the author to introduce potentially complex concepts in a simple fashion by gradually building on fundamental ideas. Bearing this point in mind, it is therefore useful to summarise how the literature has influenced and guided the present research.

The main objective of the present work is to improve the accuracy of computa-

tional analyses of high temperature power plant components. While several codes and standards have been referenced, they generally simplify the problem which increases uncertainty. Many sophisticated material models have been proposed to predict a material's behaviour for the complex loading conditions (i.e. creep, fatigue and visco-plasticity) that may be encountered by these components. The analysis procedures used to implement these models (such as FEA) are however commonly outside the reach of practising engineers.

Continuum damage mechanics has been applied for the analysis of creep (for example, through the Kachanov, Liu-Murakami and Dyson models), along with more simplistic models such as Norton's law. In the analysis of high temperature components creep is a major concern, therefore these material models have been applied to power plant components. Comments have been made on the suitability of these models and potential approximate methods that can be employed in order to make analyses easier to compute have been developed. In particular, relationships between Norton's law and continuum damage mechanics creep equations have been applied to novel and industry relevant component analyses. Using these analyses, empirical relationships have been developed that allow these more accurate methods to be easily implemented.

Visco-plastic behaviour can be described by the Chaboche model. The determination of material constants for this (and other) models can be difficult and is often dependent on some form of optimisation. In order to aid the future application of the Chaboche model in high temperature analyses, optimisation procedures and strategies have been developed. This work has established robust methods to determine material constants from experimental data.

The analysis of components is complex due to the wide range of loads, materials and geometry variations that may be present. Empirical relationships may be developed, however forming these expressions is often laborious due to the potentially large numbers of variables involved. Furthermore, these relationships may not be able to be revised when new information becomes available. Neural networks avoid these complications by simplifying an expression into nodes (neurons). Weights and biases in these networks may in turn be revised if new data is collected. This is clearly useful in the field of power plant component analyses where solutions may be dependent on not only a material but also several (system) loads. A neural network has therefore been developed that can estimate peak steady-state creep rupture stresses (which, as will be shown, are highly useful) for pipe bend sections subjected to system loads.

Chapter 3

Optimisation Methods for the Determination of the Chaboche Unified Visco-Plasticity Model Material Constants

3.1 Introduction

It may be inevitable in the design and analysis of most high temperature components (such as power industry pipe work) that variations in load and/or temperature will occur in normal operation. This presents complications in the prediction of the response of such components due to potential hardening or softening effects caused by the accumulation of plastic strain[57,58]. Furthermore, interactions between hardening (or softening) behaviour and creep may be significant, particularly in high temperature applications. The Chaboche unified visco-plasticity model is an example of a model which, with the correct modifications, shows much promise for this application[30,57,58]. Methods to approximate material constant values in the Chaboche model have been well established[100–103]; however the need for optimisation of these parameters is vital due to assumptions made in the initial estimation process[30,31]. This is a key step as the determination of initial estimates requires several assumptions to be made. Experience has shown, however, that several numerical problems may be encountered during an optimisation procedure.

In the present chapter, the uniaxial form of the Chaboche model (derived from the generalised multidimensional Chaboche model presented in section 2.3.5) is used to predict the results of experiments performed on power plant materials (namely a P91 high chrome steel and a grade 316 stainless steel). After determining initial estimates of the Chaboche material constants from experimental data, a Levenberg-Marquardt gradient optimisation algorithm (see section 2.6) is implemented.

In addition to identifying and addressing potential numerical problems in an optimisation procedure using experimental data, investigations into the effects of variations in the initial conditions on optimised material constant values and the number of data points selected for an optimisation procedure on computational times are made to aid in the application of similar optimisation procedures. Several optimisation strategies have also been developed and critiqued which can be used to determine a set of material constants when multiple experimental data sources are available (yielding a single set of optimised material parameters for a given material).

While the optimisation procedures discussed in this chapter are applied to the Chaboche material model, similar strategies may be applied for the determination of material constants for other constitutive laws (such as those used to model creep)[180].

3.2 Experimental Procedure

In the present work two main loading profiles have been applied to samples made from power plant materials. In both cases, uniaxial loading is considered for an isothermal specimen. Load cycles are controlled by monitoring strain values in the specimen gauge section (see figure 3.1) with stress values at specific time instants being recorded as the output of the experiment. An overview of the experimental procedure is given here along with the specific load profiles used, however it was developed at the University of Nottingham by Saad[181] and Hyde[182]. Please note that the P91 data presented in this chapter was provided by a previous project (the work of Saad at the University of Nottingham[181]). Experiments conducted on a 316 stainless steel have been completed as part of this project.

An Instron 8862 thermo-mechanical fatigue (TMF) machine utilising radio frequency (RF) induction heating was used to complete isothermal cyclic experiments (see figure 3.2). A sample is held between two grips which will load it according to the waveform defined by the user. Strain values are measured in the gauge section of the specimen using an extensometer and stress values are calculated based on the load cell readings in the specimen grips and the specimen cross section area. RF induction heating relies on the generation of Eddy currents in metallic materials, allowing high and consistent environment temperatures to be achieved in very short periods of time. These factors make RF heating vastly superior to traditional furnace heating for the testing of solid uniaxial specimens. Temperature calibration and the design of the induction coil is performed using a calibration specimen. Thermocouples are spot welded to the gauge section and shoulder of the specimen. Coils are then designed so that the deviation from the desired temperature was not greater than $\pm 10^{\circ}$C in the gauge section. Ratios between the temperatures recorded at the specimen shoulder and the gauge section are also recorded. During an experiment, gauge section temperatures may be controlled using a thermocouple at the shoulder of specimen. Locating control thermocouples at the shoulder of a specimen avoids failure initiating at spot welds in the gauge section,

mitigating potential concerns over "forcing" a failure location in a specimen[182].

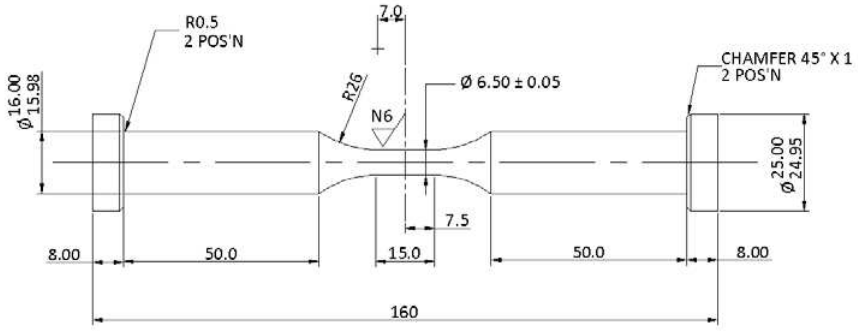

Figure 3.1: A schematic of a solid uniaxial specimen used in cyclic testing[181].

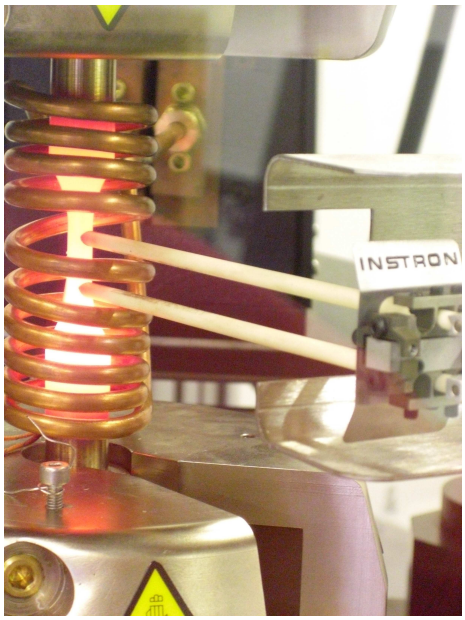

Figure 3.2: The Instron 8862 TMF machine, showing the RF induction heating coil, specimen grips and extensometer for strain measurement[182].

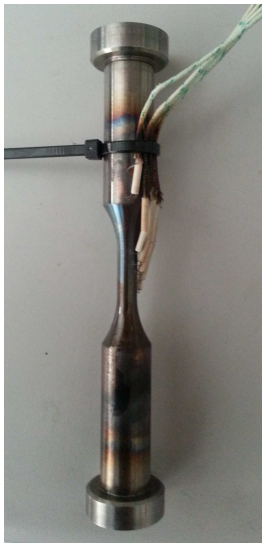

Figure 3.3: An example calibration specimen used for the design of a RF induction heating coil.

Isothermal strain loading waveforms used in the present work are divided into "saw tooth" and "relaxation" (or "dwell") types. For saw tooth loading profiles, loads are uniformly oscillated between strain limits (here set to $\pm 0.5\%$ so that plasticity effects can be observed in a loading cycle) with a fixed strain rate (see figure 3.4 (a)). This is considered to be the simplest form of loading in this testing program due to the greatly reduced dependence on creep mechanisms. Initial conditions for optimisation procedures are often derived from these results due to the dominant hardening effects observed. Additionally, relaxation testing has been completed using the same strain limits and rates as applied as in the saw tooth loading experiments. A hold period (here set to 2 minutes so that there is an appreciable relaxation in stress due to creep observed in experiments) is introduced at the end of each tensile loading region (see figure 3.4 (b)). This gives rise to a period of creep dominant behaviour, acting to relax the stresses in the specimen. This more complex behaviour can be used to demonstrate the wide applicability of the Chaboche model and to estimate the creep behaviour for a material. Typical experimental stress responses for the saw tooth and relaxation loading profiles can be seen in figure 3.4 (c) and (d), respectively.

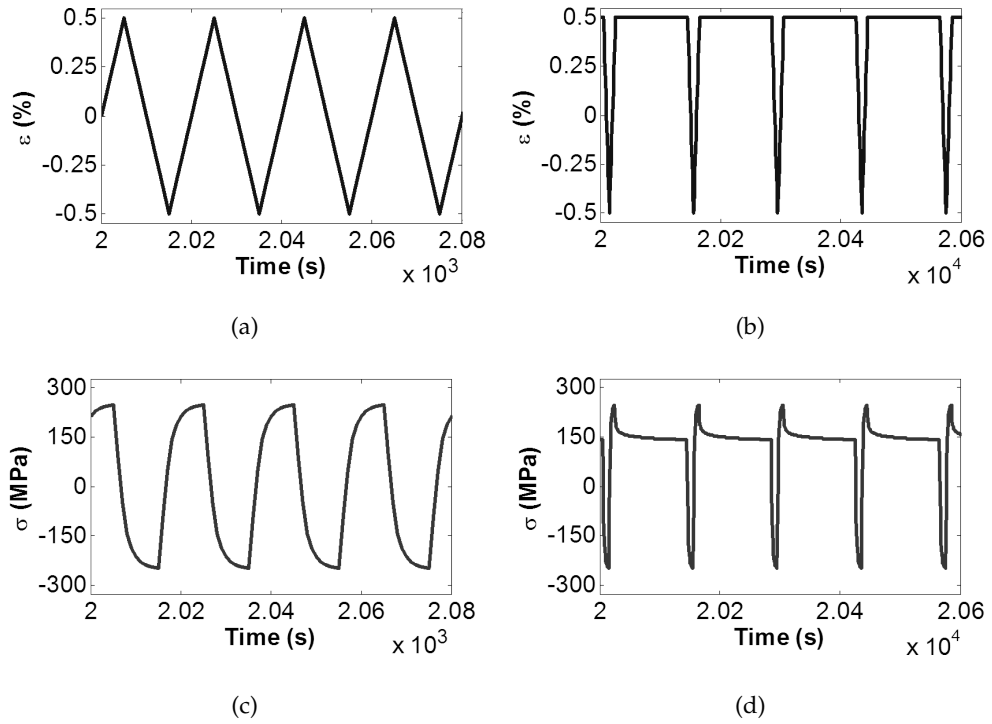

Figure 3.4: Examples of typical (a) saw tooth strain loading profile, (b) relaxation strain loading profile, (c) stress response due to saw tooth loading profile and (d) stress response due to relaxation loading profile (shown for a P91 steel at 600°C).

Strain rates in the present work are 0.1%\s for experiments performed on the P91 steel and 0.003%\s for tests using a 316 stainless steel. These have been chosen to allow cyclic tests to be completed in a reasonable amount of time while still ensuring that the results show cyclic hardening effects. Hardening is often considered (for strain controlled experiments at least) by observing the evolution of a material's stress amplitude ($\Delta\sigma/2$) with loading cycle (N) (see figure 3.5). The stress range will give a general indication of the size of a yield surface and will provide information on whether a material will harden or soften with cyclic loading. After a non-linear primary period, during which a material may either harden or soften, a linear secondary region is commonly observed. Materials will soften in the tertiary region as they approach failure. As strain rate effects are not incorporated in the present work the choice of strain rate is almost arbitrary (so long as ductile hardening behaviour is observed). Experimental data presented in this chapter is used to verify any proposed optimisation procedures and to demonstrate the wide range of material behaviours that the Chaboche model can represent. The same optimisation procedures described in this present chapter are applicable to many cyclic material experiments. Derived material constants may in turn be used in component analysis simulations[93,183].

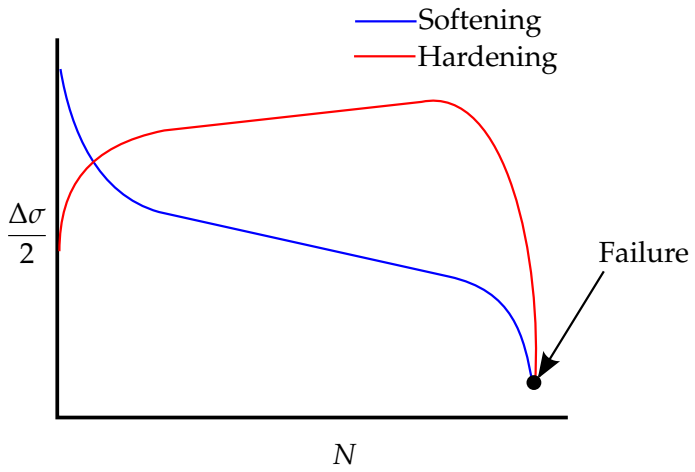

Figure 3.5: Potential material hardening behaviours in strain controlled cyclic experiments, showing materials that harden (become more difficult to deform) and soften (become easier to deform). Hardening behaviour is characterised by considering the change in a stress amplitude ($\Delta\sigma/2$, dictated by the loading strain profile) with respect to the load cycle (N).

3.3 The Uniaxial Chaboche Model

The Chaboche model in a multiaxial form was presented in section 2.3.5. The uniaxial form of the Chaboche model is applied to several optimisation methodologies in this chapter and for clarity is described here. A single yield function is defined by equation (3.1)[94,95]. Note that the quantities σ and k represent the total stress and a temperature dependent quantity related to the initial cyclic yield surface size[94,95], respectively. The constant k should not be confused with the tensile yield stress of a material. In strain controlled experimental results, k is usually taken to be the stress at which in-elastic behaviour is first observed in the first full tensile loading region of the first cycle. While initial values of k may be similar to the tensile yield stress, optimised values have been commonly found to be significantly less.

$$f = |\sigma - \chi| - R - k \leqq 0 \tag{3.1}$$

Only elastic behaviour will occur when the value of this function is less than or equal to 0. The back stress (χ) designates the centre of a yield surface and the drag stress (R) denotes the variation of its size (note this can either act to increase or decrease the size of the yield surface)[94,95]. Through the use of these quantities, kinematic and isotropic hardening may be represented, respectively. To provide a better approximation of the kinematic effects, back stress can be decomposed into several components (note in the present study, a two back stress component model was used[30,31]). An Armstrong and Frederick type kinematic hardening law is used to define the increment for each back stress component, taking the form of equation (3.2)[101].

$$d\chi_i = C_i(a_i d\varepsilon_p - \chi_i dp) \tag{3.2}$$

where a_i and C_i are both material constants (a_i defines the stationary value of the back stress and C_i dictates how quickly this value is achieved with the increase in plastic strain[101]). Additional back stress components can aid in the description of non-linear kinematic hardening behaviour. Components will be dominant in certain hardening regions and recessive in others. The use of multiple back stress components is of particular importance when describing non-linear kinematic behaviour that cannot be adequately represented by a single Armstrong-Frederick expression. Since the present work attempts to identify a preferred optimisation methodology, two back stress components have been adopted with the knowledge that the model's ability to predict experimental data may be improved by increasing the number of back stress components. The accumulated plastic strain (p), on which most of the internal variables are dependent, is a monotonic increasing quantity and is the summation of the modulus of the plastic component of total strain (ε_p), described mathematically in equation (3.3) (note that a dot denotes a rate quantity).

$$\dot{p} = \Sigma|\dot{\varepsilon}_p| \tag{3.3}$$

By decomposing the back stress into multiple components, transient and long term behaviour may be accounted for[100], here with a_1 and C_1 dictating the evolution of χ_1 (which describes initial kinematic non-linearity) and a_2 and C_2 dictating the evolution of χ_2 (describing asymptotic, stabilised behaviour), see figure 3.6. The total back stress (χ) is given as a summation of these components; therefore for N components of back stress, the total back stress (χ) is given by equation (3.4).

$$\chi = \sum_{i=1}^{N=2} \chi_i \tag{3.4}$$

The effects of isotropic hardening are represented by the scalar drag stress (R). As such, R will alter only the size of the yield surface, see equation (3.5). Note that with the drag stress equation in this form, only primary behaviour (either hardening or softening) can be represented (see figure 3.7). The drag stress will undergo some initial monotonic increase or reduction before reaching a stabilised asymptotic value[101–103] (see figure 3.7). This saturated value is signified by Q, with the rate at which the stabilised value is reached being determined by the material constant b, see equation (3.5)[102,103].

$$R = Q(1 - e^{-bp}) \tag{3.5}$$

Secondary linear effects can be represented through the addition of a linear term (equation (3.6)) in the isotropic hardening law (equation (3.5)), utilising an extra material constant (here designated H)[184], preventing the saturation of the drag stress. The signs of

the saturation constant Q and the secondary hardening rate constant H can be positive or negative, depending on whether hardening or softening behaviour is observed, respectively. Indeed, combinations of positive Q values and negative H values can be implemented for materials that primarily harden but soften in the secondary region (or vice-versa). In this way, combined isotropic hardening and softening behaviour is accounted for.

$$R = Q(1 - e^{-bp}) + Hp \tag{3.6}$$

Creep effects will be present when time or strain rate have an influence on inelastic behaviour. Time dependent creep behaviour can be introduced through the definition of a viscous stress (σ_v), forming a component of total stress, summarised by equation (3.7)[101], where the scalar components of stress act to increase or decrease the size of the yield surface around its centre (defined by the quantity χ):

$$\sigma = \chi + (R + k + \sigma_v)sgn(\sigma - \chi) \tag{3.7}$$

The viscous stress here is assumed to take the form of a power law[94,95], such as equation (3.8).

$$\sigma_v = Z\dot{p}^{1/n} \tag{3.8}$$

where Z and n are viscous material coefficients. The uniaxial plastic strain increment is given by equation (3.9). Note that, as this is the uniaxial form, σ and χ are both scalar quantities (as opposed to tensors in the multiaxial form).

$$d\varepsilon_p = \left\langle \frac{|\sigma - \chi| - R - k}{Z} \right\rangle^n sgn(\sigma - \chi)dt \tag{3.9}$$

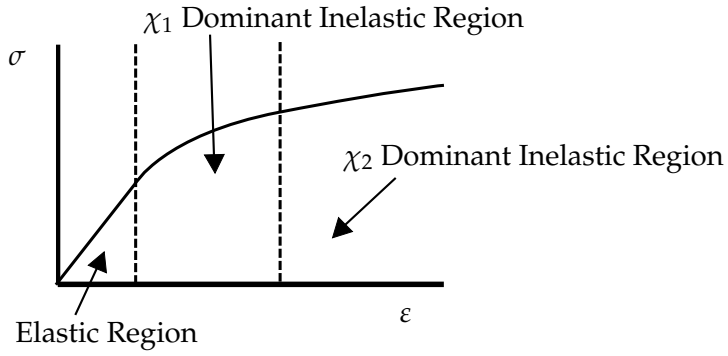

Figure 3.6: Evolution of back stress in stress strain space and illustration of dominant components.

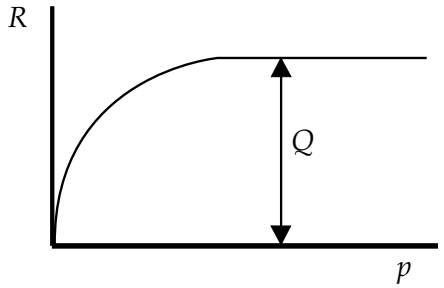

Figure 3.7: Evolution of drag stress in the original Chaboche model (shown for a material undergoing primary hardening).

3.4 Determining Initial Estimates of the Chaboche Model Material Constants

It is clear that the Chaboche model, even in its uniaxial form, contains complex interactions between several competing mechanisms (such as kinematic, isotropic and viscous effects). Determining the material constants for the Chaboche model from experimental data is therefore difficult as this interaction will be reflected in material constant values. A procedure was proposed by Tong et. al.[101–103] and will be reviewed briefly here. A more in depth examination of this procedure can be found in the work of Hyde[182]. In the present work, this method has been adapted into a bespoke MATLAB program that automates the procedure and greatly simplifies its implementation.

Cyclic tests will include an initial quarter cycle (known as the monotonic loading section) that can be used to approximate the elastic (or Young's) modulus E from the linear region (see figure 3.8). The initial size of the yield surface (k) can be estimated from the tensile part of the first full cycle, noting the stress at which the stress versus strain behaviour first becomes non-linear.

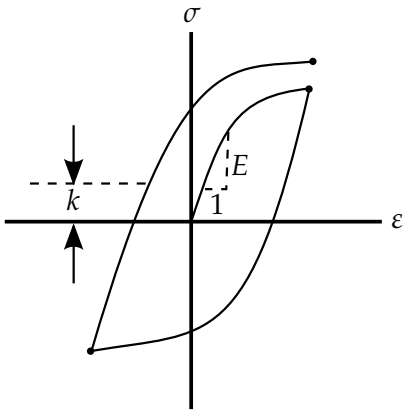

Figure 3.8: The estimation of the Chaboche material constants E and k from the monotonic loading section and first hysteresis loop of a cyclic test.

Material constants that dictate the evolution of the drag stress R, namely Q, b and H,

can be estimated by assuming that all hardening in an experiment is isotropic. The long term behaviour shown in figure 3.5 is commonly thought to be due to isotropic effects and can be divided into primary (either hardening or softening behaviour), secondary (either hardening, softening or steady-state behaviour) and tertiary (softening due to failure) regions. Equation (3.6) describes primary and secondary behaviour through the terms $Q\left(1-e^{-bp}\right)$ and Hp, respectively. The accumulated plastic strain p is found by summing plastic strain components (ε_p). For a half cycle (i.e. a tensile or compressive loading) this may be calculated by subtracting the elastic component of strain (ε_e) from the total strain (ε), see equation (3.10). ε_e is defined by the change in stress for the load cycle ($\Delta\sigma$) and the estimated value of E.

$$\varepsilon_p = \varepsilon - \varepsilon_e = \varepsilon - \frac{\Delta\sigma}{E} \tag{3.10}$$

R may be approximated by calculating the change in $\Delta\sigma$ between loading cycles. The evolution of R due to p can then be quantified, as shown in figure 3.9 for a material that cyclically softens. H may be estimated from the gradient of the secondary region and Q from the value of R at the end of the primary region. Note if the term Hp is removed from equation (3.6) (as shown in equation (3.5)), R will maintain the constant (saturated) value Q after the primary hardening region. The constant b determines how quickly the value Q is achieved. Equation (3.5) may be rearranged to give equation (3.11), allowing b to be estimated by considering a point in figure 3.9 before the end of the primary hardening region.

$$b = \left[\frac{\ln\left(1-\frac{R}{Q}\right)}{p}\right] \tag{3.11}$$

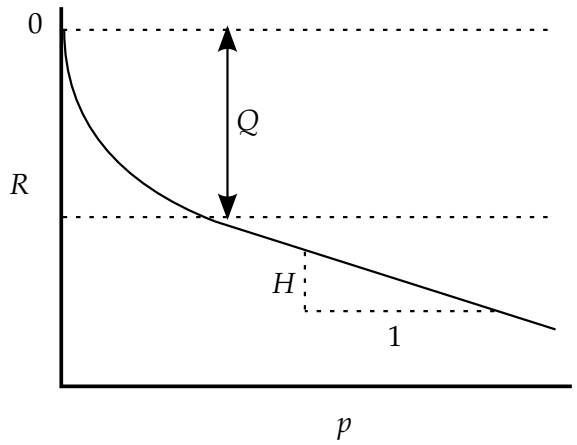

Figure 3.9: An example evolution of R due to p (note the behaviour is typical of a material that cyclically softens, such as the high chrome P91 steel).

In the present work two back stress components (χ_1 and χ_2) are applied to describe kinematic hardening. The material constants a_1, C_1 (which control the back stress χ_1), a_2 and C_2 (which control the back stress χ_2) can be estimated from the monotonic loading region by assuming all hardening is due to kinematic effects. The plastic behaviour of this first quarter cycle is assumed to comprise of χ_1 and χ_2 dominant regions, as shown in figure 3.6. It is assumed therefore that χ_2 can be neglected for initial hardening behaviour and χ_1 can be neglected in the later stages of hardening. Note in the monotonic loading region, $p = \varepsilon_p$. Equation (3.2) may be integrated with respect to time to give equation (3.12), which in turn may be substituted into equation (3.7) to give equation (3.13). In the later stages of hardening, it is assumed that $a_1\left(1 - e^{-C_1\varepsilon_p}\right) \to 0$, allowing equation (3.13) to be differentiated with respect to time and rearranged using natural logarithms to give equation (3.14).

$$\chi_i = a_i\left(1 - e^{-C_i\varepsilon_p}\right) \tag{3.12}$$

$$\sigma = a_1\left(1 - e^{-C_1\varepsilon_p}\right) + a_2\left(1 - e^{-C_2\varepsilon_p}\right) + R + k + \sigma_v \tag{3.13}$$

$$\ln\left(\frac{\delta\sigma}{\delta\varepsilon_p} - \frac{\delta R}{\delta\varepsilon_p}\right) = -C_2\varepsilon_p + \ln\left(a_2 + C_2\right) \tag{3.14}$$

Plotting $\ln\left(\dfrac{\delta\sigma}{\delta\varepsilon_p} - \dfrac{\delta R}{\delta\varepsilon_p}\right)$ versus ε_p for the experimental data yields a linear trend with a gradient approximately equal to $-C_2$. The constant a_2 can then be estimated from the Y axis intercept of this line. Note a similar approach may be used to determine a_1 and C_1 by considering only the initial plastic region. In any case, quantification of the terms $\dfrac{\delta\sigma}{\delta\varepsilon_p}$ and $\dfrac{\delta R}{\delta\varepsilon_p}$ is required. As only the monotonic region is under consideration to determine kinematic hardening material constants, $\dfrac{\delta R}{\delta\varepsilon_p}$ may be determined by differentiating equation (3.5) with respect to p, as shown in equation (3.15).

$$\frac{\delta R}{\delta\varepsilon_p} = bQe^{-b\varepsilon_p} \tag{3.15}$$

The estimation of $\dfrac{\delta\sigma}{\delta\varepsilon_p}$ is more complex. It can be shown that equation (3.16) is true (where a dot above a quantity denotes a rate term with respect to time). $\dot{\varepsilon}$ is known from the experimental set-up procedure and $\dot{\varepsilon}_p$ can be calculated using equation (3.17).

$$\frac{\delta\sigma}{\delta\varepsilon_p} = \frac{d\sigma}{d\varepsilon}\frac{1}{\dot{\varepsilon_p}}\dot{\varepsilon} \tag{3.16}$$

$$\dot{\varepsilon}_p = \dot{\varepsilon}\left(1 - \frac{1}{E}\frac{d\sigma}{d\varepsilon}\right) \tag{3.17}$$

Equations (3.16) and (3.17) are both dependent on the term $\frac{d\sigma}{d\varepsilon}$. Due to experimental scatter this can be a difficult parameter to determine. A smoothing function, such as the Ramberg-Osgood law[185,186] (defined by equation (3.18), where σ_0 and n_0 are constants), can be used, allowing equation (3.19) to be determined. This expression can be substituted into equation (3.16) and, along with equation (3.15), can be used to determine $\ln\left(\frac{\delta\sigma}{\delta\varepsilon_p} - \frac{\delta R}{\delta\varepsilon_p}\right)$ and hence the kinematic hardening material constants.

$$\frac{\varepsilon E}{\sigma_0} = \frac{\sigma}{\sigma_0} + \left(\frac{\sigma}{\sigma_0}\right)^{n_0} \tag{3.18}$$

$$\frac{d\sigma}{d\varepsilon} = \frac{\sigma_0}{\frac{\sigma_0}{E}\left(1 + n_0\left(\frac{\sigma}{\sigma_0}\right)^{n_0-1}\right)} \tag{3.19}$$

Viscous stress material parameters (Z and n) can be estimated by fitting equation (3.8) to the periods of creep dominated stress relaxation that are found in experiments that use a dwell type loading waveform. Alternatively, viscous stress materials constants may be taken from literature. Creep material models are commonly fitted to uniaxial creep test data. The power law form of equation (3.8) allows a direct comparison to other power law creep models, such as Norton's law or the Kachanov damage model. The determination of secondary material constants is discussed in section 4.2.2.

3.5 Optimisation Procedure Overview

3.5.1 Requirement

The need for optimisation procedures in determining material constant values that will result in good fits to experimental data is vital when implementing the Chaboche model. The requirement for optimisation stems from the assumptions made when estimating initial values for the material constants, namely[101]:

- Initially, all hardening is assumed to be isotropic (the kinematic state variables are assumed to be zero), allowing for the saturation value Q to be determined. The remaining isotropic hardening parameter (b) is found by considering the variation of $\Delta\sigma/2$ with the accumulated plastic strain (p) before saturation.
- When estimating kinematic hardening constants, it is assumed (for the integration of the related differential equations) that the viscous stress σ_v remains constant (i.e. it is not a function of time).
- It is assumed that the contribution of χ_1 is negligible in the latter stages of kinematic hardening. The effects of χ_2 may therefore be isolated and applied only to the later stages of hardening.

- Commonly, initial estimates of the visco-plastic material constants (Z and n) are approximated by trial and error or taken from literature to provide a reasonable fit to the stress relaxation regions.

3.5.2 General Overview and Weighting Functions

In the present work, optimisation iterations are evaluated against each other through the least squares method. In total, three general objective function forms have been developed to define the fitting quality of a predicted stress versus time profile to experimental data in the case of strain controlled isothermal cyclic testing. By using multiple objective functions, preference can be given to areas of great interest in the stress-time profile (such as peak stress values) while overall fitting is still accounted for elsewhere. Although fewer objective functions may be used, the presented combination emphasises critical areas in the stress profile and thus allows material constants which were heavily affected by the assumptions in section 3.5.1 to be determined (for example, the viscous stress material constants Z and n). General stress fitting is accounted for in the first objective function (equation (3.20)).

$$F_1(x) = \sum_{i=1}^{M_1} \left(\sigma(x)_i^{pre} - \sigma_i^{exp}\right)^2 \tag{3.20}$$

where each experimental stress value (σ_i^{exp}) is compared with the corresponding predicted stress value ($\sigma(x)_i^{pre}$). The quantity M_1 is the total number of experimental points considered in the optimisation. It is of particular importance that the optimisation takes account of the hardening/softening behaviour of the material, as this represents the evolution of the yield surface with cyclic loading. An objective function is therefore created based on the comparison of experimental and predicted stress range values. These can be found by taking the difference between the peak stresses (found at the end of a tensile loading region) and the minimum stresses (realised at the end of a compressive loading region) and dividing by two for each cycle in turn, for both predicted ($\frac{\Delta\sigma(x)_i^{pre}}{2}$) and experimental ($\frac{\Delta\sigma_i^{exp}}{2}$) results (see equation (3.21)). M_2 therefore defines the total number of loading cycles considered in the optimisation.

$$F_2(x) = \sum_{i=1}^{M_2} \left(\frac{\Delta\sigma(x)_i^{pre}}{2} - \frac{\Delta\sigma_i^{exp}}{2}\right)^2 \tag{3.21}$$

Finally, the stress relaxation (or strain hold) loading region is of interest as it represents a period of creep dominant behaviour in the model. Fitting in this region aids in the determination of the viscous stress material constants (Z and n). Stress values predicted in this section ($\sigma(x)_{RELAX\ i}^{pre}$) are compared to experimental values ($\sigma_{RELAX\ i}^{exp}$) in an additional objective function (equation (3.22)). M_3 defines the number of relaxation data points considered in the optimisation.

$$F_3(x) = \sum_{i=1}^{M_3} \left(\sigma(x)^{pre}_{RELAX\ i} - \sigma^{exp}_{RELAX\ i}\right)^2 \tag{3.22}$$

For the j^{th} objective function, a weighting value (w_j) is applied, ensuring that contributions from different data sources are kept comparable (equation (3.23)).

$$w_j = \frac{\sum_1^N M_j}{M_j \max\left|A_{ij}^{exp}\right|} \tag{3.23}$$

where M_j indicates the number of data points for the j^{th} objective function, N is the total number of objective functions and $\max\left|A_{ij}^{exp}\right|$ is the maximum experimental value from the data source associated with that objective function.

Note that the relaxation objective function (equation (3.22)) is of course omitted in optimisation procedures performed on saw tooth strain profile experimental data. Optimisation programs that consider saw tooth experimental data are therefore deemed two objective function procedures. Programs that take into account relaxation data are deemed three objective function procedures. The above objective functions are implemented in an optimisation procedure using MATLAB. The Chaboche differential equations are evaluated using ODE45[187] (using a Dormand-Prince $4/5^{th}$ order Runge-Kutta pair), with a gradient method based least squares optimisation (the Levenburg-Marquardt algorithm, seesection 2.6.4) completed using the MATLAB function LSQNONLIN[188].

3.6 Experimental Data Cleaning

3.6.1 Requirement

Experimental data will, unavoidably, include scatter. In the domain of cyclic hardening, this may be due to fluctuations in temperature during the test or due to fluctuations in strain rate. Also, inertial effects will cause the test machine to potentially slightly overshoot the maximum or minimum limit strains. Due to the large amounts of data generated, it is of critical importance that as much of the handling process is as automated as possible.

Different logic conditions may be employed, in turn, to determine the end of each of the loading branches (i.e. tensile, compressive or relaxation load periods). Scatter can however result in incorrect points being selected as the branch ends. Consider the case where an experimental point midway in the relaxation region is erroneously selected as the beginning of the compressive branch due to data scatter. From the program's perspective, a subsequent point would be expected to have a lower strain value due to the reverse loading in the compressive branch, however this may well not be the case as a result of the incorrect branch definition (the points being compared are actually both in the relaxation branch, rather than at the beginning of the compressive branch). If a

positive strain increment is calculated where a negative one is expected, the related time increment (found through use of the test strain rate) would be negative, hence causing the differential equation solver to fail.

It is proposed here that, as stress is the quantity used for the assessment of fitting quality for a given set of material parameters, cleaning the strain profile to remove scatter will not significantly alter the overall output, however it could make the automated nature of the analysis and optimisation process more robust. The cleaning process takes the form of re-defining the experimental strain profile in the strain hold branch (see figure 3.10).

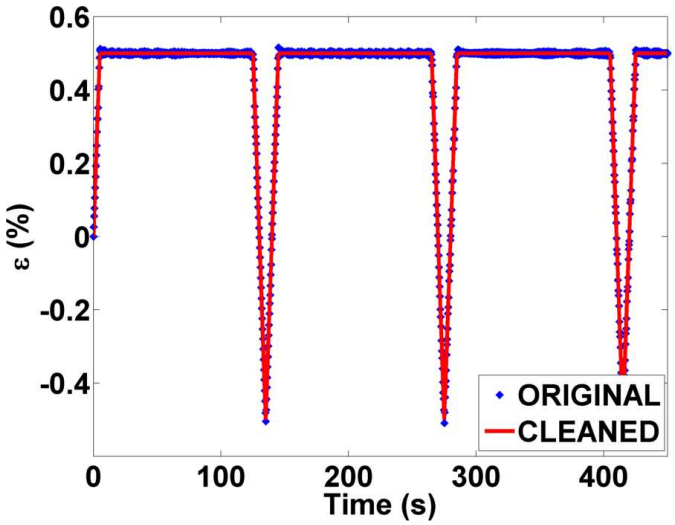

Figure 3.10: Example of the effect of cleaning on the strain profile (note the maximum strain is held over hold period in cleaned data).

3.6.2 Effects Compared to Unclean Data

Given the manipulation of the experimental data, it is of paramount importance that no corruption should take place that would otherwise cause unsatisfactory fitting after optimisation. An investigation was therefore conducted on the comparative performance between the use of cleaned and as-received experimental data using the Chaboche model. Using isothermal (600°C) experimental data for a P91 steel, with a strain limit range of $\pm 0.5\%$, a strain rate of 0.1%/s and a hold time of 2 minutes, optimisation by the two different methods was performed. In the optimisation methods, both cleaned and as-received data values were used to represent the first 49 loading cycles. Additionally, to illustrate the benefit of the robustness the cleaning procedure can offer, an optimisation procedure was conducted on a greater number of cycles (122) of the cleaned data. Due to the scatter, this number of cycles could not be considered in the original optimisation procedure for as-received data. Note that in all cases, the same initial conditions were used (see table 3.1).

The prediction of the change in stress range during cyclic softening (or hardening)

is of importance for industrial applications due to its relation to the change in yield stress of the material (with progressive cycling). The prediction of the changes in stress range for 49 cycles is presented in figure 3.11 (a), for all three optimisation scenarios. All three optimisation methods give reasonably good approximations (coefficients of determination are above 0.9) of the variations in stress range, whether scatter in the experimental data is considered or not.

In addition to the stress range prediction, specific stress magnitude predictions within cycles are also required. To illustrate this, the fitting of the penultimate cycle is provided in figure 3.11 (b). It can be seen that, generally, all of the methods give excellent estimation of the stresses generated during tensile, stress relaxation and compressive loading branches. The operation of cleaning the data prior to optimisation has not impaired the quality of the overall fit to experimental data. Cleaning will mean automated analysis can be made more robust and will avoid unexpected errors due to incorrect branch definition. For subsequent sections of this chapter, the data used will have undergone cleaning first to remove scatter in the strain hold period. The material constants that were obtained by utilising the different optimisation procedures are given in table 3.1 and in general show only small variations. On average, the percentage difference from the mean for each constant was approximately 8% (a maximum of 30% was obtained for the values of a_1 in the as-received case).

Although each of the material constant sets presented in table 3.1 describe the 49 cycles of P91 (600°C) data, it is the conclusion of this investigation that using cleaned experimental data for an optimisation procedure can aid in avoiding numerical difficulties and premature termination of the optimisation program. If a greater number of loading cycles can be considered more of the hardening behaviour of a material can be included and thus represented in the final set of material constants.

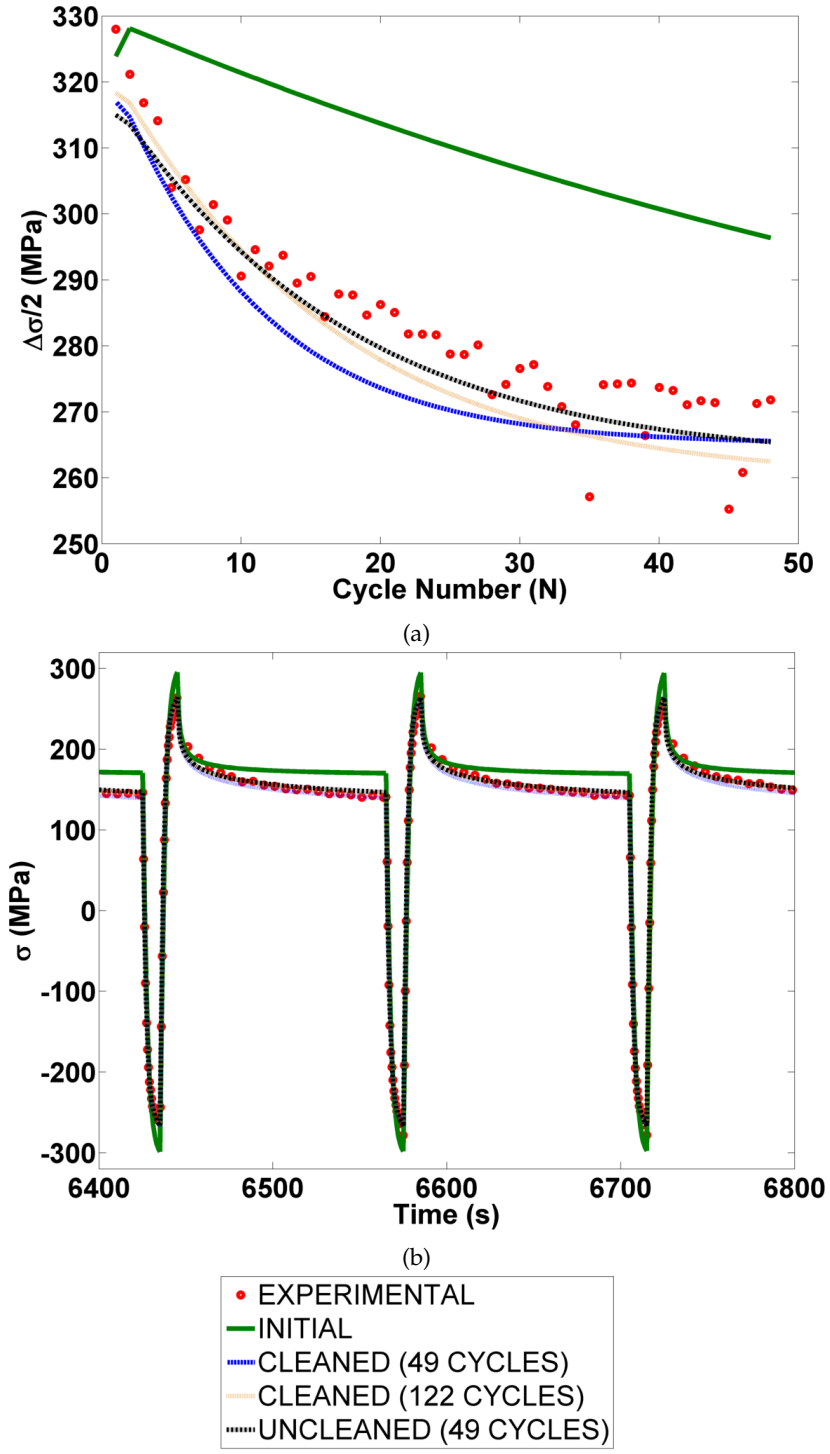

Figure 3.11: A comparison of optimised material constants for P91 data at 600°C. Optimisation procedures are performed for both "cleaned" and as-received data. Results presented show (a) the stress range variation (indicating primary softening behaviour) and (b) the stress values for the 49^{th} cycle.

Table 3.1: Optimised material constant values for the Chaboche model for P91 data at 600°C using alternative data preparation methods.

	Initial	As-Received (49 Cycles)	Cleaned (49 Cycles)	Cleaned (122 Cycles)
a_1 (MPa)	52.20	73.30	54.60	40.00
C_1	2060.00	1170.00	1080.00	1280.00
a_2 (MPa)	67.30	49.50	39.90	44.30
C_2	463.00	136.00	219.00	242.00
Z $(MPa.s^{1/n})$	1750.00	463.00	501.00	477.00
n	2.70	9.58	9.70	11.20
b	1.00	4.23	7.03	4.87
Q (MPa)	-75.40	-57.90	-59.40	-65.80
k (MPa)	85.0	0.51	0.48	0.49
E (MPa)	$1.39x10^5$	$1.60x10^5$	$1.44x10^5$	$1.33x10^5$

3.7 Investigation into the Performance of the Optimisation Program

3.7.1 Effects of Number of Data Points Chosen per Cycle

Due to the large number of data points generated during experiments, only a selected number are considered during an optimisation procedure. By using a greater number of selected experimental data points per cycle, it is expected that the fitting quality of the cyclic stress and relaxation stress values could be marginally improved (given that selected data is distributed evenly between the beginning and the end of the loading branches). Note that in practice this improvement was not noticeable as in all cases coefficients of determination were above 0.95. Increasing the number of points selected will increase the number of times that differential equations are evaluated, thus

increasing the required computational effort. Therefore, if optimisation procedures are to be used in practice, an assessment of the minimum number of points that are required for a reasonable fit to the data must be made.

An investigation using 49 cycles on P91 steel at 600°C was conducted. The same set of initial conditions were used in all cases. The number of points selected per cycle were varied between each of the optimisation program runs. The number of points selected in a specific branch type were made equal to the points selected in the other branch types. Therefore, for example, in the case where 60 points were selected per cycle, 20 points were used in the tensile branch, 20 in the stress relaxation branch and 20 in the compressive branch. This equality was enforced to ensure the same level of detail was reflected in the different parts of the stress versus time profile. In all cases, the optimisation procedure terminated when the objective function tolerance was satisfied, suggesting that the sum of residuals (r^2, a useful metric for general fitting quality) is comparable in each of the individual cases. This criterion suggests that a local minimum in optimisation space is possible.

The effect on processing time can be seen in figure 3.12 and a summary of the effects that the different number of points selected has on optimised constant values is presented in tables 3.2 and 3.3 (along with computation times). It is interesting to note that in figure 3.12, while in general an increase in the number of points selected per cycle gives rise to an increase in processing time (as expected), reducing the number of points below approximately 24 points per cycle also has the effect of increasing processing time. As the objective function is formulated by comparing the experimental and theoretical values at these points, a reduction in the number of points considered translates to less available information for the fitting quality to be evaluated (reduced constraint). It is suspected therefore that, should the objective function tolerance criterion be taken as the preferred termination criterion, a greater number of optimisation iterations may be required in order to give a suitable reduction in the residual value, hence causing an increase in the computing time.

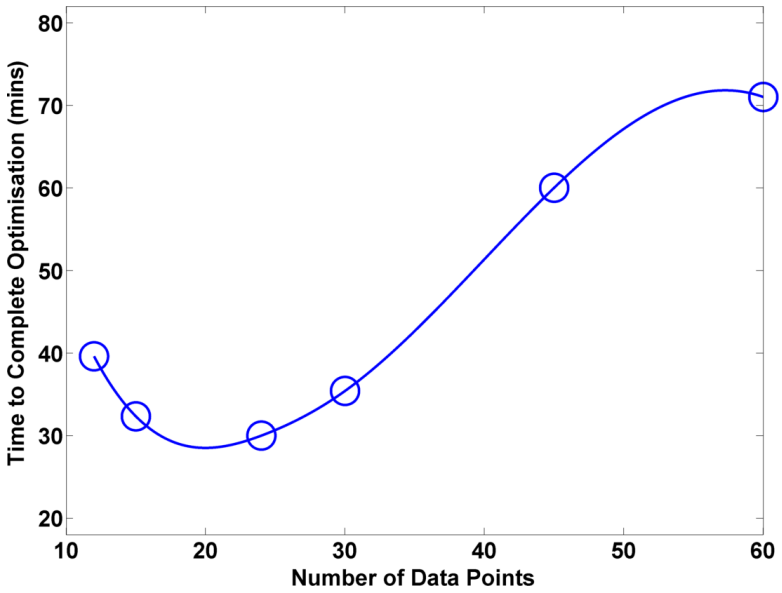

Figure 3.12: Processing time (minutes) versus number of points selected per branch (based on an investigation using 49 cycles of data for experiments on a P91 steel at 600°C). Note that these results are based on program runs completed using an i7 processor and are included for comparison only.

Table 3.2: Summary of the optimised constants for different numbers of selected points (60, 45 and 30) per cycle for P91 data at 600°C.

	Initial	60 Points	45 Points	30 Points
a_1 (MPa)	52.20	18.78	56.39	19.76
C_1	2055.00	2792.82	1057.80	8396.84
a_2 (MPa)	67.30	59.32	29.50	66.21
C_2	463.00	645.30	250.72	672.44
Z $(MPa.s^{1/n})$	1750.00	498.61	501.02	499.96
n	2.70	10.09	9.44	9.24
b	1.00	15.74	6.34	19.96
Q (MPa)	-75.40	-63.23	-57.76	-60.44
k (MPa)	85.00	0.50	0.50	5.51
E (MPa)	$1.39x10^5$	$1.38x10^5$	$1.42x10^5$	$1.40x10^5$
Time to Complete Optimisation $(mins)$		71.01	60.02	35.42

Table 3.3: Summary of the optimised constants for different numbers of selected points (24, 15 and 12) per cycle for P91 data at 600°C.

	Initial	24 Points	15 Points	12 Points
a_1 (MPa)	52.20	31.92	48.20	10.00
C_1	2055.00	5385.78	615.09	13433.08
a_2 (MPa)	67.30	66.34	20.79	50.40
C_2	463.00	592.47	626.21	678.55
Z $(MPa.s^{1/n})$	1750.00	500.51	499.95	499.93
n	2.70	8.36	8.92	9.15
b	1.00	6.85	3.44	4.24
Q (MPa)	-75.40	-51.66	-35.77	-35.19
k (MPa)	85.00	0.50	1.74	1.08
E (MPa)	$1.39x10^5$	$1.47x10^5$	$1.44x10^5$	$1.30x10^5$
Time to Complete Optimisation $(mins)$		30.01	32.34	39.61

3.7.2 Variation of Initial Conditions

The initial conditions used in the optimisation analyses can have a significant effect on the convergence to the objective function minima. In high dimension cases (such as the Chaboche model) it is difficult to visualise the full extent of the interplay between the material constants (hence sensible initial estimates, based on experimental data, are required). As such, an investigation into the effect of slight variations in initial estimates of material constants would be time consuming to explore fully. For an exhaustive analysis to be performed the variation of every material constant from some base value would have to be accounted for, along with every permutation of these variations. Conducting this analysis would, assuming 3 levels per constant, require 59049 optimisation procedures to be performed. Such an endeavour is considered outside the scope of the present work, and therefore a more simplistic analysis of the effect of material constants variations is presented. A percentage variation (20%) was applied equally to all material constants, acting to either increase or decrease the

initial value from a base set of initial conditions (initial condition set 1, see table 3.4). Separate investigations were made as to the effect of increasing (initial condition set 2, see table 3.4) or decreasing (initial condition set 3, see table 3.4) the material constants by such a variation.

Data for 30 cycles for P91 steel at 600°C was used with the same initial "base" conditions as in section 3.7.1. A summary of the results of this study is presented in table 3.4. An excellent level of agreement was found between constants optimised from the different initial conditions, with an average percentage difference between the base condition case (case 1) and the varied initial condition cases (case 2 for increased initial conditions and case 3 for reduced initial conditions) of approximately 1.2% in both scenarios. A peak percentage different of 13.5% was observed in the initial yield stress (k) value for case 2. Table 3.5 summarises the percentage differences between optimised material constant sets.

Table 3.4: Summary of optimised material constants based on different initial conditions (using 30 cycles of data, 30 points per cycle for P91 data at 600°C).

	Initial 1	Optimised 1	Initial 2	Optimised 2	Initial 3	Optimised 3
a_1 (MPa)	52.20	16.36	62.64	15.70	41.76	16.09
C_1	2055.00	6613.08	2466.00	6539.96	1644.00	6509.37
a_2 (MPa)	67.30	65.90	80.76	65.95	53.84	66.01
C_2	463.00	732.56	555.60	733.73	370.40	735.70
Z $(MPa.s^{1/n})$	1750.00	501.02	2100.00	499.88	1400.00	499.99
n	2.70	9.39	3.24	9.37	2.16	9.38
b	1.00	31.85	1.20	32.47	0.80	33.69
Q (MPa)	-75.40	-61.24	-90.48	-61.40	-60.32	-61.71
k (MPa)	85.00	10.30	102.00	11.69	68.00	11.38
E (MPa)	$1.39x10^5$	$1.39x10^5$	$1.67x10^5$	$1.39x10^5$	$1.12x10^5$	$1.39x10^5$

Table 3.5: Percentage difference between "base" optimised constants (case 1) and varied optimised constants (cases 2 and 3) (using 30 cycles of data, 30 points per cycle for P91 data at 600°C).

	Percentage difference between Optimised 2 and Optimised 1	Percentage difference between Optimised 3 and Optimised 1
a_1 (MPa)	4.03	1.65
C_1	1.11	1.57
a_2 (MPa)	-0.08	-0.17
C_2	-0.16	-0.43
Z $(MPa.s^{1/n})$	0.024	0.002
n	0.21	0.11
b	-1.95	-5.78
Q (MPa)	-0.26	-0.77
k (MPa)	-13.50	-10.49
E (MPa)	0.00	0.00

3.7.3 Summary of the Investigation into the Performance of the Optimisation Program

The addition of a data cleaning procedure prior to optimisation greatly aids the procedure and makes automated data handling more robust and reliable (as the formation of the objective function relies on accurate dissection of the stress versus time profile). Stress relaxation, which occurs during strain hold periods, can be predicted with far greater accuracy when material constants are optimised using cleaned data (compared to material constants optimised using as-received data with experimental scatter). The effect of cleaning on fitting has been assessed against as-received data to verify that cleaning the experimental data has no detrimental effect on the fitting quality.

A reduction in the number of points selected per cycle has been shown to give

a reduction in the length of time required for optimisation up to approximately 24 data points per cycle. The increase in data points necessitates a greater number of times at which the differential equations need to be evaluated, thus requiring a more lengthy computing time. Reducing the number of data points selected per cycle below 24 also gives rise to an increase in computing time. It is reasoned that this is due to the difficulties with the reduced constraint when evaluating the objective function (there is a reduced amount of information with which to calculate the objective function values). A greater number of iterations is required to make a significant change in the objective function value, such that a user defined tolerance is exceeded and the optimisation procedure terminates. The optimised constants shown tables 3.2 and 3.3 exhibit a range of values, seemingly dependent on the number of data points selected per cycle. Scatter in the experimental stress data could, when the selection procedure is applied, lead to multiple (slightly different) optimum experimental stress versus time profiles, depending on the specific points selected and rejected. Therefore constants governing the hardening or softening behaviour (such as a_1, C_1, a_2 and C_2) could show wide variance as a result of slightly different experimental hardening curves (the tensile and compressive branches) being used for the optimisation, depending on the experimental data points chosen. By comparison, viscous stress constants (Z and n) show remarkable agreement considering the variations which occur in the other values, possibly indicating that stress scatter in the stress relaxation branches (where creep is the dominant mechanism) is far less than that in the hardening data. The selection procedure implemented will always select stress values at the beginning and end of the branches (for use in stress range fitting). At a glance therefore it would be expected that isotropic hardening parameters (b and Q) would be consistent, regardless of the number of points selected. In the long term hardening effects will be dominated by isotropic behaviour, however initially kinematic effects also may play a key role[34]. Isotropic material constant values will therefore be affected by the optimised values of the kinematic material constants, suggesting the potential for variation in both.

Small uniform aberrations in initial material constant estimates were investigated, as shown in table 3.4. The optimisation procedure developed (i.e., using cleaned experimental data) converged on similar optimised material constant values, regardless of the initial conditions used. Peak differences of 13.5% were observed for the material constant k, however an average variation of 1% was found for the other Chaboche material constants (see table 3.5). In cases where a large number of loading cycles are considered, experience has shown that there is a limited dependence on the initial size of the yield surface (signified by k) due to hardening effects (either isotropic or kinematic) inducing larger changes in the yield surface.

3.8 Multiple Data Source Optimisation Strategies

3.8.1 Requirement

Preliminary studies and previous experience has highlighted that, for experiments performed using the same material being loaded under comparable strain ranges and rates (i.e. in situations where a single set of material constants should be sufficient to describe all test results), different sets of optimised material constants can be derived from each of the experimental data sets (i.e. experiments performed using saw tooth or relaxation loading profiles, see section 3.2). For the implementation of material models like the Chaboche model in component analysis, it is vital that a single set of material constants (i.e. one that is not dependent on experimental loading conditions that are accounted for in the model) that is representative of the material behaviour is derived. A general optimisation procedure has been developed to fine tune material constants in the previous section[30,31], however it is the intention here to further explore the application of optimisation for the case where two different sets of test data that should be described by the same set of material constants are available. Cao and Lin suggested that the ideal optimisation procedure, when applied to multiple data curves, should give equal opportunity for all experimental curves to be optimised against[165]. With this in mind, the proposed optimisation strategies presented here involve some form of information exchange between sub-optimisation procedures (performed on both saw tooth and relaxation type experimental data). In this way, material constants are optimised based on all available experimental data.

The inclusion of multiple sets of experimental data offers several possibilities regarding the determination of initial conditions. Hardening material constants can be determined accurately using either saw tooth or relaxation experimental data. Due to the reduced complexity in saw tooth tests (arising due to hardening mechanisms, as opposed to creep, being dominant throughout the test), these tests are more readily applicable to the initial material constant determination procedure[31,102,103]. Similarly, creep constants may be estimated from the stress relaxation periods in the relaxation tests, where creep is considered to be dominant in the strain hold region (at least, when the testing temperature is sufficiently high enough to initiate creep). The rate at which a material softens in the linear secondary region has been found to be consistent for both experimental test types; therefore H (see equation (3.6)) can be reasonably estimated from either set.

3.8.2 Methodologies

Separated Parallel Optimisation (SP)

Given that hardening material constants could be accurately derived from either data set but creep constants may only be realistically determined from relaxation data, a

method that would require only a single experimental set to be optimised against would be of great interest. Potentially, only the tests with stress relaxation periods would need to be performed, thus streamlining test programs and reducing the time expended for optimisation. To highlight this effect, separated optimisation methodologies that use different initial conditions have been performed simultaneously (see figure 3.13) for different sets of experimental data. These separated procedures entail performing a 2 objective function optimisation process on saw tooth experimental data and a 3 objective function process on the relaxation experimental data. There is no exchange of information between the two optimisation procedures. A summary of the type of experimental data used for the formulation of the objective functions for each experimental data type is presented in figure 3.14.

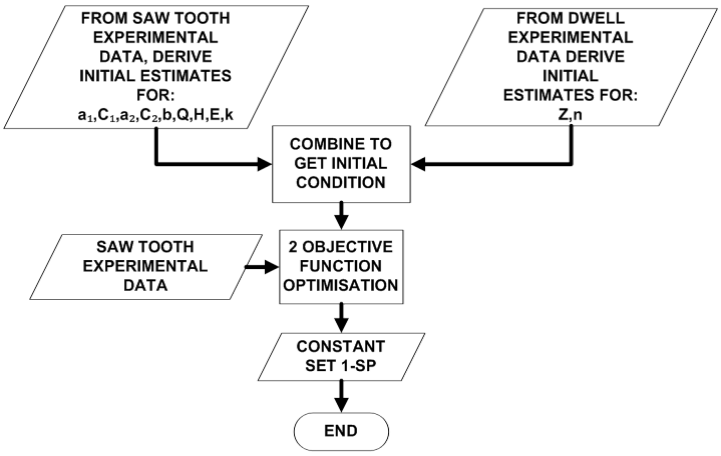

Figure 3.13: Flowchart of the separate parallel optimisation procedure, compromising of (a) a two objective function optimisation procedure using saw tooth experimental data and (b) a three objective function optimisation procedure using relaxation experimental data.

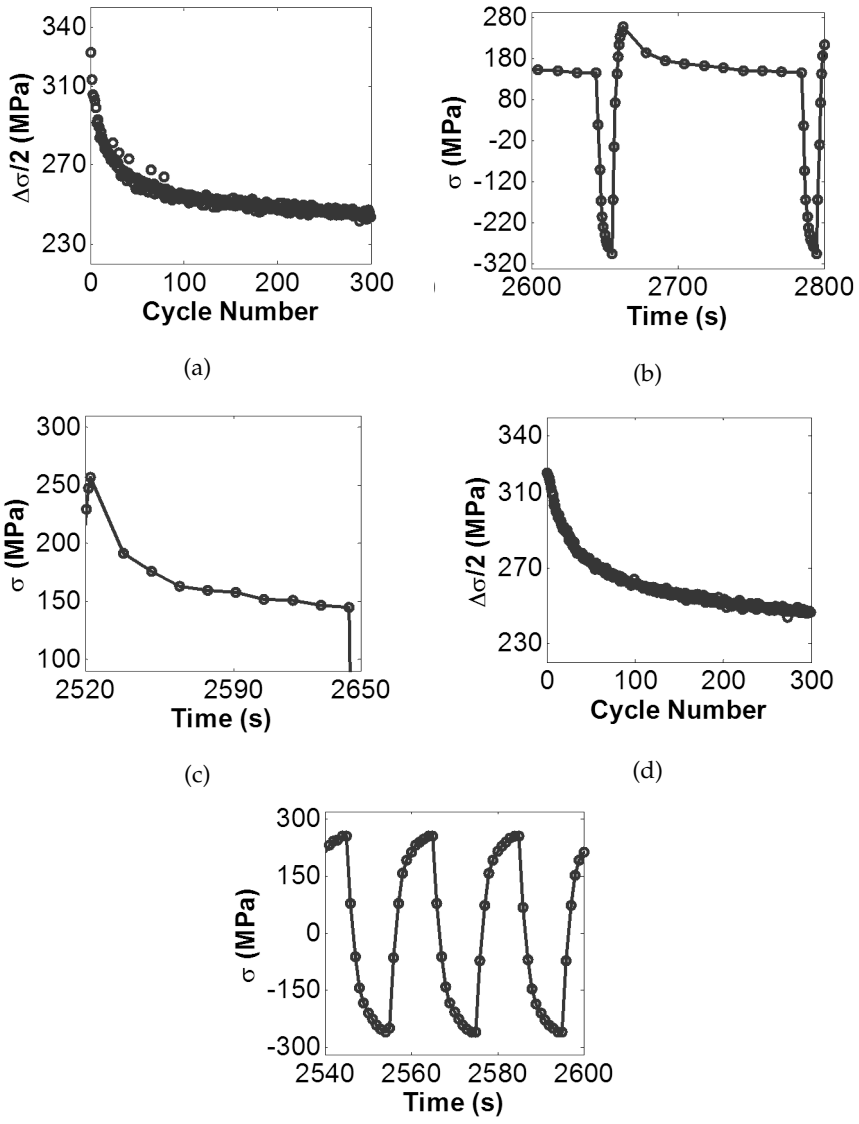

Figure 3.14: Examples of the experimental data used to formulate the objective functions for (a) stress range fitting in relaxation experimental data, (b) general stress fitting in relaxation experimental data, (c) stress relaxation region fitting in relaxation data, (d) stress range fitting in saw tooth experimental data and (e) general stress fitting in saw tooth experimental data.

Series Optimisation (S)

In the series optimisation methodology (figure 3.15), initial material constant estimates are determined from the relevant sections in each experimental data set, as described previously (i.e. hardening material constants from saw tooth experimental data and creep constants from relaxation data). An optimisation procedure is performed using the saw tooth experimental data with a view to fine tuning hardening constants. A subsequent optimisation procedure using the first optimised material constant set as

an initial condition (constant set 1-S is equal to the initial conditions for the 3 objective function optimisation process in figure 3.15) and the relaxation experimental data is completed with a view to determining creep constant values. It is suspected that the change in the hardening constants will be minimal between the constant set 1-S and constant set 2-S (see figure 3.15). Both optimised material constant sets have been evaluated and compared to both experiment data types to explore fitting quality. Note constant set 1-S is equal to constant set 1-SP in figure 3.13; however constant set 2-S is not necessarily equal to constant set 2-SP due to the different initial conditions used for the same (3 objective function) optimisation procedure.

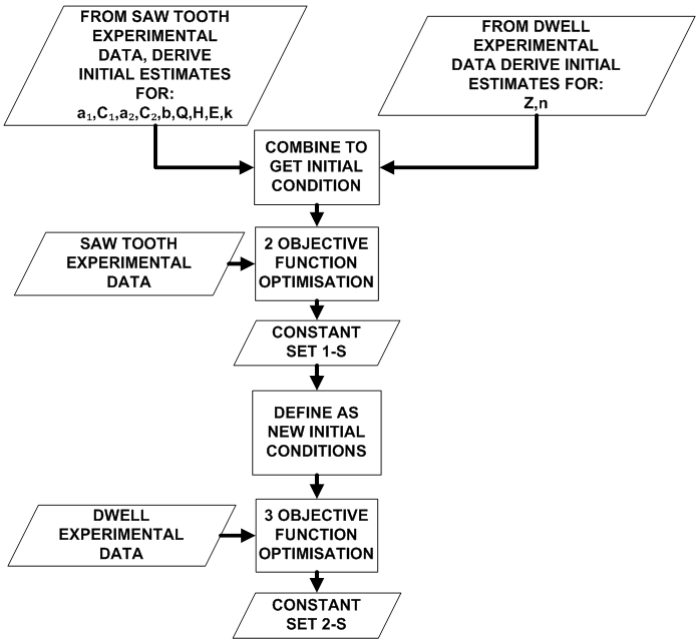

Figure 3.15: Flowchart of the series optimisation procedure.

Combined Parallel Optimisation (CP)

As an alternative to the above two methods (where each experimental data source is considered independently), it is conceivable that a single optimisation procedure could be performed that accounts for both experiment data groups, thus conducting combined parallel optimisation (see figure 3.16). Given some initial conditions (that may be derived in the most efficient way depending on the available data) a total of five objective functions could be derived that effectively combine the two and three objective function optimisation procedures in figures 3.13 and 3.15. Potentially, a single set of material parameters could be derived that would accurately represent both saw tooth and relaxation experimental data. Initial conditions could be derived from either saw tooth or relaxation type experimental data for this optimisation strategy. In the present work, both initial conditions are considered in the results section in order to determine the preferred option.

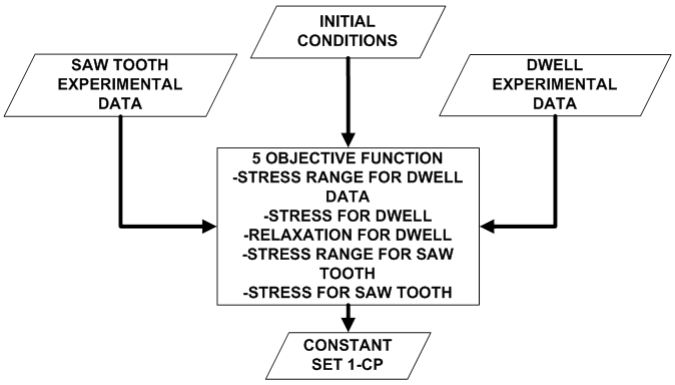

Figure 3.16: Flowchart of the combined parallel optimisation procedure (see figure 3.14 for objective function descriptions).

3.8.3 Results

In order to compare the optimisation strategies proposed each was used to optimise a material constants for test performed on a P91 steel at 600°C. Both saw tooth and relaxation type loading profiles were applied. Strain limits were set to $\pm 0.5\%$, with a 2 minute hold period at the end of each of the tensile loading regions (where applicable) and a constant strain rate of $0.1\%/s$. Two sets of initial conditions were derived for the optimisation procedures. Saw tooth and relaxation experimental data were used to find hardening and creep material constants, respectively (deemed "Saw Tooth" initial conditions, see table 3.6). Alternatively, a full set of initial conditions were determined solely from relaxation tests ("Relaxation" initial conditions, see table 3.6). In all optimisation routines the first 300 loading cycles from the experimental data sets were taken into account. 10 experimental data points were selected for each loading region (tensile, compressive or strain hold), giving 20 and 30 data points per loading cycle for saw tooth and relaxation type data, respectively. This value was chosen to minimise the amount of time required to complete the optimisation procedure, as identified in section 3.7.1.

Optimisation Results

In the separated parallel optimisation procedure, optimisation programs based on the formulation of 2 or 3 objective functions are performed on the relevant experimental data sets. The 2 objective function optimisation is equivalent to the first step in the series optimisation methodology shown in section 4.2.1, therefore the results (constant set 1-S) are identical and are shown in table 3.7 as constant set 1-SP. Results of the 3 objective function optimisation (constant set 2-SP) are also presented in table 3.7.

Using series optimisation, hardening material constants are fine-tuned from the initial conditions derived from both saw tooth and relaxation experimental data using a 2 objective function optimisation procedure (considering the fitting to saw tooth data

only). This gives rise to constant set 1-S (equivalent to 1-SP in table 3.7), which is used as an initial condition in the 3 objective function optimisation that fine tunes creep material constants, incorporating relaxation experimental data (constant set 2-S, see table 3.7 for results). Hardening material constants should be common for both data sets as creep is a dominant mechanism only in the stress relaxation loading regions, therefore it is to be expected that constant set 2-S should represent both sets of experimental data well.

In combined parallel optimisation, a single procedure is undertaken that evaluates 5 objective functions, calling both sets of experimental data for comparison. Initial conditions could be determined using both saw tooth and relaxation data or just relaxation data (see table 3.7).

Table 3.6: Summary of initial estimates for the Chaboche model for P91 at 600°C, derived using either relaxation or saw tooth data.

	Saw tooth initial constants	Relaxation initial constants
a_1 (MPa)	85.18	92.91
C_1	1360.66	1164.23
a_2 (MPa)	95.81	104.03
C_2	551.75	433.47
Z $(MPa.s^{1/n})$	752.99	752.99
n	6.87	6.87
b	1.86	3.67
Q (MPa)	-70.64	-74.56
k (MPa)	9.39	33.33
E (MPa)	$1.40x10^5$	$1.48x10^5$
H (MPa)	-2.99	-3.16

Table 3.7: Summary of the optimised values for the Chaboche model material constants for P91 at 600°C using different optimisation strategies.

	Constant set 1-SP (equal to Constant set 1-S)	Constant set 2-SP	Constant set 2-S	Constant set 1-CP from Saw tooth initial conditions	Constant set 1-CP from Relaxation initial conditions
a_1 (MPa)	2.81	66.90	18.06	80.96	86.75
C_1	2132.51	2516.18	538.24	1572.18	1422.08
a_2 (MPa)	62.19	88.93	50.79	90.69	59.85
C_2	644.01	506.55	586.93	519.50	671.78
Z $(MPa.s^{1/n})$	1259.01	683.03	1004.19	697.45	674.11
n	4.11	5.01	3.16	5.44	5.00
b	5.41	1.18	34.65	4.64	2.92
Q (MPa)	-38.49	-84.06	-71.85	-77.78	-84.14
k (MPa)	0.51	30.90	143.90	146.04	30.66
E (MPa)	$1.40x10^5$	$1.53x10^5$	$1.41x10^5$	$1.46x10^5$	$1.54x10^5$
H (MPa)	-3.74	-2.83	-1.98	-3.06	-2.82

3.8.4 Comparative Plots

Saw Tooth Waveform Prediction

In order to assess the predictive capability of the Chaboche model using optimised material constant sets, "plotting" programs were implemented. Strain limits and rates

from experimental data sets were used to define a loading profile with uniform time and strain increments. The Chaboche model is used to calculate the evolution of the state variables using this uniform profile; hence noise and scatter that are apparent in the experimental data are not reproduced, making study of the resultant curves easier. Comparison between this predictive curve and the original experimental data is still valid as both are dependent on loading profiles generated using the same characteristic parameters (such as strain limits values or strain rate). Through comparison of predicted and experimental data, the coefficient of determination (r^2) may be calculated for each optimised material constant set (see table 3.8). These values provide a metric by which to judge the fitting quality of a predictive model (compared to the experimental data)[162]. Coefficients of determination are calculated from equation (3.24) for N data points, where EXP_i and $PRED_i$ are the i^{th} experimental and predicted values, respectively, and σ_{EXP} is the standard deviation of the experimental data. A perfect fitting (i.e. with no error between experimental and fitted data points) would result in an r^2 value of 1. Note that, in the present work, all available experimental data was used to determined r^2 values (this differs from the optimisation process, where only a selected number of experimental points were implemented in order to keep computation times reasonable). Plots comparing predicted behaviour to the corresponding experimental data are presented for stress range evolution and general cyclic stress fitting for the middle (150^{th}) cycle. For clarity, the profiles predicted by each constant set are separated into multiple plots. Those predicted from initial conditions may be found in figure 3.17. Profiles predicted from the results of separated parallel or series optimisation can be seen in figure 3.18. Profiles predicted using the results of combined parallel optimisation are given in figure 3.19.

$$r^2 = 1 - \sum_{i=1}^{N} \frac{(EXP_i - PRED_i)^2}{N\sigma_{EXP}^2} \tag{3.24}$$

Table 3.8: Summary of coefficients of determination for fitting to saw tooth experimental data using different material constant sets.

	r^2
Saw tooth initial conditions	0.7630
Relaxation initial conditions	0.7215
1-SP (equal to 1-S)	0.9977
2-SP	0.9907
2-S	0.9958
1-CP - Saw tooth initial conditions	0.9765
1-CP - Relaxation initial conditions	0.9988

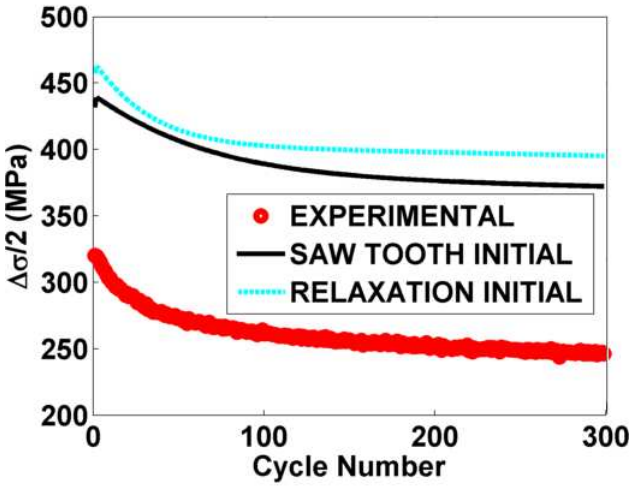

(a)

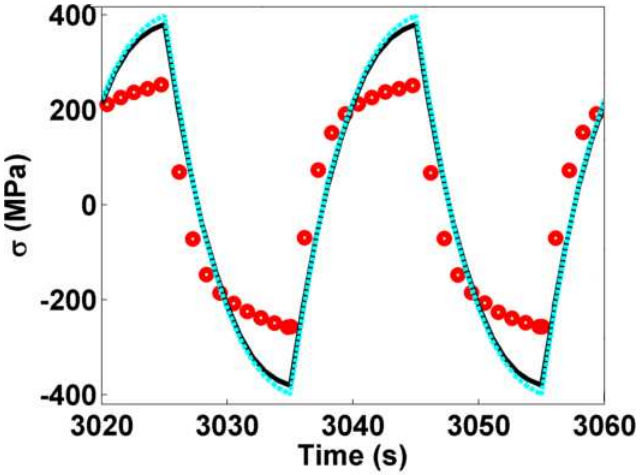

(b)

Figure 3.17: Illustration of fitting quality for the saw tooth loading profile using initial estimates of the material constants, showing (a) stress range evolution with cycle number and (b) stress fitting for the middle (150^{th}) cycle.

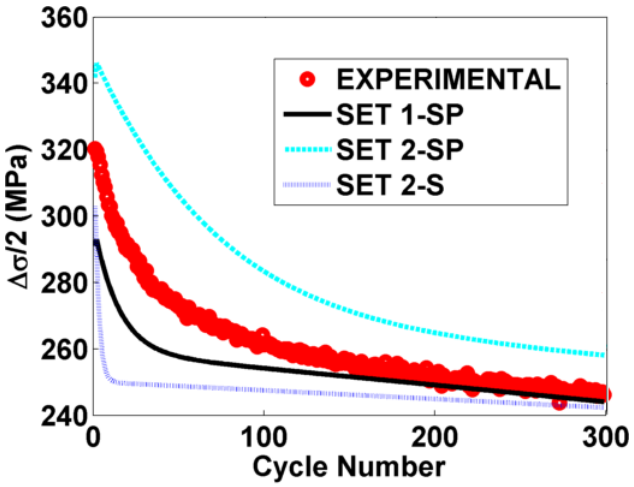

(a)

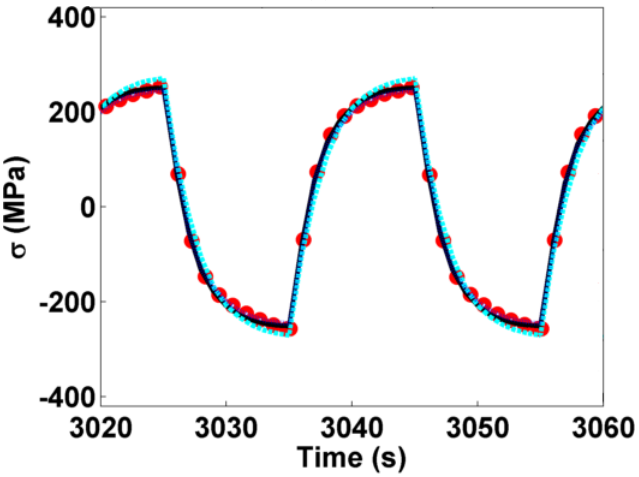

(b)

Figure 3.18: Illustration of fitting quality for the saw tooth loading profile using optimised values of the material constants from series and separate parallel optimisation procedures. Plots shown are (a) stress range evolution with cycle number and (b) stress fitting for the middle (150^{th}) cycle.

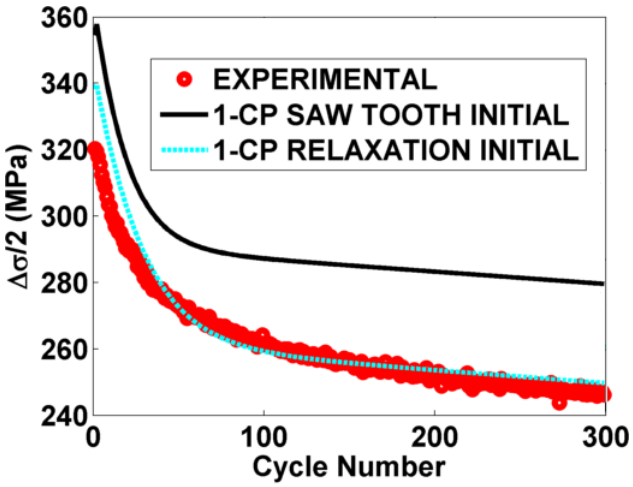

(a)

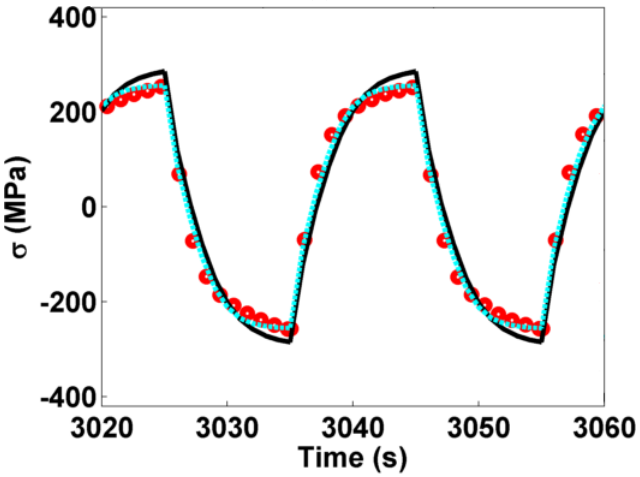

(b)

Figure 3.19: Illustration of fitting quality for the saw tooth loading profile using optimised values of the material constants from combined parallel optimisation procedures, showing (a) stress range evolution with cycle number and (b) stress fitting for the middle (150^{th}) cycle.

Relaxation Waveform Prediction

Similar to section 6.1, coefficient of determination (r^2) values are presented for each material constant set based on relaxation experimental data (see table 3.9). To demonstrate the relative fitting of the predicted profiles (based on different material constant sets), plots comparing the predicted behaviour to the experimental data are presented for stress range prediction and general cyclic stress fitting for the middle (150^{th}) cycle. For clarity, the predicted profiles are also separated into initial conditions, series and separated parallel optimisation results and combined parallel optimisation results groups (see figures 3.20 to 3.22, respectively).

Table 3.9: Summary of coefficients of determination for fitting to relaxation experimental data using different material constant sets.

	r^2
Saw tooth initial conditions	0.7599
Relaxation initial conditions	0.6909
1-SP (equal to 1-S)	0.9310
2-SP	0.9853
2-S	0.9947
1-CP - Saw tooth initial conditions	0.9786
1-CP - Relaxation initial conditions	0.9994

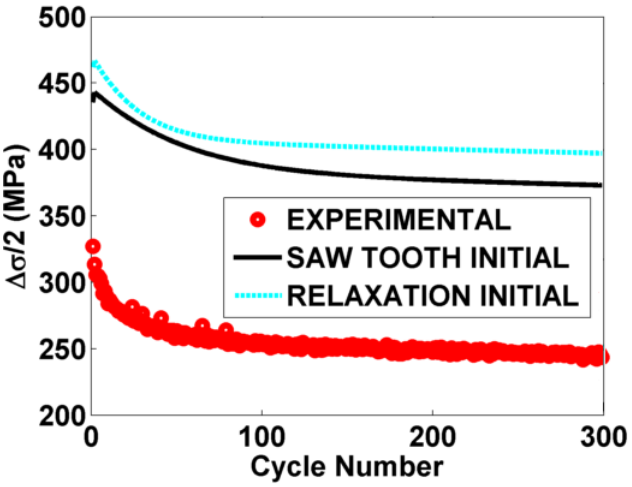

(a)

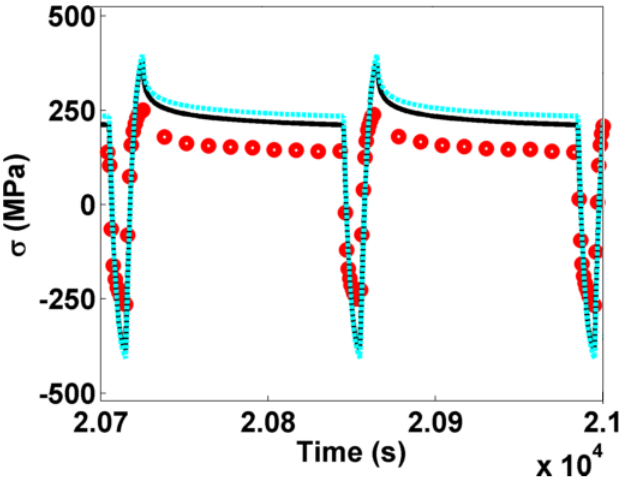

(b)

Figure 3.20: Illustration of fitting quality for the relaxation loading profile using initial estimates of the material constants, showing (a) stress range evolution with cycle number and (b) stress fitting for the middle (150^{th}) cycle.

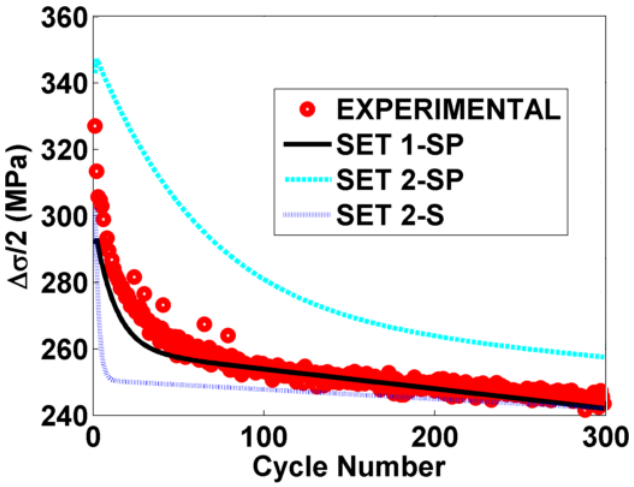

(a)

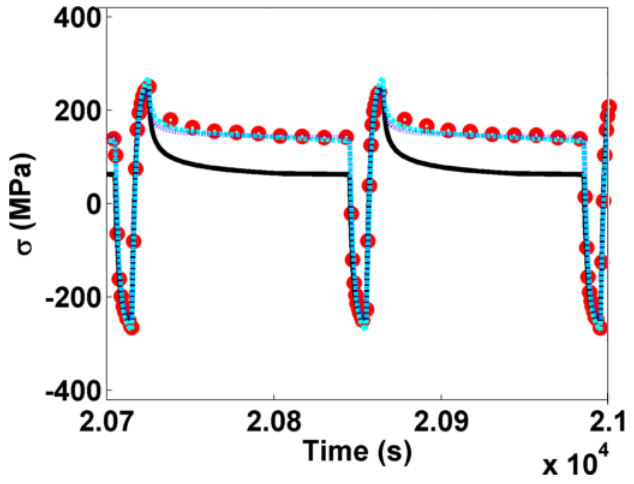

(b)

Figure 3.21: Illustration of fitting quality for the relaxation loading profile using optimised values of the material constants from series and separate parallel optimisation procedures. Plots show (a) stress range evolution with cycle number and (b) stress fitting for the middle (150^{th}) cycle.

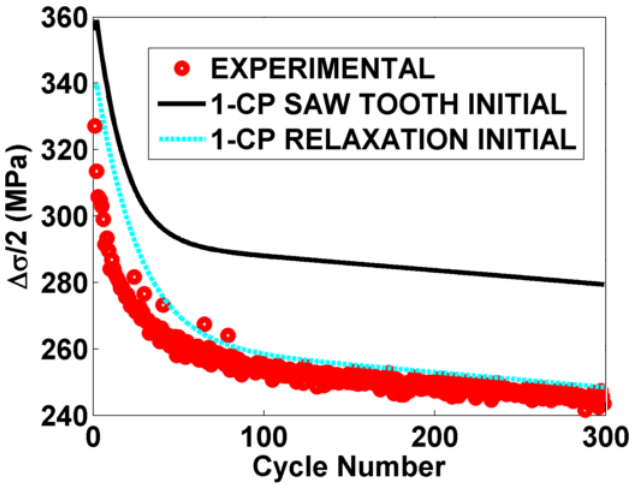

(a)

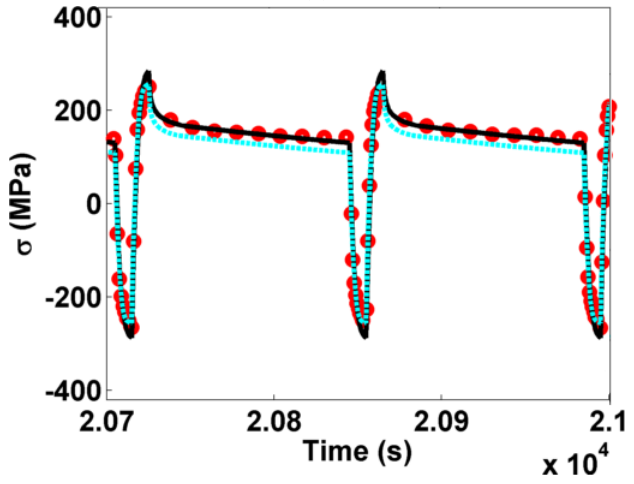

(b)

Figure 3.22: Illustration of fitting quality for the relaxation loading profile using optimised values of the material constants from combined parallel optimisation procedures, showing (a) stress range evolution with cycle number and (b) stress fitting for the middle (150^{th}) cycle.

3.8.5 Summary of the Investigation into Multiple Data Source Optimisation Strategies

A single set of material constants for the Chaboche visco-plasticity model should be sufficient to describe multiple sets of experimental data if the tests were performed under the same characteristic conditions (e.g. multiple isothermal tests at the same temperature, similar strain rates and limit strain values). Several optimisation strategies have been presented to meet this expectation. While the resultant material constant sets from the optimisation procedures differ considerably, the general fitting quality was greatly improved and was generally consistent (see tables 3.8 and 3.9) through

optimisation (highlighting the complex interplay between material constants in the Chaboche model). The first step in the practical application of a model is to determine a single, representative set of material constants.

Optimisation procedures using the separated parallel strategy ran simultaneously (but with no exchange of information between the two procedures). While constant set 1-SP is slightly better (r^2 equals 0.9977 compared to 0.9901 for constant set 2-SP) at predicting saw tooth experimental data, constant set 2-SP is significantly more adept at predicting relaxation experimental data (r^2 equals 0.9853 compared to 0.9310 for constant set 1-SP, see table 3.9). Such behaviour is to be expected as constant set 1-SP is not the result of an optimisation based on experimental data containing stress relaxation regions, therefore creep material constants cannot be fitted to a creep dominant region. The separated nature of this methodology means that inevitably one of the optimised material constant sets is redundant; therefore the experimental data related to this redundant material constant set is not represented in the final solution. If multiple experimental data sets are available, the maximum confidence in the final solution's ability to predict experimental data can be obtained by applying the highest level of constraint to an optimisation procedure.

The series optimisation strategy (figure 3.15) effectively dissects sources of experimental data on a mechanism basis. Completion times for this optimisation methodology have been found to be relatively lengthy (approximately 8 hours compared to 5 hours for the separate parallel optimisation procedures). More importantly however, the subsequent consideration of relaxation data after the saw tooth optimisation procedure could detract from the ability of the final result to predict the saw tooth experimental response. Given slight experimental discrepancies between the hardening sections in both experimental data sets, it is reasonable to assume that different optimum hardening material constants (i.e. a_1, C_1, a_2, C_2, b and Q) will better predict these marginally different stress profiles. As the relaxation experimental data is considered last, its hardening loops are treated preferentially, altering the material constant values that predict the saw tooth data well in order to predict the relaxation data. The fitting quality to saw tooth experimental data is thus compromised. Such behaviour can be observed in table 3.8, noting that the coefficient of determination value reduces marginally between constant set 1-S (0.9977) and 2-S (0.9958). When predicting relaxation data, the additional optimisation procedure improves the fitting quality (the coefficient of determination value is greater for constant set 2-S than 1-S see table 3.9). In order to give adequate and equal consideration to both sources of experimental data, simultaneous (or parallel) optimisation must be performed.

In the combined parallel optimisation strategy (figure 3.16), objective functions are formed using both sets of experimental data simultaneously. Completion times are generally significantly less for the combined parallel optimisation methodology (approximately 3 hours) than for the alternatives suggested. It is suspected that this is

due to the high level of constraint in this methodology. The formation of the objective function is dependent on several sub-objective functions, therefore the gradient based optimisation method used in LSQNONLIN has more information to determine the direction of greatest decent. Minimum (either global or local) solutions can therefore be obtained in a shorter time.

Initial estimates derived from either set of experimental data generally predict the same hardening behaviour (see figure 3.17); despite slight differences in the related material constant values. Although the creep constants Z and n are identical for the two initial condition sets (having both been derived from relaxation data), a small discrepancy can be observed between the stress relaxation curves predicted by the saw tooth initial condition set and the relaxation initial condition set in figure 3.20. It should be remembered that the stress relaxation region in the relaxation experimental data does not represent a period of solely creep dependant behaviour. Isolation of material constants based on controlling deformation mechanisms has not been possible in the present work and should only be undertaken with extreme care.

All optimised material constant sets appear to predict saw tooth experimental data well (see figures 3.18 and 3.19 and table 3.8). Constant set 1-SP (or 1-S) appears to give the optimum solution for the prediction the results of saw tooth experiments (see table 3.8). This is to be expected as the constant set is determined based solely on objective functions formed from saw tooth experimental data. The lack of additional constraint from other experimental data sources means that the fitting quality of this material constant set is not impaired (when compared to saw tooth experimental data). Note that for constant set 1-CP Relaxation (see table 3.8), the fitting quality is approximately the same as for constant sets 2-SP and 2-S (approximately 0.99). Lower r^2 values are observed for constant sets 1-CP Saw Tooth. A potential explanation for this phenomenon is that the combination of initial condition values derived from both saw tooth and relaxation experimental data does not represent a unified material constant set. The division of initial condition values based on a mechanism basis does not reflect the interplay between hardening and creep effects present in the Chaboche model. These initial conditions therefore may cause the optimisation to localise on non-optimum solutions, impairing the fitting quality in some cases and resulting in a lower r^2 value.

The comparative plotting results for the prediction of relaxation experimental data are more complex, owing to the rejection of creep dominant regions for the optimisation of some material constant sets (constant set 1-SP). The effects of not optimising using experimental data with creep dominant regions can be illustrated by the relatively poor prediction of stress relaxation using material constant set 1-SP (see figure 3.21 and table 3.9). A marked improvement in creep response prediction can be seen for constant set 2-S (i.e. after constant set 1-S has been optimised based on data with creep dominant regions). Both combined parallel optimisation material constant sets estimate the relaxation experimental data well, however the inclusion of congruent initial conditions

(i.e. derived from one experimental data source; the relaxation experimental data) in determining the constant set 1-CP Relaxation seems to provide a better approximation of the stress range evolution, compared to constant sets 1-CP Saw Tooth.

Optimisation procedures may also result in the determination of physically unrealistic constants. Alternatively, a dependence may be observed between a particular optimisation method and the solution. It should be noted that, particularly in the case of the Chaboche model presented here, the highly multi-dimensional (i.e. numerous parameters to be optimised) nature of the optimisation creates a complex topology. This is exacerbated by the potential for strong dependencies between material constants. It is therefore possible for gradient methods to converge on drastically different minima with only slight difference in initial estimate. This point is particularly true in the context of the present work, where prior optimisation procedures yield the initial estimates for subsequent optimisations (see figure 3.15 for example). Solutions can be made more reliable by using side constraints in the optimisation. Isotropic parameters in such as Q and H can typically be determined with a great deal of certainty (the values of these constants are not heavily affected by the assumptions in section 3.5.1 and optimised values are typically within $\pm 10\%$ of the initial estimates). Tight upper and lower limits can therefore be applied to these constants, while allowing the other material constants to be fully optimised. Applying tight side constraints must be done with caution due to potential parameter interactions. Additionally, the maximum level of constraint should be enforced from experimental data. It is the conclusion of this work that all available experimental data (even when it is from different sources/tests) should be used to evaluate objective functions in the same optimisation iteration.

3.9 The Prediction of the Cyclic Hardening Behaviour of P91 and 316 Steel

3.9.1 Experimental data for a P91 steel and 316 Stainless Steel

In this chapter, several sub-investigations have been conducted in order to establish a robust method for the determination of material constants of the Chaboche unified visco-plasticity model. To demonstrate the high level of fitting quality that may be achieved by implementing these procedures they have been applied to experimental data for a high chrome steel (grade P91) and a stainless steel (grade 316), both of which have been used in power plant. The chemical composition of these materials can be seen in tables 3.10 and 3.11, respectively.

Table 3.10: Chemical composition (wt %) of P91 steel.

Cr	Mo	Mn	Si	Ni	V	C	Cu
8.49	0.978	0.43	0.37	0.32	0.2	0.11	0.07
Nb	Co	P	W	S	Ti	Al	Fe
0.06	0.02	0.014	< 0.02	0.008	< 0.002	< 0.001	Balance

Table 3.11: Chemical composition (wt %) of 316 stainless steel.

Cr	Ni	Mo	Mn	Si	Cu	V	Co
16.8	11.8	2.15	1.42	0.5	0.49	0.08	0.07
S	C	Nb	W	Al	P	Ti	Fe
0.03	0.02	0.02	< 0.02	0.01	0.01	0.01	Balance

Strain limits were set to $\pm 0.5\%$, with a 2 minute hold period at the end of each of the tensile loading regions (where applicable) and a constant strain rate of 0.1%/s for P91 tests and 0.003%/s for 316 steels. P91 tests were conducted at 600°C, 500°C and 400°C. 316 tests were conducted at 600°C. 10 experimental data points were selected for each loading region (tensile, compressive or strain hold), giving 20 and 30 data points per loading cycle for saw tooth and relaxation type data, respectively. The number of cycles considered in each optimisation routines was chosen so that primary and secondary behaviour was considered. For P91, 400, 600 and 1000 cycles of data were included for the 600°C, 500°C and 400°C data, respectively. 600 cycles of data were considered for the optimisation of the 316 data at 600°C. Cyclic softening behaviour (represented by a reduction in stress range with increased accumulated plastic strain) was observed in both test types for P91 (see figures 3.23 to 3.25). Cyclic hardening behaviour was observed for the 316 material (see figure 3.26). The inclusion of materials that cyclically soften and harden illustrates the wide applicability of the Chaboche model and the optimisation procedure developed. Initial conditions were derived from relaxation type experimental data for the reasons given in section 3.8.5. A summary of these initial conditions and the optimised values is given in tables 3.12 and 3.13 for P91 and 316, respectively.

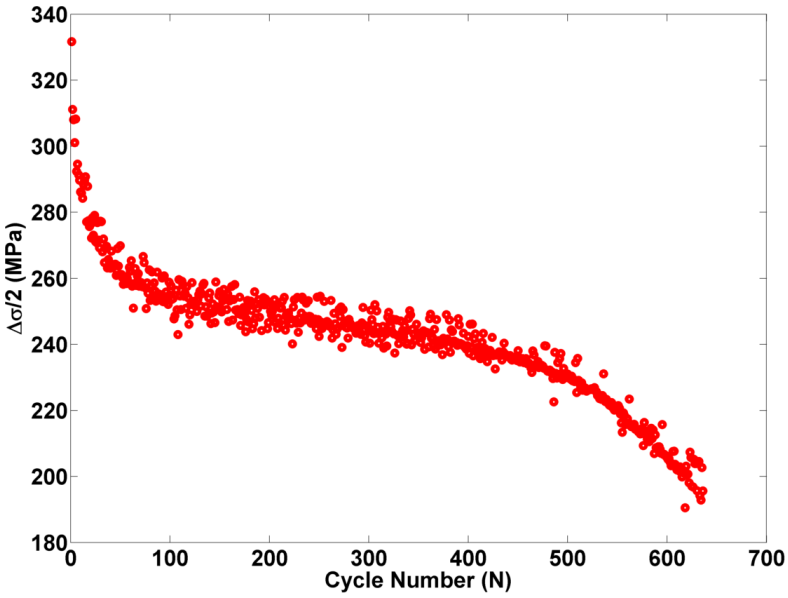

(a)

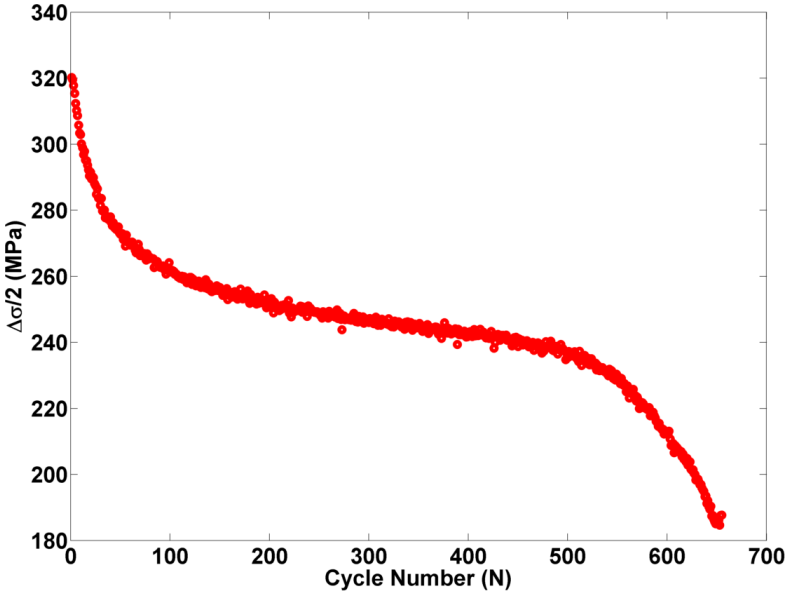

(b)

Figure 3.23: The evolution of stress range ($\Delta\sigma/2$) for a P91 steel at 600°C under (a) relaxation and (b) saw tooth type loading profiles.

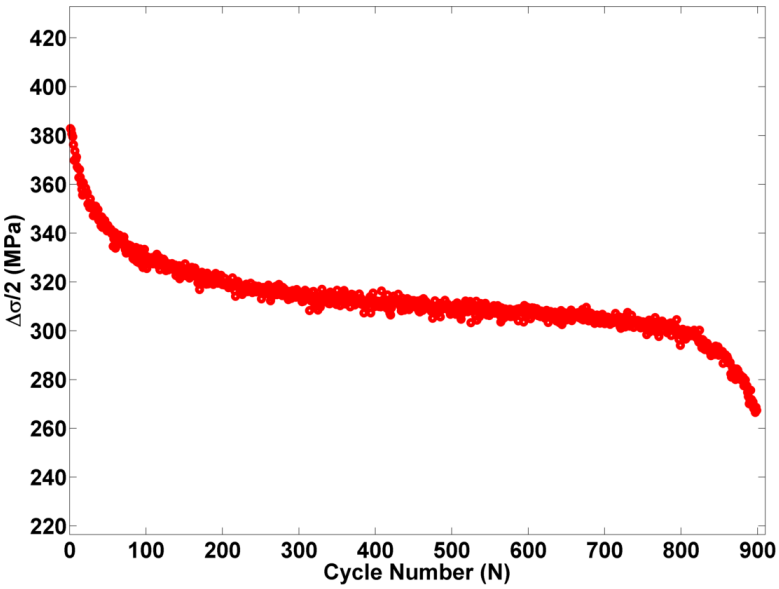

(a)

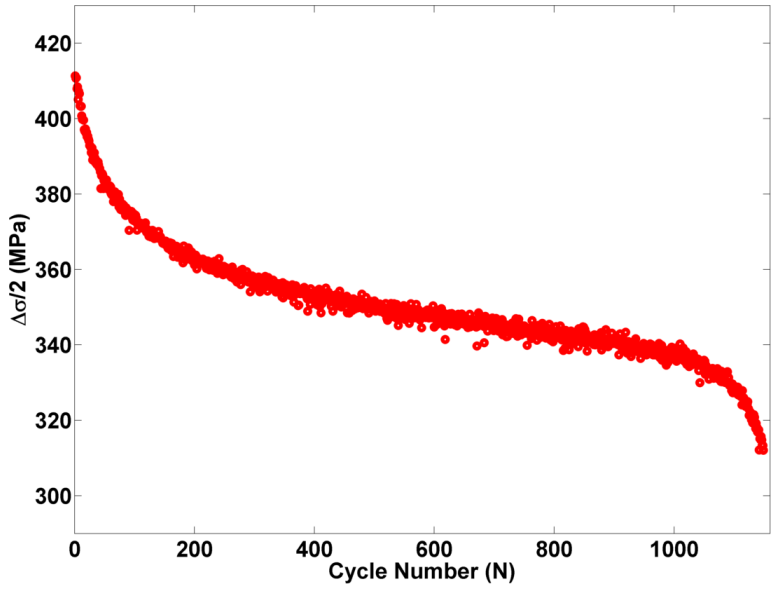

(b)

Figure 3.24: The evolution of stress range ($\Delta\sigma/2$) for a P91 steel at 500°C under (a) relaxation and (b) saw tooth type loading profiles.

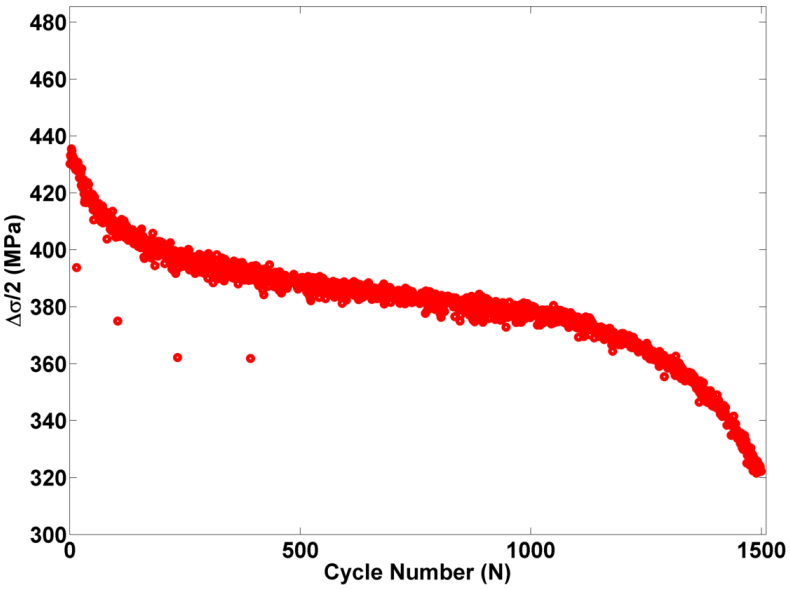

(a)

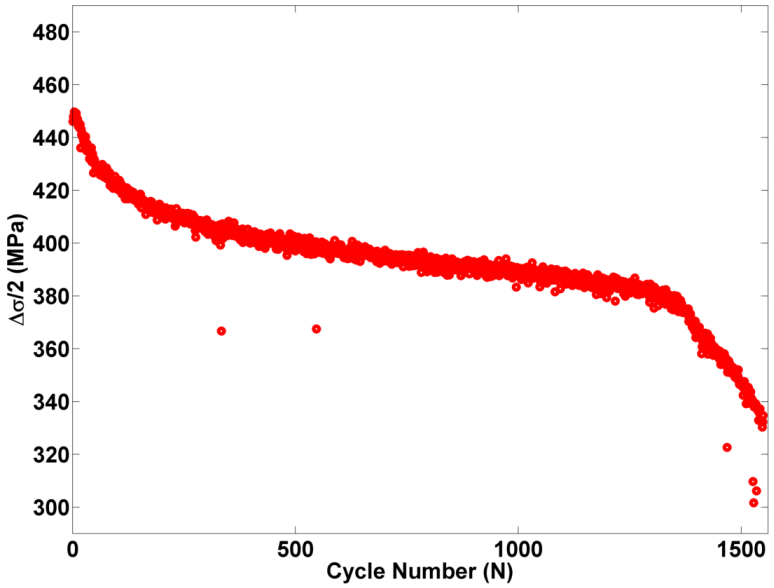

(b)

Figure 3.25: The evolution of stress range ($\Delta\sigma/2$) for a P91 steel at 400°C under (a) relaxation and (b) saw tooth type loading profiles.

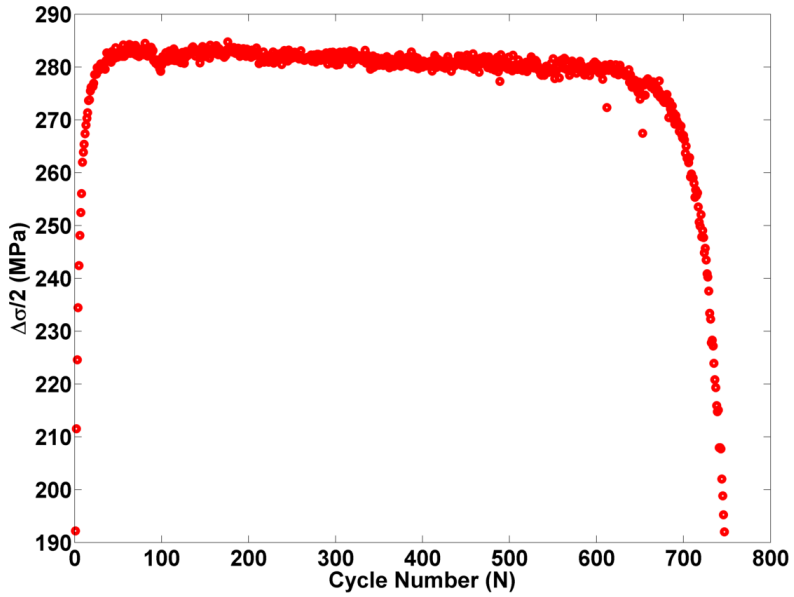

(a)

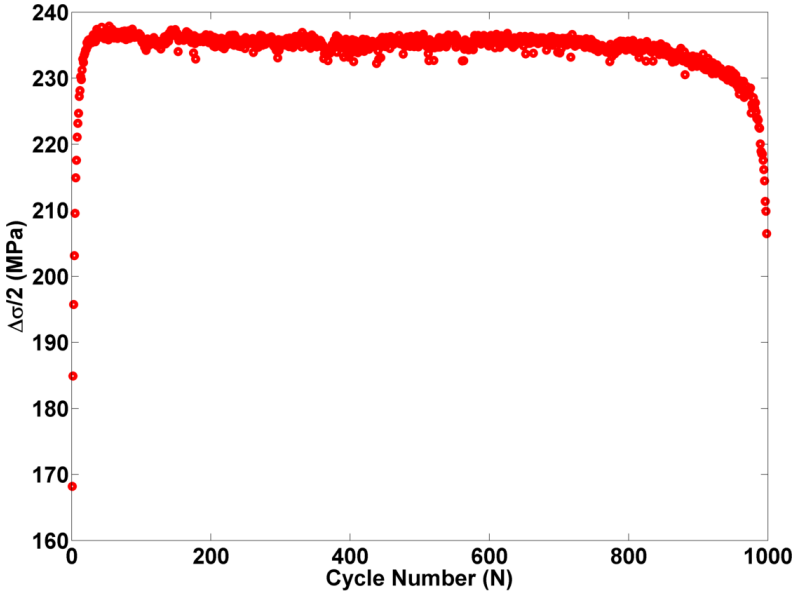

(b)

Figure 3.26: The evolution of stress range ($\Delta\sigma/2$) for a 316 steel at 600°C under (a) relaxation and (b) saw tooth type loading profiles.

Table 3.12: Summary of initial estimates and optimised values for the Chaboche model material constants for a P91 steel at 600°C, 500°C and 400°C.

	600°C Initial Estimates	600°C Optimised Values	500°C Initial Estimates	500°C Optimised Values	400°C Initial Estimates	400°C Optimised Values
a_1 (MPa)	33.62	58.2	59.86	66.27	23.63	33.71
C_1	4758.44	11400.00	7347.50	2736.28	9026.53	7764.29
a_2 (MPa)	30.21	51.20	59.11	74.59	30.63	72.19
C_2	290.14	609.00	539.93	432.74	724.40	582.79
Z $(MPa.s^{1/n})$	1019.72	844.12	492.77	370.79	455.71	382.93
n	6.51	3.43	16.54	6.56	42.57	18.94
b	3.80	1.50	1.50	1.53	0.74	0.78
Q (MPa)	-60.79	-62.21	-47.55	-47.98	-30.32	-33.35
k (MPa)	91.05	91.19	98.44	96.04	98.44	77.35
E (MPa)	$1.44x10^5$	$1.41x10^5$	$1.78x10^5$	$1.62x10^5$	$1.83x10^5$	$1.75x10^5$
H (MPa)	-4.06	-1.98	-2.55	-2.70	-1.52	-1.56

Table 3.13: Summary of initial estimates and optimised values for the Chaboche model material constants for a 316 steel at 600°C.

	600°C Initial Estimates	600°C Optimised Values
a_1 (MPa)	51.31	53.48
C_1	931.29	1193.05
a_2 (MPa)	55.83	48.40
C_2	303.12	275.28
Z $(MPa.s^{1/n})$	959.18	297.93
n	7.52	6.59
b	13.72	9.77
Q (MPa)	67.77	60.01
k (MPa)	47.81	79.54
E (GPa)	$1.28x10^5$	$1.36x10^5$
H (MPa)	-0.07	-0.90

3.9.2 P91 Steel Results

3.9.3 P91 Steel at 600°C

The results of a combined parallel optimisation using cleaned experiential data for a P91 steel at 600°C are presented below. The prediction of stress range ($\Delta\sigma/2$) versus load cycle number N is presented for both saw tooth and relaxation type load profiles in figures 3.27 and 3.31, respectively. Hysteresis loops for the 1^{st}, 200^{th} and 400^{th} load cycles are also presented to show the quality of fit for hardening curves. These plots are provided for saw tooth (figures 3.28 to 3.30) and relaxation (figures 3.32 to 3.34) type load profiles. Relaxation figures also include plots of stress relaxation regions for the

same load cycles, verifying the prediction of creep dominated behaviour.

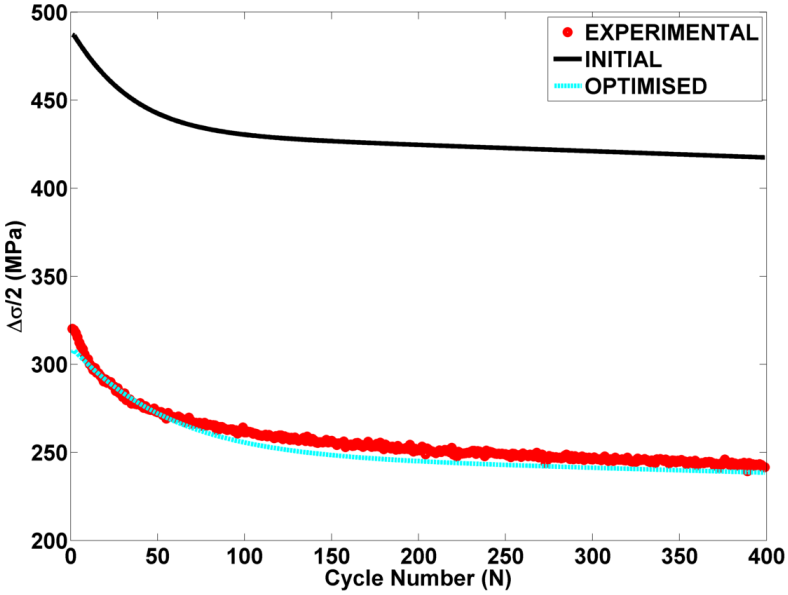

Figure 3.27: The prediction of the evolution of stress range ($\Delta\sigma/2$) for a P91 steel at 600°C due to a saw tooth type loading profile, showing the behaviour predicted by the initial estimates of material constants and the optimised values.

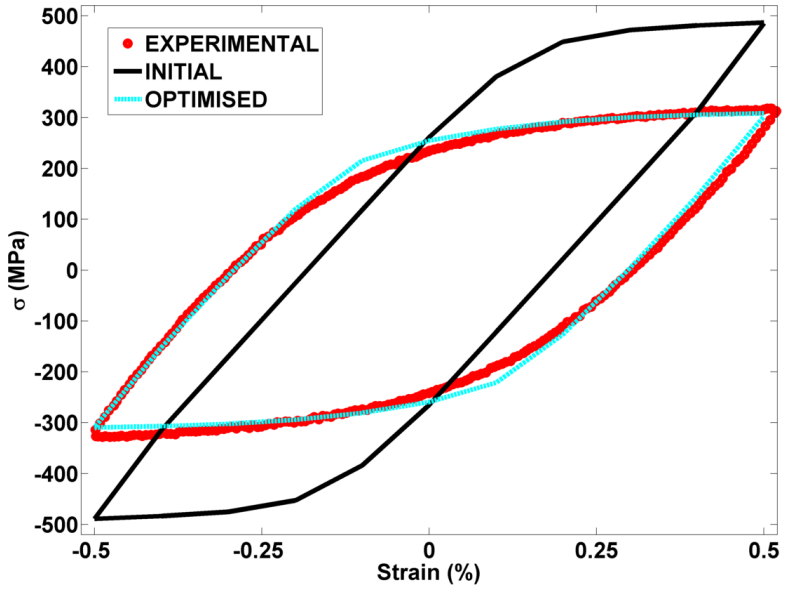

Figure 3.28: The prediction of the 1^{st} hysteresis loop for a P91 steel at 600°C due to a saw tooth type loading profile, showing the behaviour predicted by the initial estimates of material constants and the optimised values.

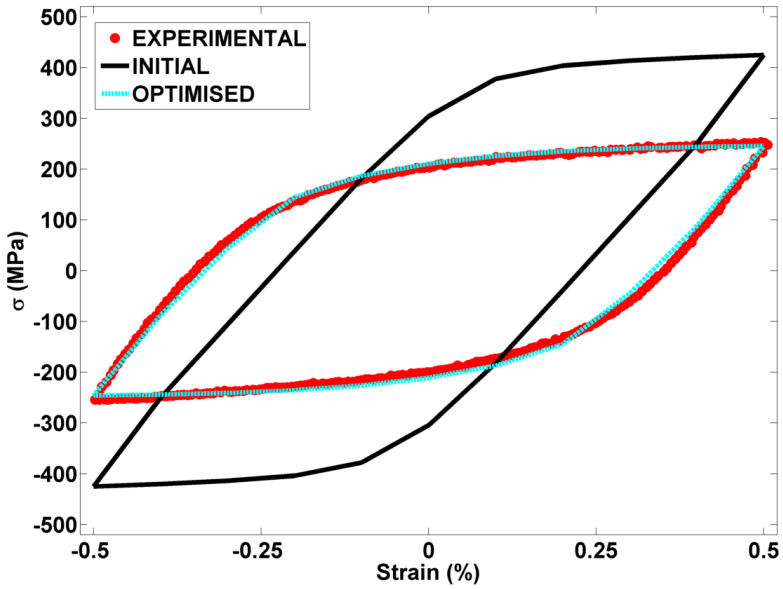

Figure 3.29: The prediction of the 200^{th} hysteresis loop for a P91 steel at 600°C due to a saw tooth type loading profile, showing the behaviour predicted by the initial estimates of material constants and the optimised values.

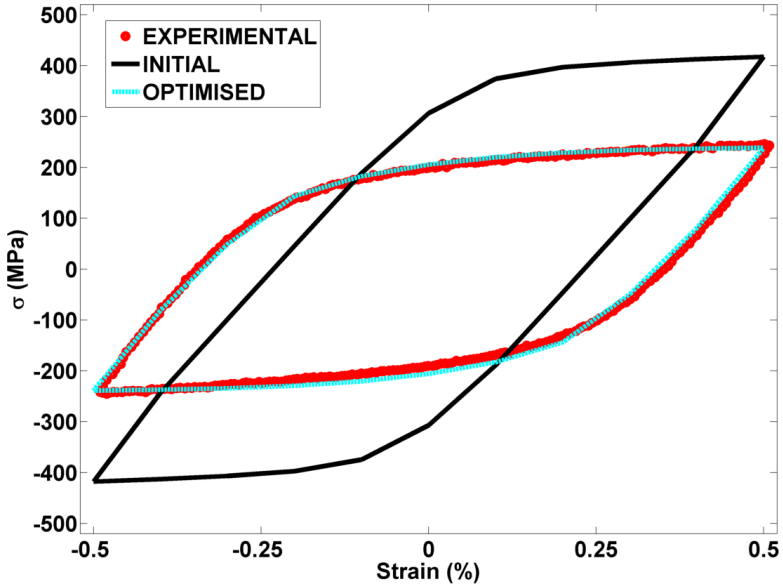

Figure 3.30: The prediction of the 400^{th} hysteresis loop for a P91 steel at 600°C due to a saw tooth type loading profile, showing the behaviour predicted by the initial estimates of material constants and the optimised values.

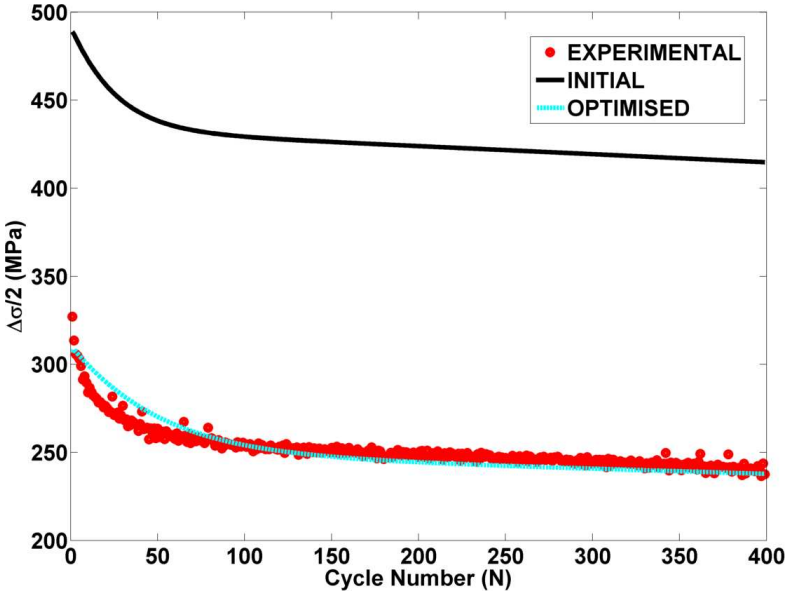

Figure 3.31: The prediction of the evolution of stress range ($\Delta\sigma/2$) for a P91 steel at 600°C due to a relaxation type loading profile, showing the behaviour predicted by the initial estimates of material constants and the optimised values.

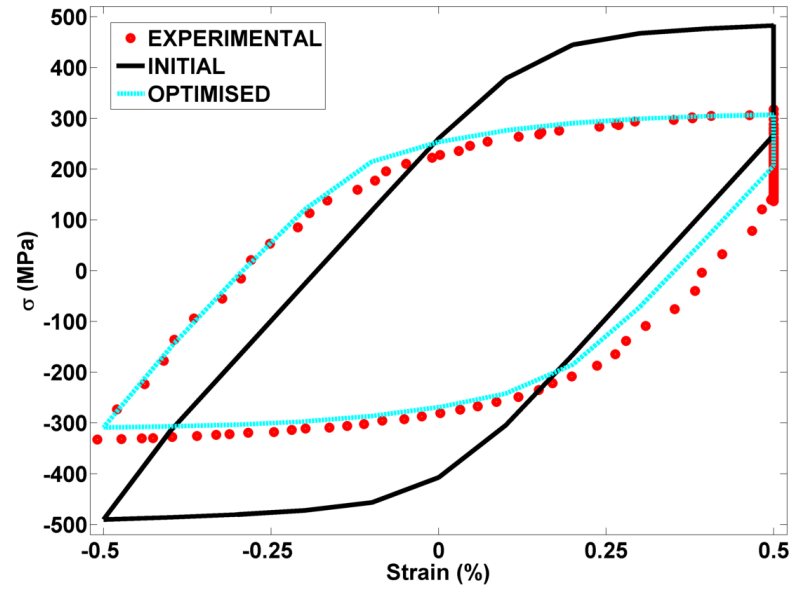

(a)

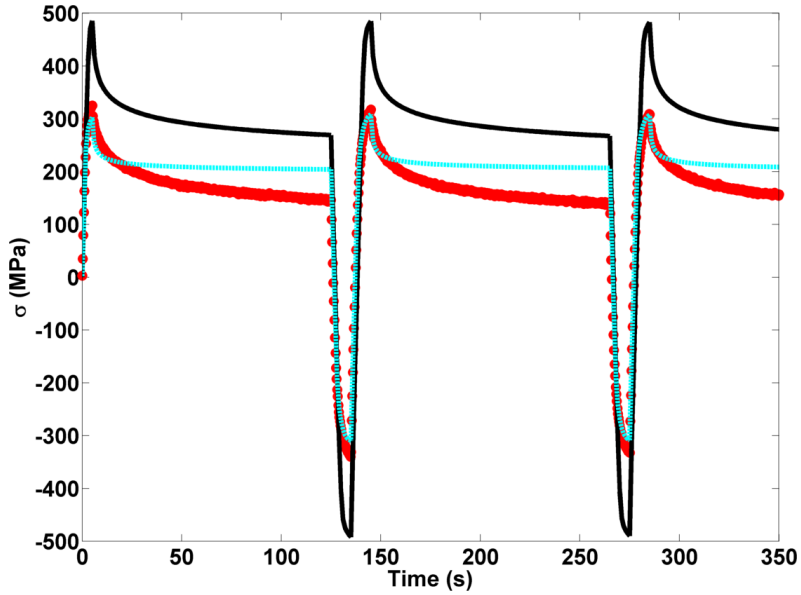

(b)

Figure 3.32: The prediction of (a) the 1^{st} hysteresis loop and (b) the stress relaxation region for the 1^{st} loading cycle for a P91 steel at 600°C due to a relaxation type loading profile, showing the behaviour predicted by the initial estimates of material constants and the optimised values.

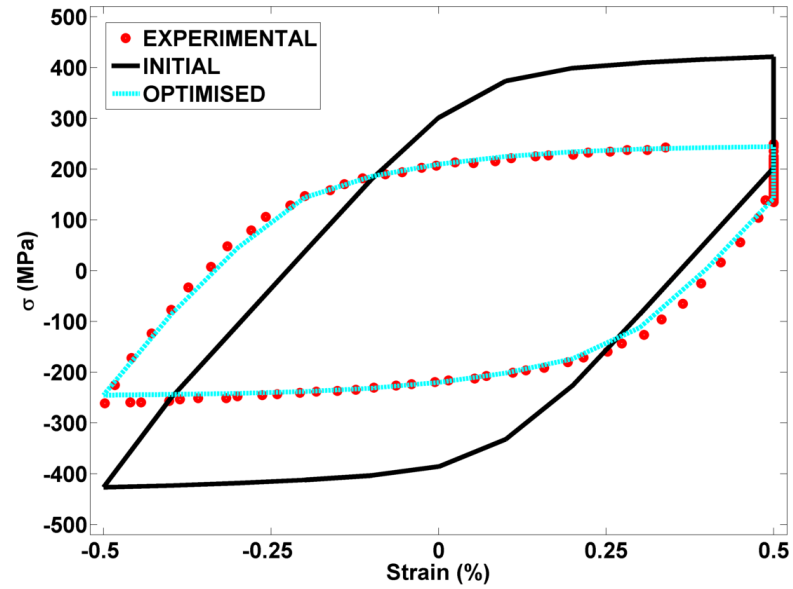

(a)

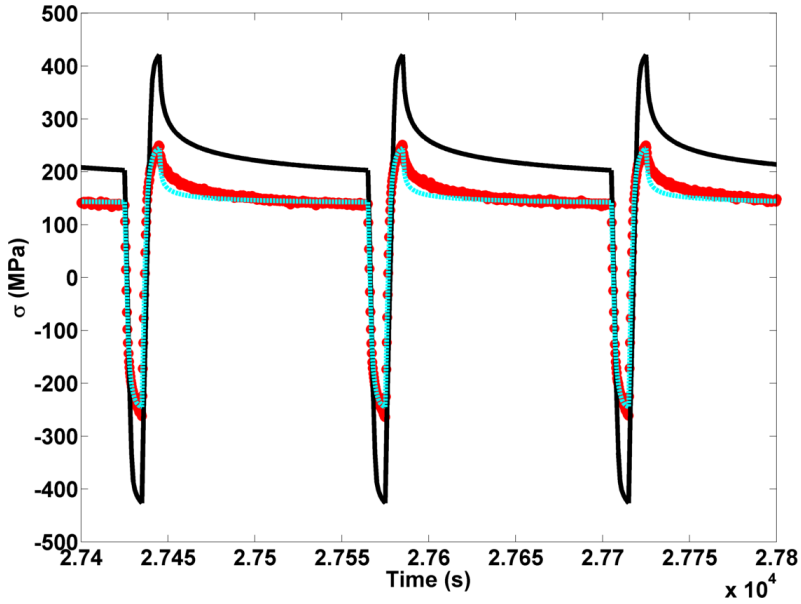

(b)

Figure 3.33: The prediction of (a) the 200^{th} hysteresis loop and (b) the stress relaxation region for the 200^{th} loading cycle for a P91 steel at 600°C due to a relaxation type loading profile, showing the behaviour predicted by the initial estimates of material constants and the optimised values.

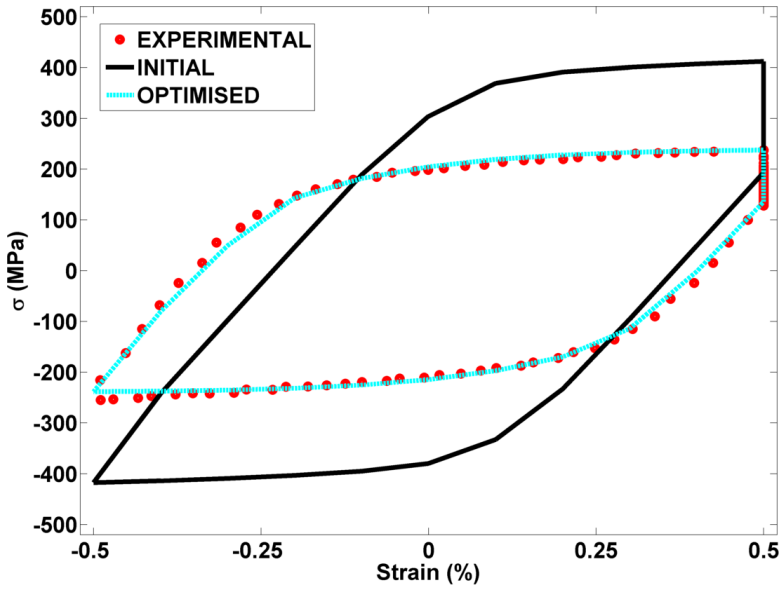

(a)

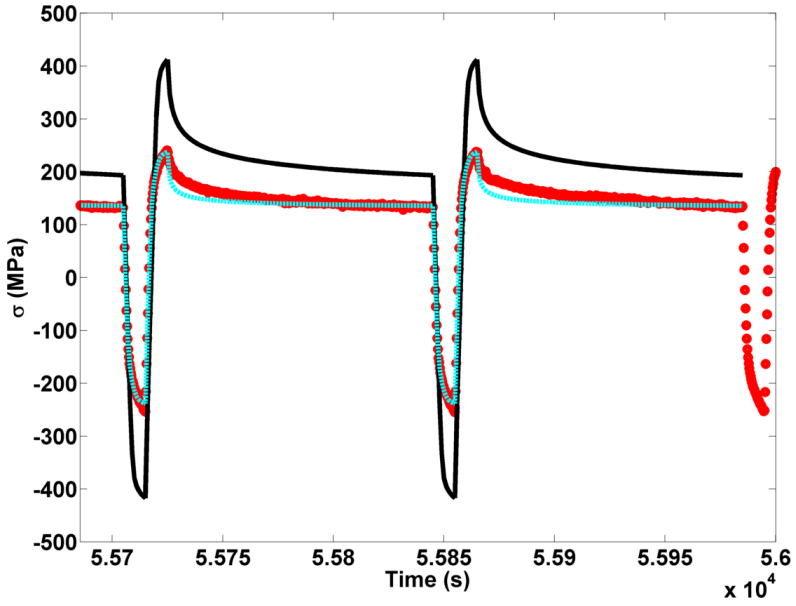

(b)

Figure 3.34: The prediction of (a) the 400^{th} hysteresis loop and (b) the stress relaxation region for the 400^{th} loading cycle for a P91 steel at 600°C due to a relaxation type loading profile, showing the behaviour predicted by the initial estimates of material constants and the optimised values.

3.9.4 P91 Steel at 500°C

The results of a combined parallel optimisation using cleaned experiential data for a P91 steel at 500°C are presented below. The prediction of stress range ($\Delta\sigma/2$) versus load cycle number N is presented for both saw tooth and relaxation type load profile in figures 3.35 and 3.39, respectively. Hysteresis loops for the 1^{st}, 300^{th} and 600^{th} load cycles are also presented to show the quality of fit for hardening curves. These plots are

provided for saw tooth (figures 3.36 to 3.38) and relaxation (figures 3.40 to 3.42) type load profiles. Relaxation figures also include plots of stress relaxation regions for the same load cycles, verifying the prediction of creep dominated behaviour.

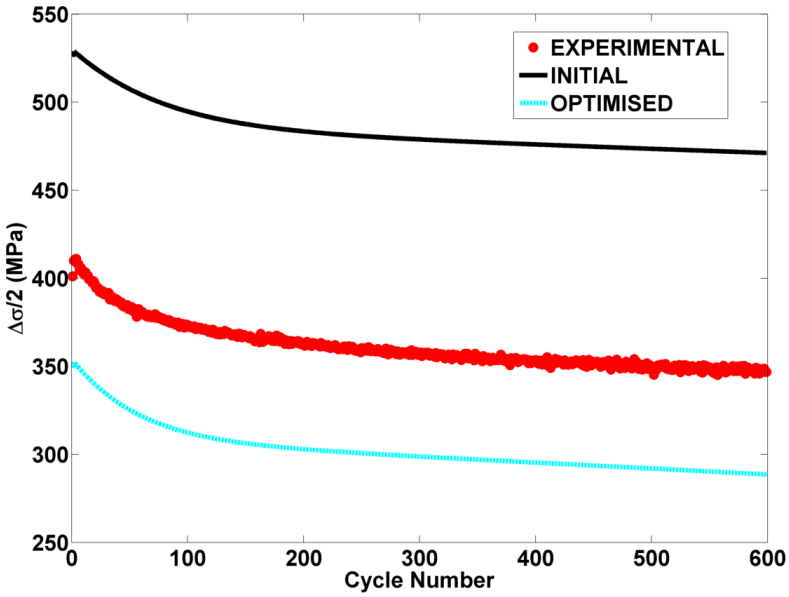

Figure 3.35: The prediction of the evolution of stress range ($\Delta\sigma/2$) for a P91 steel at 500°C due to a saw tooth type loading profile, showing the behaviour predicted by the initial estimates of material constants and the optimised values.

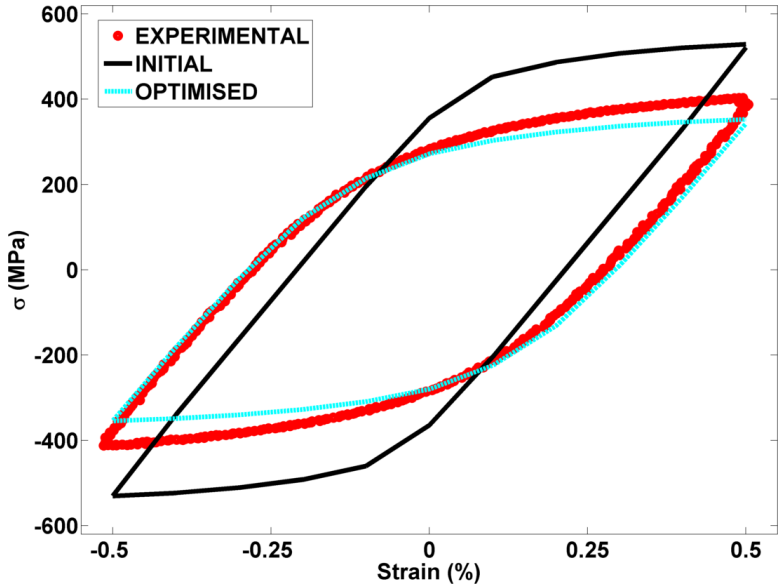

Figure 3.36: The prediction of the 1^{st} hysteresis loop for a P91 steel at 500°C due to a saw tooth type loading profile, showing the behaviour predicted by the initial estimates of material constants and the optimised values.

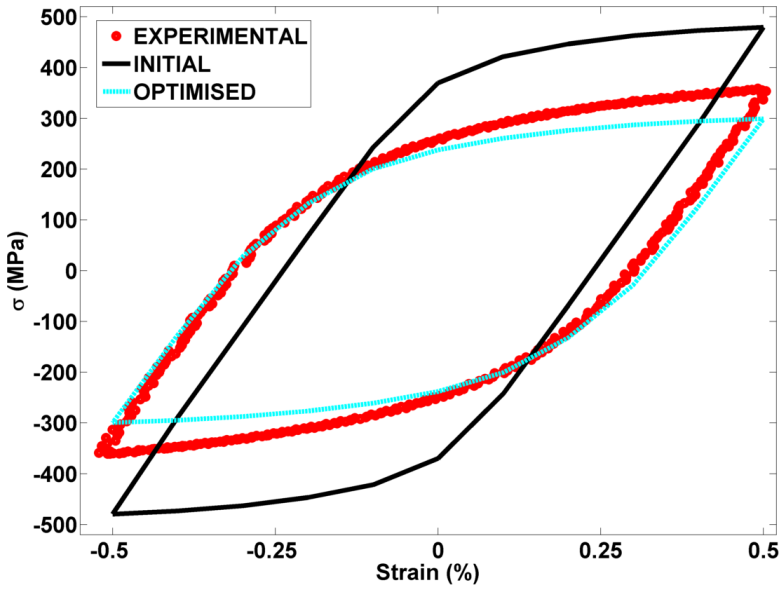

Figure 3.37: The prediction of the 300^{th} hysteresis loop for a P91 steel at 500°C due to a saw tooth type loading profile, showing the behaviour predicted by the initial estimates of material constants and the optimised values.

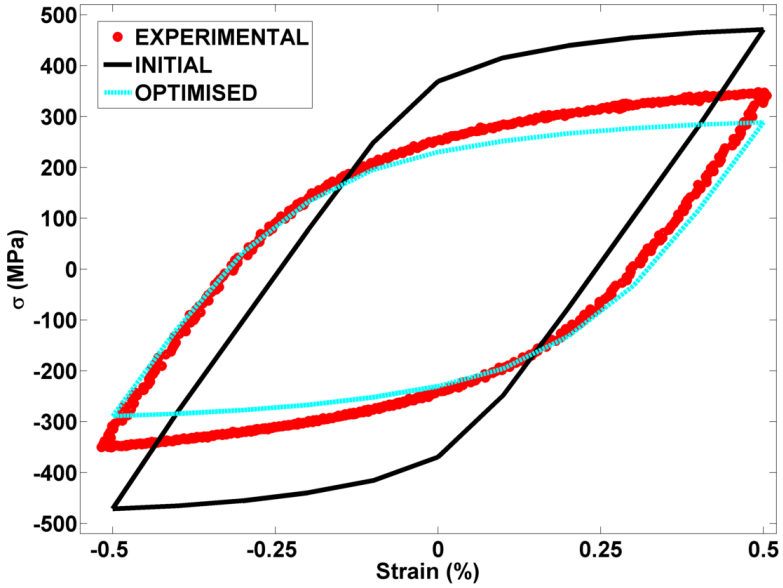

Figure 3.38: The prediction of the 600^{th} hysteresis loop for a P91 steel at 500°C due to a saw tooth type loading profile, showing the behaviour predicted by the initial estimates of material constants and the optimised values.

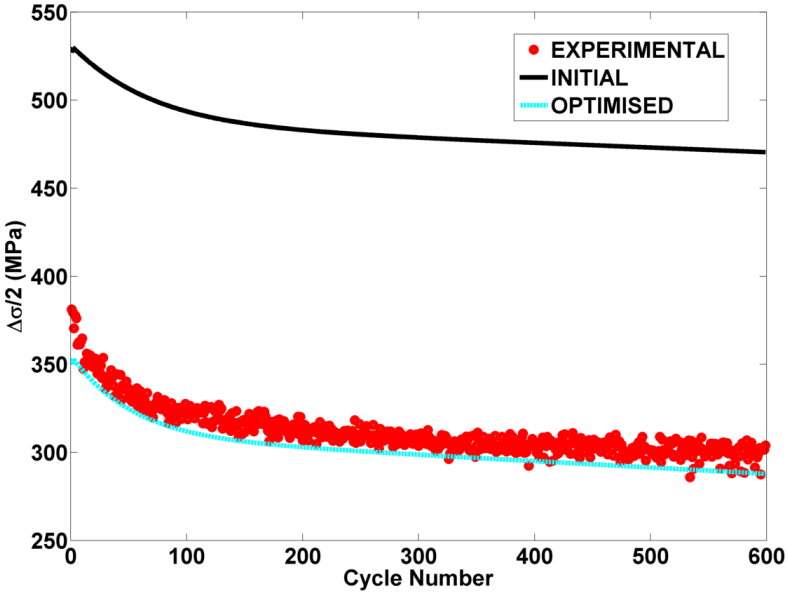

Figure 3.39: The prediction of the evolution of stress range ($\Delta\sigma/2$) for a P91 steel at 500°C due to a relaxation type loading profile, showing the behaviour predicted by the initial estimates of material constants and the optimised values.

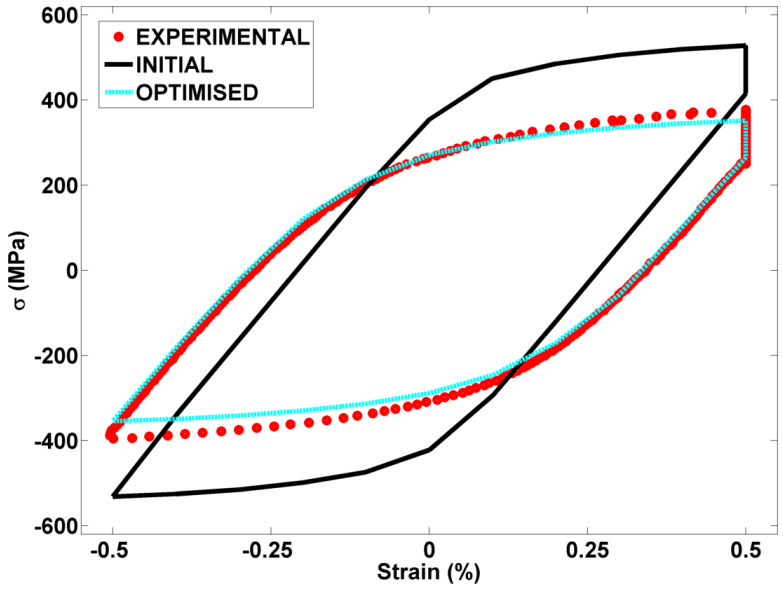

(a)

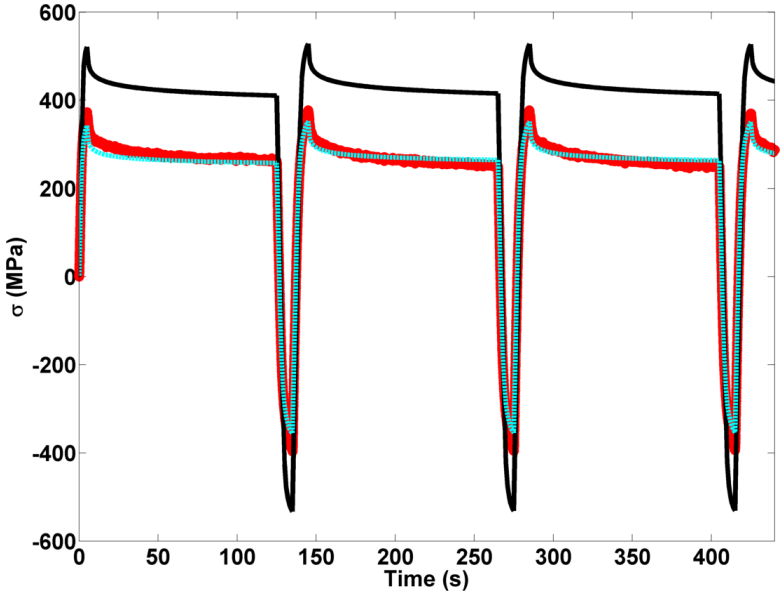

(b)

Figure 3.40: The prediction of (a) the 1^{st} hysteresis loop and (b) the stress relaxation region for the 1^{st} loading cycle for a P91 steel at 500°C due to a relaxation type loading profile, showing the behaviour predicted by the initial estimates of material constants and the optimised values.

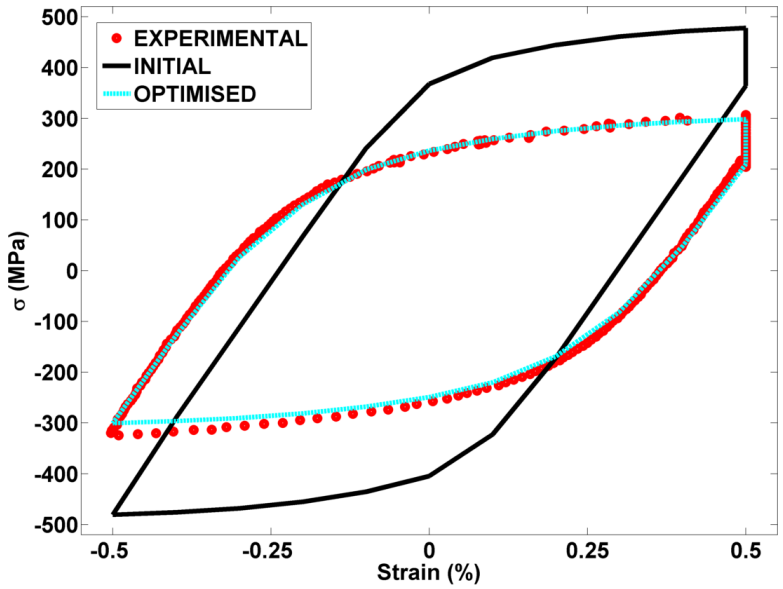

(a)

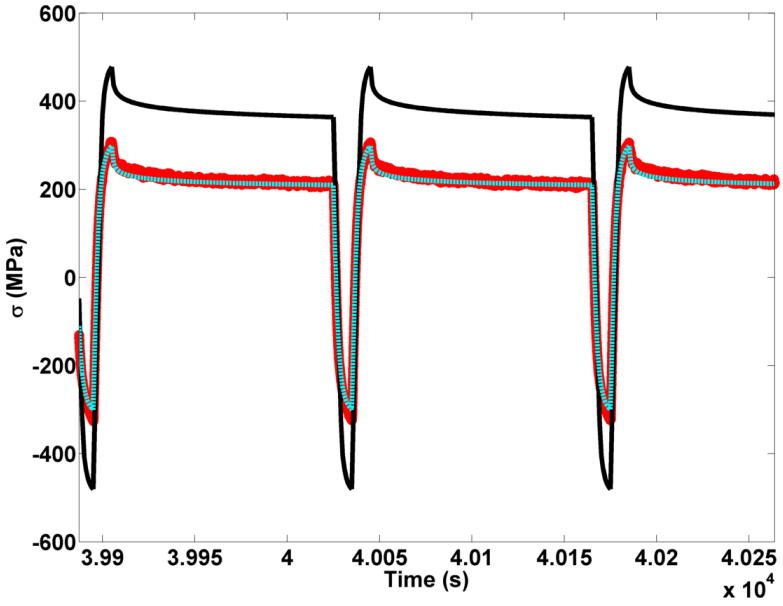

(b)

Figure 3.41: The prediction of (a) the 300^{th} hysteresis loop and (b) the stress relaxation region for the 300^{th} loading cycle for a P91 steel at 500°C due to a relaxation type loading profile, showing the behaviour predicted by the initial estimates of material constants and the optimised values.

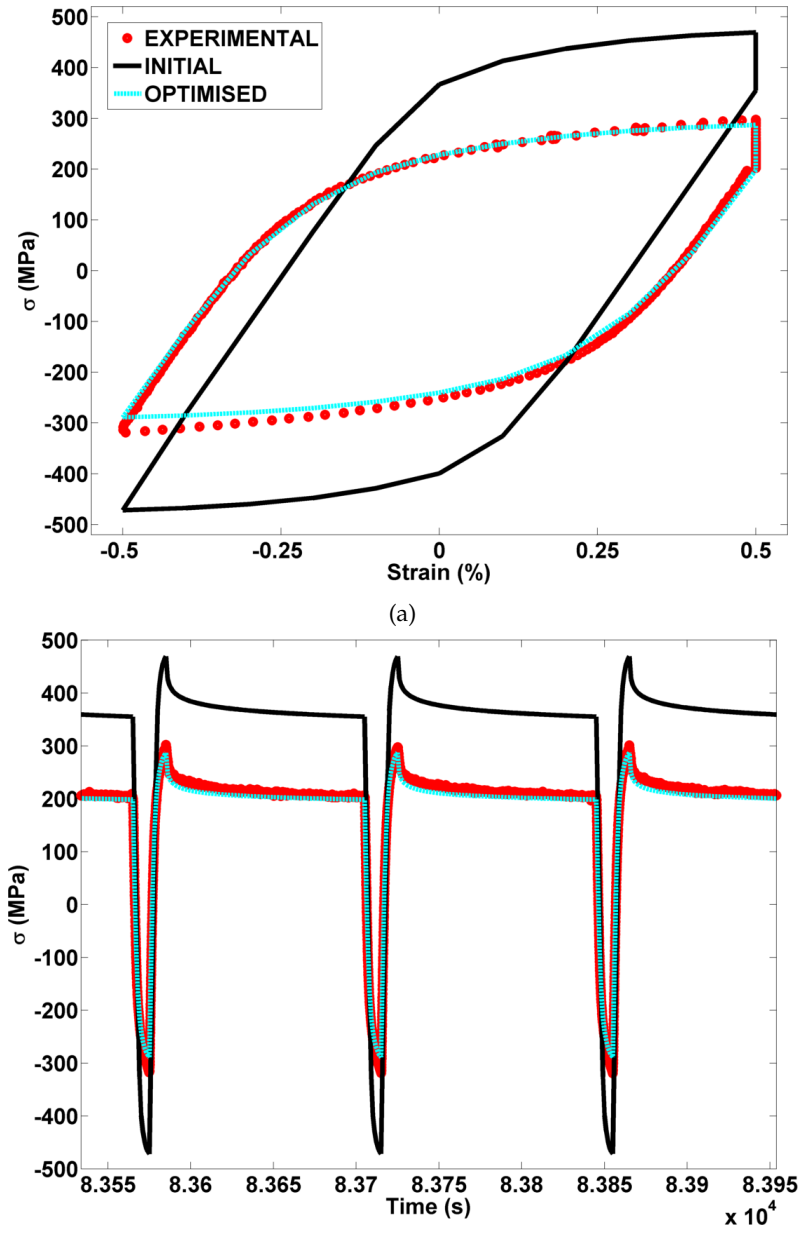

Figure 3.42: The prediction of (a) the 600^{th} hysteresis loop and (b) the stress relaxation region for the 600^{th} loading cycle for a P91 steel at 500°C due to a relaxation type loading profile, showing the behaviour predicted by the initial estimates of material constants and the optimised values.

3.9.5 P91 Steel at 400°C

The results of a combined parallel optimisation using cleaned experiential data for a P91 steel at 400°C are presented below. The prediction of stress range ($\Delta\sigma/2$) versus load cycle number N is presented for both saw tooth and relaxation type load profile in figures 3.43 and 3.47, respectively. Hysteresis loops for the 1^{st}, 500^{th} and 1000^{th} load cycles are also presented to show the quality of fit for hardening curves. These plots are

provided for saw tooth (figures 3.44 to 3.46) and relaxation (figures 3.48 to 3.50) type load profiles. Relaxation figures also include plots of stress relaxation regions for the same load cycles, verifying the prediction of creep dominated behaviour.

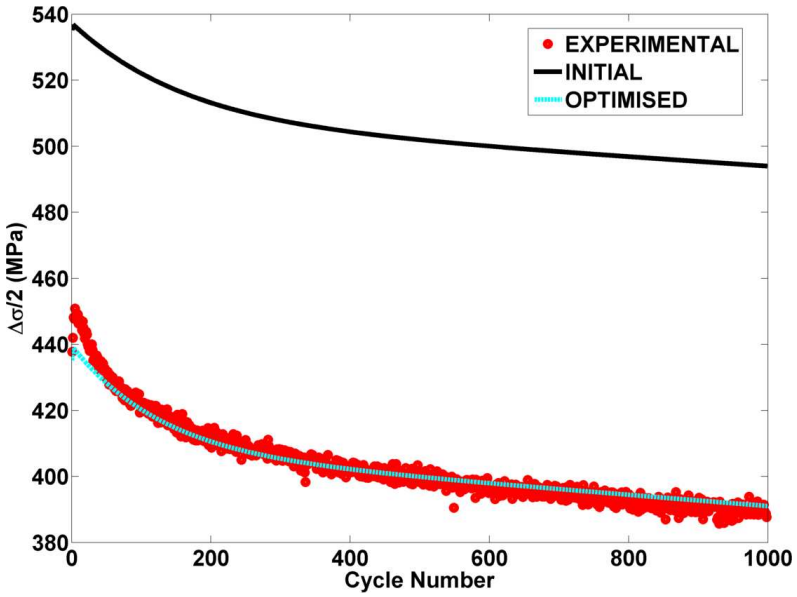

Figure 3.43: The prediction of the evolution of stress range ($\Delta\sigma/2$) for a P91 steel at 400°C due to a saw tooth type loading profile, showing the behaviour predicted by the initial estimates of material constants and the optimised values.

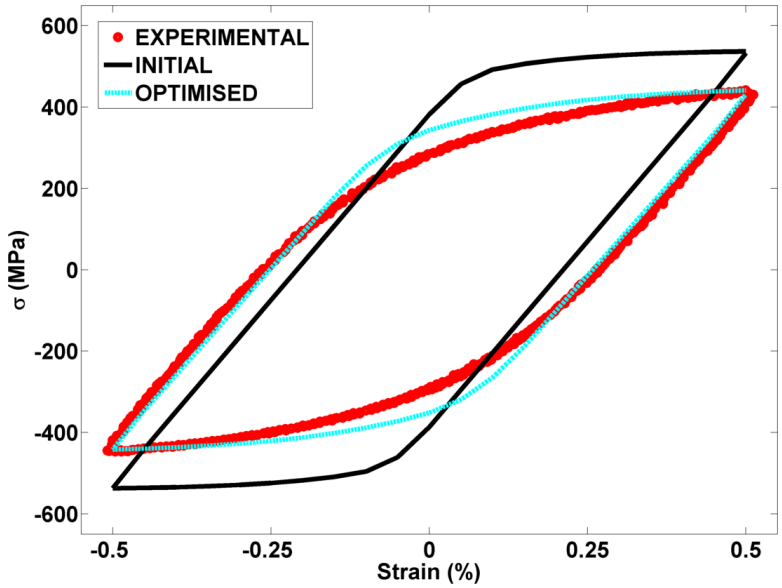

Figure 3.44: The prediction of the 1^{st} hysteresis loop for a P91 steel at 400°C due to a saw tooth type loading profile, showing the behaviour predicted by the initial estimates of material constants and the optimised values.

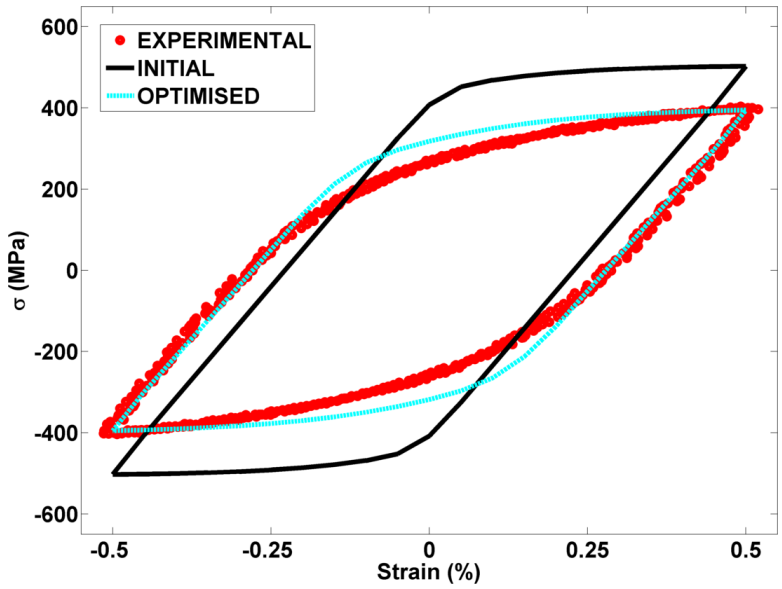

Figure 3.45: The prediction of the 500^{th} hysteresis loop for a P91 steel at 400°C due to a saw tooth type loading profile, showing the behaviour predicted by the initial estimates of material constants and the optimised values.

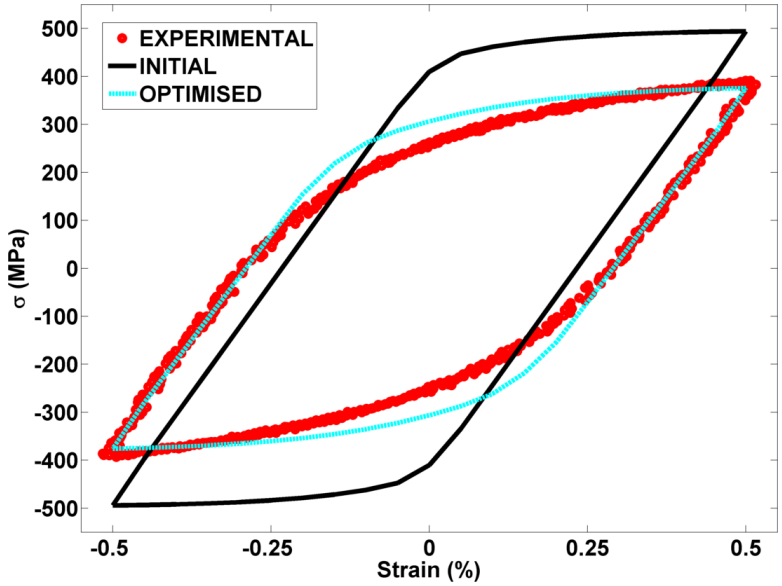

Figure 3.46: The prediction of the 1000^{th} hysteresis loop for a P91 steel at 400°C due to a saw tooth type loading profile, showing the behaviour predicted by the initial estimates of material constants and the optimised values.

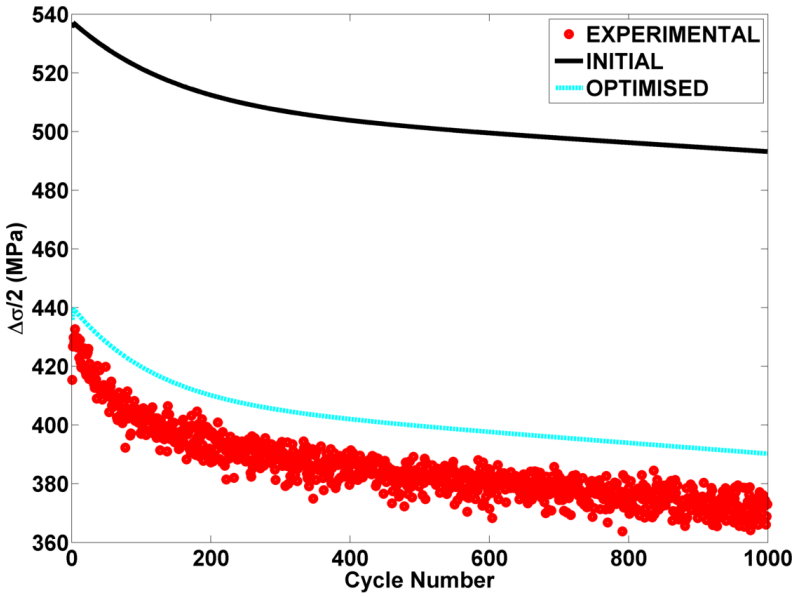

Figure 3.47: The prediction of the evolution of stress range ($\Delta\sigma/2$) for a P91 steel at 400°C due to a relaxation type loading profile, showing the behaviour predicted by the initial estimates of material constants and the optimised values.

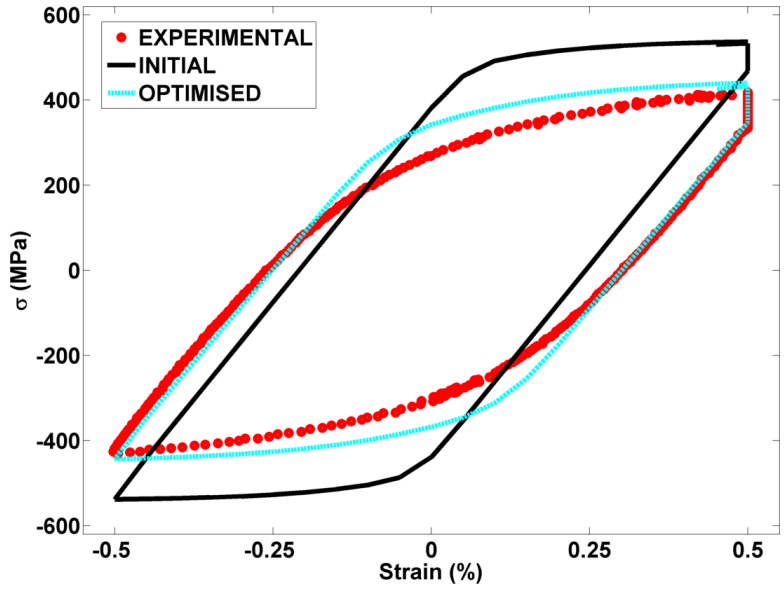

(a)

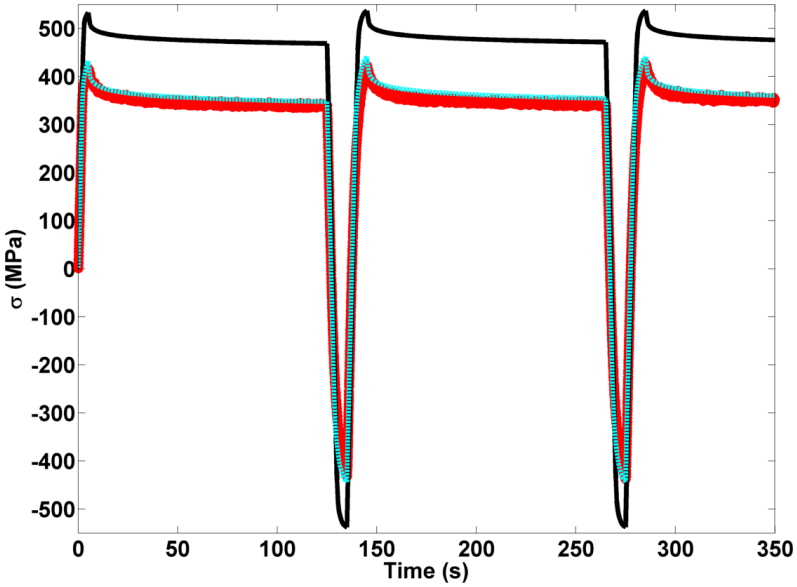

(b)

Figure 3.48: The prediction of (a) the 1^{st} hysteresis loop and (b) the stress relaxation region for the 1^{st} loading cycle for a P91 steel at 400°C due to a relaxation type loading profile, showing the behaviour predicted by the initial estimates of material constants and the optimised values.

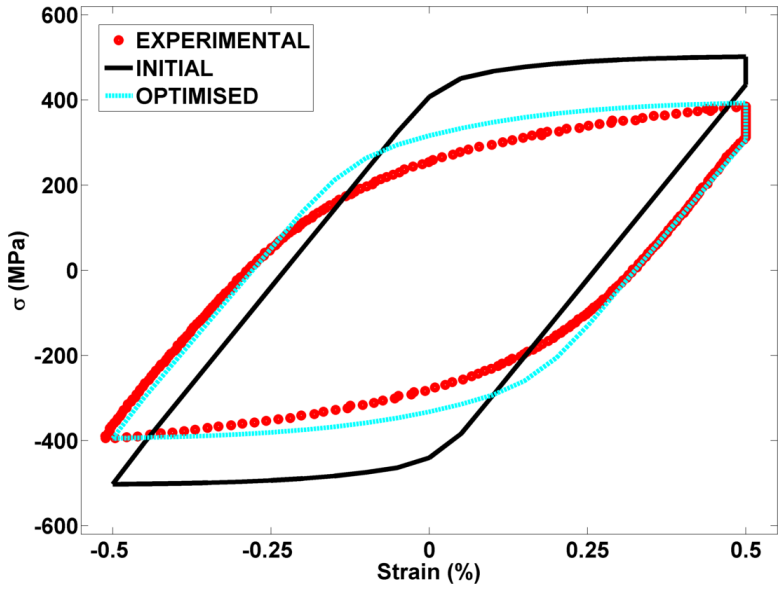

(a)

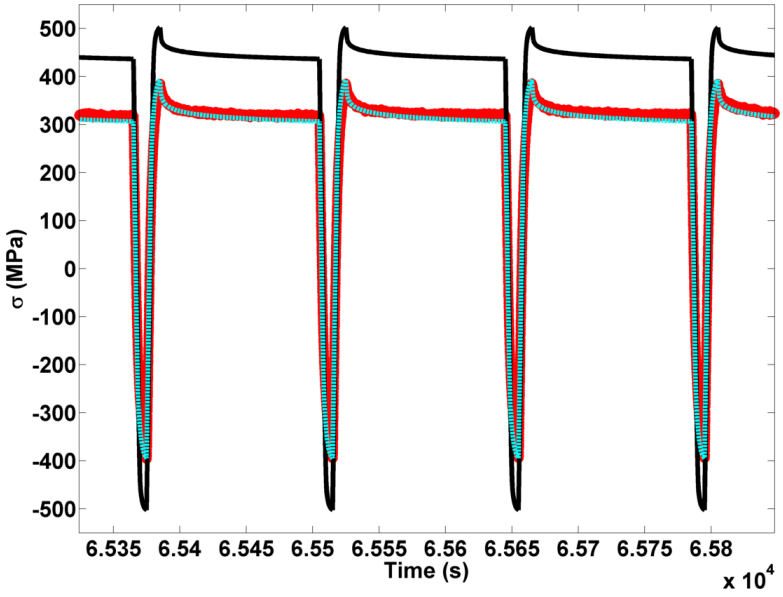

(b)

Figure 3.49: The prediction of (a) the 500^{th} hysteresis loop and (b) the stress relaxation region for the 500^{th} loading cycle for a P91 steel at 400°C due to a relaxation type loading profile, showing the behaviour predicted by the initial estimates of material constants and the optimised values.

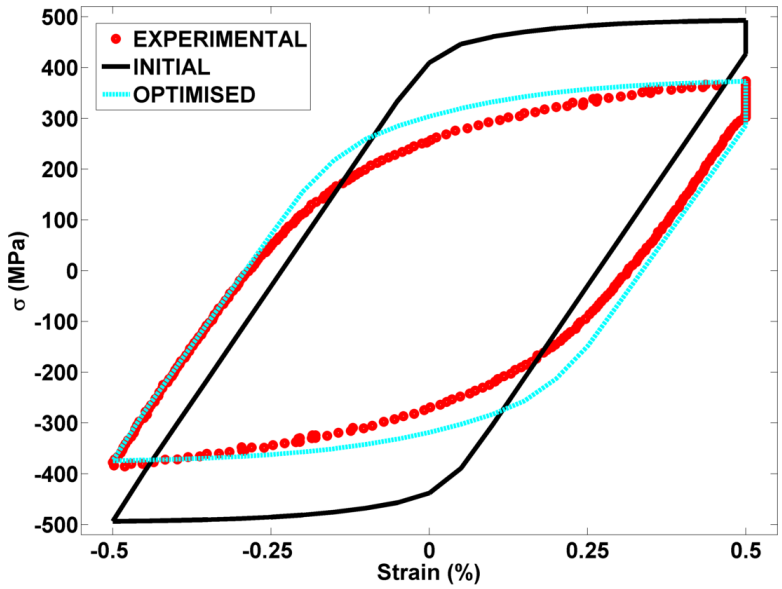

(a)

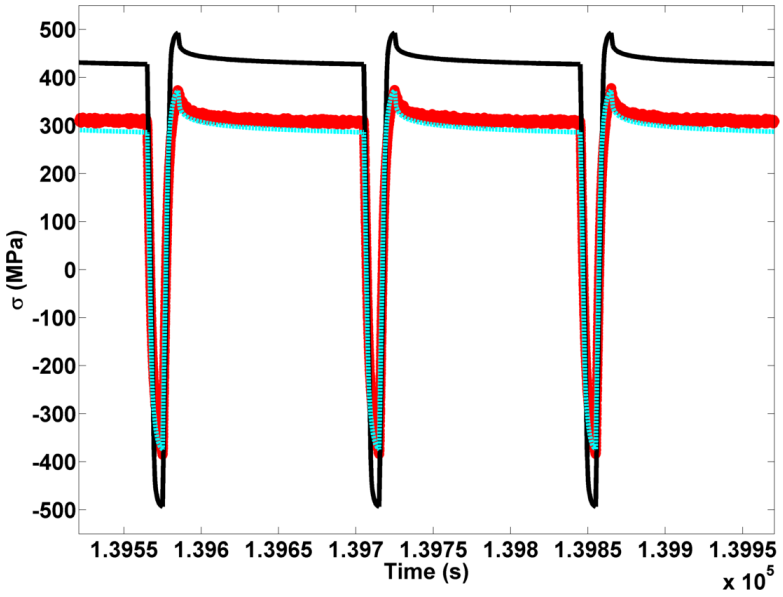

(b)

Figure 3.50: The prediction of (a) the 1000^{th} hysteresis loop and (b) the stress relaxation region for the 1000^{th} loading cycle for a P91 steel at 400°C due to a relaxation type loading profile, showing the behaviour predicted by the initial estimates of material constants and the optimised values.

3.9.6 316 Stainless Steel Results

The results of a combined parallel optimisation using cleaned experiential data for a 316 steel at 600°C are presented below. The prediction of stress range ($\Delta\sigma/2$) versus load cycle number N is presented for both saw tooth and relaxation type load profile in figures 3.51 and 3.55, respectively. Hysteresis loops for the 1^{st}, 300^{th} and 600^{th} load cycles are also presented to show the quality of fit for hardening curves. These plots are

provided for saw tooth (figures 3.52 to 3.54) and relaxation (figures 3.56 to 3.58) type load profiles. Relaxation figures also include plots of stress relaxation regions for the same load cycles, verifying the prediction of creep dominated behaviour.

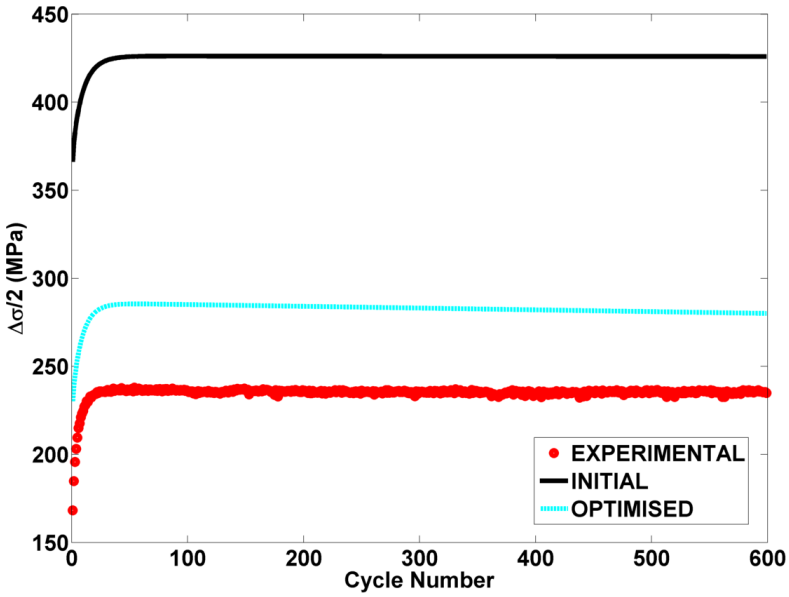

Figure 3.51: The prediction of the evolution of stress range ($\Delta\sigma/2$) for a 316 steel at 600°C due to a saw tooth type loading profile, showing the behaviour predicted by the initial estimates of material constants and the optimised values.

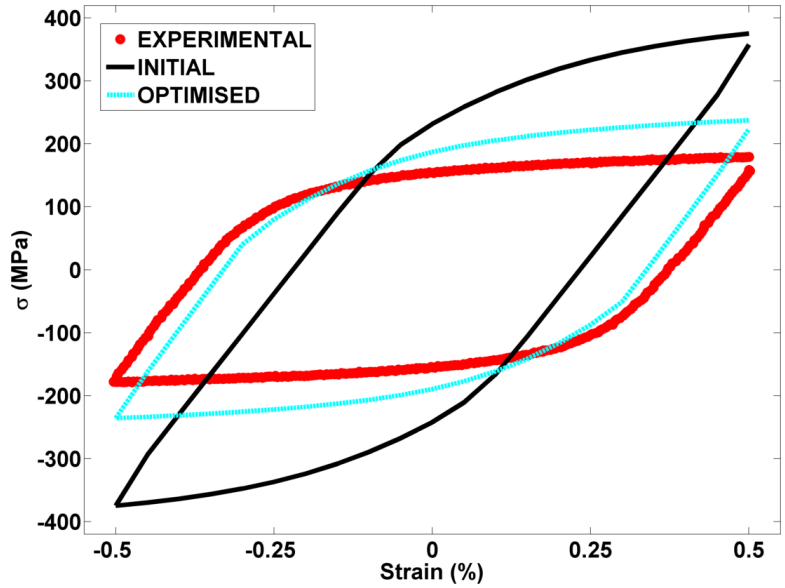

Figure 3.52: The prediction of the 1^{st} hysteresis loop for a 316 steel at 600°C due to a saw tooth type loading profile, showing the behaviour predicted by the initial estimates of material constants and the optimised values.

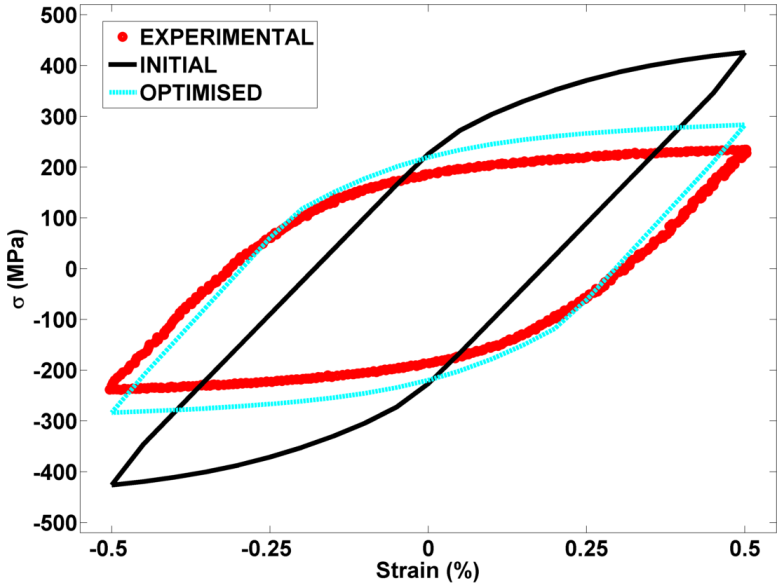

Figure 3.53: The prediction of the 300^{th} hysteresis loop for a 316 steel at 600°C due to a saw tooth type loading profile, showing the behaviour predicted by the initial estimates of material constants and the optimised values.

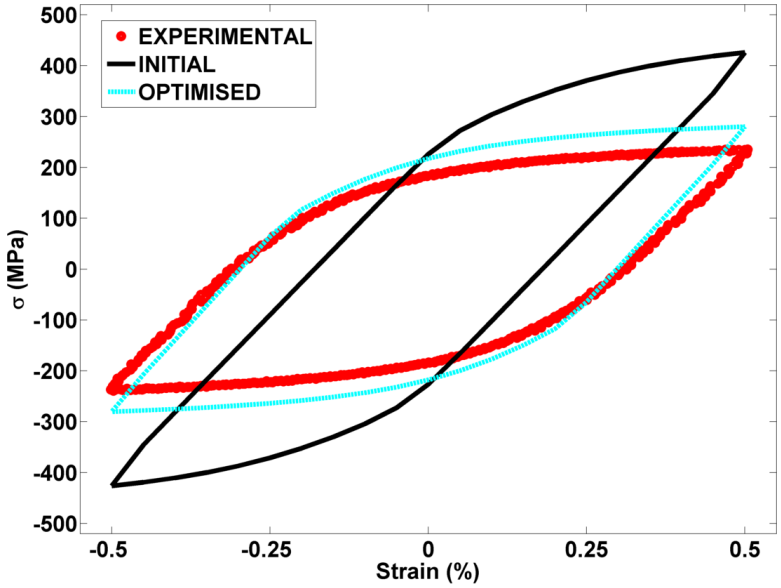

Figure 3.54: The prediction of the 600^{th} hysteresis loop for a 316 steel at 600°C due to a saw tooth type loading profile, showing the behaviour predicted by the initial estimates of material constants and the optimised values.

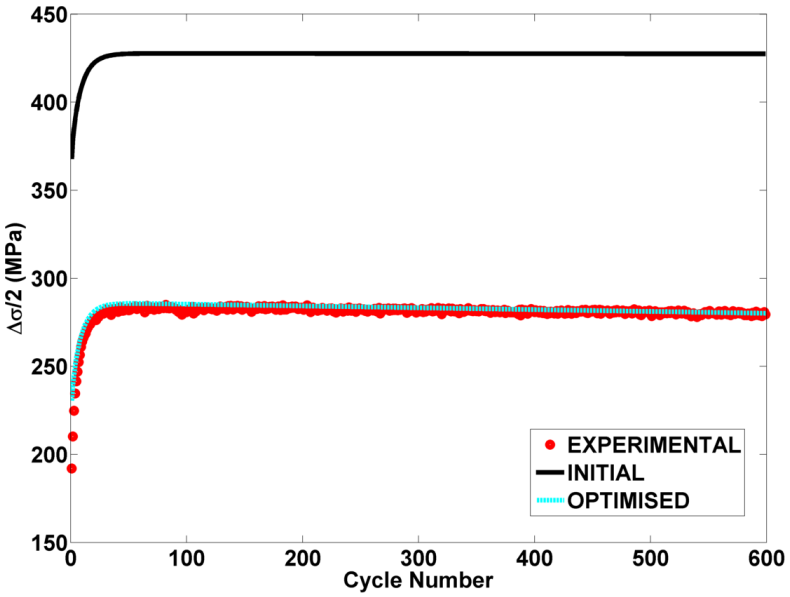

Figure 3.55: The prediction of the evolution of stress range ($\Delta\sigma/2$) for a 316 steel at 600°C due to a relaxation type loading profile, showing the behaviour predicted by the initial estimates of material constants and the optimised values.

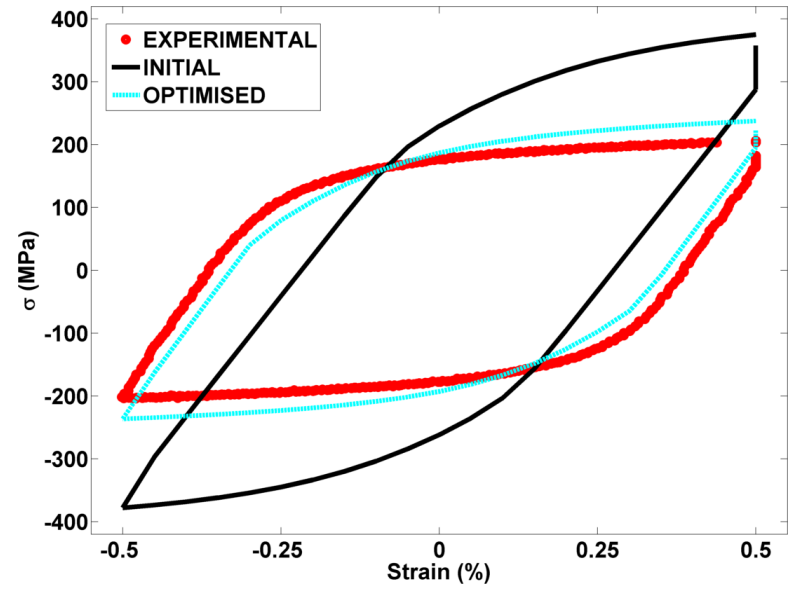

(a)

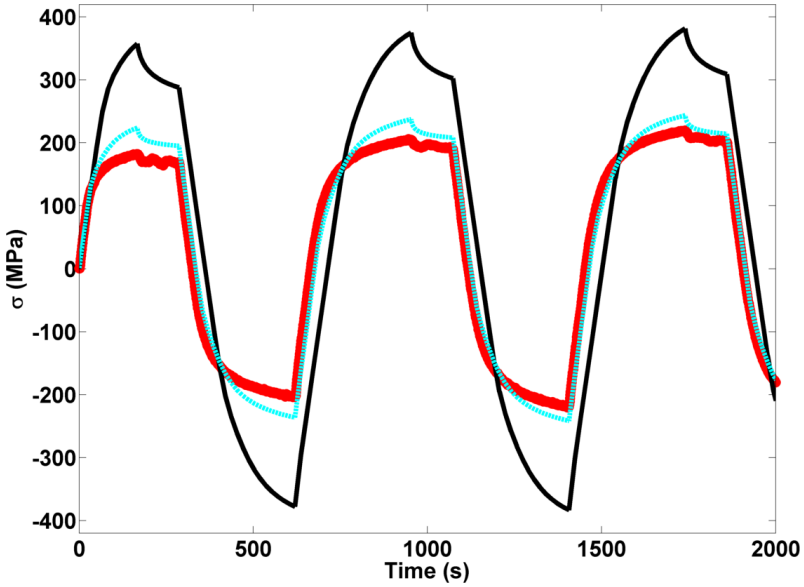

(b)

Figure 3.56: The prediction of (a) the 1^{st} hysteresis loop and (b) the stress relaxation region for the 1^{st} loading cycle for a 316 steel at 600°C due to a relaxation type loading profile, showing the behaviour predicted by the initial estimates of material constants and the optimised values.

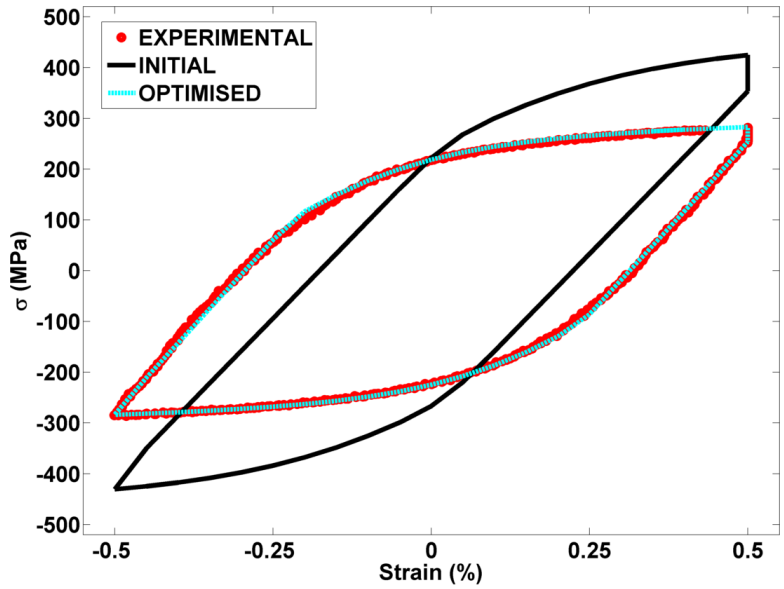

(a)

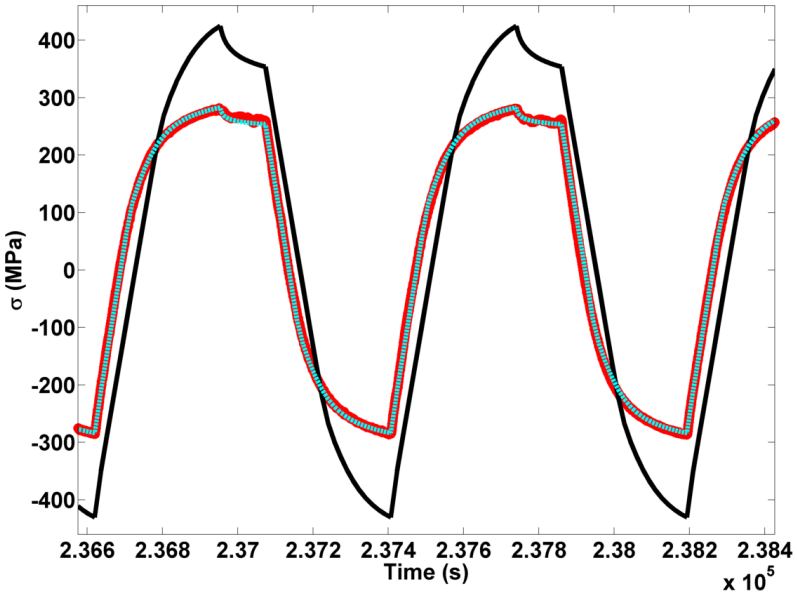

(b)

Figure 3.57: The prediction of (a) the 300^{th} hysteresis loop and (b) the stress relaxation region for the 300^{th} loading cycle for a 316 steel at 600°C due to a relaxation type loading profile, showing the behaviour predicted by the initial estimates of material constants and the optimised values.

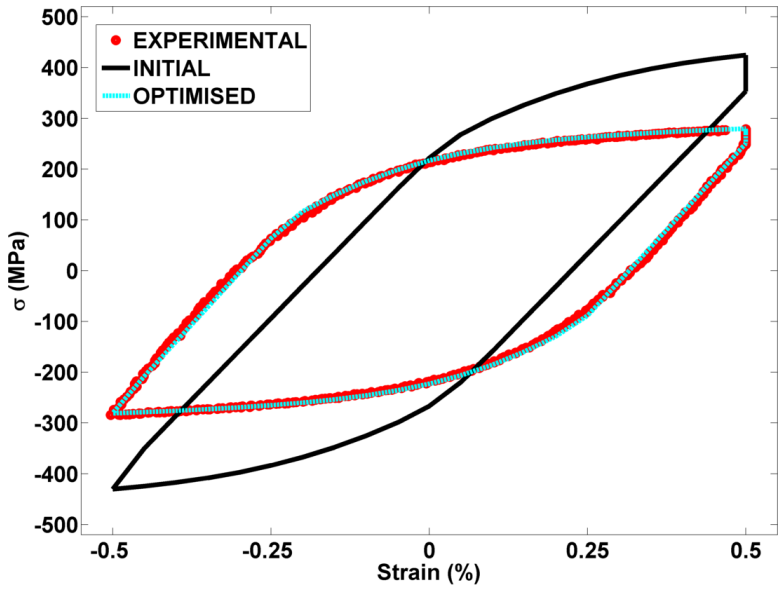

(a)

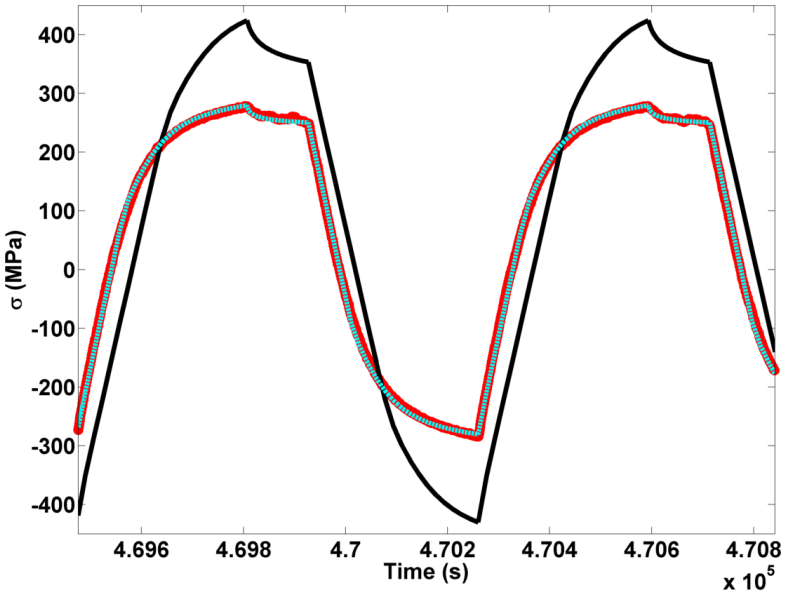

(b)

Figure 3.58: The prediction of (a) the 600^{th} hysteresis loop and (b) the stress relaxation region for the 600^{th} loading cycle for a 316 steel at 600°C due to a relaxation type loading profile, showing the behaviour predicted by the initial estimates of material constants and the optimised values.

3.10 Conclusions

The objective of this chapter was to develop a robust method to optimise the material constants for the Chaboche unified visoc-plasticity model. This would allow future cyclic analyses of high temperature components to be completed with confidence. Through several investigations, a procedure that conducts combined parallel optimisation (utilising all available experimental data) on cleaned experimental data has been shown

to be the most robust. This procedure enforces the suitable level of constraint on the material constant optimisation, ensuring that a single set of representative material constant values are achieved in a reasonable amount of time. Cleaning the data prior to the optimisation reduces the likelihood of encountering numerical problems as a result of inaccurate load cycle definition. In section 3.9 it has been shown that using this optimisation strategy results in a significantly improved prediction of experimental data (compared to predictions using the initial estimates of material constants). Generally, cyclic hardening behaviour and periods of creep relaxation are predicted with excellent accuracy, however several anomalies have been noted and will be addressed.

Commonly, stress relaxation in the first cycles (see figure 3.32 (b), for example) of data is not accurately predicted. Stress relaxation prediction improves greatly for later cycles however. Although the quality of fit in the first load cycle is not as relevant to practical problems as predicting later load cycles (components are not likely to fail after one load cycle), it is important to address the potential shortcomings of the presented Chaboche model. The difficulties in predicting creep behaviour for cyclically loaded specimens have been noted previously by Tong and Vermeulen[100] and by Zhan and Tong[102,103]; who suggested that the poor creep prediction may be due to neglecting static/time recovery effects in the Chaboche model[100]. A modification (applied to the kinematic hardening law) was suggested that appeared to address this deficiency[101–103], however this explanation does not suggest why creep behaviour is predicted with a greater degree of accuracy in the later cycles. Potentially, the viscous stress term is sufficient to describe the creep response for the hold period considered in these experiments, however the material has undergone microstructural changes after cycling, therefore the creep response for the first and last cycle cannot be explained by a single set of material constants. A compromise is made in the optimisation procedure to accurately predict the greatest number of stress relaxation branches as possible, thus sacrificing the quality of the fit of the stress relaxation branches for the initial cycles. Future work will look to address these discrepancies.

In some cases (such as P91 at 500°C and the 316 data) a large discrepancy is observed for the prediction of the stress range evolution with load cycle for the saw tooth type data that is not seen in the same plot for relaxation type data (for example, see figures 3.51 and 3.55, respectively). The excellent fitting quality observed for stress range evolution in the relaxation data and for the hardening cycles in general suggests that the optimisation has been successful in determining the most representative material constant values for the material at the specific temperature. Error sources in the experimental procedure may however result in two sets of experimental data that cannot be predicted by a single set of material constants. In addition to slight material composition variations and fluctuations in the testing temperature and loading strain values, a source of error that could contribute to discrepancies in stress fitting was proposed by Lin et al.[189,190] and relates to the cyclic specimen design. It is assumed that the "uniaxial" specimens

used in cyclic testing are subject to uniaxial stress and strain fields, however this may not be the case. Ridges for the extensometer arms and blending radii at the top of the specimen, together with a short specimen length (used to avoid buckling in reverse loading) have been shown to cause constraint in the specimen which induces multiaxial stress and strain fields[189,190]. Actual strain levels in some regions of the specimen may be $\pm$20% of the value inferred from the extensometer. This phenomenon would cause localised hardening, distorting the stress readings as a result. Such effects may be more pronounced in cases where necking and failure occurs closer to the extensometer ridges and should be considered when analysing the fitting quality of results from optimisation procedures.

A single testing condition was considered in the present work. The Chaboche model implemented does not include strain rate, strain range or temperature effects, therefore the material constants derived cannot be applied to other testing conditions (although limited extrapolation may be possible in a range that does not change the controlling deformation mechanism). Some success has been achieved in the past by interpolating material constant values for different loading conditions (e.g. temperature); however future work will look to expand the applicability of the Chaboche model. The optimisation procedure detailed in the present work can then be implemented with confidence in order to determine related material constants, allowing for more complex and more accurate component analyses (such as full thermo-mechanical fatigue, TMF) to be conducted.

Chapter 4

A Comparative Assessment of Several Creep Damage Models in the Life Prediction of Power Plant Components

4.1 Introduction

The accurate prediction of creep life is of great importance for the structural integrity of many high temperature components (such as those used in power generation plant) if safe, efficient and economic operation is to be achieved. Furthermore, in some high temperature applications such as aero engine design, a limiting strain due to design constraints may be present; indicating that predicted values of plastic and creep strain would also be useful to the practising engineer. Continuum damage mechanics (CDM) can be used in conjunction with FEA to provide a fundamental step in modelling creep failure. Material constants used in these models however are often derived from accelerated creep rupture test data, performed using higher stresses and/or temperatures than would normally be experienced by real world components.

In this chapter, the results of a comparative assessment of extrapolated (i.e. outside the original test stress range) failure times for several creep damage models are presented. This study has been undertaken for uniaxial, notched bar, closed end straight pipe section and idealised pipe bend geometries (note the pipe geometry was typical of that used in power generation). Material constants for each model were determined using creep rupture tests performed on a P91 based reference steel (BAR 257) under uniaxial loading conditions and using notched bar samples to introduce multiaxial stress states.

The material models considered in the present chapter are the Kachanov[53,55] and Liu-Murakami[62] power law models and the Dyson sinh model[65,66]. A review of the multiaxial form of these models is given in section 2.3.3.

4.2 Determination of Material Constants

Before the application of any material model, representative material constants must be determined from experimental data. For creep damage models, isothermal uniaxial constant load creep rupture tests (see figure 4.1 (a)) are completed for a range of creep stresses in order to determine uniaxial material constants. Values for multiaxial material constants (such as α in the Kachanov and Liu-Murakami models[53,55,62]) may be determined from notched bar tests (see figure 4.1 (b)) once the uniaxial constant values have been found.

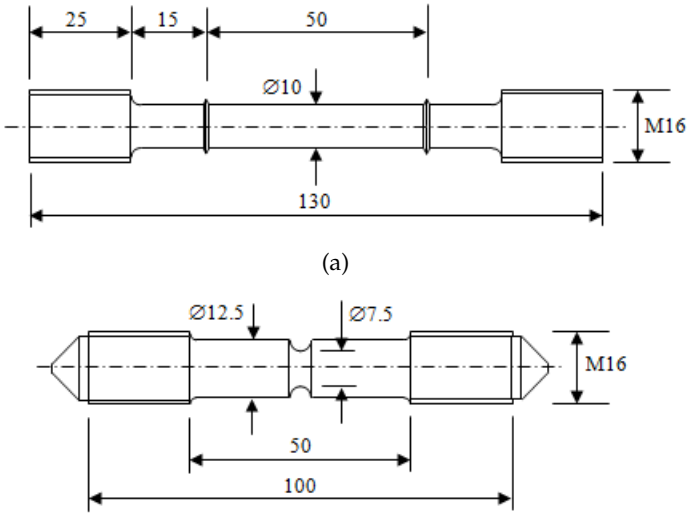

Figure 4.1: Schematics of (a) the uniaxial and (b) the notched bar specimens used for the determination of material constants for creep models.

In practice, only initial estimates of the model's material constants are determined directly from experimental data. These initial estimates are then fine tuned using an optimisation procedure; fitting the predicted behaviour of a material model to the true experiential response. An overview of several optimisation algorithms is given is section 2.6. Additionally, several key factors in applying an optimisation procedure to experimental data have been addressed in chapter 3 for a material model that is significantly more complex than the creep models described in the present chapter. The optimisation procedures described in these two sections may be applied to any of the creep models discussed in the present chapter.

An optimisation iteration (i.e. an instantaneous solution for the optimum set of material constants) is based on the evaluation of an objective function. For the optimisation of creep material parameters the objective function may take the form of equation (4.1), where M_1 is the number of creep tests performed and M_2 is the number of data points for the i^{th} creep curve. Experimental and predicted strain values (ε_j^{exp}

and $\varepsilon_j^{pre}(\boldsymbol{x})$, respectively, where $\boldsymbol{x}$ is a set of material constants) are compared for each data point in each creep curve. Predicted and experimental times to failure ($t_{f\,i}^{pre}$ and $t_{f\,i}^{exp}$, respectively) are also compared by using the weighting value w_i to ensure that times and strains are are accounted for with similar magnitudes.

$$F(x) = \sum_{i=1}^{M_1} \left\{ \left[\sum_{j=1}^{M_2} \left(\varepsilon_j^{pre}(\boldsymbol{x}) - \varepsilon_j^{exp} \right)^2 \right]_i + w_i \frac{\left| t_{f\,i}^{pre}(\boldsymbol{x}) - t_{f\,i}^{exp} \right|}{t_{f\,i}^{exp}} \right\} \rightarrow \min \tag{4.1}$$

4.2.1 Experimental Procedure

Creep testing has been completed using a Mayes ESM 250 tensile testing machine (see figure 4.2). During a creep test a constant load is applied by a servo hydraulic load actuator. Temperature uniformity was confirmed by monitoring thermocouples that were attached at the top, middle and bottom of the 3 region Mayes $3kW$ furnace. Variations in temperatures along gauge length were within $\pm 1°C$ and the temperatures were held constant to within $\pm 1°C$. Specimen elongation as a result of creep strain is measured by through extensometer arms attached to ridges on the specimen and a linear variable differential transformer (LVDT). A National Instruments USB-6210 data logging system was used to record the temperature and extensometer readings at regular intervals.

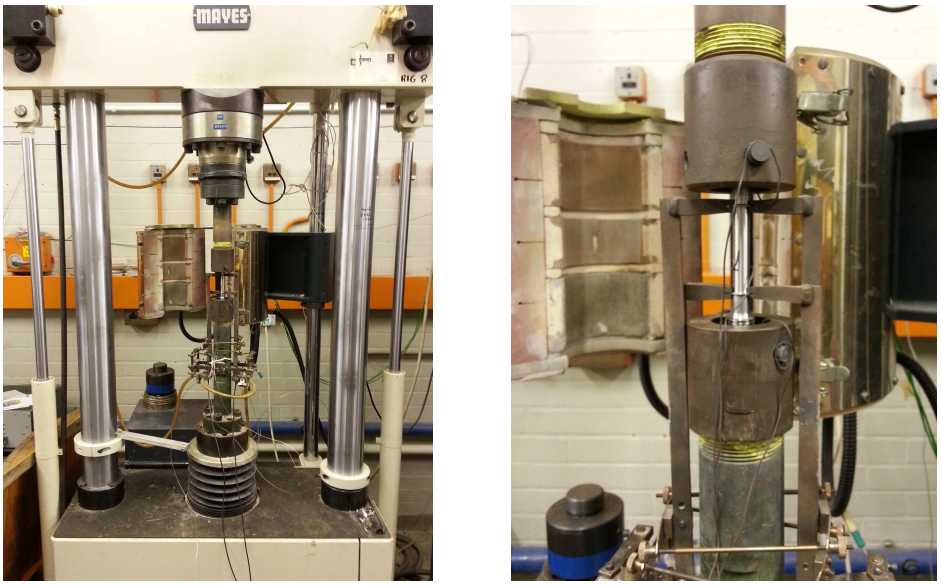

(a) (b)

Figure 4.2: Photos of the Mayes ESM 250 tensile testing machine, showing (a) an overview of the experimental set-up and (b) a close up of the specimen with extensometer arms and thermocouples attached.

4.2.2 Initial Estimates of the Kachanov Damage Law Material Constants

Uniaxial equations for the creep strain rate ($\dot{\varepsilon}_c$) and damage rate ($\dot{\omega}$) can be derived from the generalised multiaxial form of Kachanov's model (equations (2.50) and (2.51), respectively) by noting that, under uniaxial conditions, $S_{ij} = \sigma_{EQ} = \sigma_R = \sigma$. The uniaxial equations, which will be used to predict the results of uniaxial experiments in order to determine material parameters, are given in equations (4.2) and (4.3) for $\dot{\varepsilon}_c$ and $\dot{\omega}$, respectively. Initial estimates of material parameters are determined by manipulating these expressions for specialised conditions and correlating them to regions of the experimental creep curves[64,67,180].

$$\dot{\varepsilon}_c = A \left(\frac{\sigma}{1-\omega} \right)^n t^m \tag{4.2}$$

$$\dot{\omega} = B \left(\frac{\sigma^\chi}{(1-\omega)^\phi} \right) t^m \tag{4.3}$$

Material constants that describe secondary creep (A and n) are determined by considering the minimum creep strain rate ($\dot{\varepsilon}_{c\,min}$) from experiments for several creep stresses. Assuming that damage only accumulates during tertiary creep and neglecting primary creep effects ($m = 0$), equation (4.2) may be simplified to Norton's law ($\dot{\varepsilon}_{c\,min} = A\sigma^n$, see equation (2.47)). A linear relationship may in turn be developed from this expression, as shown in equation (4.4). Plotting $\log(\sigma)$ versus $\log(\dot{\varepsilon}_{c\,min})$ therefore yields a line with a gradient equal to n and an intercept of $\log A$ (see figure 4.3 for an example of this plot for tests conducted on a P91 steel at 600°C).

$$\log\left(\dot{\varepsilon}_{c\,min}\right) = n\log(\sigma) + \log(A) \tag{4.4}$$

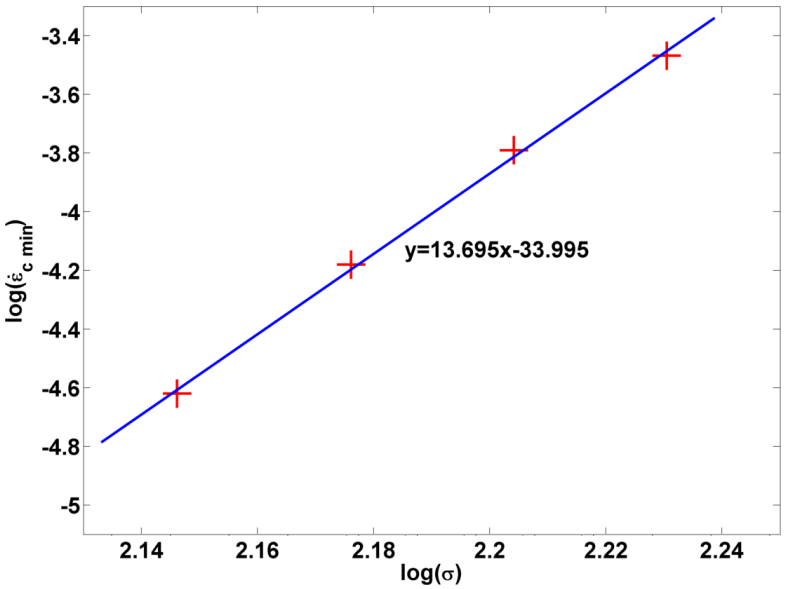

Figure 4.3: An example plot of $\log(\sigma)$ versus $\log(\dot{\varepsilon}_{c\ min})$, showing a linear relationship for a P91 steel at 600°C (where stresses are reported in MPa and minimum creep strain rates are given in $\%/s$).

The estimation of material constants that describe tertiary creep behaviour is dependent on the integration of equation (4.3). Equation (4.5) shows a general solution for this integration with the upper limits t and ω (i.e. the specimen has a damage ω at time t).

$$\begin{aligned} \int_0^{\omega} (1-\omega)^{\phi}\, d\omega &= \int_0^{t} B\sigma^{\chi} dt \\ \left[\frac{-(1-\omega)^{\phi+1}}{\phi+1}\right]_0^{\omega} &= \left[B\sigma^{\chi} t\right]_0^{t} \end{aligned} \tag{4.5}$$

A special condition of equation (4.5) is the point of failure, when $t = t_f$ and $\omega = 1$[15]. An expression for t_f is given in equation (4.6). By making the substitution $M = B(\phi+1)$ and taking logarithms, the linear expression shown in equation (4.7) can be derived. The line resulting from the plot $\log(\sigma)$ versus $\log\left(t_f\right)$ therefore has the gradient $-\chi$ and the intercept $\log\left(\frac{1}{M}\right)$ (an example of this plot can be seen in figure 4.4). By assuming that $\phi \approx \chi$, B may be determined from the definition of M.

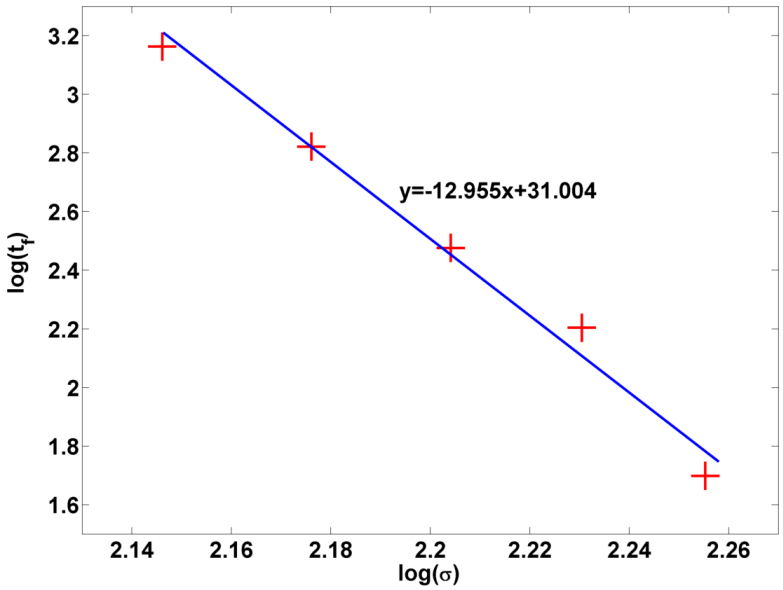

Figure 4.4: An example plot of $\log(\sigma)$ versus $\log\left(t_f\right)$, showing a linear relationship for a P91 steel at 600°C (where stresses are reported in MPa and times to failure are given in hours).

$$t_f = \left(\frac{1+m}{B(1+\phi)\sigma^{\chi}}\right)^{\frac{1}{m+1}} \approx \frac{1}{B(1+\phi)\sigma^{\chi}} \tag{4.6}$$

$$\log\left(t_f\right) = -\chi\log(\sigma) + \log\left(\frac{1}{M}\right) \tag{4.7}$$

If equation (4.5) is evaluated for the limits t and ω, an expression for damage at the time t may be found (see equation (4.8)). This may in turn be substituted into an integration of equation (4.2) (with the limits t and ε_c) to give an expression for ε_c at time t (equation (4.9)). Solving this equation is useful in an optimisation procedure as it avoids the computational expensive process of solving differential equations.

$$\omega = 1 - \left[1 - B\left(\phi+1\right)\sigma^{\chi}t\right]^{\frac{1}{\phi+1}} \tag{4.8}$$

$$\varepsilon_c = \frac{A\sigma^{(n-\chi)}}{B(n-\phi-1)}\left(\left[1 - \frac{B(1+\phi)\sigma^{\chi}t^{1+m}}{1+m}\right]^{\frac{\phi+1-n}{\phi+1}} - 1\right) \tag{4.9}$$

4.2.3 Initial Estimates of the Liu-Murakami Damage Law Material Constants

A procedure similar to that used to determine the initial estimates of the Kachanov material constants (see section 4.2.2) may be used to estimate the values of the Liu-

Murakami model constants. Uniaxial forms of the strain rate and damage rate equations for this model are given in equations (4.10) and (4.11), respectively[61,62]. Note that, if damage is neglected, equation (4.10) simplifies to Norton's law therefore the same procedure used to determine A and n described in section 4.2.2 may be used here.

$$\dot{\varepsilon}_c = A\sigma^n \exp\left[\frac{2(n+1)}{\pi\sqrt{1+(3/n)}}\omega^{3/2}\right] \tag{4.10}$$

$$\dot{\omega} = \frac{B\left[1-e^{-q_2}\right]}{q_2}\sigma^p e^{(q_2\omega)} \tag{4.11}$$

Considering the substitution shown in equation (4.12) (which for a particular creep stress will be constant) the integral shown in equation (4.13) may be constructed from equation (4.11).

$$\Omega = \frac{B\left[1-e^{-q_2}\right]}{q_2}\sigma^p \tag{4.12}$$

$$\int_0^1 e^{-q_2\omega} d\omega = \Omega \int_0^{t_f} dt \tag{4.13}$$

Evaluating equation (4.13) yields an expression for time to failure (t_f), shown in equation (4.14)[61,62]. A linear relationship may then be found by taking logarithms of this expression (see equation (4.15)). Plotting $\log(\sigma)$ versus $\log(t_f)$ for the experimental data therefore allows for the approximation of $-p$ (from the plot's gradient) and $\log\left(\frac{1}{B}\right)$ (from the plot's intercept). Commonly, it is assumed that $q_2 \approx p$ to determine the remaining material constants.

$$t_f = \frac{1}{\Omega}\frac{1-e^{-q_2}}{q_2} = \frac{\sigma^{-p}}{B} \tag{4.14}$$

$$\log t_f = -p\log(\sigma) + \log\left(\frac{1}{B}\right) \tag{4.15}$$

It is worth pointing out that the uniaxial Liu-Murakami model may be expressed by a single equation if the integral shown in equation (4.13) is modified to include the upper limits t and ω. This yields an expression for the damage at time t (equation (4.16)), which may be substituted into equation (4.10) to give equation (4.17).

$$\omega = \frac{\ln\left(1-\Omega q_2 t\right)}{q_2} \tag{4.16}$$

$$\dot{\varepsilon}_c = A\sigma^n \exp\left[\frac{2(n+1)}{\pi\sqrt{1+(3/n)}}\left(\frac{\ln\left(1-\Omega q_2 t\right)}{q_2}\right)^{3/2}\right] \tag{4.17}$$

4.2.4 Initial Estimates of the Dyson Damage Law Material Constants

Dyson's sinh law uses several internal variables to predict a material's creep behaviour, as opposed to the single damage variable ω used in the Kachanov and Liu-Murakami models. From the multiaxial form of Dyson's equations (see equations (2.56) to (2.59)), a uniaxial expression for the creep strain rate ($\dot{\varepsilon}_c$) can be derived (shown in equation (4.18)). This is based on the evolution of a hardening variable (H, see equation (4.19)) that allows for the description of primary creep and two damage variables that describe ageing (ϕ, see equation (4.20)) and the formation of creep cavities (ω_2, see equation (4.21)).

$$\dot{\varepsilon}_c = A \sinh \left\{ \frac{B\sigma(1-H)}{(1-\omega_2)(1-\phi)} \right\} \tag{4.18}$$

$$\dot{H} = \frac{h}{\sigma}\dot{\varepsilon}_c \left(1 - \frac{H}{\acute{H}}\right) \tag{4.19}$$

$$\dot{\phi} = \frac{K_c}{3}(1-\phi)^4 \tag{4.20}$$

$$\dot{\omega}_2 = DN\dot{\varepsilon}_c \tag{4.21}$$

Clearly, the sinh expression used for creep strain rate equation (see equation (4.18)) prevents it from being simplified to Norton's power law (as has been done for the Kachanov and Liu-Murakami models). Instead, to consider secondary creep, the saturated condition of the hardening variable H must be determined ($H = \acute{H}$). Applying this condition and removing damage terms from equation (4.18) allows equation (4.22) to be derived for the minimum creep strain rate $\dot{\varepsilon}_{c\,min}$ (note $\acute{B} = B(1-\acute{H})$). By recalling the definition of sinh in terms of exponentials ($\sinh(x) = (e^x - e^{-x})/2$), a linear expression may be derived (see equation (4.23)) to determine the constants A and $\acute{B}$ from a plot of σ versus $\ln(2\dot{\varepsilon}_{c\,min})$.

$$\dot{\varepsilon}_{c\,min} = A \sinh\left(B\sigma(1-\acute{H})\right) = A \sinh\left(\acute{B}\sigma\right) \tag{4.22}$$

$$\ln\left(2\dot{\varepsilon}_{c\,min}\right) = \ln A + \acute{B}\sigma \tag{4.23}$$

Integrating equation (4.19) with respect to H and t gives equation (4.24) (where $\varepsilon_{c\,p}$ is the creep strain at the end of primary creep). At the end of primary creep $H \to \acute{H}$, therefore values for the ratio $\dfrac{h}{\acute{H}}$ may be estimated for each experimental curve by assuming that $\dfrac{H}{\acute{H}} \approx 0.9999$. An average of the $\dfrac{h}{\acute{H}}$ values that have been calculated may then be assumed. Using the conditions defining $\dfrac{h}{\acute{H}}$ and $\acute{B}$, equations (4.19) and (4.25) are used to fit the primary creep regions and hence determine that values of h, $\acute{H}$ and B.

$$\frac{h}{\acute{H}} = -\left(\frac{\sigma}{\varepsilon_{c\,p}}\right)\ln\left(1-\frac{H}{\acute{H}}\right) \tag{4.24}$$

$$\dot{\varepsilon}_c = A\sinh\left\{B\sigma(1-H)\right\} \tag{4.25}$$

Equation (4.20) can be integrated to give equation (4.26) which, when substituted into a form of equation (4.18) that ignores the ω_2, is used to give equation (4.27). Rearranging the expression yields a linear function between $\left(\ln(2\dot{\varepsilon}_c/A)\right)^3$ and t. The slope of the this plot will be equal to $\left(B\sigma(1-\acute{H})\right)^3 K_c$ (note B and $\acute{H}$ have been calculated previously, therefore K_c may be estimated). Commonly, initial estimates of the damage material constant D in equation (4.21) are found by assuming $D \approx \dfrac{0.3}{\varepsilon_{c\,f}}$, where $\varepsilon_{c\,f}$ is the creep failure strain as a percentage[66].

$$(1-\phi) = (1+K_c t)^{-1/3} \tag{4.26}$$

$$\dot{\varepsilon}_c = A\sinh\left\{\frac{B\sigma(1-\acute{H})}{(1+K_c t)^{-1/3}}\right\} \tag{4.27}$$

4.2.5 Multiaxial Material Constant Determination

Multiaxial material properties (α in the Kachanov and Liu-Murakami models and ν in Dyson's model) are determined by matching the time to failure predicted by a set of material constants to an experimental value for a multiaxial loading case (note uniaxial material constants are determined using the procedures described in the previous sections and a suitable optimisation method). The most simplistic example of a multiaxial loading case is a notched bar.

Commonly, an experimental program will include at least two notched bar tests. Candidate multiaxial material constant values are tested using FEA simulations of a notched bar (a description of this model is given in section 4.3). These candidate values are selected to span a range defined either by the logical constraints of a constant ($0 \geq \alpha \geq 1$) or a commonly observed range ($0 \geq \nu \geq 15$). The times to failure predicted by the FEA simulations are interpolated to the experimental values to give the multiaxial constant value. A graphical representation of this procedure for the steel BAR 257 at 650°C can be seen in figure 4.5.

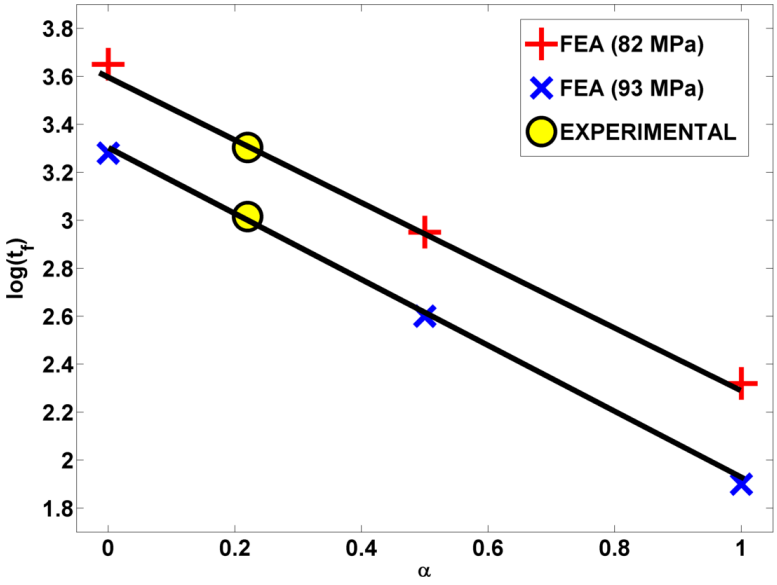

Figure 4.5: An example plot to show the determination of α by comparing failure times from FEA simulations of a notched bar to experimental values, shown for the steel BAR 257 at 650°C.

4.3 FEA Models

4.3.1 Notched Bar

After fitting to uniaxial data to find the majority of material constants, multiaxial material constants must be found by comparing FEA results of notched bar tests (using a range of multiaxial axial constant values) to experimental notched bar failure times. To perform this, a mesh must be created of the semi-circular Bridgeman[64] notched bar specimen (see figure 4.6) used for experimental testing. The mesh has been refined at the notch to better calculate the damage in this critical region and uses axi-symmetric reduced integration quadratic elements (designated CAX8R in the commercial FEA package ABAQUS[191]). Applied stresses (σ_{APP}) were back calculated to ensure that the mean axial stresses at the notch tip are the same as the mean stresses used in laboratory tests and comparable to the stresses used in uniaxial testing.

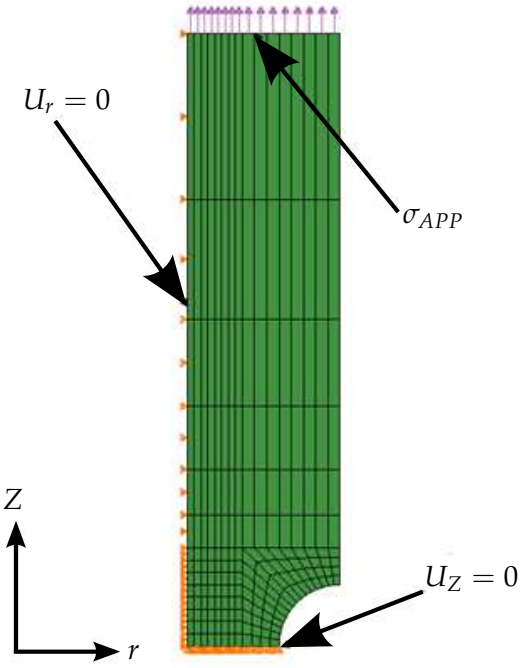

Figure 4.6: A notched bar FEA mesh (generated in ABAQUS[191]) used to determine multiaxial material constants in creep damage models. The applied pressure σ_{APP} is varied to control notch tip stresses.

4.3.2 Idealised Straight Pipe Section (Closed End)

Assuming closed end conditions[192] with no system loading (i.e. the only stresses present are primary and due to internal pressure), a straight pipe section may be greatly simplified to the mesh shown below in figure 4.7. The key pipe dimensions are considered to be the outside pipe radius R_O ($175mm$) and the inside radius R_I ($115mm$). Values were chosen to reflect in service power plant steam pipe dimensions. To maintain accurate boundary conditions, an axial load (σ_{AX}) was applied to represent the closed end with a constant displacement constraint. This load can be calculated from equation (4.28)[192].

$$\sigma_{AX} = \frac{P_i}{\left(\frac{R_O}{R_I}\right)^2 - 1} \tag{4.28}$$

where P_i is the internal pressure. The validity of the model was checked by comparing hoop stresses (σ_θ) found from analytical elastic and steady-state (i.e. after stress redistribution) creep solutions (see equation (2.104)) and the results of FEA simulations (using some arbitrary but practically viable value of the Norton's law stress exponent n, namely 4.5). A plot of this comparison can be seen in figure 4.8, and shows excellent agreement between the different solution methods. Again, axi-symmetric reduced integration quadratic elements were implemented (CAX8R in ABAQUS[191]).

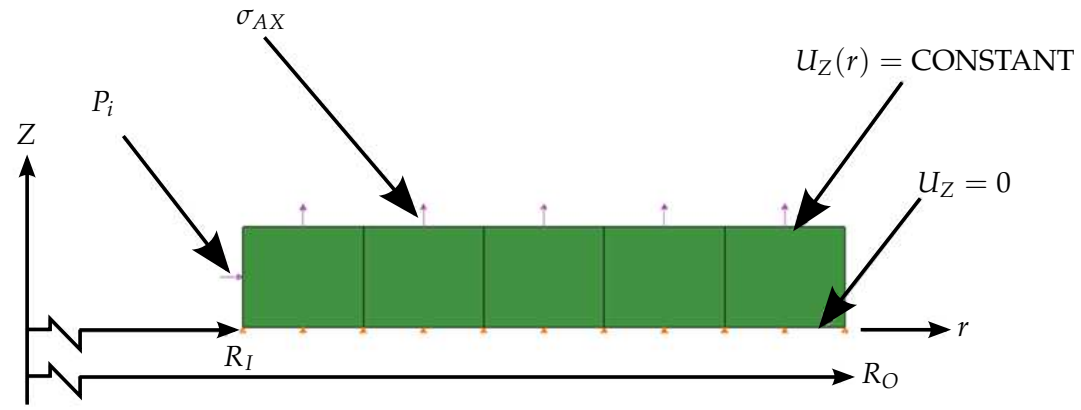

Figure 4.7: Example of a closed end straight pipe section mesh.

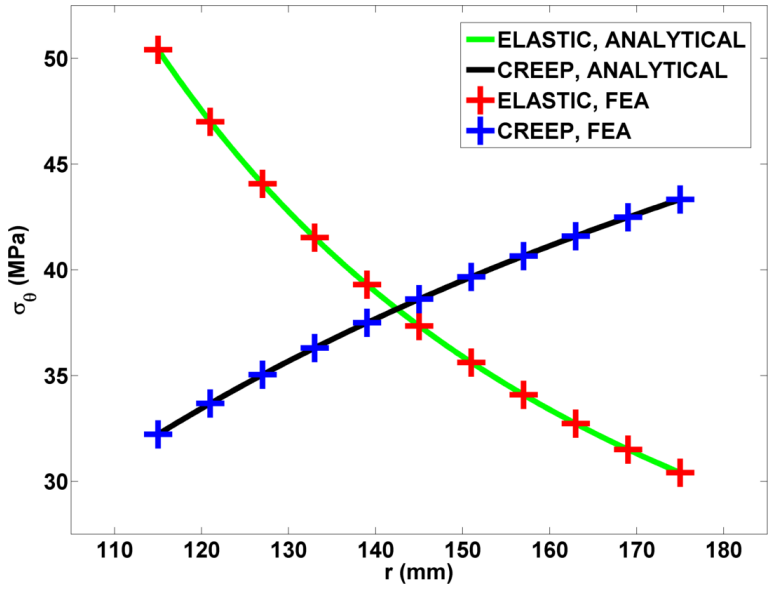

Figure 4.8: A comparison of analytical and FEA hoop stress (σ_θ) solutions for a closed end straight pipe model under steady state creep (using a Norton's law stress exponent of $n = 4.5$) and elastic conditions. The pipe section is loaded by an internal pressure of 20 MPa and has the dimensions $R_I = 115\ mm$ and $R_O = 175\ mm$.

4.3.3 Idealised Pipe Bend Section

Using the same pipe diameter and wall thickness as assumed for the straight pipe mesh, an idealised pipe bend model was created (see figure 4.9). Here it is assumed that no wall thinning and thickening (at the extrados and intrados respectively) is observed. It is important to note that, in practice, this variation will inevitably take place as a result of the pipe bend manufacturing process[104,139,193]. In addition to this, an initial ovality in the pipe cross section may be present[104,139,193]. For simplicity, these variations have been neglected. A discussion of these factors can be found in section 2.4.1.

Taking these geometric assumptions into account and realising that they enforce two planes of symmetry, the FEA problem can be greatly simplified by considering a quarter model[139]. It has been demonstrated that, given a free end condition and considering the symmetric plane cross section of the pipe (i.e. $\varphi = 45°$), a two dimensional analysis will show good agreement in both magnitude and location of maximum principal and von Mises equivalent stresses (noting that these are usually the stresses on which creep damage constitutive laws are dependent, see equation (2.52)) when compared with full three dimensional analyses[139]. Therefore, to greatly reduce computing time, the pipe bend has been approximated by a 2D axi-symmetric mesh, effectively portraying the pipe bend as a torus. Past research has shown that damage is localised to the intrados[193], i.e. when $\theta = 0$ (defined in figure 4.10). The mesh has therefore been refined in this area to aid in confirming failure location (see figure 4.10). The same elements were used as in the previous two meshes. Note that a bend radius, R_M, of $2m$ was assumed (this is a realistic value for industrial pipe bends). Research in the past has identified that the change in geometry of the pipe dimensions due to large deformation assumptions (as opposed to the near constant deformation assumptions usually implemented in FEA, known as small deformation assumptions), known as geometric non-linearity (GNL) will have an influence on stresses encountered in the pipe wall thickness after stress redistribution[104]. This usually has the effect of reducing life expectancy of a component, with strain and damage versus time curves generally having the same shape[104] as geometric linear (GL) simulations. The effect therefore is only to scale a failure time to a reduced value, meaning its inclusion or omission will have no effect on relative model performance. To keep computing time manageable, GNL has not been included in these analyses.

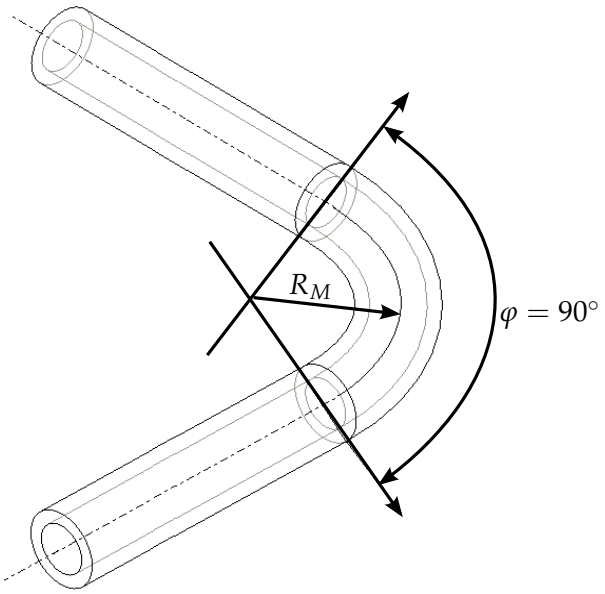

Figure 4.9: A three dimensional 90° pipe bend model.

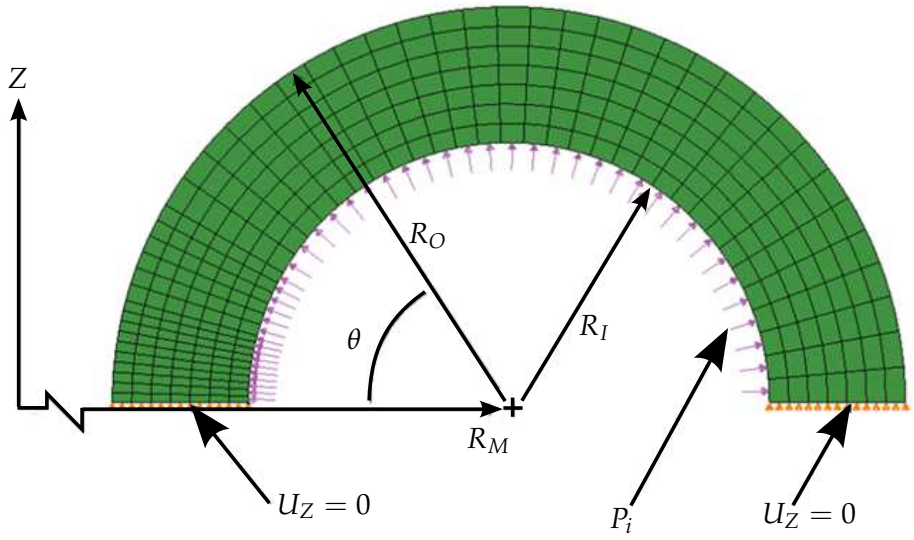

Figure 4.10: Example of idealised pipe bend ("torus") mesh.

4.4 Material Constant Values

4.4.1 BAR 257 Steel at 650°C

Constant stress uniaxial bar tests and notched bar tests, all at 650°C , were performed over a range of nominal stresses. BAR 257 is the designation given to a pipe reference material based on P91[64,67,104]. It is worth noting that this material has a far lower creep rupture stress than a P91 material[67] and was intended to be used as a reference material. The composition of this material is provided in table 4.1.

Table 4.1: Chemical composition (wt %) of the BAR 257 reference steel.

C	Mn	Si	N	Cr
0.11	0.36	Si	0.048	8.74
Mo	Ni	Cu	V	Fe
0.98	0.12	0.08	0.21	Balance

For uniaxial tests five applied stresses were used, namely 100, 93, 87, 82 and 70MPa (see figure 4.11), giving a maximum failure time of approximately 1010 hours and failure strains (ε_f) in the order of $30 - 40\%$ (results and information key to the determination of material constants has been summarised in table 4.2). Notched bar creep rupture tests were also completed to derive the multiaxial material constants, conducted at 93 and 82 MPa, giving failure times of 1037.2 hours and 2012.1 hours, respectively.

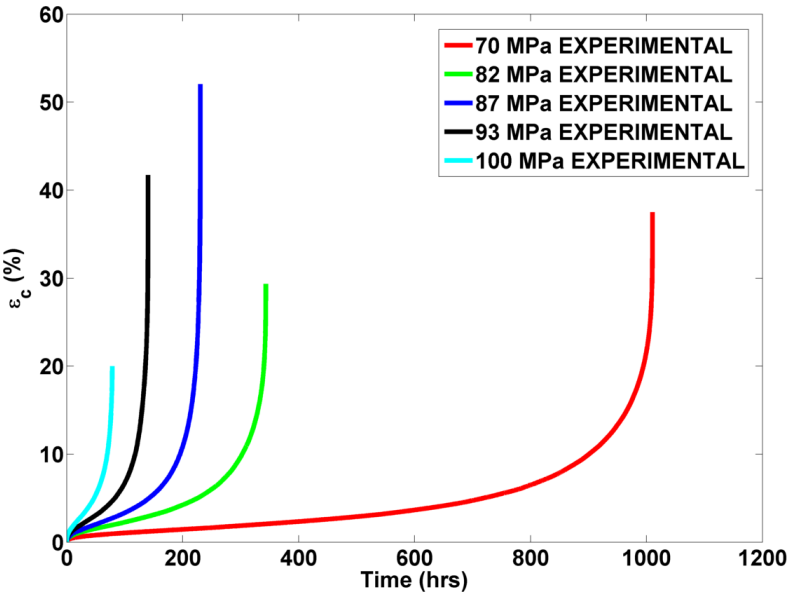

Figure 4.11: Uniaxial creep rupture test results for BAR 257 at 650°C.

Table 4.2: A summary of the results for uniaxial creep tests on BAR 257 at 650°C.

σ_{APP} (MPa)	t_f (hrs)	ε_f (%)	$\dot{\varepsilon}_{c\ min}$ (hr^{-1})	Time at End of Primary Creep (hrs)	Strain at End of Primary Creep (%)
100	78.60	20.00	$8.40x10^{-4}$	4.67	1.27
93	140.29	41.71	$4.12x10^{-4}$	5.99	1.04
87	230.60	52.04	$2.61x10^{-4}$	13.00	1.06
82	343.54	29.36	$6.61x10^{-5}$	25.47	1.15
70	1010.40	37.50	$2.05x10^{-5}$	34.47	0.71

The predicted creep strain curves for each model are presented below (figure 4.12 for Kachanov, figure 4.13 for Liu-Murakami and figure 4.14 (a) for Dyson's model). In the cases where primary creep has been isolated and fitted (i.e. the Dyson model), individual plots for primary creep strain have also been included (see figure 4.14 (b)), as this fitting can be difficult to observe over the full creep strain range. Care has been taken when optimising material constants to ensure that not only are primary creep strain values predicted but also that the strain hardening parameter (H, which controls primary creep) saturates at its maximum value ($\acute{H}$) at the end of primary creep. By fitting

the predicted response from the three models to the experimental data complete sets of uniaxial material constants may be derived. Multiaxial material constants are derived using the results of notched bar creep rupture tests. Full sets of material properties for the material BAR 257 at 650°C can be seen in tables 4.3 to 4.5 for the Kachanov, Liu-Murakami and Dyson material models, respectively.

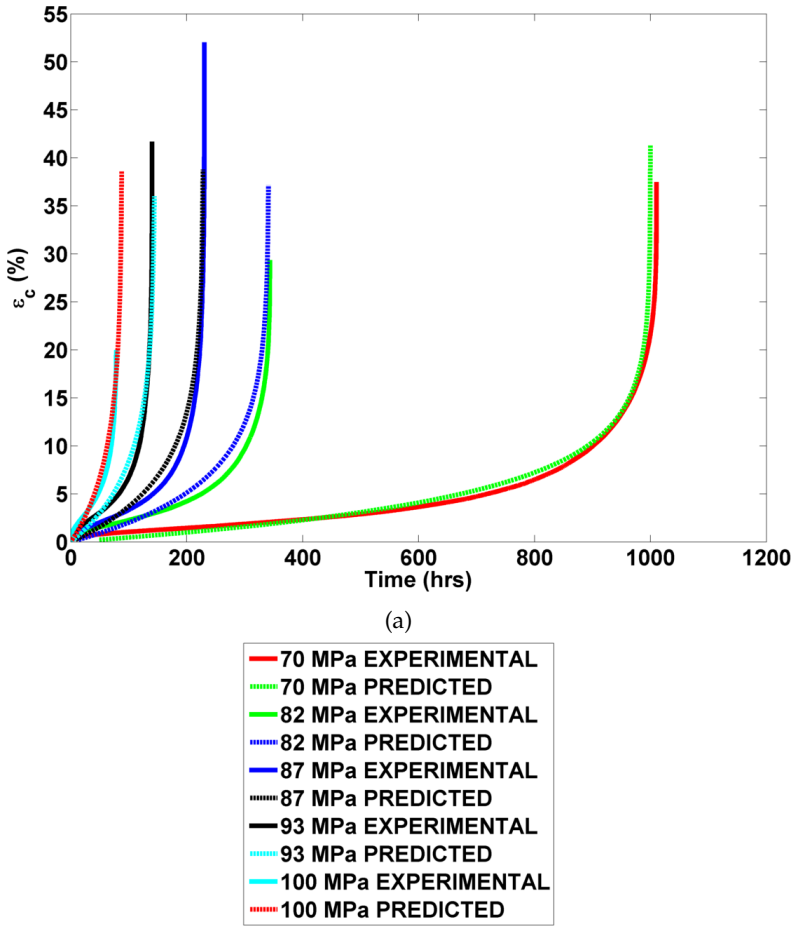

(a)

Figure 4.12: The prediction of BAR 257 (650°C) uniaxial creep tests using the Kachanov CDM model and the constants shown in table 4.3.

Table 4.3: A summary of the optimised material constants for BAR 257 at 650°C for the Kachanov creep damage model (where σ is given in terms of MPa, strains are given as a percentage and time is given in hours).

A	$1.09x10^{-20}$
B	$3.54x10^{-17}$
n	8.46
χ	6.79
ϕ	7.35
m	$-4.75x10^{-4}$
α	0.22

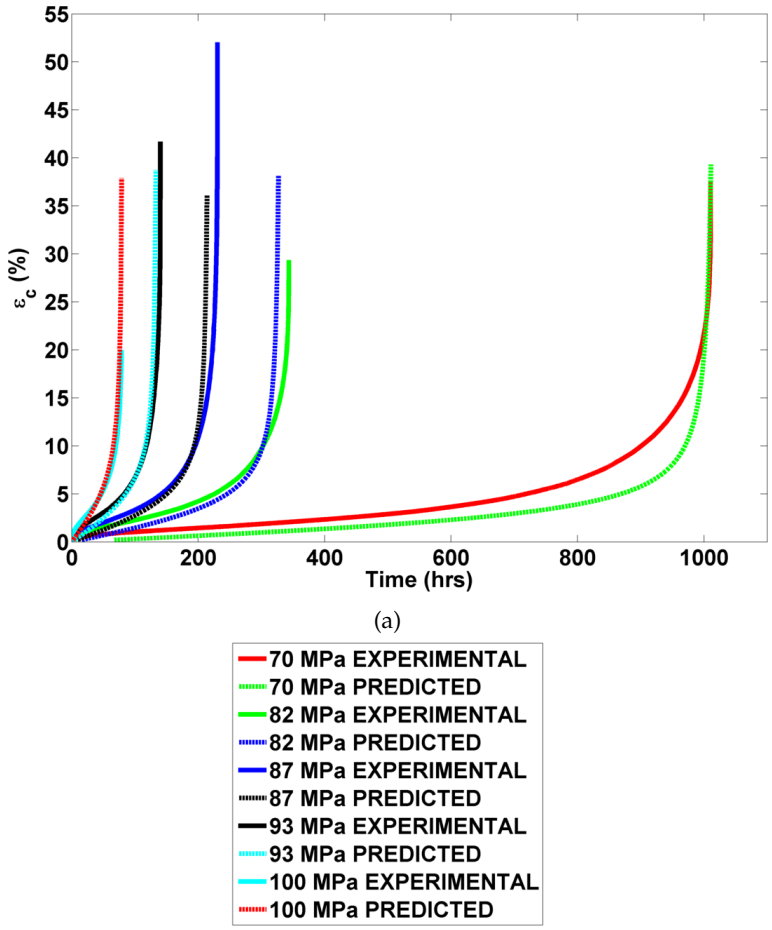

Figure 4.13: The prediction of BAR 257 (650°C) uniaxial creep tests using the Liu-Murakami CDM model and the constants shown in table 4.4.

Table 4.4: A summary of the optimised material constants for BAR 257 at 650°C for the Liu-Murakami creep damage model (where σ is given in terms of MPa, strains are given as a percentage and time is given in hours).

A	$1.09x10^{-20}$
B	$7.85x10^{-17}$
n	8.46
p	7.10
q_2	4.00
α	0.19

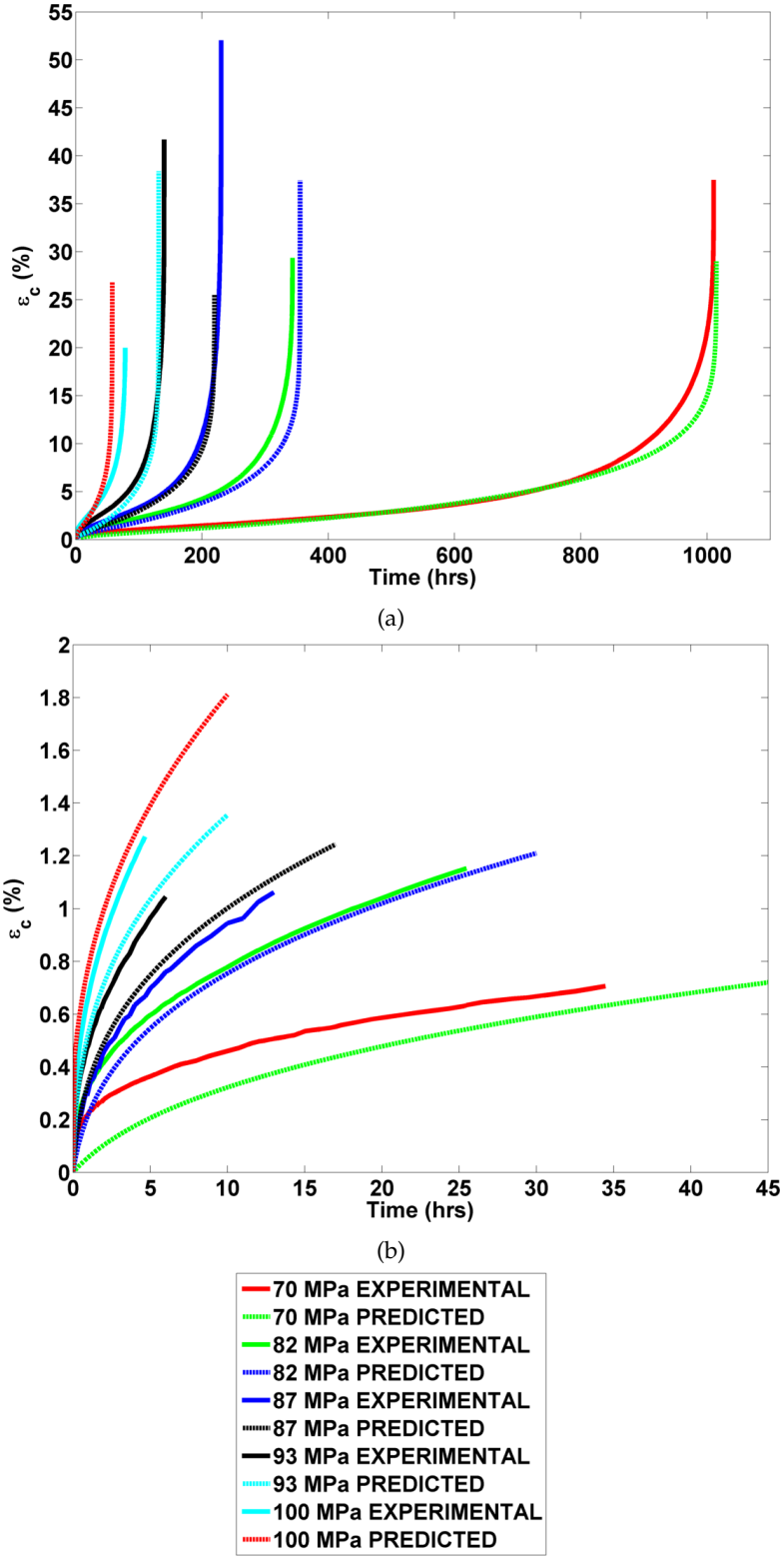

Figure 4.14: The prediction of BAR 257 (650°C) uniaxial creep tests using the Dyson CDM model and the constants shown in table 4.5. Plots show the prediction of (a) the full creep strain curve and (b) the primary creep region.

Table 4.5: A summary of the optimised material constants for BAR 257 at 650°C for the Dyson creep damage model (where σ is given in terms of MPa, strains are given as a percentage and time is given in hours).

A	$6.15x10^{-8}$
B	0.15
h	10100.00
$\acute{H}$	0.34
D	2.00
K_c	$5.00x10^{-4}$
ν	2.38

Using the LSQNONLIN MATLAB function, sets of material constants have been determined for the Kachanov, Liu-Murakami and Dyson creep damage models based on experimental data for the material BAR 257 at 650°C. The optimisation procedure often requires that a compromise is made between the fitting of individual creep curves (for example see figure 4.13). As no preferential treatment is given to a particular creep curve, it is reasoned that this compromise results in the most representative set of constants for the material. The derived material constant sets are used in the extrapolated stress simulations presented later in this chapter.

4.4.2 P91 Steel at 600°C

Failure times calculated for the material BAR 257 in the present work are generally of a relatively low order of magnitude (10,000 hours) at the lowest considered extrapolated stress level (approximately 25 MPa, a reasonable approximation of stresses induced by main steam pressure in power generation plant, see section 4.5.1). Actual components have been observed to have lives that can stretch to several hundred thousand hours when operating under more arduous, fluctuating conditions. This is explained by recalling that BAR 257 was designed only as a reference material[64], being made intentionally weak, and is not used in the manufacture of any real world components. The only experimental data available at time of writing for BAR 257 were the uniaxial and notched bar accelerated tests used to determine material constants, therefore it is not possible to compare extrapolated failure times to "real world" values and make a recommendation as to which CDM model to use in design and analysis problems. To address this and to demonstrate the applicability of this work to practically used materials, a P91 steel (composition given in table 4.6) at 600°C under extrapolated uniaxial creep conditions has been considered for the three models (Kachanov, Liu-Murakami and Dyson).

Table 4.6: Chemical composition (wt %) of P91 steel.

Cr	Mo	Mn	Si	Ni	V	C	Cu
8.49	0.978	0.43	0.37	0.32	0.2	0.11	0.07
Nb	Co	P	W	S	Ti	Al	Fe
0.06	0.02	0.014	< 0.02	0.008	< 0.002	< 0.001	Balance

Uniaxial creep rupture tests have been completed for a P91 steel at 600°C for a stress range of 180 to 140MPa. A summary of these tests can be seen in table 4.7, with a plot of the uniaxial creep curves in figure 4.15. Uniaxial material constants for the Kachanov, Liu-Murakami and Dyson models have been derived using the procedures described in section 4.2. Summaries of the optimised material constants and plots of the fitting to experimental uniaxial creep strain curves are given in tables 4.8 to 4.10 and figures 4.16 to 4.18 for Kachanov, Liu-Murakami and Dyson models, respectively.

Table 4.7: A summary of the results for uniaxial creep tests on P91 at 600°C.

σ_{APP} (MPa)	t_f (hrs)	ε_f (%)	$\dot{\varepsilon}_{c\,min}$ (hr^{-1})	Time at End of Primary Creep (hrs)	Strain at End of Primary Creep (%)
180	50	35.406	$1.03x10^{-3}$	2.75	0.85
170	160	30.406	$3.40x10^{-4}$	17.61	1.33
160	299	27.02	$1.62x10^{-4}$	31.88	1.35
150	663	30.15	$6.60x10^{-5}$	75.53	1.39
140	1454	29.23	$2.40x10^{-5}$	87.04	1.18

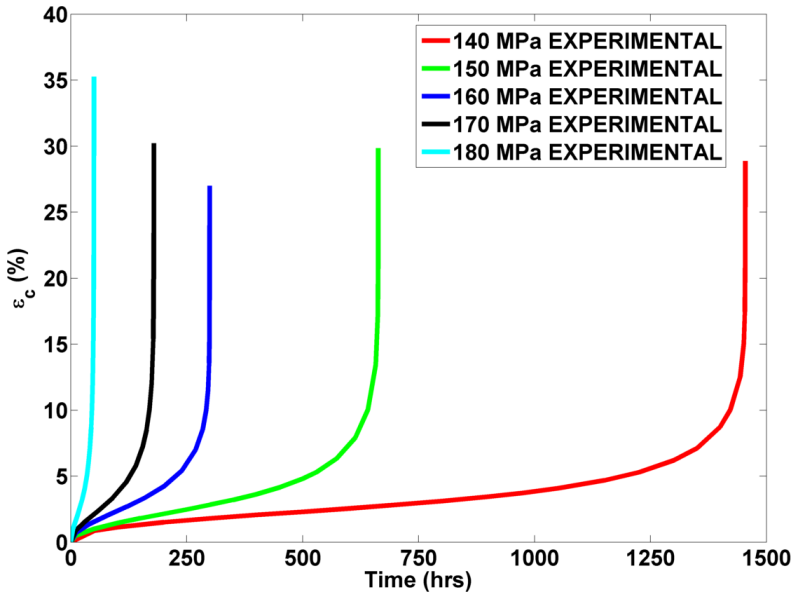

Figure 4.15: Uniaxial creep rupture test results for P91 at 600°C.

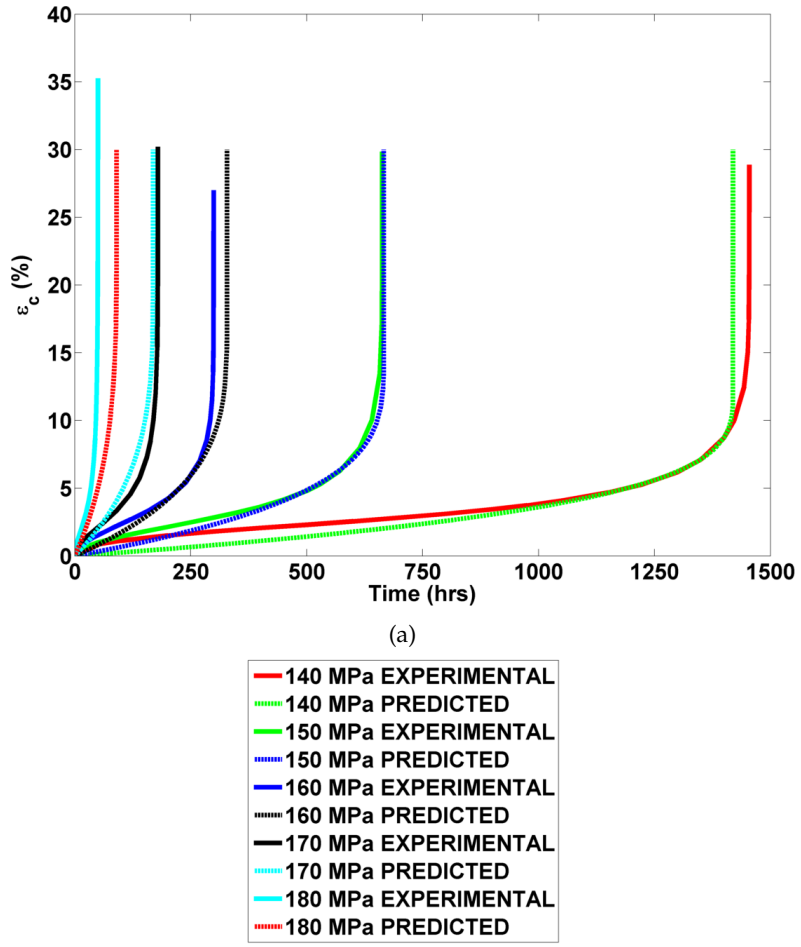

Figure 4.16: The prediction of P91 (600°C) uniaxial creep tests using the Kachanov CDM model and the constants shown in table 4.8.

Table 4.8: A summary of the optimised material constants for P91 at 600°C for the Kachanov creep damage model (where σ is given in terms of MPa, strains are given as a percentage and time is given in hours).

A	$1.00x10^{-34}$
B	$1.12x10^{-28}$
n	13.69
χ	10.96
ϕ	18.00
m	0.00

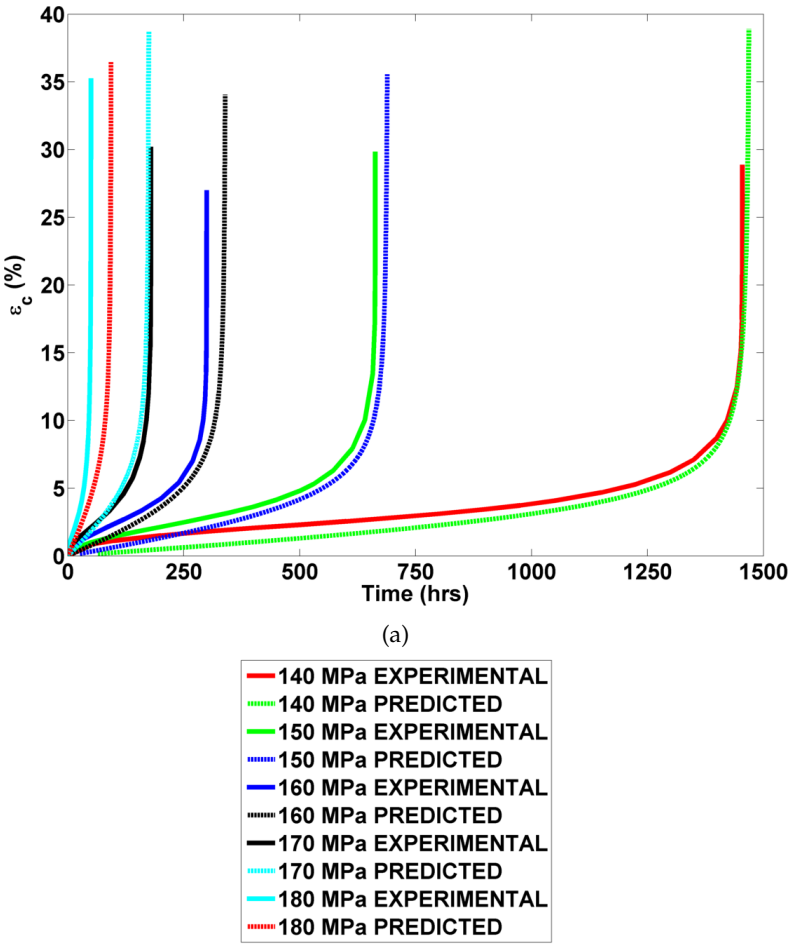

(a)

Figure 4.17: The prediction of P91 (600°C) uniaxial creep tests using the Liu-Murakami CDM model and the constants shown in table 4.9.

Table 4.9: A summary of the optimised material constants for P91 at 600°C for the Liu-Murakami creep damage model (where σ is given in terms of MPa, strains are given as a percentage and time is given in hours).

A	$1.00x10^{-34}$
B	$2.12x10^{-27}$
n	13.69
p	10.95
q_2	6.00

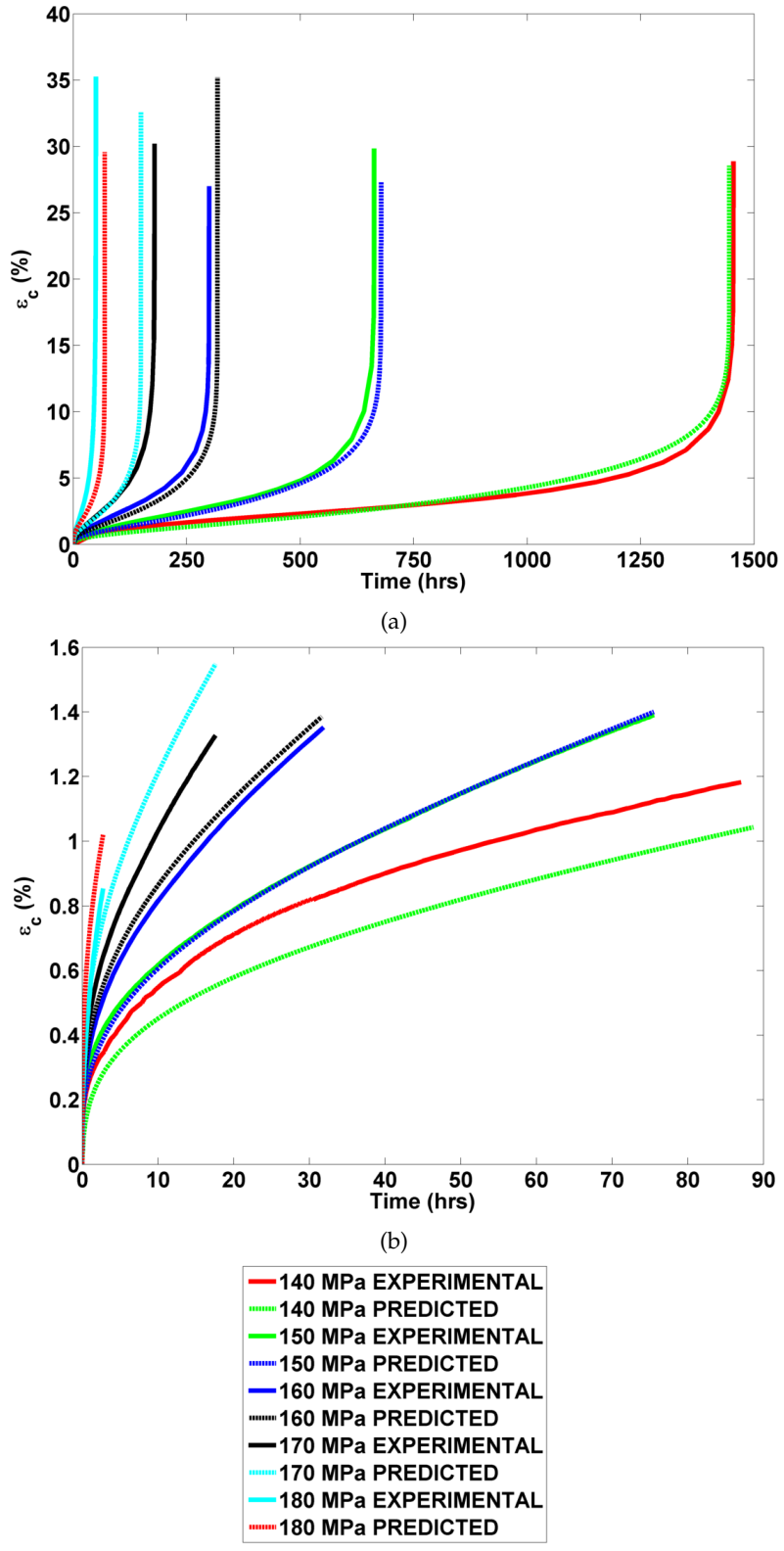

Figure 4.18: The prediction of P91 (600°C) uniaxial creep tests using the Dyson CDM model and the constants shown in table 4.10. Plots show the prediction of (a) the full creep strain curve and (b) the primary creep region.

Table 4.10: A summary of the optimised material constants for P91 at 600°C for the Dyson creep damage model (where σ is given in terms of MPa, strains are given as a percentage and time is given in hours).

A	$3.44x10^{-9}$
B	0.10
h	13669.67
$\acute{H}$	0.34
D	2.60
K_c	$2.00x10^{-6}$

Using the LSQNONLIN MATLAB function, sets of material constants have been determined for the Kachanov, Liu-Murakami and Dyson creep damage models based on experimental data for the material P91 at 600°C. The derived material constant sets are used in the extrapolated stress simulations presented later in this chapter. Predicted failure times for uniaxial specimens are also compared with ECCC long term creep tests and results predicted by Orr's parametric equation.

4.5 Reduced Stress Extrapolation

4.5.1 BAR 257 Extrapolation

Uniaxial Extrapolation

Taking two of the stresses used in the uniaxial testing of BAR 257 (see section 4.4.1) that fall in the middle of the experimental stress range (93 and 83MPa) as starting points; additional low stress simulations of a uniaxial specimen were performed (see table 4.11 for a summary). These stresses were chosen to reflect the behaviour of the model over an extended stress range. A plot of the results of these reduced uniaxial stress simulations is provided in figure 4.19, allowing for the general relative performance of the models to be seen more easily.

Table 4.11: A summary of reduced stress uniaxial FEA simulations for BAR 257 at 650°C.

σ_{APP} (MPa)	Kachanov t_f (hrs)	Liu-Murakami t_f (hrs)	Dyson t_f (hrs)
93	140.39	140.20	140.29
82	343.64	343.55	343.54
50	9951.01	9822.24	4258.51
35	$1.12x10^5$	$1.32x10^5$	11494.49
25	$1.10x10^6$	$1.44x10^6$	24559.46

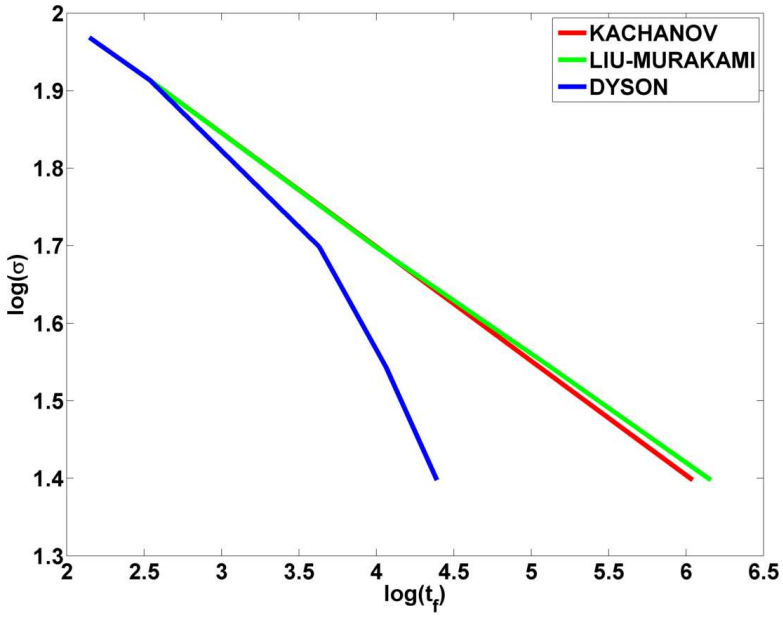

Figure 4.19: Low stress extrapolation of the Kachanov, Liu-Murakami and Dyson creep damage models under uniaxial conditions for the material BAR 257 at 650°C.

Notched Bar Extrapolation

As with the uniaxial specimen, reduced stress tests were completed for the notched bar using a similar stress range (note applied stresses are not used but rather mean notch tip stresses, shown in table 4.12). An example damage contour plot at failure (taken as being the point when several Gauss point values reach the predefined maximum damage parameter value) for the notched bar mesh is provided in figure 4.22. Peak damage values are enforced to avoid the numerical difficulties encountered in some models as the damage parameter approaches its theoretical maximum value (see section 2.3.3).

For the Kachanov model, a peak damage value of 0.98 is applied, which by experience has been shown to be suitable. Again the results of the reduced stress simulations are shown graphically in figure 4.21, providing a simpler method of comparison.

Table 4.12: A summary of reduced stress notched bar FEA simulations for BAR 257 at 650°C.

σ_{APP} (MPa)	Kachanov t_f (hrs)	Liu-Murakami t_f (hrs)	Dyson t_f (hrs)
93	1037.20	1037.21	1037.23
82	2012.13	2012.14	2012.13
50	$6.15x10^4$	$8.03x10^4$	$4.76x10^4$
35	$6.88x10^5$	$1.02x10^6$	$1.67x10^5$
25	-	-	$4.13x10^5$

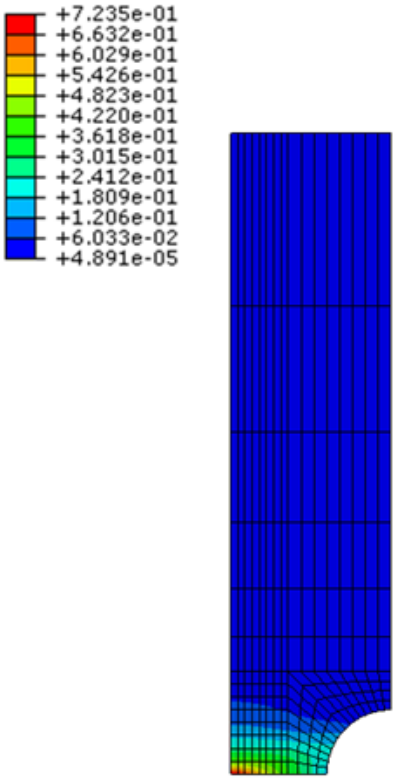

Figure 4.20: An example damage contour plot for notched bar mesh (Kachanov model with 35MPa notch stress).

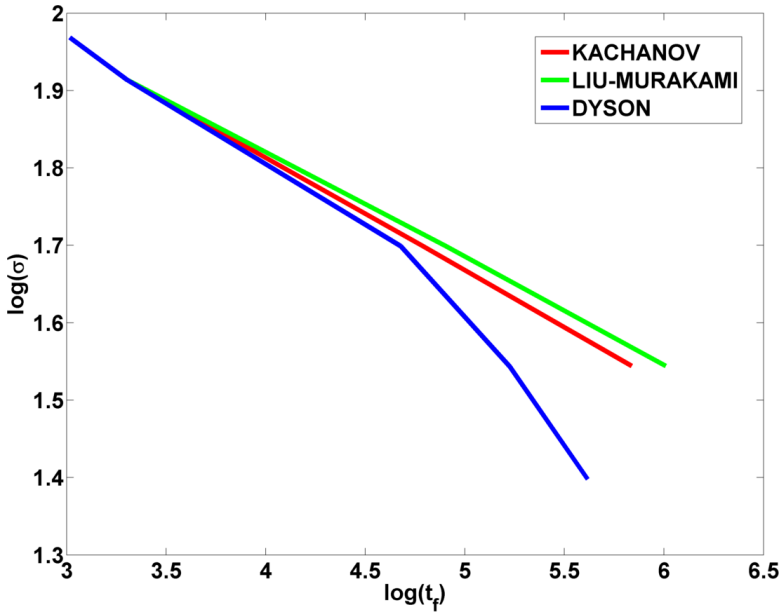

Figure 4.21: Low stress extrapolation of the Kachanov, Liu-Murakami and Dyson creep damage models for a notched bar FEA mesh for the material BAR 257 at 650°C.

Straight Pipe Section Extrapolation

Using the mesh representing a straight pipe, discussed in section 4.3.2, simulations using a range of stresses were performed (the results of which are summarised in table 4.13 and figure 4.22). In the case of the pipe analyses, the mean diameter hoop stress (σ_{MDH}) was used to gauge the considered stress range, and can be expressed as equation (4.29)[193].

$$\sigma_{MDH} = \frac{P_i \left(R_O/R_I + 1\right)}{2\left(R_O/R_I - 1\right)} \tag{4.29}$$

Internal pressures therefore were chosen such that σ_{MDH} would be in a comparable range to the stresses used in the uniaxial and notched bar analyses. Note additional simulations were used to confirm the behaviour of the models, particularly the Dyson model around the "knee" point. An example damage contour plot is given in figure 4.23. Peak damage values were found to be on the outside surface of the pipe, concurring with the location of maximum rupture stress after stress redistribution. For pipe simulations, failure life is defined as all of an element's Gauss points reaching the critical damage value.

Table 4.13: A summary of reduced stress FEA simulations for an idealised straight pipe section FEA mesh for BAR 257 at 650°C.

σ_{APP} (MPa)	Kachanov t_f (hrs)	Liu-Murakami t_f (hrs)	Dyson t_f (hrs)
93	487.81	486.02	487.24
82	1174.94	1175.14	1174.65
60	9112.18	9519.47	9105.05
50	$3.10x10^4$	$3.48x10^4$	$3.00x10^4$
48	$4.15x10^4$	$4.78x10^4$	$3.97x10^4$
41	$1.20x10^5$	$1.50x10^5$	$8.63x10^4$
35	$2.93x10^5$	$3.67x10^5$	$1.48x10^5$
30	-	-	$3.13x10^5$

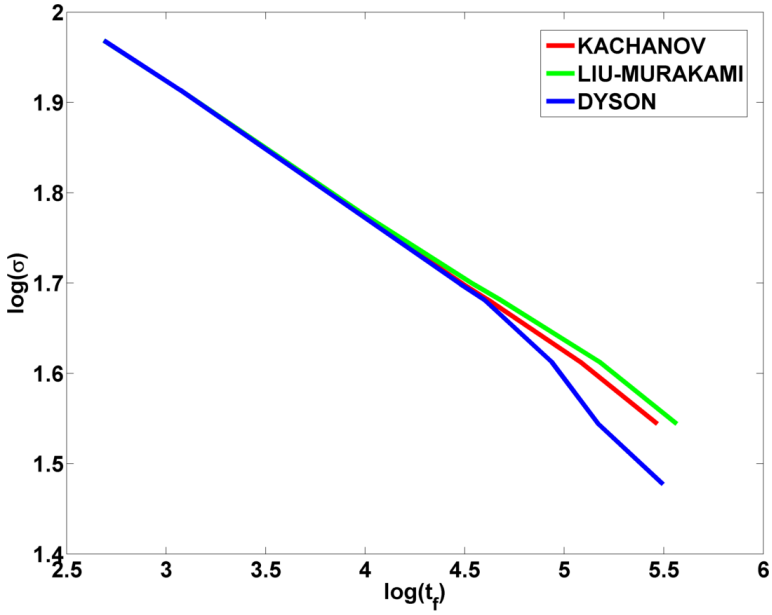

Figure 4.22: Low stress extrapolation of the Kachanov, Liu-Murakami and Dyson creep damage models for an idealised straight pipe section FEA mesh for the material BAR 257 at 650°C.

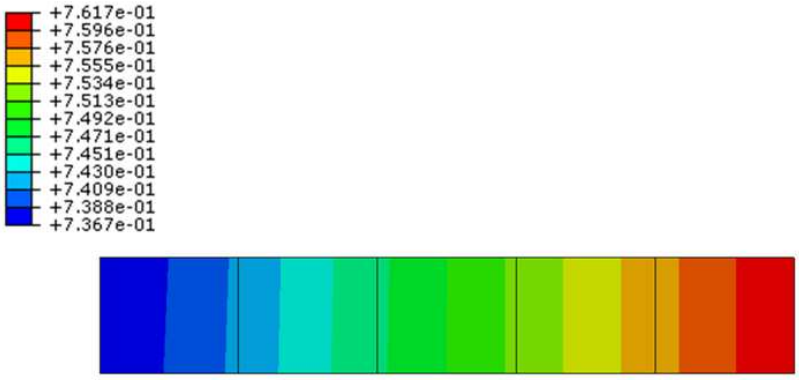

Figure 4.23: An example damage contour plot for an idealised straight pipe mesh (Liu-Murakami model with an internal pressure (P_i) giving rise to a mean diameter hoop stress (σ_{MDH}) of $35MPa$).

Idealised Pipe Bend Extrapolation

Using a similar internal pressure range to the straight pipe case (and hence σ_{MDH} range, given that pipe dimensions are the same for the straight pipe and pipe bend meshes), FEA analyses have been completed for a pipe bend mesh (an example damage contour plot can be seen in figure 4.25). Failure locations were confirmed to be in agreement with those presented in literature[193] (i.e. at the mid wall position in the intrados). General behaviour was similar to that displayed in the other geometries, shown in figure 4.25, with the actual failure times presented in table 4.14.

Table 4.14: A summary of reduced stress FEA simulations for an idealised pipe bend FEA mesh for BAR 257 at 650°C.

σ_{APP} (MPa)	Kachanov t_f (hrs)	Liu-Murakami t_f (hrs)	Dyson t_f (hrs)
93	371.82	371.82	375.54
82	874.35	882.85	815.25
50	$2.51x10^4$	$2.66x10^4$	$2.58x10^4$
35	$2.84x10^5$	$3.27x10^5$	$1.87x10^5$
25	-	-	$4.43x10^5$

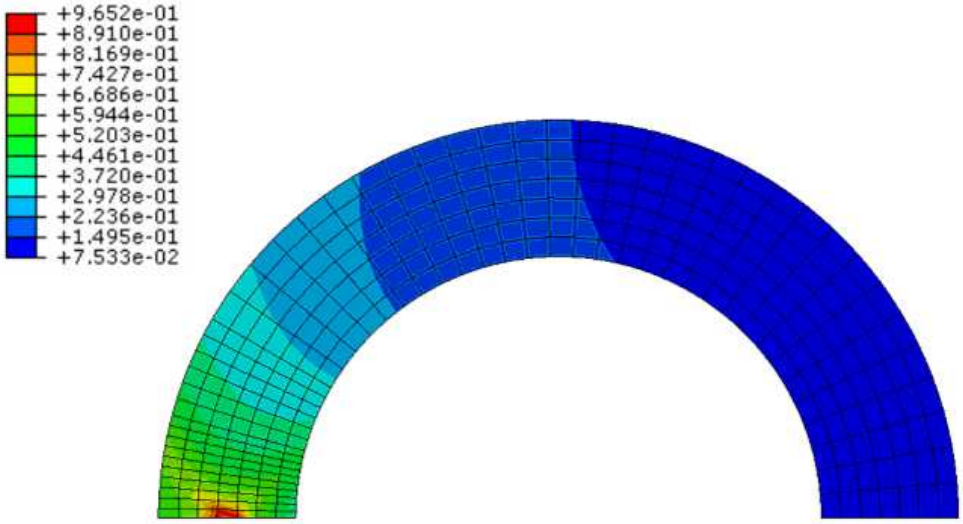

Figure 4.24: An example damage contour plot for an idealised pipe bend mesh (Dyson model, showing the dominant cavitation damage parameter ω_2, with an internal pressure (P_i) giving rise to a mean diameter hoop stress (σ_{MDH}) of 82 MPa).

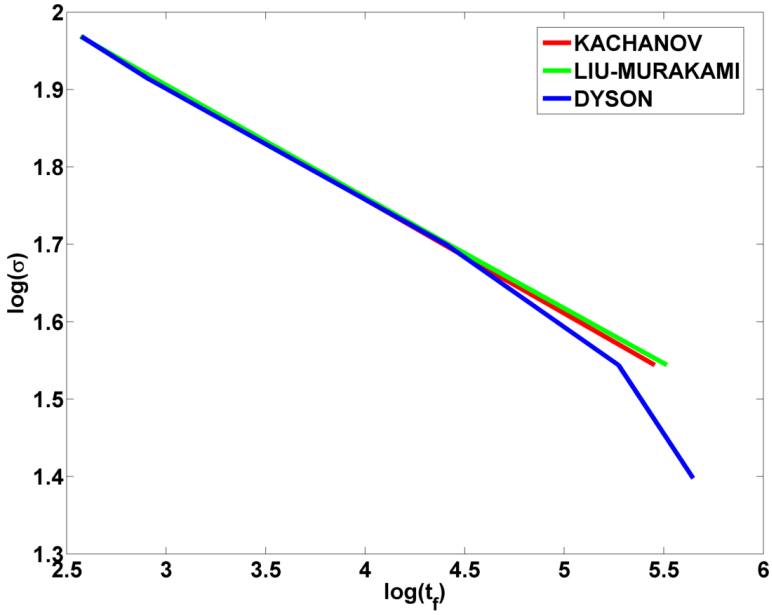

Figure 4.25: Low stress extrapolation of the Kachanov, Liu-Murakami and Dyson creep damage models for an idealised pipe bend FEA mesh for the material BAR 257 at 650°C.

4.5.2 P91 Steel Extrapolation

Orr developed a parametric equation[64,194] (equation (4.30), referred to as Orr's equation) that allows for the failure lives (t_f) to be determined at a given stress and temperature (T). This requires seven material constants to be derived (a, b, c, d, e, t_a and T_a), the values of which are based on extensive experimental testing over a range of stresses and temperatures, which clearly demands high investment in terms of both finance and time. Constants for this equation are therefore limited, however values for P91 have been derived and published in literature (see table 4.15)[64]. Using this method, extrapolated failure times based directly on experimental testing at similar stress levels and temperatures can be derived. This has been completed for P91 at 600°C , the results of which can be seen in table 4.16, along with extrapolated failure times predicted from the three CDM models considered. Parametric equation results have been verified by considering results taken from European Creep Collaborative Committee (ECCC) data sheets for P91[195], summarised in table 4.17. As with previous extrapolated results, the relative performance of the models has been plotted (figure 4.26), however experimental and parametric data is also included.

$$P(\sigma) = a + b[\log(\sigma)] + c[\log(\sigma)]^2 + d[\log(\sigma)]^3 + \cdots \\ \cdots e[\log(\sigma)]^4 = \left[\frac{\log(t_f) - \log(t_a)}{T - T_a}\right] \tag{4.30}$$

Table 4.15: A summary of material constants for P91 for Orr's equation (see equation (4.30))[64].

a	-0.49382779
b	0.974988639
c	-0.767101705
d	0.266840726
e	-0.035136841
$\log t_a$	24.75553894
T_a	370

Table 4.16: A summary of reduced stress uniaxial simulations for P91 at 600°C.

σ_{APP} (MPa)	Orr t_f (hrs)	Kachanov t_f (hrs)	Liu-Murakami t_f (hrs)	Dyson t_f (hrs)
180	181.32	50.12	50.12	50.14
170	369.75	179.22	179.22	179.12
160	750.99	299.54	299.54	299.66
150	1522.96	663.41	663.41	663.60
140	3093.96	1454.21	1454.21	1454.72
100	59687.68	56699.89	58568.51	28579.87
80	$3.18x10^5$	$6.54x10^5$	$6.75x10^5$	$1.16x10^5$
60	$2.15x10^6$	$1.53x10^7$	$1.58x10^7$	$4.09x10^5$
40	$1.53x10^7$	$1.30x10^9$	$1.34x10^9$	$1.31x10^6$

Table 4.17: A summary of ECCC uniaxial failure times for P91 at 600°C[195].

Applied Stress (MPa)	ECCC Rupture Time (hrs)
123	10000
108	30000
94	100000
86	200000

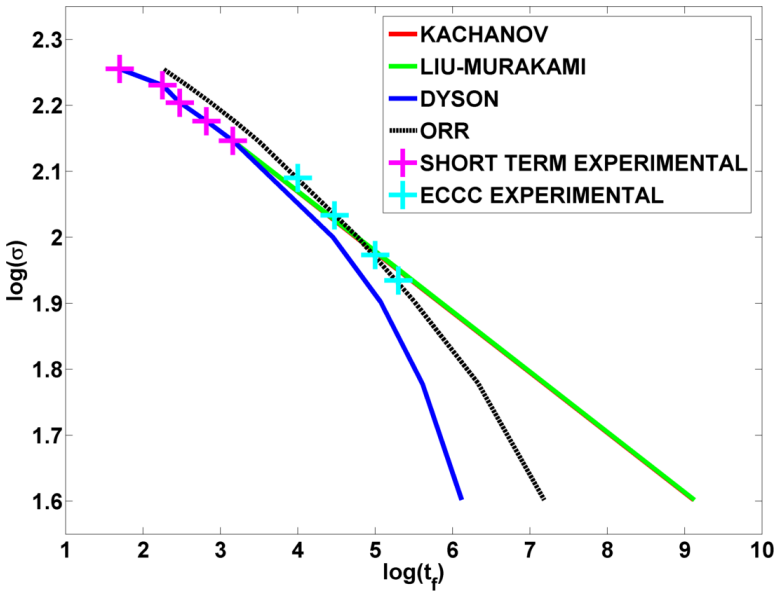

Figure 4.26: A plot of the relative performance of several creep damage models at reduced stresses (under a uniaxial condition) for a P91 steel at 600°C with parametric (Orr's equation) and long term (ECCC data) experimental results. Note that the level of agreement between the power law models is such that the Liu-Murakami results overlay the Kachanov line.

4.6 Conclusions

As was alluded to in the introduction of this chapter, a main practical consideration when deciding on the uses of a CDM model is how the model reacts as damage approaches unity (signifying failure). A dependency of $1/(1-\omega)$ exists in some material models (where ω is some damage parameter) and as damage approaches the limit

of 1 (indicating failure) damage rates will approach infinity. When such models are implemented in FEA packages (for example ABAQUS through the use of specially written CREEP user subroutines[191]), time step lengths will be significantly reduced to limit the rate of change of the state dependent variables. This action drastically increases computing time and output file size, potentially making even simple analyses difficult to complete fully[62,67]. The usual solution for this problem is to limit damage to a high value that is indicative of immanent failure due to load transfer on to ligaments with lower damage, however this can make failure criterion subjective and possibly imprecise. It is interesting to note that in the Dyson model, the carbide precipitate coarsening damage variable, ϕ, achieves a very low value (0.1) when failure occurs due to the other damage variable, ω_2, representing cavitation damage. This is in agreement with published literature, which suggests that damage due to so called ageing is minimal[66]. The evolution of the damage variable ϕ is dependent only on its initial value (i.e. there is no relationship to the stress state of the specimen). High damage rates are not observed at failure for either of the Dyson damage parameters.

In the case of an idealised pipe bend, where published examples exist, the considered models all demonstrated a localised peak damage at the intrados of the bend (on the plane of symmetry), approximately at half the wall thickness. Contour plots (figure 4.24) also indicate lower damage regions either side of the peak damage region. This is in perfect agreement with literature by Hyde et. al.[67], for which a similar multiaxial constant α value was used (0.3[193], compared to ≈ 0.2 for BAR 257 in the present work) for power law damage models such as the Kachanov and Liu-Murakami models. On the subject of pipe analyses, it is worth noting that the mean diameter hoop stress (σ_{MDH}) is not directly equivalent to the applied or notch tip stresses used in the uniaxial and notched bar analyses, respectively. In the uniaxial case the rupture stress (which drives damage accumulation) is equivalent to the applied stress. In the multiaxial notched bar and pipe bend cases however the rupture stress depends on both the von Mises and maximum principal stresses (both of which are dependent on specimen geometry and loading). While there is a relation between peak rupture stress values and the notch tip/mean diameter hoop stresses, it is not the same as that present for the uniaxial condition. Care must be taken therefore if pipe results are to be compared directly to the results of uniaxial/notched bar tests. The use of σ_{MDH} was intended only as a method to ensure similar stress states were applied to the two pipe meshes. The effect of this non-equivalence can be seen in the nominal stress versus rupture time plots for the four considered conditions, noting in particular that the nominal stress at which the Dyson model begins to diverge in the simpler geometries (uniaxial and notched bar, figures 4.19 and 4.21 respectively) is far greater (approximately 80 MPa compared to 45 MPa) than for the pipe geometries (figures 4.22 and 4.25 for the straight pipe and pipe bend sections, respectively). Confidence is given to the results of pipe analyses by noting that rupture times for straight pipe sections are significantly longer than

pipe bends at similar internal pressures (and hence σ_{MDH}), which has been previously observed by Sun et. al.[192] and is in agreement with industry observed failures (note very few failures have been noticed on plain pipe section, with most failures being located around discontinuities such as pipe bends or weldments[193]). Over all models and for the stress range considered, the ratio of the pipe bend failure time to the straight pipe failure time was approximately 0.8.

So severe is the discrepancy between predicted rupture lives for Dyson's model and the power law models that, in all but the simplest uniaxial case (where time marching was used), producing failure analyses for the power law models at the lowest stresses became too lengthy to practically achieve (time step lengths are limited to ensure convergence in FEA solvers). For this reason, the lowest stress results are omitted for power law models in comparative study summary tables. The linear relationship between time to failure and stress for the power law models is verified with the supplied results. The Dyson model value has been included to verify the general shape of the failure time curve in the extended stress range. The divergence of Dyson's model at reduced stresses is dependent on the use of a hyperbolic sine function, rather than a power law relationship[67]. Power law models will inherently make the assumption that the stress exponent (often characterised by n), will remain constant[65]. While this is true over a small stress range (in particular for ferritic steels and nickel-base super alloys), some form of continuous alteration to the equivalent stress exponent term (designated B in the Dyson model given in this chapter, see equation (2.56)), is required over an extended stress range[65]. This is provided by the sinh relationship used in the Dyson model. Comparing the Dyson rupture times to the Kachanov results (bearing in mind that Liu-Murakami results are in good agreement with Kachanov results), it can be seen that, at its most extreme (the uniaxial case), the Dyson failure life represents only 2.23% of the predicted Kachanov life, however this increases to 24.27% in the more complex multiaxial stress state experienced in the notched bar. For pipe analyses at the lowest nominal stress, Dyson rupture times drew closer to Kachanov failure times, being 50.51% and 58.80% for the straight pipe and pipe bend simulations respectively.

As was mentioned in section 4.4.2, additional uniaxial extrapolation for a P91 material at 600°C was undertaken to investigate the relative performance of the models with respect to actual experimental data at similar stress levels, as well as considering failure times that are practically representative. The results of a parametric equation (Orr's equation[64,194]) and limited intermediate stress experimental data (ECCC data sheets[195]) displayed a high level of agreement (see figure 4.26). Power law and sinh function based models showed similar behaviours in an extrapolated stress range for P91 to the behaviours observed for BAR 257 (figure 4.19). A plot of the comparative performance of the different methods for predicting failure times can be seen in figure 4.26. In the high stress range, i.e. the stresses used to determine material constants, all CDM models showed slightly conservative time to failure predictions (approximately 150 to

170 hours less) when compared to the parametric data at the same stress levels. Outside of this region (particularly below 100 MPa) however the models will begin to diverge in their predictions and the parametric data falls between the Dyson curve and power law models (Kachanov and Liu-Murakami), leading to a large discrepancy between predicted failure times. At the lowest stress considered (40 MPa), the Dyson failure time represented only 0.1% of the Kachanov failure time, however it was 8.5% of the parametric Orr failure time. In terms of absolute time, the discrepancy between the Dyson and Orr failure time is approximately 14 million hours, which is substantially less than 1.2 billion hour difference observed between the Orr's equation result and the power law model results. Note these failure times are not in any way representative of observed life times for power plant components. The lack of additional system or multiaxial loads and operation cycling means these analyses are greatly conservative. The intention of the present work is only to compare the multiple CDM models available and highlight the difference between the failure times predicted from these models when applied stresses are different to the stress levels used to determine material constants.

It has been demonstrated that when CDM models are used to predict failure lives of components experiencing stresses lower than those used in material constant determination experiments, models using different relationships (for example power law and sinh functions) can give widely different failure times. With the absence of experimental failure lives at these stress levels (which are often not practical to obtain), CDM models provide a flexible way to predict these. It is important however, bearing in mind the increasing need to anticipate failure using measured damage levels (most notably in the power industry), to consider the divergent behaviour of the chosen model. A compromise must therefore be struck between the need for conservative results and the additional time required to derive and optimise the additional material constants used in the more complex models (for example, the Dyson model uses a total of 7 material constants, whereas Liu-Murakami uses 6). In the interest of safe and conservative analysis and based on the study of extrapolated P91 uniaxial failure times, it would be preferable to use the Dyson model, or similar sinh based law, to predict component failure lives from material constants which have been derived from tests performed at far higher stresses.

Chapter 5

The Effects of Scoop Sampling on the Creep Behaviour of Power Plant Straight Pipe Sections

5.1 Introduction

Given the large range in properties that can exist in apparently identical materials (due to for example chemical composition variations between heats, manufacturing processes or service exposure), the accurate characterisation of a material on a local basis is important for component life assessment[136,196]. A potential solution to this concern is to take scoop samples from in service components. Novel small specimens can then be manufactured and evaluated without requiring full component replacement or extensive repair (see section 2.4.2). Most research attention in the field of small specimen testing has focused on the interpretation of experimental outputs in order to convert these results to those of conventional tests (for example, uniaxial creep tests). This is particularly true for the small punch creep test (SPCT) method, which has the potential to produce data for material failure characterisation. More established small specimen techniques, such as the impression creep test, have been shown to have the ability to accurately determine secondary creep material properties from small samples of material[136].

If any possible detrimental effects of scoop sampling on the remnant life of sampled components could be accurately evaluated, condition monitoring could be conducted in a more efficient way throughout a component's life. In addition to more established techniques such as the replica method and ultrasonic inspection, small scoop samples could be taken from critical components. Small specimen testing could then be implemented to provide local and "up to date" material data for use in component life analysis. Potentially, critical components could operate for longer with more confidence. Condition monitoring methodologies are of great interest to the power generation industry. Future operation trends are likely to require more severe loading gradients,

inducing pronounced cyclic behaviour when attempting to match market demands. With the higher confidence offered by condition monitoring (supplemented by small specimen testing), these more profitable generation strategies could be adopted safely.

In this chapter, the effect of scoop sampling on power plant straight pipe components under creep conditions is investigated. Sample depth is varied based on a commonly used hemispherical cutter geometry. Steady-state creep rupture stresses are calculated in the vicinity of the scoop sample using FEA sub-modelling procedures. Several system loading situations are represented in order to highlight potential "at risk" loading scenarios.

5.2 Modelling Methodology

5.2.1 Material Models

Elastic-creep analyses have been conducted using the FEA package ABAQUS[191]. Stresses predicted by the analyses are below the typical yield stress for power plant steels, therefore the exclusion of any plastic analysis is valid. In low load cases, the constant strain rate secondary creep region may represent the majority of a component's life. By achieving a steady-state condition, constant stresses found in two separate structures are comparable, even if exposure times are not the same. In the present chapter, time dependent strain rate behaviour is assumed to be negligible, therefore secondary creep behaviour is represented by equation (5.1) (Norton's Law, see section 2.3.3). In the FEA analyses, the constants A and n are defined as $6.599x10^{-16} MPa^{1/n}.hr$ and 6.108, respectively, for the material $1/2Cr1/2Mo1/4V$ at 640°C[139]. These material constant values are determined for stress values given in terms of MPa, time periods given in hours and absolute strain values. This unit convention is applied throughout the present chapter.

$$\dot{\varepsilon}_{c\,ij} = \frac{3}{2} A \sigma_{EQ}^{n-1} S_{ij} \tag{5.1}$$

The constitutive continuum damage equations proposed by Kachanov[53] and later modified by Robotnov[54] can be used to estimate the accumulation of creep damage in a component, therefore predicting creep life (see equations (2.50) and (2.51)). The triaxial stress state material constant, α ($0 \geq \alpha \geq 1$), determines the value of the rupture stress, σ_R ($\sigma_R = \alpha\sigma_1 + (1-\alpha)\sigma_{EQ}$), where σ_1 is the maximum principal stress and σ_{EQ} is the von Mises equivalent stress). It can be demonstrated that, by assuming that negligible damage accumulation occurs prior to the tertiary creep region, Kachanov's model reduces to Norton's law (equation (5.1), see section 4.2.2). Therefore if a steady-state analysis is performed with Norton's material law, a calculation of σ_R is still valid. As damage accumulation is dependent on the rupture stress (σ_R), the position of a localised peak rupture stress is an indication of the failure location in a creeping structure[104].

The peak value of the rupture stress in a structure under steady-state conditions is designated by $\hat{\sigma}_R$. The damage differential equation (equation (2.51)) in Kachanov's modes can be integrated between limits to find an expression for time to failure (t_f, see equation (4.6)). A reference (peak) rupture stress from a Norton's law analysis can be used in this expression (equation (5.2)), allowing the time to failure for a creeping structure to be quickly estimated without the need for complex non-linear damage analysis[138,139,192]. In the present work, an α value of 0.3 for the $1/2Cr1/2Mo1/4V$ pipe steel at 640°C has been used[139].

$$t_f = \frac{1}{B(1+\phi)\hat{\sigma}_R^{\chi}} \tag{5.2}$$

5.2.2 Power Plant Pipe Geometry and System Loading

Piping components used in power plant are modelled in the present work. Due to the scoop sampling procedure removing material from the wall thickness of pipes, a thick pipe section (an outer diameter D_O of $360mm$ and a wall thickness Th of $60mm$) has been assumed for the initial investigation. Assuming a closed end condition, an axial load (σ_{AX}) must be applied to replicate the constraint of an infinitely long pipe section which is loaded by an internal pressure (P_i). This load may be calculated from equation (4.28)[192]. Additional loads may also be imposed on a component by the piping system, which can be characterised by a loading factor k (see equation (5.3)). This loading factor can vary between 0, where no additional load is applied (equivalent to an internal pressure loading under closed end conditions only), to 1, where the total axial stress (due to the closed end condition and system loading) is equal to a maximum allowable axial load ($\sigma_{AX\,MAX}$). In the present work, system loads are considered through the application of an additional axial load or an in-plane bending moment. An additional axial load ($\sigma_{AX\,A}$) may be imposed by either system loading condition, which may be compared to $\sigma_{AX\,MAX}$ to find the corresponding k value. For a loading condition, the total axial load ($\sigma_{AX\,T}$) is given by equation (5.4).

$$k = \frac{\sigma_{AX\,A}}{(\sigma_{AX\,MAX} - \sigma_{AX})} \tag{5.3}$$

$$\sigma_{AX\,T} = \sigma_{AX} + \sigma_{AX\,A} \tag{5.4}$$

From PD 5500[127], the total axial loading on a pipe component is limited to the pipe's mean diameter hoop stress (σ_{MDH}, see equation (5.5)), therefore $\sigma_{AX\,MAX} = \sigma_{MDH}$. For a bending moment ($M_Z$), the additional axial load $\sigma_{AX\,A}(r)$ is dependent on the radial position r, see equation (5.6). The second moment of area (I_Z) for a pipe is given by equation (5.7). Assuming that no axial load should exceed σ_{MDH} when $k = 1$ and noting that the maximum additional axial load due to the application of a bending moment occurs at $r = R_O$, equation (5.8) may be derived for the moment M_Z. Scoop sample

depths were assumed to vary between 1 and $5mm$. Industrial scoop sample depths are typically $3-4mm$, therefore this range is reasonable. The hemispherical cutter diameter was assumed to be $50mm$, which is typical of a scoop sampler[151]. In the present chapter, an internal pressure (P_i) of $20MPa$ was applied, giving rise to a closed end axial pressure (σ_{AX}) equal to $16MPa$. The maximum total axial load is therefore limited to $50MPa$ by equation (5.5). The maximum bending moment is $124.97kNm$. Note that both of these conditions relate to a loading factor (k) of 1.

$$\sigma_{MDH} = \frac{P_i\left(\frac{R_O}{R_I}+1\right)}{2\left(\frac{R_O}{R_I}-1\right)} \tag{5.5}$$

$$\sigma_{AX\,A}(r) = \frac{M_Z r}{I_Z} \tag{5.6}$$

$$I_Z = \frac{\pi}{4}\left(R_O^4 - R_I^4\right) \tag{5.7}$$

$$M_Z = \frac{\pi}{8}kP_i\left[\left(\frac{R_O}{R_I}+1\right)^2 - 2\right]\frac{R_I^3}{(R_O/R_I)}\left[\left(\frac{R_O}{R_I}\right)^2 + 1\right] \tag{5.8}$$

5.2.3 FEA Models

A sub-modelling technique has been used in the representation of a scoop sample region. This keeps computation times manageable while allowing for fine mesh densities to be implemented in the regions of interest (i.e. in the vicinity of the scoop sample excavations). Planes of symmetry were enforced, allowing only quarter models of the scoop sample site to be modelled (note the displacement boundary conditions, restricting U_X and U_Y, in figure 5.1). 3D FEA global and sub-models have been generated using ABAQUS CAE (Computer Aided Engineering). All elements used are 20 node (quadratic) hexahedral reduced integration ($C3D20R$ in ABAQUS[191]).

An equation constraint[191] was applied in cases where axial loads were implemented. This was done in order to ensure the free ZX plane of the global model remains plane during deformation, representing the constraint of the rest of the straight pipe. Bending moments were applied about the X axis (hence in plane) in a direction to open the scoop excavation (this represents the "worst case" bending moment orientation). Moments were applied to the model using ABAQUS's coupling constraint[191].

Sub-models were created using the surface interaction approach[191]. Global model simulations were completed first, allowing the displacement boundary conditions (that vary with time) at the sub-model connecting faces to be determined (figure 5.1). Sub-models, with refined meshes, were then analysed in order to determine the detailed stress distribution around the excavation. Internal pressure and system loads were

applied to the global model. After this analysis had been completed, time dependent displacement conditions were taken from the global model and were used to control the deformation of the sub-model at the interface. The deformation of the rest of the sub-model was determined from these interface displacement conditions. Sub-model regions were made sufficiently large in order to encapsulate all of the local effects of the excavation. A $30mm$ cubic sub-model was found to be sufficient. An idealised scoop sample has been modelled in the present work. The scoop excavation procedure will often leave a rough surface finish in the sampled component. These grooves may cause highly localised stress concentrations. These localised stress concentrations due to the scoop excavation could then act as initiation points for surface cracks. When analysing the results presented in this chapter, it should be remembered that it is assumed that no surface defects were present prior to loading and such defects may reduce the remnant life of the component.

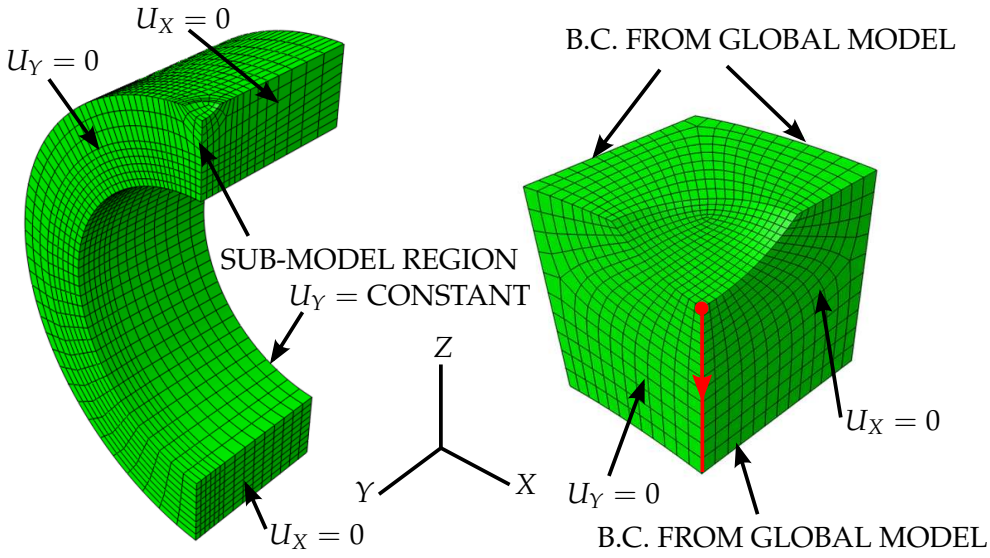

Figure 5.1: Illustrations of global and sub-models used in the analysis of scoop sample sites in straight pipe sections. Boundary conditions and coupling constraints (used for the application of bending system loads) are shown. A path is highlighted from the tip of the scoop in the sub-model, which is used in some result plots.

The stress values in the vicinity of the scoop may be mesh dependent (due to the stress concentration effect of the scoop excavation). It is therefore important that a mesh sensitivity study is conducted to ensure that accurate solutions are obtained for the chosen mesh density. The size of the cube shaped elements at the notch of the sub-model were varied, with rupture (assuming $\alpha = 0.3$), von Mises and maximum principal stresses recorded at the scoop excavation tip (this is the peak stress location and the area of most interest). Convergent behaviour can be seen in figure 5.2 for all three stress components with reducing element size, therefore cube shaped elements with dimensions of approximately $1mm$ have been applied in the vicinity of the scoop

excavation in the sub-models.

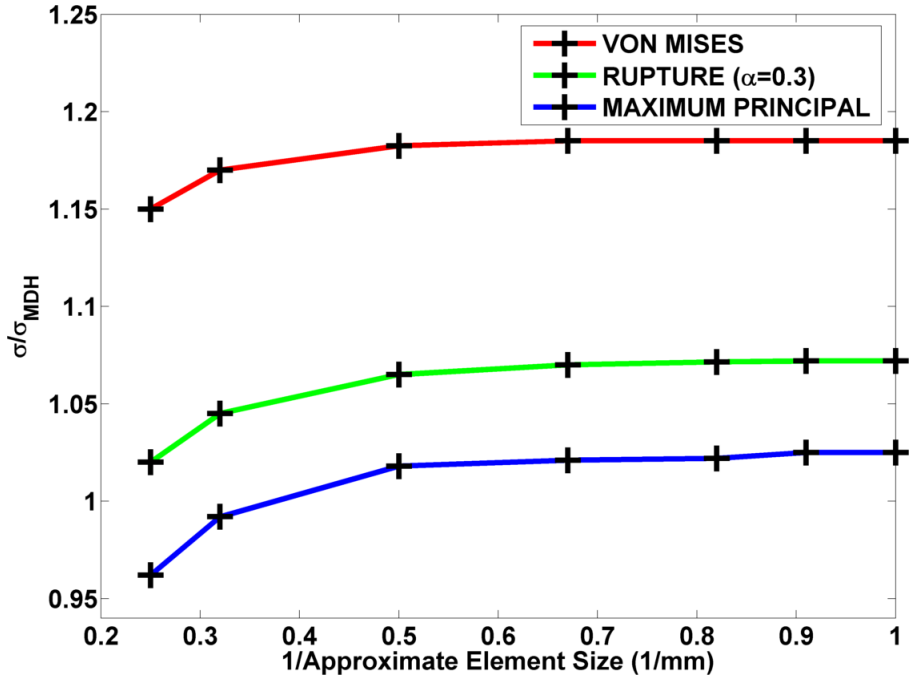

Figure 5.2: Mesh sensitivity study results for a 5 *mm* deep scoop excavation sub-model under internal pressure and maximum permissible bending moment loading.

5.3 Results

5.3.1 Typical Stress Distributions

In the majority of the loading scenarios simulated, similar behaviours were observed for the steady-state stress variation in the through wall thickness direction (see figure 5.3). Stress concentrations are significant at the excavation, with peak localised stresses at the tip of the scoop. The inclusion of the scoop increases the multiaxial nature of the stress state in the vicinity of the excavation and creates a stress concentration. Equivalent von Mises stresses and maximum principal stresses are therefore greater near the scoop. The effects of the stress concentration become less evident with increasing distance into the wall thickness (see figure 5.1). At a certain distance into the wall thickness, the sampled stress distribution is identical to that of the unsampled (plain pipe) stress distribution. The application of system loads tends to increase the stress concentration effect. Differences between local stresses around the scoop and typical stress distributions in unsampled pipe sections are greater for cases where system loads are applied. This is particularly true for cases where opening bending moments are applied. These cause large tensile stresses on the upper surface of pipe section (where the scoop excavation is located). From a component lifing perspective, it is important that a comparison be drawn between the localised peak stress at the scoop excavation and the stresses that would normally occur in a plain pipe component subjected to the

same loads. If the peak stresses at the sample site are lower than the peak through wall thickness stresses in the unsampled pipe (figure 5.3 (a) and (b)), it is reasonable to assume that scoop sampling does not have a detrimental effect. The critical cut depth is therefore the cut depth which induces stresses at the sample site greater than those in the unsampled pipe. In the following result plots (figures 5.4 to 5.6, 5.8 and 5.9), localised peak stresses (at the scoop excavation tip) are plotted against cut depth. These can be easily compared to the peak stresses observed in a plain pipe (shown by the "UNSAMPLED MODEL" line), highlighting potential "at risk" cases. All stresses are normalised against the mean diameter hoop stress (σ_{MDH}) which does not vary with scoop excavation depth (it is only dependent on the pipe section dimensions and internal pressure loading). In all cases, a pipe section with an outer diameter (D_O) of 360mm and a wall thickness (Th) of 60mm has been used. Stress distributions will be dependent on the chosen value of the multiaxial material constant (α, assumed to be 0.3 here). These effects are discussed in detail in section 5.3.5.

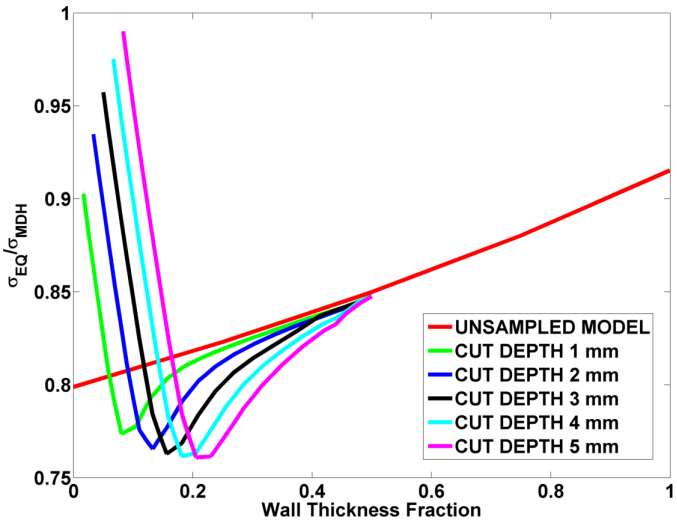

(a)

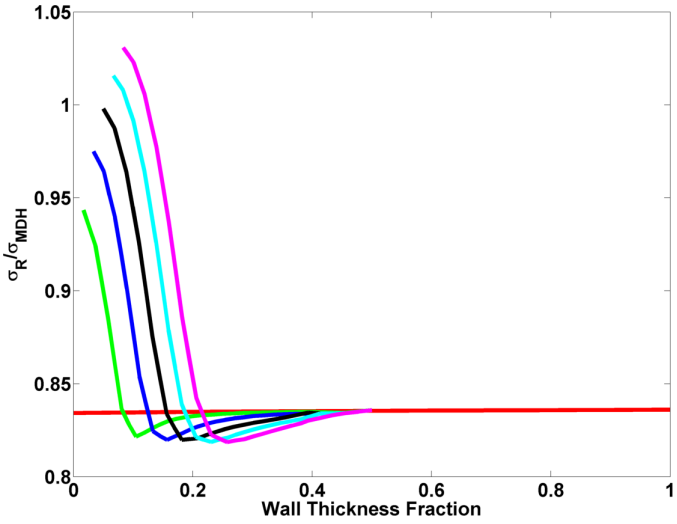

(b)

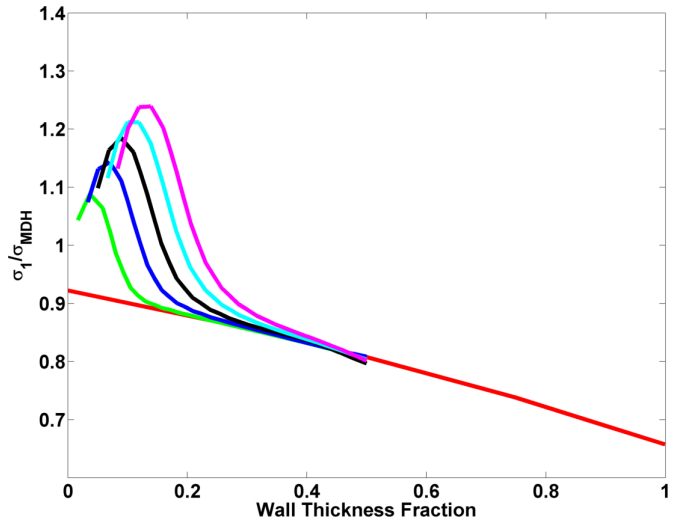

(c)

Figure 5.3: Typical variations of stress for a range of scoop sample depths. Behaviour is shown for (a) von Mises, (b) rupture ($\alpha = 0.3$) and (c) maximum principal stress.

5.3.2 Internal Pressure Loading Only (Closed End Condition)

Steady-state creep FEA analyses were conducted on straight pipe sections loaded only by an internal pressure (assuming closed end conditions). The equivalent von Mises (σ_{EQ}), rupture (σ_R, assuming $\alpha = 0.3$) and maximum principal stresses (σ_1) at the scoop excavation tip are plotted against cut depth in figure 5.4 (a)-(c), respectively.

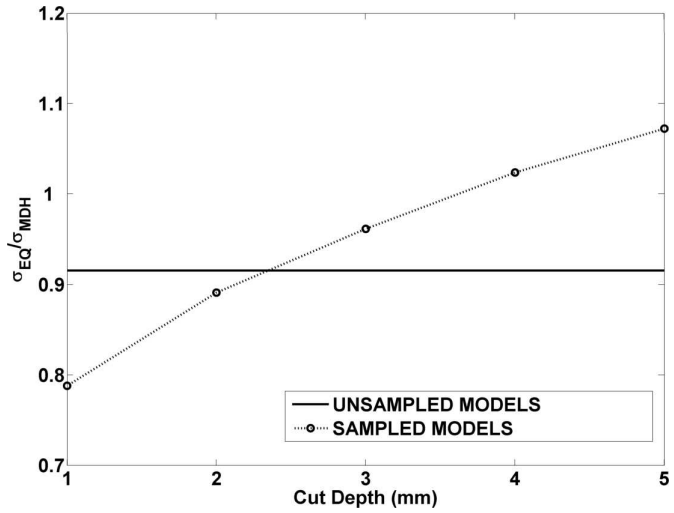

(a)

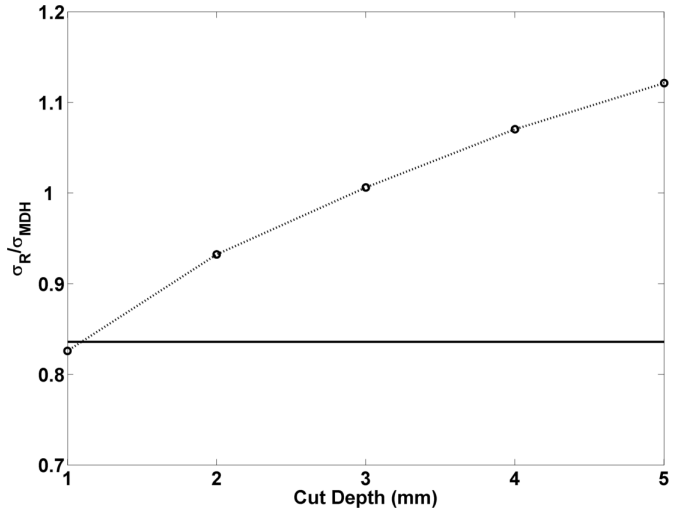

(b)

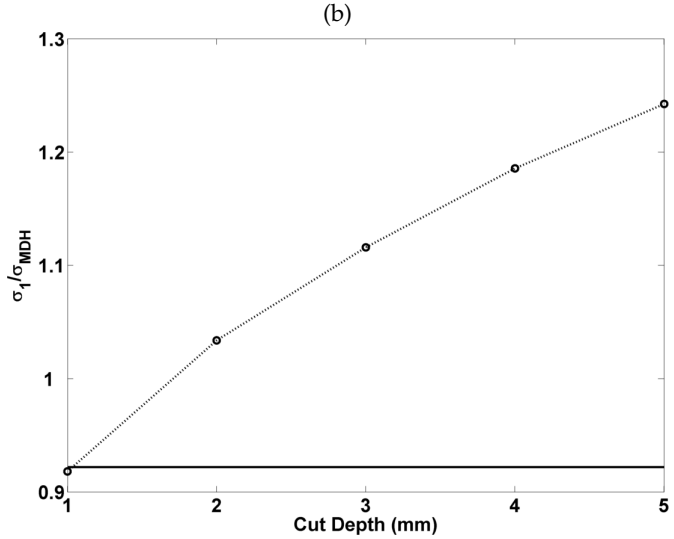

(c)

Figure 5.4: Results of FEA models (normalised to σ_{MDH}) loaded by internal pressure only (assuming closed end condition), showing (a) von Mises stress (σ_{EQ}), (b) rupture stress (σ_R, $\alpha = 0.3$) and (c) maximum principal stress (σ_1). Results are shown for a pipe with an outer diameter (D_O) of 360mm and a wall thickness (Th) of 60mm.

5.3.3 Internal Pressure and Additional Axial System Loading

Additional axial loads were applied to replicate system loading imposed on the pipe section. Two axial load magnitudes were applied in the tensile direction, namely the maximum permissible by PD 5500 (giving rise to a total axial load of $50MPa$) and a midway axial load (giving rise to a total axial load of $33MPa$). Using the loading parameter k, these loading conditions relate to k values of 1 and 0.5, respectively. Again, von Mises, rupture ($\alpha = 0.3$) and maximum principal stresses were recorded at the scoop excavation tip for a range of cut depths (see figures 5.5 and 5.5). The case where the only axial load applied is to satisfy the closed end condition represents a minimum axial load scenario (i.e. there is no additional axial load, therefore $k = 0$). Using the results in figures 5.5 and 5.5, the effects of additional axial loading (based on the parameter k) can be approximated (see figure 5.7).

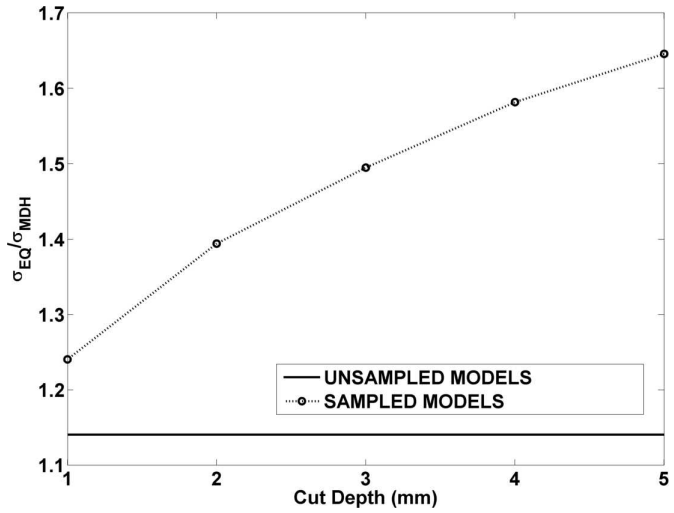

(a)

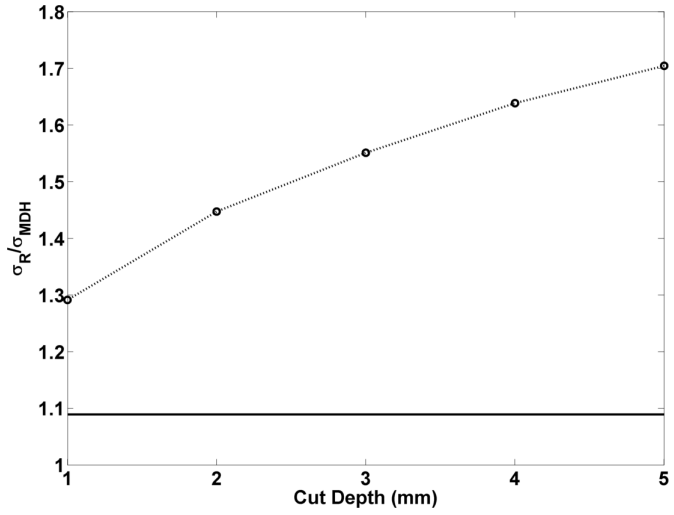

(b)

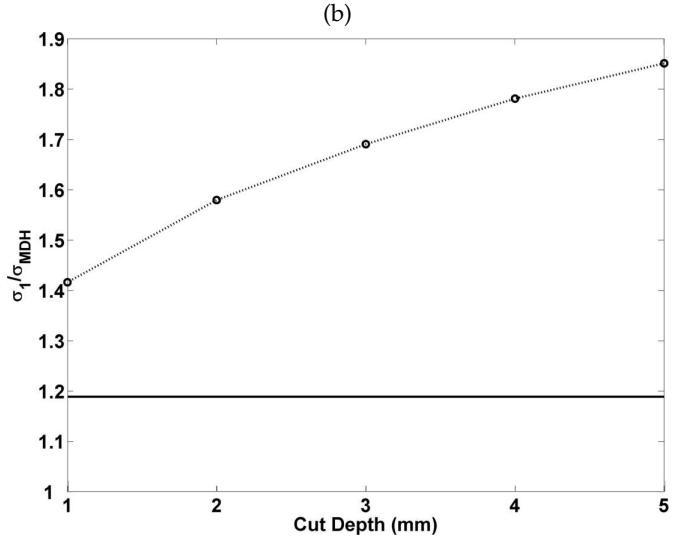

(c)

Figure 5.5: Results of FEA models (normalised to σ_{MDH}) loaded by internal pressure and additional axial loading (total axial pressure equal to a maximum of 50 MPa, or $k = 1$), showing (a) von Mises stress (σ_{EQ}), (b) rupture stress (σ_R, $\alpha = 0.3$) and (c) maximum principal stress (σ_1). Results are shown for a pipe with an outer diameter (D_O) of 360mm and a wall thickness (Th) of 60mm.

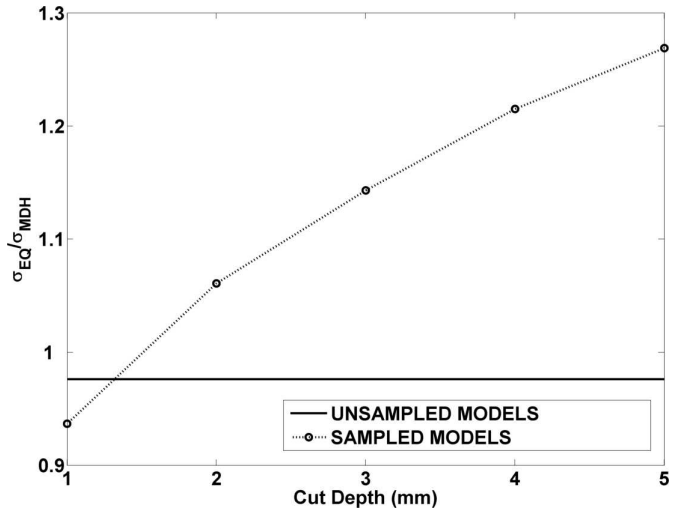

(a)

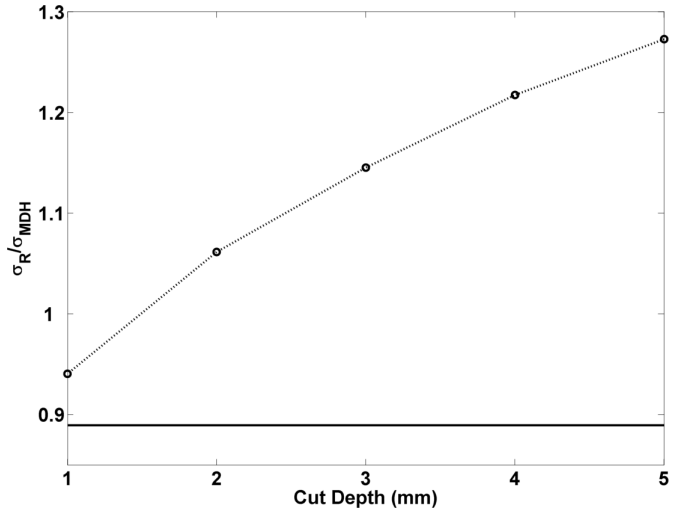

(b)

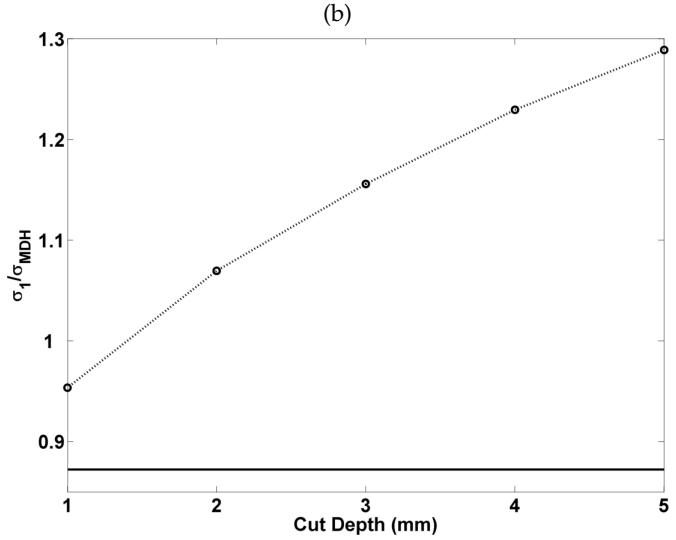

(c)

Figure 5.6: Results of FEA models (normalised to σ_{MDH}) loaded by internal pressure and additional axial loading (total axial pressure equal to 33 MPa, or $k = 0.5$), showing (a) von Mises stress (σ_{EQ}), (b) rupture stress (σ_R, $\alpha = 0.3$) and (c) maximum principal stress (σ_1). Results are shown for a pipe with an outer diameter (D_O) of 360mm and a wall thickness (Th) of 60mm.

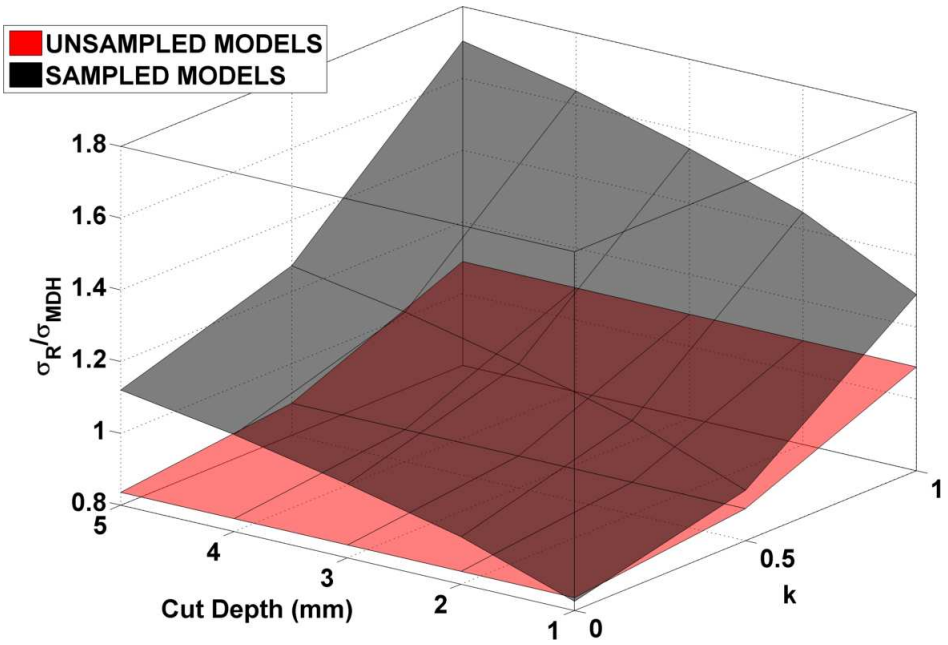

Figure 5.7: The effect of axial loading on the scoop excavation tip rupture stresses (σ_R, $\alpha = 0.3$) of a straight pipe section (outer diameter D_O of 360mm and a wall thickness Th of 60mm.). Note all stresses are normalised against σ_{MDH}. Results for an unsampled straight pipe section are included for comparison and to highlight possible "at risk" situations.

5.3.4 Internal Pressure and Bending System Loading

In plane bending moments were applied to the pipe section in the manner described in section 5.2.3. An axial load was applied in order to satisfy the closed end condition. The loading factor (k) in equation (5.8) was set to two values; 1, giving a maximum bending moment of 124.97 kNm and 0.5, giving a bending moment of 62.48 kNm. Stresses at the scoop excavation tip for a range of cut depths can be seen in figures 5.8 and 5.9, respectively. When $k = 0$, no bending moment is applied. This is equivalent to the model where only internal pressure loading is applied (section 5.3.2). A range of k values has therefore been simulated and its effect on rupture stress ($\alpha = 0.3$) can be approximated (see figure 5.10).

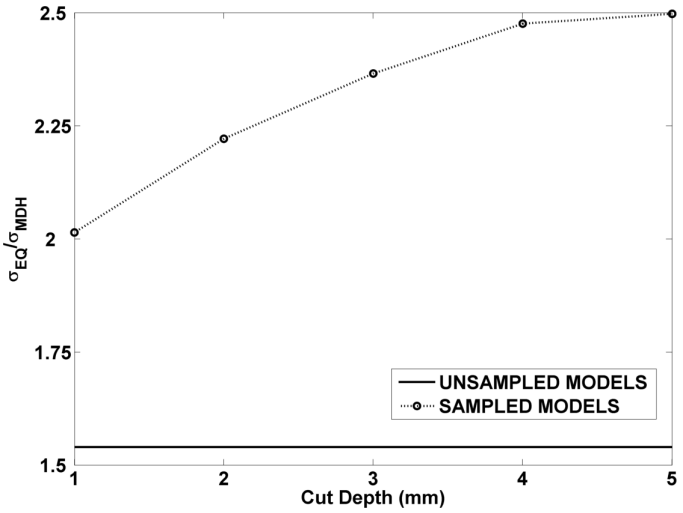

(a)

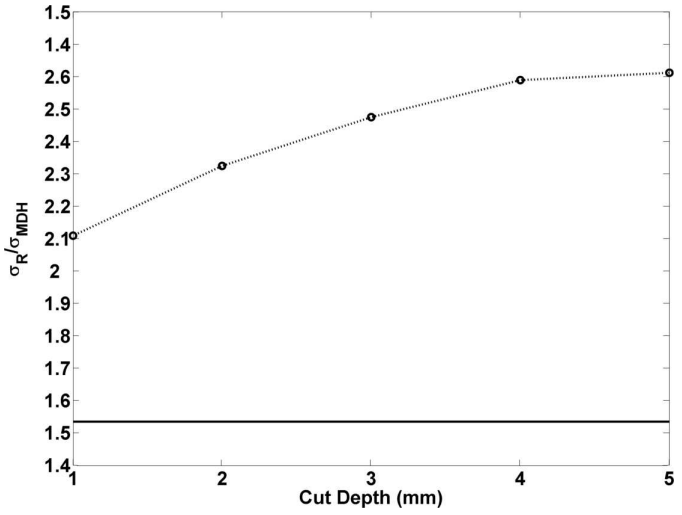

(b)

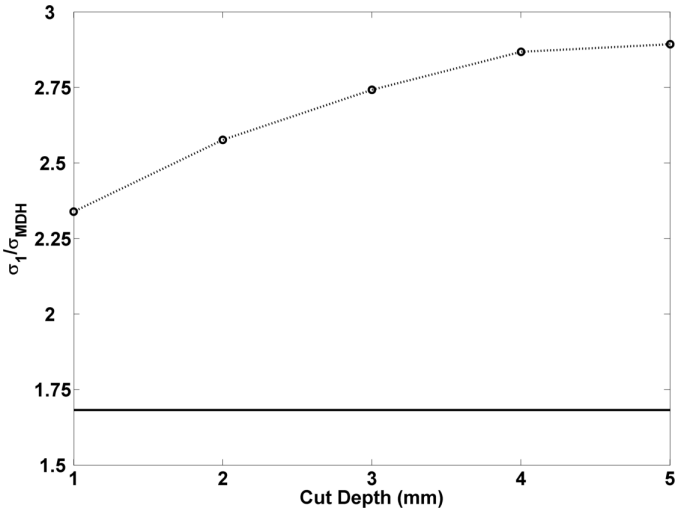

(c)

Figure 5.8: Results of FEA models (normalised to σ_{MDH}) loaded by internal pressure and an in plane bending moment ($k = 1$), showing (a) von Mises stress (σ_{EQ}), (b) rupture stress (σ_R, $\alpha = 0.3$) and (c) maximum principal stress (σ_1). Results are shown for a pipe with an outer diameter (D_O) of 360mm and a wall thickness (Th) of 60mm.

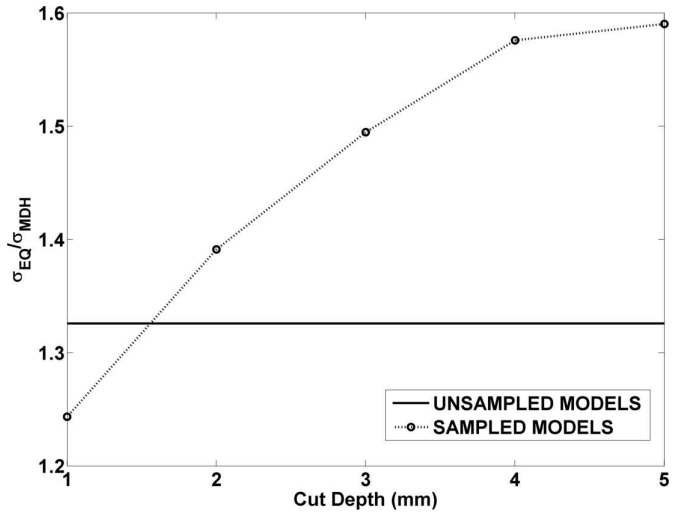

(a)

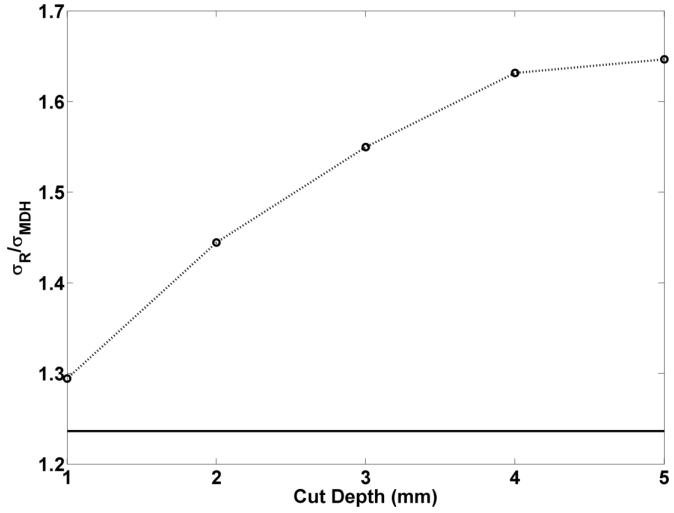

(b)

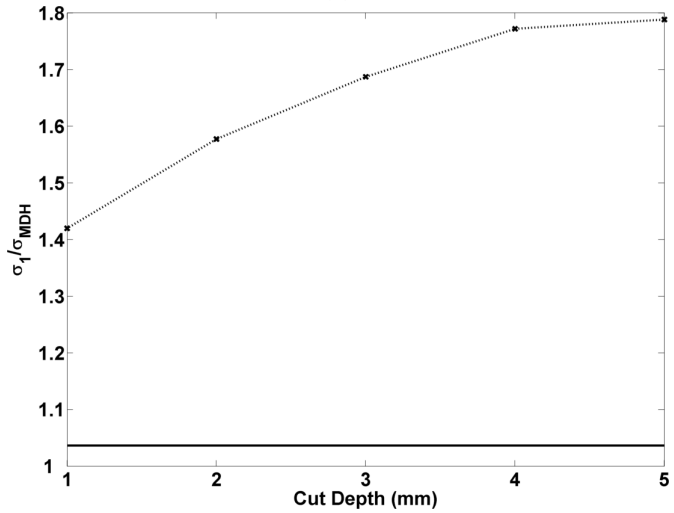

(c)

Figure 5.9: Results of FEA models (normalised to σ_{MDH}) loaded by internal pressure and an in plane bending moment ($k = 0.5$), showing (a) von Mises stress (σ_{EQ}), (b) rupture stress (σ_R, $\alpha = 0.3$) and (c) maximum principal stress (σ_1). Results are shown for a pipe with an outer diameter (D_O) of 360mm and a wall thickness (Th) of 60mm.

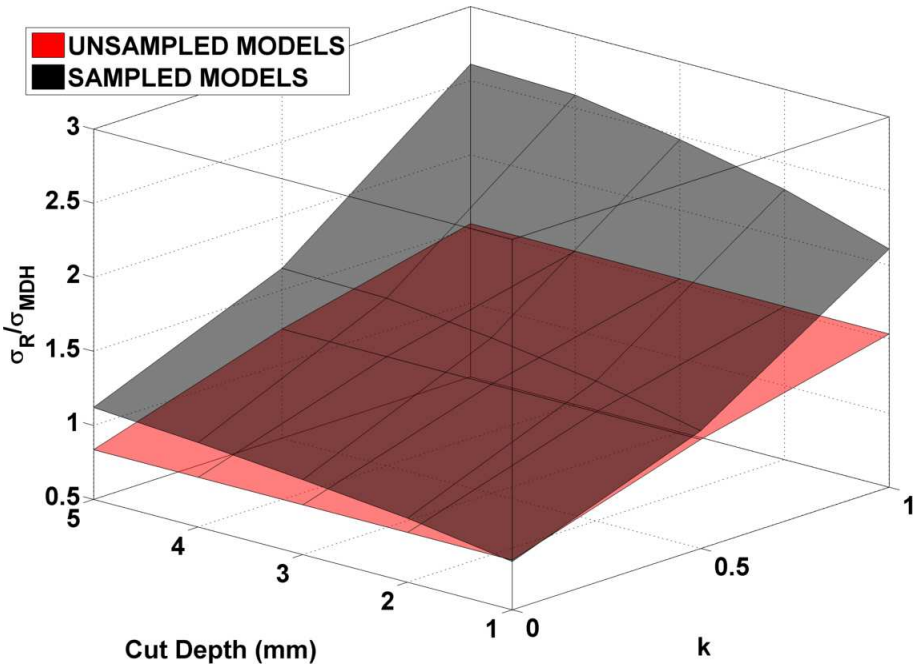

Figure 5.10: The effect of in plane bending moment loading on the scoop excavation tip rupture stresses (σ_R, $\alpha = 0.3$) of a straight pipe section (outer diameter D_O of 360mm and a wall thickness Th of 60mm). Note all stresses are normalised against σ_{MDH}. Results for an unsampled straight pipe section are included for comparison and to highlight possible "at risk" situations.

5.3.5 Effects of Tri-axial Material Constant (α) Values

A value of α has been assumed (0.3) for the calculation of rupture stress in the above analyses. Rupture stresses for the limiting values of α (0 and 1) are equivalent to the von Mises and maximum principal stresses, respectively. The dependency between the multiaxial material constant (α) and the rupture stress in scoop excavation models can therefore be estimated (for a given n value, namely 6.108) for each of the loading conditions considered so far (see figure 5.11).

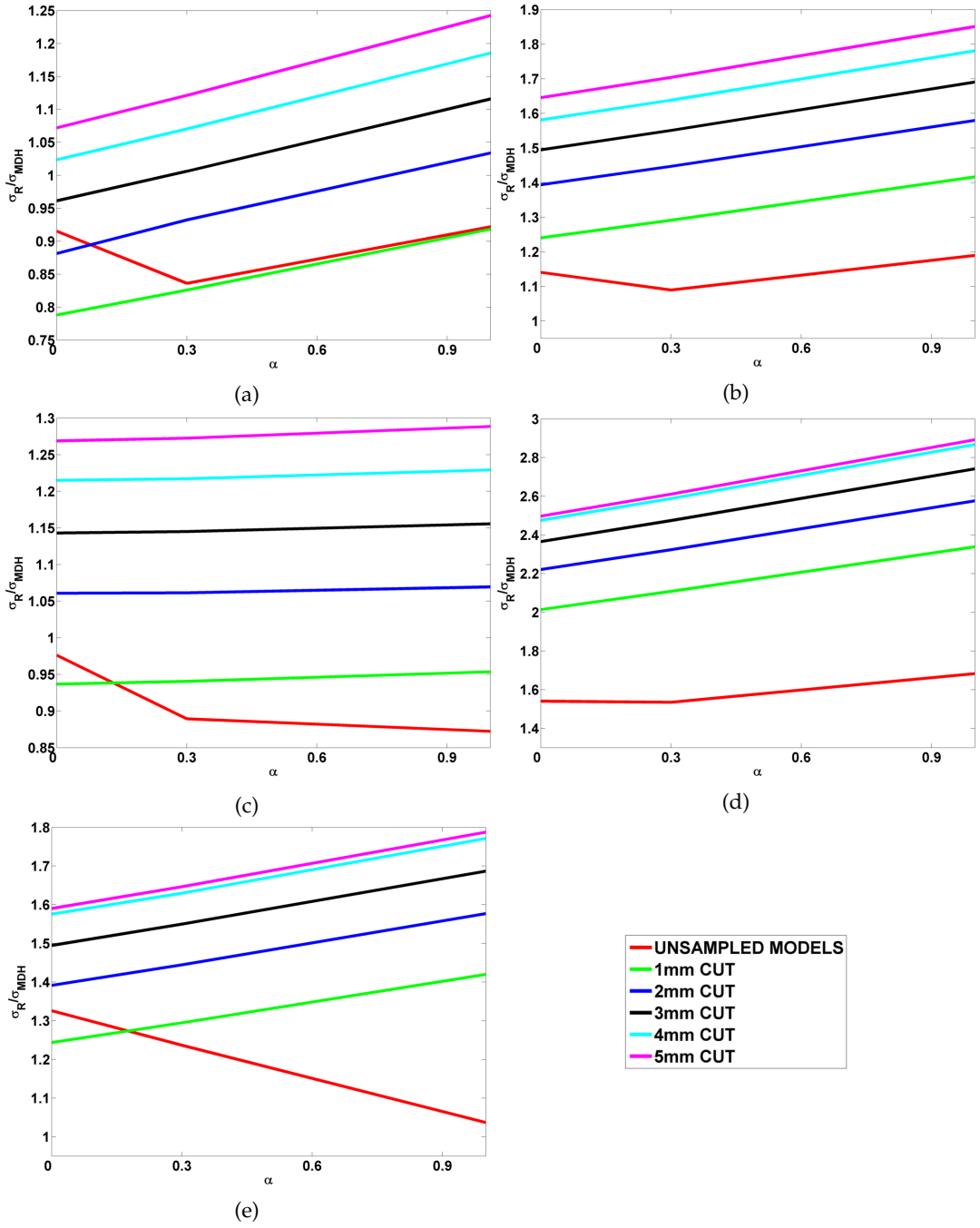

Figure 5.11: The effect of triaxial material constant (α) value on rupture stress (σ_R). Loading conditions shown are (a) internal pressure loading only assuming closed end condition, (b) internal pressure loading with an additional axial system load, totalling $50MPa$ ($k = 1$), (c) internal pressure loading with an additional axial system load, totalling $33MPa$ ($k = 0.5$), (d) internal pressure with an in plane bending moment, $k = 1$ and (e) internal pressure with an in plane bending moment, $k = 0.5$. Note all rupture stresses are normalised against σ_{MDH}. Results for an unsampled straight pipe section subjected to the same loading condition are included for comparison. Results are shown for a pipe with an outer diameter (D_O) of $360mm$ and a wall thickness (Th) of $60mm$.

5.3.6 Effect of Pipe Outer Diameter and Wall Thickness

In the previous sections, the stresses around a scoop excavation have been analysed for a single pipe geometry (characterised by an outer diameter, D_O, and a wall thickness, Th). In reality, a range of pipe section dimensions may be implemented on a power plant that are potential candidates for scoop sampling. In order to extend the applicability of the present work, several alternative pipe geometries with scoop samples have been simulated using the sub-modelling procedure.

In this study, four levels were defined for the outer pipe diameter D_O ($210mm$, $260mm$, $310mm$ and $360mm$) and for the pipe wall thickness Th ($40mm$, $50mm$, $60mm$ and $70mm$). Two cut depths (referred to as the parameter h in the parametric equation (5.9)) were also chosen, namely $2mm$ and $5mm$. Global and sub-models were created for each permutation of the above parameters, using the material constants $A = 6.599x10^{-16}MPa^{1/n}$ and $n = 6.108$ (note these are identical to the values used in the previous analyses). Two loading conditions were also applied, namely the closed end and maximum permissible axial load (i.e. total axial load is equivalent to σ_{MDH}) conditions. Using the results for these two load cases as limits, the effects of a range of system axial loads can be estimated. After completing the study described therefore, for each loading condition, FEA steady-state results were available for a range of pipe geometries ($210mm \geq D_O \geq 360mm$ and $40mm \geq Th \geq 70mm$) with two different cut depths ($2mm$ and $5mm$). Additionally, results from the previous analyses allowed for the consideration of a range of cut depths ($1mm \geq h \geq 5mm$) for a fixed pipe geometry ($D_O = 360mm$ and $Th = 60mm$).

Generally, pipe sections with identical h values and D_O/Th ratios have similar rupture stress values at the scoop excavation tip. Therefore, in an attempt to approximate the steady-state rupture stress response of a sampled straight pipe section, a polynomial expression (equation (5.9)) was developed, with the parameters h and D_O/Th acting as independent variables. The constants $A - I$ are material and loading case dependent, and were determined using a polynomial fitting procedure, implemented in MATLAB[187,188]. These values can be seen in table 5.1, with a plot of the parametric equation and FEA results shown in figure 5.12. Typically, the fitted surface defined by equation (5.9) lead to coefficients of determination (r^2, see section 3.8.5) greater than or equal to 0.94. Stresses in plain pipes under steady-state conditions can be determined using equation (2.104)[130], and so "at risk" sampling conditions can be identified.

$$\begin{aligned}\frac{\sigma_R}{\sigma_{MDH}}\left(\frac{D_O}{Th},h\right) = A\frac{D_O}{Th}^4 + B\frac{D_O}{Th}^3 + C\frac{D_O}{Th}^2 + Dh^2 + \cdots \\ \cdots E\left(\frac{D_O}{Th}^2 + h^2\right) + F\frac{D_O}{Th} + Gh + H\left(\frac{D_O}{Th} + h\right) + I\end{aligned} \tag{5.9}$$

Table 5.1: Fitting constants for the parametric equation (5.9), giving steady-state rupture stresses ($\alpha = 0.3$) at a scoop excavation tip (assuming the material constants $A = 6.599x10^{-16} MPa^{1/n}$ and $n = 6.108$).

Constant	Closed End Condition	Maximum Axial Load
A	$-3.9368x10^{-3}$	$-1.6471x10^{-4}$
B	$1.0158x10^{-1}$	$4.0671x10^{-3}$
C	$-6.3298x10^{-2}$	$4.3038x10^{-1}$
D	$8.9586x10^{-1}$	$4.6312x10^{-1}$
E	$-8.9664x10^{-1}$	$-4.6490x10^{-1}$
F	2.4479	$6.1983x10^{-1}$
G	-1.4768	$5.4876x10^{-1}$
H	1.5044	$-5.1636x10^{-1}$
I	-5.0899	1.1498

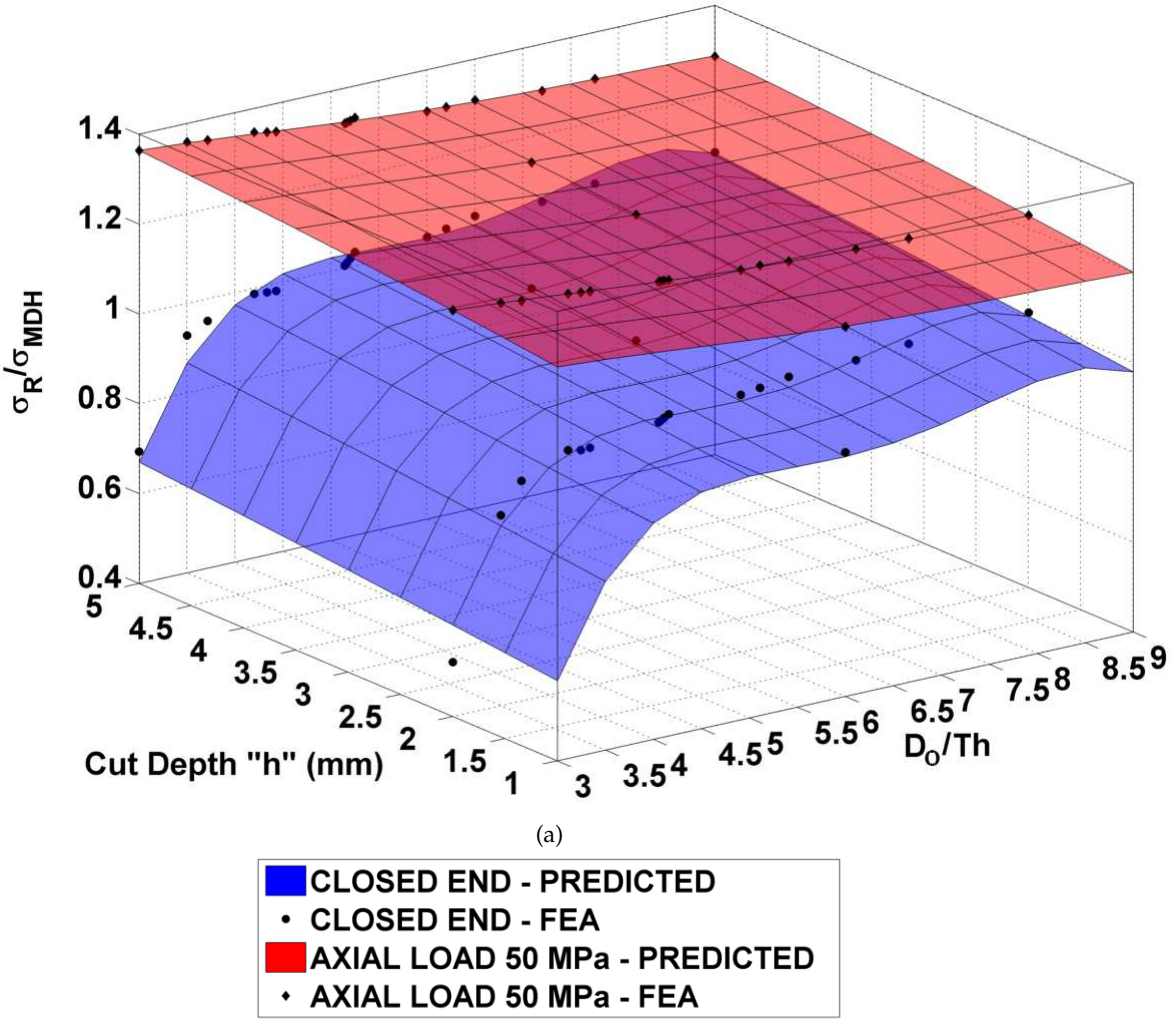

(a)

Figure 5.12: Steady-state rupture stress surfaces predicted by the parametric equation (5.9). FEA results are included for comparison.

Using equation (5.9) and the constants given in table 5.1, steady-state rupture stresses can be determined for a material with the stress exponent (n) equal to 6.108. In reality a range of n values will be encountered for different materials under various operating conditions[196]. A linear relationship has been established between the steady-state creep stress at a point in a structure and $1/n$ by Calladine[197] (see figure 5.13). Localised peak rupture stresses will occur at the scoop excavation tip; therefore the linear relationship is valid and can be applied for a range of stress exponent values. To interpret this linear relationship for any n value, at least two data points will be required. A limit value for the steady-state stress can be found by assuming $n = 1$, which is equivalent to the linear elastic solution. Constants for equation (5.9) are provided in table 5.2 that predicted linear elastic rupture stresses at the scoop excavation tip. By calculating steady-state rupture stresses for the two reference n values ($n = 6.108$ and $n = 1$) and evaluating Calladine's linear relationship, an estimation of the steady-state rupture stress at a notch

tip can be made for any n value.

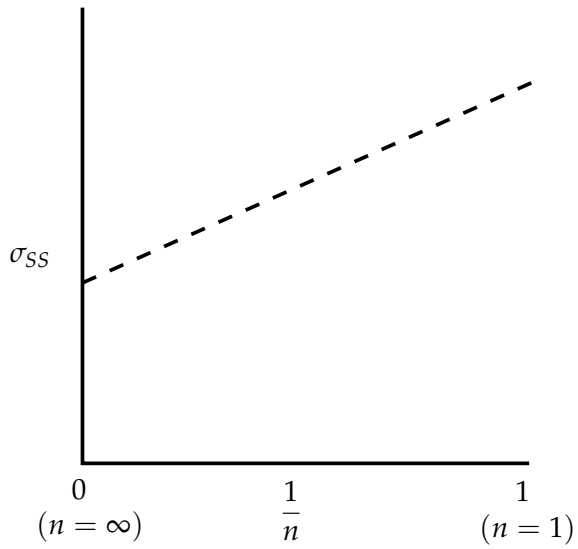

Figure 5.13: Illustration of the linear effect of the inverse of the stress exponent $(1/n)$ on the steady-state creep stress (σ_{SS}), identified by Calladine[197,198].

Table 5.2: Fitting constants for the parametric equation (5.9), giving linear elastic rupture stresses ($\alpha = 0.3$) at a scoop excavation tip (assuming the material constants $E = 200GPa$ and $\nu = 0.3$).

Constant	Closed End Condition	Maximum Axial Load
A	$-1.1124x10^{-3}$	$3.2907x10^{-5}$
B	$3.0901x10^{-2}$	$-1.4179x10^{-3}$
C	$2.7403x10^{-1}$	$4.5524x10^{-1}$
D	$5.9248x10^{-1}$	$4.2252x10^{-1}$
E	$-6.0312x10^{-1}$	$-4.3724x10^{-1}$
F	1.2981	$5.0501x10^{-1}$
G	$-2.3963x10^{-1}$	$7.5943x10^{-1}$
H	$3.7362x10^{-1}$	$-5.6899x10^{-1}$
I	-2.6954	1.1318

To verify that the parametric equation and optimised fitting constants allow for accurate estimation of localised rupture stresses, several sampling cases have been

simulated that were not included in the original study. Geometries are typical of those used in power plant and are located around the centre of the tested ranges of D_O/Th and h. These were applied to both the closed end and maximum allowable axial load cases (see tables 5.3 and 5.4, respectively). Both steady-state and elastic rupture stresses have been compared. Typically, errors are less that 1%, with a peak error of 2.79%. The parametric equation is therefore deemed to be representative and applicable.

The predicted interpolation results (shown in tables 5.3 and 5.4) have been used in conjunction with Calladine's method to predict steady-state creep peak rupture stresses for alternative n values (n does not equal the elastic value of 1 or the considered creep value of 6.108). These are presented in table 5.5. A peak error of 5.69% is observed, however the results for n values closer to the reference value (6.108) are generally predicted with a greater degree of accuracy (less than 1%). Linear interpolation and extrapolation between the surfaces predicted by equation (5.9) is therefore considered to be viable.

Table 5.3: Comparison of predicted (from parametric equation (5.9)) and FEA localised (at the scoop excavation tip) peak rupture stresses ($\alpha = 0.3$) for a straight pipe section acting under a closed end loading condition. Note that material constants are assumed to be $E = 200GPa$, $\nu = 0.3$, $A = 6.599x10^{-16}MPa^{1/n}$ and $n = 6.108$.

Model	σ_R/σ_{MDH} - FEA, Steady-State Creep	σ_R/σ_{MDH} - FEA, Elastic	σ_R/σ_{MDH} - Predicted, Steady-State Creep	σ_R/σ_{MDH} - Predicted, Elastic	% Error, Steady-State Creep	% Error, Elastic
$D_O = 270mm$ $Th = 41mm$ $h = 2.6mm$	1.0024	1.0497	0.9802	1.0511	2.21	0.13
$D_O = 320mm$ $Th = 61.5mm$ $h = 3.2mm$	0.9819	0.9333	0.9902	0.9508	0.85	1.88
$D_O = 260mm$ $Th = 50mm$ $h = 3mm$	0.9826	0.9326	0.9856	0.9367	0.31	0.44
$D_O = 300mm$ $Th = 65mm$ $h = 4mm$	0.9775	0.8857	1.0016	0.9090	2.47	2.63

Table 5.4: Comparison of predicted (from parametric equation (5.9)) and FEA localised (at the scoop excavation tip) peak rupture stresses ($\alpha = 0.3$) for a straight pipe section acting under the maximum allowable axial load loading condition. Note that material constants are assumed to be $E = 200GPa$, $\nu = 0.3$, $A = 6.599x10^{-16}MPa^{1/n}$ and $n = 6.108$.

Model	σ_R/σ_{MDH} - FEA, Steady-State Creep	σ_R/σ_{MDH} - FEA, Elastic	σ_R/σ_{MDH} - Predicted, Steady-State Creep	σ_R/σ_{MDH} - Predicted, Elastic	% Error, Steady-State Creep	% Error, Elastic
$D_O = 270mm$ $Th = 41mm$ $h = 2.6mm$	1.2239	1.5408	1.2581	1.5437	2.79	0.19
$D_O = 320mm$ $Th = 61.5mm$ $h = 3.2mm$	1.2911	1.5571	1.2913	1.5693	0.02	0.78
$D_O = 260mm$ $Th = 50mm$ $h = 3mm$	1.2886	1.5443	1.2870	1.5494	0.12	0.33
$D_O = 300mm$ $Th = 65mm$ $h = 4mm$	1.3177	1.6056	1.3183	1.6217	0.05	1.00

Table 5.5: Comparison of predicted (from parametric equation (5.9)) and FEA localised (at the scoop excavation tip) steady-state peak rupture stresses ($\alpha = 0.3$) for a range of pipe geometries and Norton's law stress exponent (n) values. Note that elastic material constants are assumed to be $E = 200GPa$ and $\nu = 0.3$.

Model	σ_R/σ_{MDH} - FEA, Steady-State Creep	σ_R/σ_{MDH} - Predicted, Steady-State Creep	% Error, Steady-State Creep
$D_O = 270mm$, $Th = 41mm$, $h = 2.6mm$, $n = 5$, Closed End Condition	1.0426	0.9833	5.69
$D_O = 320mm$, $Th = 61.5mm$, $h = 3.2mm$, $n = 7$, Maximum Axial Load Condition	1.2807	1.2844	0.29
$D_O = 260mm$, $Th = 50mm$, $h = 3mm$, $n = 3$, Closed End Condition	0.9329	0.9757	4.59
$D_O = 300mm$, $Th = 65mm$, $h = 4mm$, $n = 8$, Maximum Axial Load Condition	1.2953	1.3043	0.69

5.4 Discussion

Scoop sampling from in service high temperature components is gaining popularity as a method to retrieve material for the manufacture of novel small specimens. Small specimen tests could be used to determine material constants for constitutive models (if adequate interpretation techniques can be established) or alternatively to perform ranking studies to identify degraded components. It is vital that scoop sampling itself does not impair the structural integrity of the sampled component and thus limit future operation. A thick walled main steam type pipe section (a potential candidate for scoop sampling) has been considered in the present work (with an external diameter of $360mm$ and a wall thickness of $60mm$). Scoop excavations (of various depths) have been approximated using FEA sub-modelling techniques. In addition to loading due to internal pressure, system loads such as axial pressures and bending moments have also been applied. Generalised parametric equations have been proposed and verified for a range of pipe geometries and cut depths.

Examination of the "UNSAMPLED MODEL" curves in figure 5.3 highlights that steady-state rupture stresses are approximately constant through the wall thickness of the pipe if $\alpha = 0.3$ (a typical value). This is distinctly different to the von Mises and maximum principal stresses, where peak values may be observed at the external and

internal surfaces (depending on the loads applied to the pipe section). It can be seen from all of the results plots that stress profiles converge on this "UNSAMPLED MODEL" plain pipe profile with increasing distance along the wall thickness. The effects of a scoop excavation are therefore localised around the notch. The inclusion of a scoop excavation causes a stress concentration at the tip of the notch (see figure 5.14), however this concentrated stress may not exceed the magnitude of the maximum stress in the unsampled model (see figure 5.3 (a)). In these situations, it is reasonable therefore to expect that failure is controlled by the highly stressed region at, say, the inside surface of the pipe (in the present work, this is considered a "safe" condition). These observations are drawn from static loading analyses. Under cyclic loading conditions the effects of the scoop excavation may be exacerbated, therefore this will be the focus of future work.

Under internal pressure loading only (closed end condition, see figure 5.4 (b)), almost all scoop excavations appear to have peak localised rupture stresses that are greater than the stresses normally encountered in an identically loaded plain pipe section (i.e., the excavations are not considered safe). Shallow scoop samples ($\approx 1mm$ deep) however have been shown to be safe as even peak maximum principal stresses in the vicinity of the scoop sample are less than those in the unsampled pipe. It can therefore be concluded that, for most power plant materials at least, shallow scoop sampling in thick walled straight pipework is safe provided that system loads are negligible in the pipe section. After the application of an additional axial load however ($50MPa$ and $33MPa$ total axial loading, shown in figures 5.5 and 5.6, respectively), all scoop samples exhibit failure dominant stress states. Bending moments were applied to the pipe models in order to approximate an alternative system load (figures 5.8 and 5.9). In general the effect of the application of a bending moment is the same as that of an additional axial load, in so much as the rupture stress in the vicinity of the excavation exceeds that of the plain pipe maximum rupture stress. The orientation of the bending moment is such that a tensile stress is induced in the upper section of the pipe (i.e. the scoop excavation is opened). When considering these above results it is important to bear in mind that while the orientation of the bending loads is the "worst case", the load magnitudes are permissible by PD 5500 and it is therefore reasonable to consider these loading conditions potentially occurring. An increase in the loading parameter k generally reduces the critical cut depth (see figures 5.7 and 5.10), however bending moment effects tend to be more severe due to the "opening" loading orientation.

By noting that the limits of the steady-state rupture stresses (i.e. when $\alpha = 0$ or 1) are the equivalent von Mises and maximum principal stresses, respectively, the effect of the value of α can be estimated in the present work (figure 5.11). The general trend observed is that, in all loading cases, an increase in the multiaxial material constant α leads to a greater proportion of the scoop sampling situations being at risk (i.e. the critical depth of scoop sample reduces with increasing α). This effect is due to the increasing dependence on the maximum principal stress with an increasing α when calculating the rupture

stress. With a scoop excavation feature acting as a stress concentration, maximum principal stresses are typically far more sensitive to excavation depth variations than von Mises stresses. In ductile failure conditions, a shear stress failure criterion may be appropriate, hence the von Mises stress (octahedral shear stress criterion[28], see section 2.3.2) is controlling. In brittle situations, a maximum principal stress failure criterion is more representative, hence the values of α for those materials would be tend to 1. While most materials deform in a ductile fashion under power plant loading, it is foreseeable that for some materials, such as the heat affected zone (HAZ) regions of weldments, brittle deformation mechanisms may be present. Due to the small amount of HAZ material and its critical importance in component analysis, this region is a candidate for scoop sampling. Scoop sampling of HAZ regions must therefore be conducted with great care due to their commonly brittle nature and the effects of the scoop sample acting as a stress concentration.

Under system loading, the inclusion of a notch can cause a shift in the direction of the maximum principal stress. Hoop direction maximum principal stresses are observed for the closed end condition loading (figure 5.14 (a)), however these shift to axial direction maximum principal stresses for cases with system loading (figure 5.14 (b), (c), (d) and (e)). In the case of bending system loads, it has been observed that there is a transition between an axial principal stress (induced by the bending system load) and, some way into the wall thickness, a hoop principal stress (induced by the internal pressure loading). Figure 5.14 (e) verifies that at the external surface of the pipe the maximum principal stress is axial in direction. The stress concentration effects of the scoop excavation may have more serious consequences if a defect (such as a crack) is present in the notch. It is foreseeable that such defects could be initiated by the sample extraction process. High stress regions in the excavation could cause the propagation of these cracks, particularly in terms of maximum principal stresses which could potentially open the defect in mode 1 deformation[28]. The variation in maximum principal stress direction could potentially lead to cracks in almost any direction propagating under transient system loading. This effect would be exacerbated if loadings are cyclic (which is typical of power plant components).

In order to highlight the effect of localised scoop excavation rupture stresses on failure time of a pipe component, rupture times were calculated from the rupture stresses for the $\phi = 360mm$ and $t = 60mm$ study. This was done using equation (5.2) and the material constants given in table 5.6. Results are presented in figure 5.15. Values of k used are 0, 0.5 and 1. Predicted times to failure (t_f) have been normalised against the predicted time to failure for an unsampled pipe component ($t_{f\,o}$). "At risk" sampling scenarios lead to $t_f/t_{f\,o}$ ratios less than 1. Under additional axial loading (see figure 5.15 (a)), it can be seen that failure is not controlled at the scoop excavation tip for a $1mm$ deep cut, therefore taking the scoop sample is considered to be "safe". Conversely, a $5mm$ deep cut in a pipe with a maximum permissible axial load can lead to a failure time

which is approximately 20% of the original components. Similar trends can be observed for the bending moment loading cases (see figure 5.15 (b)); however critical cut depths are far less. It should be noted that, when using the steady-state reference rupture stress method, rupture is assumed to occur only in the element of material subjected to the peak rupture stress. In situations other than simple uniaxial loading, this may relate to the formation of a surface crack rather than full thickness cleavage.

Table 5.6: Kachanov law material constants for $1/2Cr1/2Mo1/4V$ at 640°C[139].

A	n	B	χ	ϕ	m	α
$6.599x10^{-16}$	6.108	$1.091x10^{-14}$	5.767	4.5	0.00	0.3

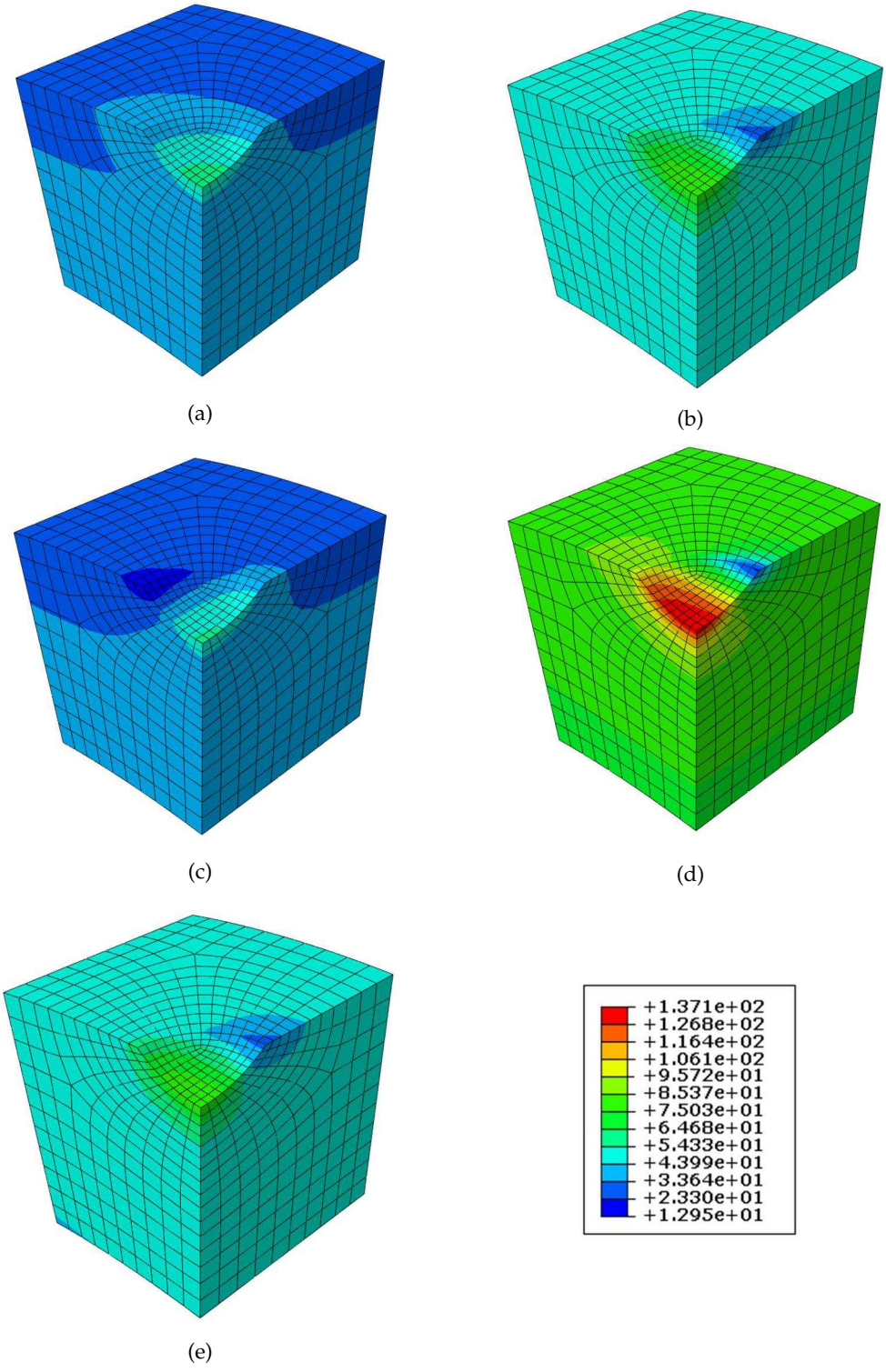

Figure 5.14: Example FEA contour plots showing maximum principal stress for (a) internal pressure loading only, assuming closed end condition, (b) internal pressure loading with an additional axial system load, totalling $50MPa$ ($k = 1$), (c) internal pressure loading with an additional axial system load, totalling $33MPa$ ($k = 0.5$), (d) internal pressure with an in plane bending moment, $k = 1$ and (e) internal pressure with an in plane bending moment, $k = 0.5$. Results are shown for a pipe with an outer diameter of $360mm$ and a wall thickness of $60mm$. A $3mm$ cut depth (h) has been applied.

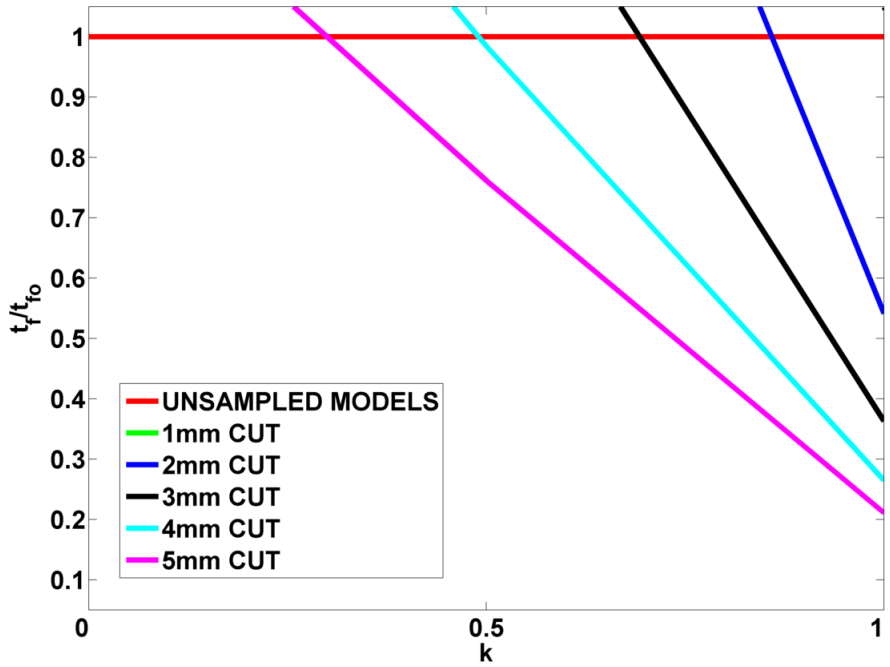

(a)

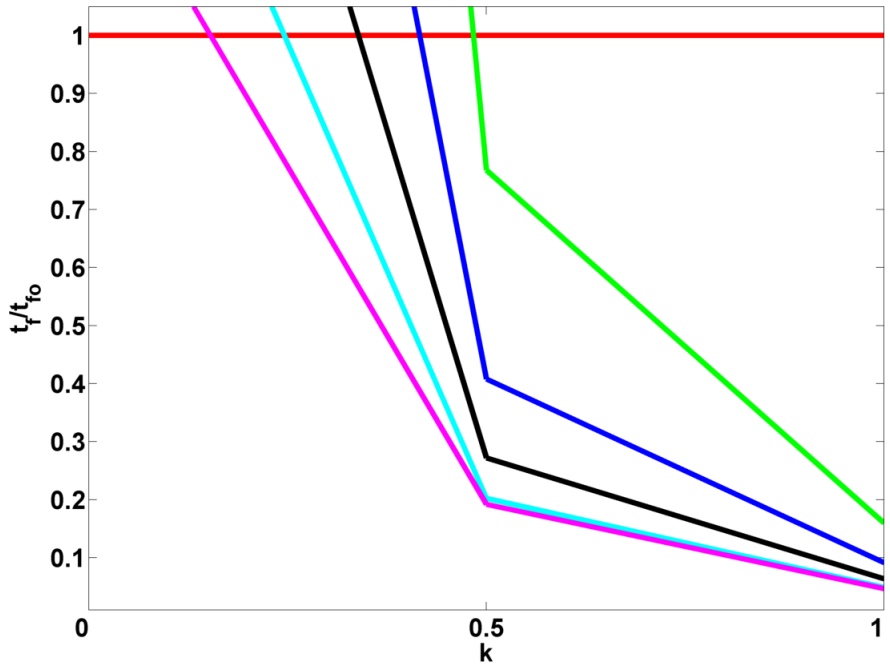

(b)

Figure 5.15: The effect of scoop sampling on predicted rupture times (t_f) for pipe components. Note all rupture times are normalised against the rupture time for an unsampled pipe component ($t_{f\,o}$). Loading conditions considered are (a) additional axial loading and (b) in-plane bending moment loading. Values greater than 1 are omitted, as this does not represent scoop controlled failure of the component. Results are shown for a pipe with an outer diameter of $360mm$ and a wall thickness of $60mm$.

5.5 Conclusions

Small specimen testing is an exciting field that has the potential to address the practical limitations of conventional full size specimen testing. One such advantage is the ability to perform mechanical tests on material from in service components without compromising structural integrity and future operation. Samples can be taken from these in service components using novel in situ techniques such as the scoop sample machine developed by Rolls-Royce[151]. To analyse the effects of scoop sampling on the creep response of straight pipe sections, an investigation was carried out whereby the depth of excavation was varied between $1mm$ and $5mm$. The pipe sections were loaded by an internal pressure and, in some cases, additional system (axial pressure or in-plane bending moment) loading. An in depth investigation has been completed for one pipe geometry ($D_O = 360mm$ and $Th = 60mm$) for a range of cut depths and loading conditions. For two of the most applicable loading conditions (a closed end condition and a maximum permissible additional axial load), a range of pipe geometries were simulated in FEA and a parametric expression has been proposed to predict the rupture stress at the excavation tip.

The application of internal pressure loading alone tends to lead to safe operating conditions (i.e. failure of the component is controlled by the same stress state as the unsampled pipe component) for shallow excavations ($1mm$). The application of system loading, either by additional axial load or an opening bending moment, leads to a reduction in the critical scoop sample depth (i.e. the depth at which the stress state localised around the scoop exceeds the stress in the plain pipe section). Increasing values of the multiaxial material constant (α) also reduces the critical scoop depth by promoting an increased dependence on the maximum principal stress in rupture stress calculations. Using the trends described and the parametric equation proposed the scoop sample stress concentration effect can be estimated for a wide range of materials and pipe geometries.

Straight pipe section will not be the only locations of scoop sampling and loads will commonly not be steady. Transient periods will almost certainly be encountered as generators attempt to match market trends to energy requirements. This potentially induces cyclic hardening or low cycle fatigue in power plant components. Furthermore, the behaviour of potentially weak discontinuities in pipe systems, such as weldments or bends, will hold the greatest concern for practising engineers. Future work will therefore focus on the effects of scoop sampling under these conditions. Additionally, it has been noted that there is a similarity between the scoop type excavation and penny shaped cracks. Future work will also therefore attempt to generalise the derived empirical equation to include elliptical excavations.

Chapter 6

Novel Characterisation and Modelling Methods for Power Plant Pipe Bends

6.1 Introduction

Pipe bends represent geometric discontinuities in the steam pipe systems of power plants, therefore understanding the behaviour of these potential locations of weakness is of great industrial importance for component inspection, design and analysis. Due to the high operating temperatures encountered, the failure mechanism of creep is a justified concern. Furthermore, while the geometry of pipe bends appears to be simplistic, the manufacturing process employed results in variations to the critical dimensions of the pipe bends. It is these variations in geometry that can cause potentially significant differences in peak steady-state rupture stress magnitude (approximately 48% in some of the cases considered in the present chapter). Commonly dimension variation is either not incorporated into design calculations or is greatly simplified (see section 2.4), therefore components are oversized with conservative life estimations[107]. A method is therefore required that can characterise the complex dimension variation observed in pipe bends so that comparative studies can be completed.

In the present chapter (through analysis of industrial data supplied by E.On UK), several novel non-dimensional parameters have been established, allowing for (with suitable constraint equations depending on the type of bends analysed) the approximation of the complexity of pipe bend geometry in only a few dimension factors. Using these factors, systematic FEA studies may be completed (with these non-dimensional parameters taking account of a range of geometry variation). Using this philosophy, the stress states and failure lives of pipe bends of the same type (i.e. Hot Reheat or Main Steam types) with similar, but not identical, dimensions may be estimated and compared using approximations of the peak rupture stress function. By way of example,

this procedure is applied to thick walled Main Steam and thinner walled Hot Reheat type 90° pipe bend geometries under internal pressure loading only.

Fitting constants used in the non-dimensional parameter characteristic equations (which will be pipe bend type dependent) may be determined from 3D FEA analyses. It can be computationally expensive however to perform these analyses. A novel interpolation method is presented at the end of this chapter which addresses this problem. Several axi-symmetric 2D analyses are preformed that represent the cross sections of a 3D pipe bend model with dimension variation at specific bend positions. The overall stress state of the 3D pipe model (in particular, the peak rupture stress value and location) can be estimated by interpolating between these 2D approximations.

6.2 Background

The degree of wall thickness variation (with respect to some nominal value such as the uniform wall thickness of the straight pipe section) will differ around the pipe bend. Despite this known variation in geometry, most work to date has focused on idealised dimensions (for example, assuming a uniform thickness or constant cross section around the bend section). While bespoke pipe bend FEA analysis may yield a solution in which the user has some confidence, the investment of both time and expertise in establishing such models often places this analysis option outside the reach of practising engineers wishing to make some assessment on component structural integrity. Alternatively, non-destructive testing[105] may be used to evaluate the remnant life of pipe work. However, this is also time consuming, demands specialist equipment and requires prior knowledge of the approximate location of failure. Appropriate FEA has clear advantages, but representative 3D modelling methodologies need to be developed to ensure the consistency of results. Also, the results of the simulations need to be presented in an easy to access and practically relevant form.

Given that pipe work used in power plant generally operates at high temperatures and is subjected to an internal pressure, creep is of great concern and there is a clear industrial demand for methods which can be used to estimate the residual creep life in areas of potential weakness (such as pipe bends). Such procedures would enable more effective inspection and replacement strategies. Due to the complex nature of the loading of pipework systems (i.e. fluctuations in operating temperature, internal pressure and system loading etc.), plant was often originally commissioned based on conservative life estimates. Retired components therefore commonly have been found to still be serviceable[105,107]. A greater understanding of creep life in areas of interest within a pipe system could aid in operating the plant for extended periods with confidence. Furthermore, as power generation companies attempt to maximise plant efficiency by operating at higher steam temperatures and pressures, loading on these components will become more arduous. Additionally, improved generation flexibility (implemented in order to meet varying market demands) would impose greater transient loads on

system components. A greater understanding and predictive capability of the creep behaviour of critical plant components would allow these practices to be adopted safely.

For 3D pipe bend analysis, a large proportion of the published literature is concerned with the determination of plastic collapse loads for pipe bends[118,120,132,134,135]. However, relatively little work has been reported to date relating to the effects of the variation in cross section dimensions around pipe bends on the reduction of the component's creep life. Usually, simplified creep analyses are performed, assuming rotational symmetry and/or constant wall thickness[139]. Under these conditions and assuming that system loading is negligible (i.e. internal pressure is the only loading) steady-state stresses in a 2D axi-symmetric approximation are very close to those in the 90° pipe bend[118,138]. Providing good estimations of stresses in power plant components is of critical importance as the effects of inaccurate prediction of stress states can be severe in plant integrity assessment procedures. The R5 procedure, for example, is widely applied to the analysis of high temperature power plant structures[125] and can accommodate creep in its failure criterion[199]. It is dependent upon determining an elastic stress for the structure which can be related to a reference stress (σ_{REF})[125]. The danger posed by various failure criteria (such as creep rupture or creep fatigue interaction) may then be assessed. For elastic stresses to be estimated in complex structures however, detailed FEA may be required. Accurate methods for characterising pipe bends (with cross sectional dimension variations) in FEA packages are therefore in high demand. Parametric studies used to characterise 90° pipe bends in the past have usually involved the use of 2D FEA approximations. Most notably, Yaghi et. al.[104] developed parametric functions for the determination of steady-state peak rupture stresses, based on five geometric factors and two material constants.

In the present chapter, a simple Norton's material behaviour model has been used to represent a pipe bend material in FEA. Norton's law describes the steady-state creep region strain rate using a stress multiplier (A) and exponent (n). The stress exponent value can give an indication to the controlling mechanism for creep deformation. Given the relatively low stresses encountered in industrial pipe work systems, the majority of life is usually spent in the secondary or steady-state creep region, after the initial period of stress redistribution is experienced within the structure[138,192]. As creep stresses will be constant in a geometrically linear structure during steady-state creep, comparative assessments of pipe bends with different geometries can be performed. During the steady-state region, rupture stresses (σ_R) may be evaluated and thus an approximation of the failure location and failure life may be found (as discussed in section 5.2.1). The rupture stress (σ_R) may be calculated using the material constant α. A value of approximately 0.3 is often found to be applicable for CrMoV and P91 power plant steels (section 5.2.1). As such, $\alpha = 0.3$ has been used in most of the analyses included in the present work. Using the steady-state peak rupture stress ($\hat{\sigma}_R$) within a structure and integrating the Kachanov damage equation with respect to time, the life of a

component may be estimated (see equation (5.2)). Typically, this approach leads to slightly underestimated failure times compared with full damage analyses, representing conservatism in the analysis[138,139].

6.3 Variations in Pipe Bend Cross Section Dimensions

6.3.1 Pipe Bend Geometry

For power plant applications, pipe bends are generally manufactured from straight pipe sections using an induction heating ring and a fixed radius arm driven on an arc by a hydraulic ram[116]. Due to the tensile stress state along the outside arc of the bend (the extrados, see figure 6.1 (a)), a reduction in the wall thickness will occur[117,118]. Additionally, the compression along the inside arc (the intrados, see figure 6.1 (a)) generally results in an increase in wall thickness. Given the variation in bending stresses which occur when the pipe is bent, the degree of divergence from the straight pipe wall thickness in the intrados and extrados will not be consistent around the pipe bend. The definition of bend geometry is made more complex through the tendency of bends to become oval under a bending moment (the von Karman effect[119]). Initial ovality in the pipe bend cross section will occur during bending as the pipe flattens in the vertical direction. Under internal pressure alone during service, the pipe will attempt to inflate, regaining a more circular cross section[119,120]. Under additional system loading and the loading imposed by the pipe hanger support systems (both potentially causing torques or closing bending moments), the ovality of the pipe cross section may become more pronounced after a long term service at high temperature. The manufacturing process will induce residual stresses in the pipe bend. Unlike weldments, for which heat treatment methods exist (which act to relax residual stresses through creep[112]), it may not be possible to heat treat pipe bends due to the sheer size of the components. Residual stresses in welded pipes have been shown to relax quickly during service exposure in creep conditions[114], therefore similar behaviour is expected for pipe bends. As such, the effects of residual stresses are not considered in the present study. As steady-state peak rupture stresses are the main area of interest it is reasonable to assume that any manufacturing residual stress will have relaxed away when a steady-state condition is achieved and that residual stresses will not significantly affect the magnitudes of the steady-state stresses.

The case of a 90° pipe bend is considered for most of the present chapter. Depending on plant requirements and the flexibility of the pipe work system design, bend angles of less than this value may be used. However, a 90° bend represents an upper limit for most industrial applications. In the interest of representing the most arduous analytical case therefore (i.e. with the greatest variation in dimension changes), 90° bends have been used as a practical maximum.

New build plant (in the UK) is, at the time of writing, designed and built to BS EN

13480[128]. Much of the plant currently in service was however commissioned prior to 2002, hence it adheres to the now superseded BS 806[129]. Using this earlier code, the recommended minimum bend radii (the distance from the centreline of the pipe to the centre point of the bend) for the pipes used in this study (with outside diameters of approximately 350mm for Main Steam pipes and 490mm for Hot Reheat pipes, see figure 6.1 (b)) can be found. This is typically in the region of 2m for both pipe bend types[129], agreeing with industrial suggestions. Clearly, a smaller bend radius results in a tighter bend, giving rise to a greater difference between intrados, extrados and average wall thicknesses around the pipe bend. As it is this divergence from the straight pipe wall thickness that causes the potential for localised failure at the pipe bends, tight bends will be the areas of most concern. Larger bend radii are used whenever possible (i.e. where the size envelope or system layout does not necessitate tight bend radii) to negate this concern. In order to demonstrate that this work is applicable to the most extreme dimension conditions that are used in industry (and thus to make it relevant to those who may apply it), a constant bend radius of 2m was used for all of the bends modelled.

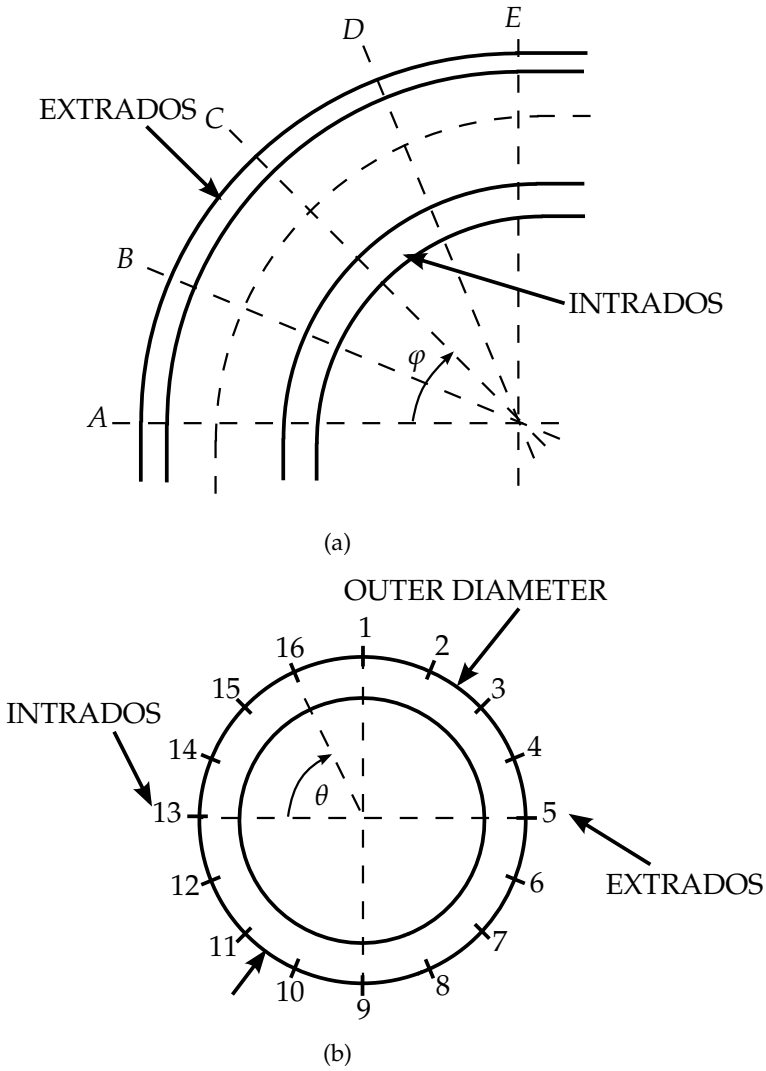

Figure 6.1: Illustrations of (a) bend position angle (φ) and bend position and (b) circumferential position angle (θ) of the pipe cross section.

6.3.2 Industrial Data and Trends

Non-destructive testing of in service pipe bends can take several forms. Changes in the pipe diameter at critical locations or the degree of ovality, for example, can be assessed through the use of calliper measurements or strain gauges over the structure, allowing the physical dimensions to be recorded. Additionally, hardness or replica analysis between components of the pipe bend may be conducted at key locations in order to perform comparative analysis or establish potential behavioural trends across the piping system. Ultrasonic or magnetic surveys may also be implemented in order to determine wall thicknesses at key locations (such as the pipe bend intrados and extrados for multiple bend position angles (φ), see figure 6.1 (a)) or to detect defects and the initiation of cracks. Present research is assessing the viability of localised strain measurement over critical areas (such as pipe bends or weldments) using speckle pattern

analysis and automated image correlation[105]. Developments similar to this could be used in the future to verify FEA modelling, refine lifing predictions or to back calculate estimates of wall thickness variation. In any case, condition monitoring techniques are well established in the power industry and much of the complex details in pipe bend dimensions that have been discussed so far may well already be archived in routine inspection reports. This data should be fully exploited in any new analysis techniques for pipe bends before it is suggested that additional laborious component measurement and characterisation be carried out. Such considerations will help encourage any new developments to be adopted in the power industry. Bearing this criterion in mind, the methodologies described in the present chapter have been developed using standard survey data supplied by the power industry.

Two pipe bend types are considered in the present chapter, namely Main Steam and Hot Reheat configurations. Typically, the Hot Reheat pipe bend type will have a larger diameter but smaller wall thickness than the Main Steam type. In both cases, inspection of the diameter measurements around the bend revealed little variation. Furthermore, little evidence of ovality in the pipe cross section was present. Based on these observations, initial ovality was neglected from the modelling procedure and constant outer diameter 3D FEA models were created (D_O is equal to $490mm$ and $356mm$ for the Hot Reheat and Main Steam pipe sections, respectively). Examination of the wall thickness variation with respect to circumferential position angle (θ) suggested that, for a given bend position angle (φ), pipe cross sections were almost symmetric in the bending plane (i.e. the wall thickness values found at the top and bottom of the pipe cross section, positions 1 and 9 respectively in figure 6.1 (b), are approximately the same). An example of this can be seen in figure 6.2, where the quantity Th is a circumferential position's wall thickness and Th_{AV} is the average wall thickness value for the particular pipe cross section. The "sinusoidal" tendency of this profile for each circumferential position angle (θ) position suggests that a plane of symmetry exists in the bending plane. Half of the pipe may therefore be modelled with confidence (given suitable boundary conditions replicating the constraint of the rest of the pipe and bend). The variation in wall thicknesses at circumferential positions 1 and 9 around the pipe bend are minimal and in close agreement with the straight pipe values. This leads to the observation that the bending process has a limited effect on the wall thickness at the top or bottom of the bend cross section. Consistent wall thickness values for circumferential position 1 may therefore be applied at each of the bend positions without a great deviation from plant data. Note that in the industrial pipe bend data provided to produce figure 6.2 included the results of NDT surveys on several pipe bends. Some surveys were more extensive than others however, therefore assumed profiles have been taken from surveys that measured wall thicknesses at 16 circumferential positions. Surveys that used 4 measurement points are included for comparison.

System loading is clearly specific to a given power station layout. For example,

primary system stresses which are associated with the self-weight of the pipe work will be dependent on hanger arrangement[108]. Additional system stresses may arise due to thermal expansion; however the global system constraint will also cause a complex application of these loads. The combination of these stress sources is very complex and strongly depends on the constraint imposed by a specific pipe system. For simplicity, system loads have been neglected from this study and pipe bends will be assumed to be subjected to internal pressure only.

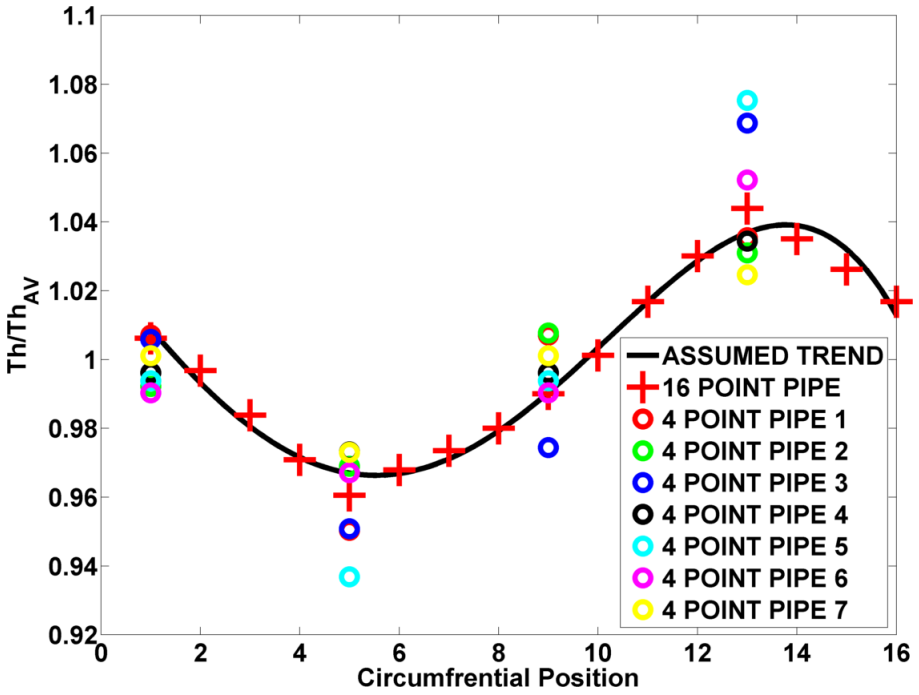

Figure 6.2: Example of the variation of normalised wall thickness with circumferential position (see figure 6.1 (b)) at a specific bend position angle (φ).

6.3.3 Definition of Parameters for Empirical Stress Functions

Industrial data indicates several important trends which may be exploited to describe a pipe bend geometry. For example, if the points of maximum variation from the straight pipe wall thickness (i.e. the intrados ($Th_{In}(\varphi)$) and extrados ($Th_{EX}(\varphi)$) wall thicknesses, circumferential positions 13 and 5 respectively, see figure 6.1 (b)) at each bend position (see figure 6.1 (a)) are normalised with respect to the average (or nominal) wall thickness ($Th_{NOM}(\varphi)$), plots similar to figure 6.3 may be produced. Note that all three parameters are functions of the bend position angle (φ). The intrados and extrados factors ($In(\varphi)$ and $Ex(\varphi)$, respectively) may therefore be defined by equation (6.1). It can be seen from figure 6.3 that the variations in $In(\varphi)$ and $Ex(\varphi)$ along the bend appear to be related (for example, an increase in $In(\varphi)$ tends to result in a decrease in $Ex(\varphi)$ at the same bend position). It is a valid deduction therefore that volume transfer during the bending process occurs almost in plane, giving rise to the constraint equation (6.2), defining the relationship between $In(\varphi)$ and $Ex(\varphi)$. The values of the intrados and extrados

factors are generally not symmetric about the crown of the bend (bend position C in figure 6.1). Symmetry is often assumed in this plane in the cases where 3D models are produced [120,132,135,200]. Inspection of industrial data however indicates that this may be unrealistic. Taking into account the fact that the fluctuations in the two factors are far greater in bend positions $A - C$ than $C - E$, it is proposed that a symmetry plane at bend position C is suitable only if the geometry described by the factors at bend positions $A - C$ is applied to the model. In this way, the worst case (i.e. with greatest variation) is modelled, returning a greater estimate of the peak rupture stress than if the nearer uniform geometry of bend positions $C - E$ were applied. It is worth pointing out that, although 5 data points seems sparse for data fitting in figures 6.3 and 6.4, this is representative of the frequency used in industry during routine non-destructive evaluations. Ideally, a greater sampling frequency would be implemented on bends which are a concern to operators. If the plane of symmetry at bend position C is adopted in the manner described above, along with the plane of symmetry in the bending plane described in figure 2.37, only a quarter of the pipe bend needs to be modelled in FEA. Computing time both in terms of running the analysis and in initially producing the component model can therefore be minimised. In the analyses performed in the present chapter quarter models have been implemented; each case representing the greatest variation in $In(\varphi)$ and $Ex(\varphi)$.

$$\begin{aligned} In(\varphi) &= \frac{Th_{In}(\varphi)}{Th_{NOM}(\varphi)} \\ Ex(\varphi) &= \frac{Th_{Ex}(\varphi)}{Th_{NOM}(\varphi)} \end{aligned} \tag{6.1}$$

$$In(\varphi) \approx 2 - Ex(\varphi) \tag{6.2}$$

Turning attention to the variations in the average wall thickness ($Th_{NOM}(\varphi)$, see figure 6.4) around the bend, similar trends may be observed as with $In(\varphi)$ in figure 6.3. Maximum fluctuations can be seen at bend positions $A - C$, which agrees with the quarter model assumption.

Using the above, the wall thickness variation in a pipe bend may be dimensionally characterised by 2 factors ($In(\varphi = 0)$ and $Th_{NOM}(\varphi = 0)$), the constraint equation (6.2) (dictating that $Ex(\varphi = 0)$ may be determined from $In(\varphi = 0)$ or vice versa) and two characteristic equations that describe how $In(\varphi)$ and $Th_{NOM}(\varphi)$ vary with the bend position angle. A range of pipe bends may be considered by defining practical limits for $In(\varphi = 0)$ and $Th_{NOM}(\varphi = 0)$ and then performing FEA simulations for every permutation (assuming a suitable number of levels for the factors $In(\varphi = 0)$ and $Th_{NOM}(\varphi = 0)$). Peak rupture stress surfaces can then be established for a particular material (in this study defined by the stress exponent, n, see figure 6.5). Once these surfaces have been established approximate parametric equations could be developed to fit the surfaces, allowing for interpolation in the tested geometry and material ranges.

By way of example, the characterisation and systematic study method described above has been applied to industrial data for Main Steam and Hot Reheat type pipe bends.

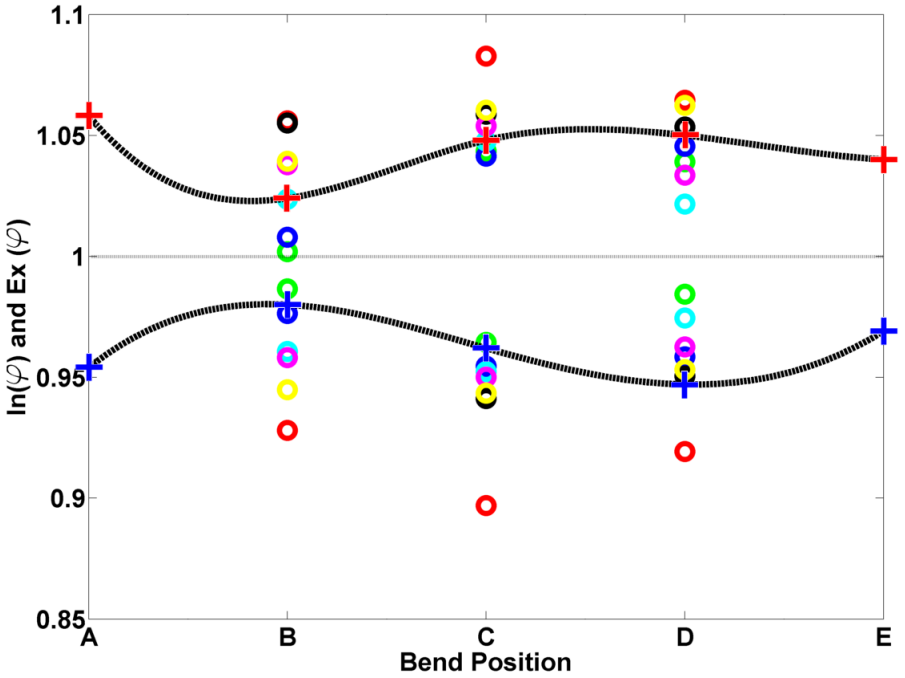

Figure 6.3: Variations of $In(\varphi)$ and $Ex(\varphi)$ with bend position for a Main Steam type of pipe bend geometry.

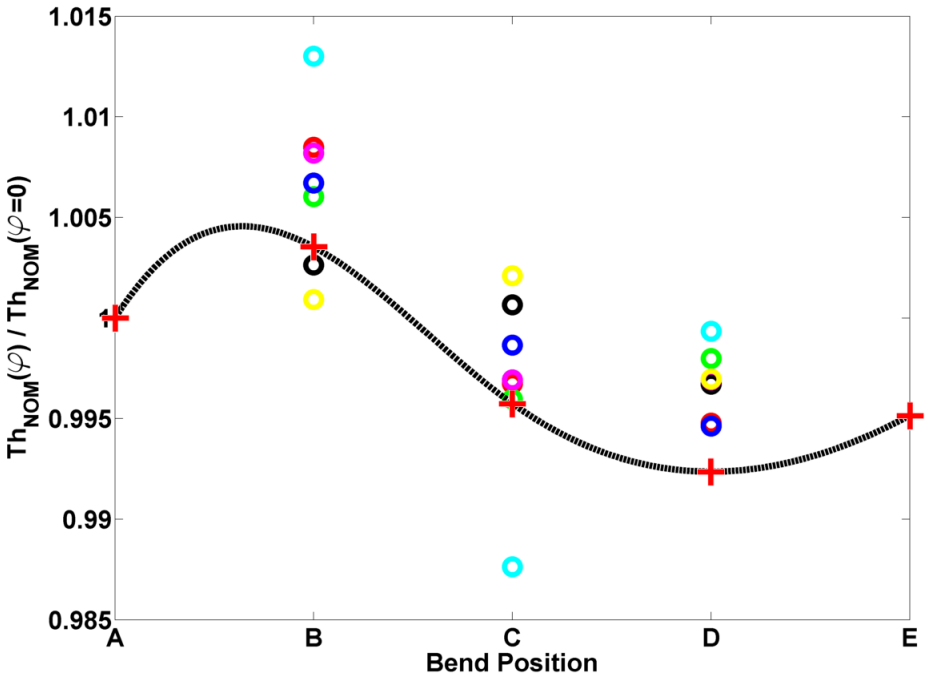

Figure 6.4: Variations of $Th_{NOM}(\varphi)$ with bend position for Main Steam type of pipe bend geometry.

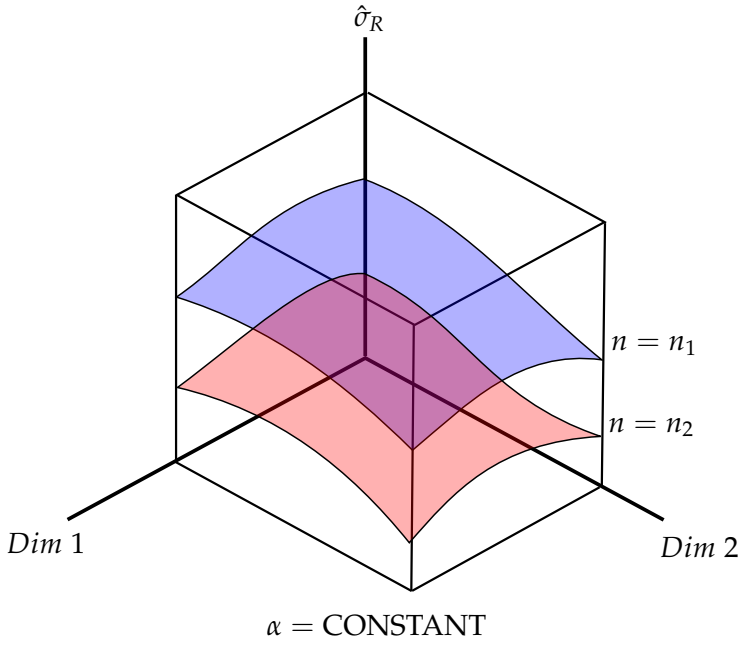

Figure 6.5: Illustration of peak steady-state rupture stress ($\hat{\sigma}_R$) surfaces for two different stress exponent values (n_1 and n_2). Note that the surfaces are dependent on the dimensional factors (Dim 1 and Dim 2, equivalent to $In(\varphi = 0)$ and $Th_{NOM}(\varphi = 0)$) and that, for a given set of surfaces, α is assumed constant.

6.4 Finite Element Modelling

6.5 Methodology

As justified in section 2.4.1, a 3D quarter model can be used to represent the complexity of a pipe bend (an example mesh is presented in figure 6.6). Planes of symmetry were assumed in the bending plane and at bend position C (see figure 6.1). Straight lengths of pipe were attached to the end of the bend section in the model. These were made long enough ($18m$, found through a sub-investigation) to ensure that the conditions at the straight/bend interface were modelled correctly while not unnecessarily increasing computing time[137]. Note that in figure 6.6 the straight section is truncated in order to show the mesh density in the bend section with greater clarity. In the straight pipe section, a uniform wall thickness is assumed. A full description of this model is presented in section 2.4.1.

As the weld section is not within the scope of the present work, a $2m$ linear transition region is included in the model to provide an interface between the bend (with variable cross section dimensions) and the straight (with uniform circular cross section dimensions) without a step change in dimensions (which would represent a stress concentration). It is the intention of the present work to highlight the effects of dimensional variation on the steady-state stress distribution of pipe bends. The inclusion of material

and geometry discontinuities presented by a weldment will greatly complicate the analyses and potentially distort the deformation characteristics of the bend. Excluding the weld will not affect the characterisation method defined in the present work. A finer mesh density was used in the transition region (see figure 6.6), reducing the possibility of convergence errors between the finer bend mesh and the coarser straight mesh. A sparse mesh is utilised in the straight pipe section in order to reduce the computational time. A minimum of three elements were used over the wall thickness.

The internal pressure was applied as a distributed load on the inside surface of the pipe and bend. The magnitude of the internal pressure was chosen to ensure that the average mean diameter hoop stresses (σ_{MDH}) for both pipe bend types was approximately $30MPa$. This is well below the typical yield stress for commercial steels, validating the use of the elastic-creep analyses performed (elastic steps are included to ramp up the loads before the creep step). To model the constraint of the rest of the pipe, the free end of the bend section is limited to deflections in the XY plane[139] (see figure 6.6) and the bend plane surface (the XZ plane in figure 6.6) is restricted not to move in the Y direction. All elements are solid reduced integration quadratic hexahedral type (C3D20R in ABAQUS[132,191]). Shell elements, although not as computationally time consuming as solid elements, can exhibit large errors for thick sections[134] therefore their use is discouraged. Deformations are assumed to be small meaning that the cross sectional stiffness properties will not change by a significant amount. Geometric non-linearity (GNL) is, therefore, not used in the analyses[132,193]. This assumption has been verified in the work of Hyde et. al.[193]. Discrepancies between geometric linear (GL) and GNL analyses only become significant in the tertiary creep region (i.e. towards failure). As the present work concerns itself with steady-state stress distributions, GNL has been neglected in order to manage computational times. Final deflections are small compared to the structure dimensions, therefore cross sectional properties are retained and stiffness matrices do not need to be re-evaluated after each time step[137].

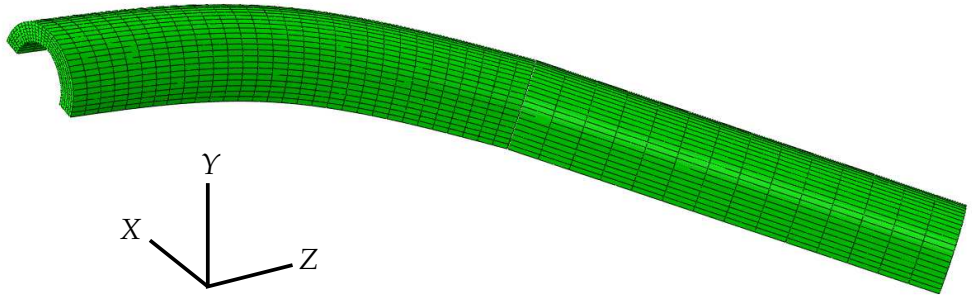

Figure 6.6: Example of a 3D quarter model FEA mesh (truncated to remove straight pipe section) for a Main Steam type of pipe bend.

6.6 Systematic Study and Results

A least squares fitting procedures using a quadratic function was implemented in order to determine the characteristic equations that describe the variation of $In(\varphi)$ and $Th_{NOM}(\varphi)$ with bend position angle. Examples of these characteristic equations for the Main Steam and Hot Reheat pipe bend types are given in equations (6.3) and (6.4) and equations (6.5) and (6.6), respectively. Note that the bend position angle, φ, is given in terms of radians.

$$In(\varphi) = 0.1812\varphi^2 - 0.1553\varphi + In(\varphi = 0) \tag{6.3}$$

$$Th_{NOM}(\varphi) = -2.533\varphi^2 + 1.6154\varphi + Th_{NOM}(\varphi = 0) \tag{6.4}$$

$$In(\varphi) = 0.1649\varphi^2 - 0.1172\varphi + In(\varphi = 0) \tag{6.5}$$

$$Th_{NOM}(\varphi) = 2.27\varphi^2 - 4.12\varphi + Th_{NOM}(\varphi = 0) \tag{6.6}$$

Industrial data also yields upper and lower limits for the two factors. For the Main Steam pipe geometry type, $1.033 \leq In(\varphi = 0) \leq 1.06$ and $60mm \leq Th_{NOM}(\varphi = 0) \leq 75mm$. For the Hot Reheat type of pipe geometry, $1.021 \leq In(\varphi = 0) \leq 1.05$ and $20mm \leq Th_{NOM}(\varphi = 0) \leq 27.5mm$. Four levels were chosen for each of the two factors, giving rise to a total of 16 permutations for each pipe bend type. According to Calladine[197,198] (see figure 5.13), an approximate linear relationship may be noticed between the peak stationary state stress and $1/n$ (inverse of the stress exponent material constant from the Norton power law), providing that the peak stress point in the structure does not vary with $1/n$. To exploit this relationship later for the interpolation of the stress function, several stress exponent (n in Norton's Law) values were applied to each geometry definition case.

In the interest of clarity, please note that the arguments of equations (6.4) and (6.6) are not normalised to any reference value (i.e. $Th_{NOM}(\varphi)$ and $Th_{NOM}(\varphi = 0)$ are absolute dimension values). Equations (6.3) to (6.6) were used to generate pipe bends for the systematic study (i.e. for a range of absolute $Th_{NOM}(\varphi = 0)$ values and $In(\varphi = 0)$ intrados factor values).

A typical value of n for P91 (a commonly used power plant material) is 8.46[67] and hence this was used in the analyses. To extend the applicability of the work, values of 4 and 6 were also used as they fall in the practical range of n. The material parameter n is not only dependent on the specific material composition but also temperature[201]. Therefore, the n range used in the parametric equation allows for the interpretation of many of the materials and operating conditions observed in power plants. Results of this study can be seen in tables 6.1 and 6.2. Peak rupture stresses have been normalised

with respect to the internal pressure. These steady-state creep stresses should have an approximately linear relationship to the internal pressure loading (if internal pressure is the only load applied, see equation (2.104)), therefore normalising the results in this way provides a method for engineers to quickly determine peak rupture stresses for a range of steam pressures. An example contour plot, showing the peak normalised rupture stress for $\alpha = 0.3$, is given in figure 6.7. In all cases, the peak values of the steady-state rupture stresses occur in the bend section at the intrados (at a bend position angle of approximately 24°; corresponding to the point of greatest variation between the intrados and extrados wall thicknesses).

Table 6.1: Normalised FEA results for Main Steam pipe bend type study.

Identifier	$Th_{NOM}(\varphi = 0)\ (mm)$	$In(\varphi = 0)$	$Ex(\varphi = 0)$	$\hat{\sigma}_R / P_i (n = 8.46)$	$\hat{\sigma}_R / P_i (n = 6)$	$\hat{\sigma}_R / P_i (n = 4)$
MS_1	60	1.033	0.967	2.31	2.96	3.69
MS_2	65	1.033	0.967	2.07	2.89	3.50
MS_3	70	1.033	0.967	1.87	2.78	3.24
MS_4	75	1.033	0.967	1.70	2.67	3.01
MS_5	60	1.04	0.96	2.29	3.01	3.78
MS_6	65	1.04	0.96	2.06	2.88	3.63
MS_7	70	1.04	0.96	1.86	2.77	3.21
MS_8	75	1.04	0.96	1.69	2.66	2.99
MS_9	60	1.05	0.95	2.27	2.99	3.75
MS_10	65	1.05	0.95	2.04	2.87	3.44
MS_11	70	1.05	0.95	1.84	2.77	3.19
MS_12	75	1.05	0.95	1.67	2.66	2.98
MS_13	60	1.06	0.94	2.26	3.01	3.76
MS_14	65	1.06	0.94	2.02	2.89	3.46
MS_15	70	1.06	0.94	1.83	2.78	3.22
MS_16	75	1.06	0.94	1.66	2.68	3.01

Table 6.2: Normalised FEA results for Hot Reheat pipe bend type study.

Identifier	$Th_{NOM}(\varphi = 0)\ (mm)$	$In(\varphi = 0)$	$Ex(\varphi = 0)$	$\hat{\sigma}_R / P_i (n = 8.46)$	$\hat{\sigma}_R / P_i (n = 6)$	$\hat{\sigma}_R / P_i (n = 4)$
HR_1	20	1.021	0.979	14.93	22.87	25.46
HR_2	22.5	1.021	0.979	12.94	20.40	21.51
HR_3	25	1.021	0.979	11.38	17.41	18.50
HR_4	27.5	1.021	0.979	10.15	15.64	16.17
HR_5	20	1.03	0.97	14.80	20.83	25.22
HR_6	22.5	1.03	0.97	12.81	19.09	21.25
HR_7	25	1.03	0.97	11.27	17.25	18.28
HR_8	27.5	1.03	0.97	10.06	15.48	15.98
HR_9	20	1.04	0.96	14.66	20.70	24.86
HR_10	22.5	1.04	0.96	12.68	18.94	20.97
HR_11	25	1.04	0.96	11.16	17.08	18.04
HR_12	27.5	1.04	0.96	9.96	15.31	15.77
HR_13	20	1.05	0.95	14.51	20.58	24.54
HR_14	22.5	1.05	0.95	12.34	18.65	20.47
HR_15	25	1.05	0.95	11.05	16.91	17.81
HR_16	27.5	1.05	0.95	9.86	15.13	15.56

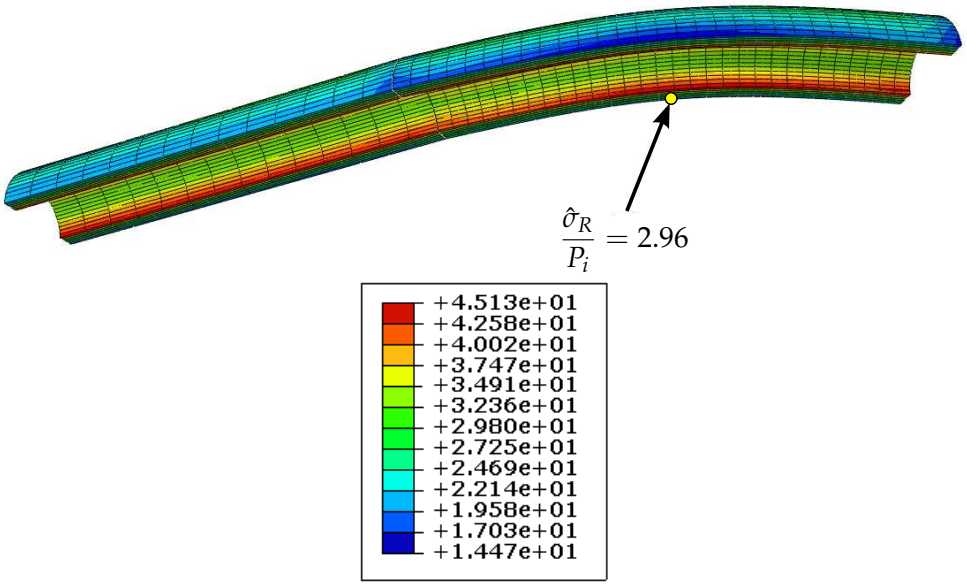

Figure 6.7: Example contour plot showing peak normalised rupture stress for case MS_1 where $n = 6$ and $\alpha = 0.3$. Note the peak stress is found at $\theta = 0^\circ$ (the intrados) and $\varphi = 24^\circ$.

6.7 Stress Functions

6.7.1 Fitting Procedure

Multiple potential forms of the parametric function to describe the rupture stress surface were evaluated and compared through the use of a purpose written MATLAB script. This uses the MATLAB optimisation toolbox (more specifically, the least squares optimisation function LSQNONLIN[202]) to determine values for the coefficients used in the parametric equations. Each form of the parametric equation was a function of the two parameters ($Th_{NOM}(\varphi = 0)$ and $In(\varphi = 0)$) and contained multiple fitting constants (which were to be determined through optimisation). After several iterations, the parametric function shown in equation (6.7) was adopted. Note that A and B are the fitting constants, which are valid for a specific peak steady-state rupture stress surface. Using the steady-state ruptures stresses shown in tables 6.1 and 6.2 for Hot Reheat and Main Steam pipe bends, values for A and B were determined based on each rupture stress surface (see table 6.3, where r^2 is the coefficient of determination and is defined by equation (3.24)).

$$\hat{\sigma}_R = A \cos\left(In(\varphi = 0)^2 + Th_{NOM}(\varphi = 0)^2\right) + B \tag{6.7}$$

Table 6.3: Fitted A and B value for use with equation (6.7) and coefficient of determination (r^2) values for the tested n values.

Data Set	A (MPa)	B (MPa)	r^2
Main Steam $n = 8.46$	23.6832	46.5652	0.9976
Main Steam $n = 6$	8.6351	49.7642	0.9498
Main Steam $n = 4$	27.4350	70.7222	0.9619
Hot Reheat $n = 8.46$	28.1744	57.6642	0.9956
Hot Reheat $n = 6$	34.8817	80.6423	0.9383
Hot Reheat $n = 4$	54.9203	101.3772	0.9962

6.7.2 Empirical Steady-State Rupture Stress Function

Fitting coefficients (A and B) for the parametric equation (6.7) have been determined for a range of n values for the two geometry types (Hot Reheat and Main Steam). Using the n values and specific $Th_{NOM}(\varphi = 0)$ and $In(\varphi = 0)$ values that lie in the calculated range, stress surfaces defined by the parametric equation may be compared to those obtained directly from FEA. Additionally the quality of the fitting (between parametric and FE results) may also be established through inspection of the coefficient of determinations (r^2) for each stress surface (note that n is constant for a specific stress surface)[166]. Generally, the fitting quality is good, indicated by the high coefficient of determination values which were all greater than 0.93. A graphical comparison between the FEA and parametric results can be seen in figures 6.8 and 6.9 for the Main Steam and Hot Reheat pipe bend types, respectively.

Trends, based on the variation of the fitting constants (A and B) with the stress exponent (n) value, could enable interpolation of results for any other n, $In(\varphi = 0)$ and $Th_{NOM}(\varphi = 0)$ values in the range. Such trends are presented in figures 6.10 and 6.11 for the Main Steam and Hot Reheat pipe bend types, respectively. Functions fitted to these plots allow for A and B values to be approximated for any intermediate n value. To explore the interpolation capability of the parametric equations, additional meshes were created (with geometry factors falling in the centre of the tested geometry factor ranges) and submitted for analysis. It is worth pointing out that, given the variation in A in figure 6.10 (a) and the lack of a guarantee of converging on a global minimum in the optimisation procedure, interpolation of fitting constant values may not be advisable without a greater frequency of analyses (i.e. more tested n values). The brief examination given here serves to demonstrate what may be achieved with a more limited amount of data. Factors of $In(\varphi = 0)$ equal to 1.045 and $Th_{NOM}(\varphi = 0)$ equal to 67.5 were used for the Main Steam analyses and $In(\varphi = 0)$ equal to 1.1875 and $Th_{NOM}(\varphi = 0)$ equal to 23.75 were used for the Hot Reheat analyses. Three stress exponent values were chosen, two of which fell between the stress exponents tested (7 and 5, testing the interpolation capability for variations in n) and one at a tested value (6, effectively demonstrating the interpolation quality due to geometric changes alone). These conditions gave rise to a total of six testing scenarios (three for each pipe bend type). Results based on FE and

parametric equation analysis (with the percentage difference between the two) for the three stress exponent values are presented in tables 6.4 to 6.6. Note that peak rupture stresses are again normalised with respect to internal pressure.

Table 6.4: Results of interpolation study using both FEA and parametric equation methods for $n = 7$ (peak stresses are normalised with respect to internal pressure).

Pipe Type	$Th_{NOM}(\varphi = 0)\ (mm)$	$In(\varphi = 0)$	$\hat{\sigma}_R / P_i$ FEA	$\hat{\sigma}_R / P_i$ Stress Function	% Difference
Main Steam	67.5	1.045	1.96	2.54	25.78%
Hot Reheat	23.75	1.035	13.26	15.82	17.61%

Table 6.5: Results of interpolation study using both FEA and parametric equation methods for $n = 6$ (peak stresses are normalised with respect to internal pressure).

Pipe Type	$Th_{NOM}(\varphi = 0)\ (mm)$	$In(\varphi = 0)$	FEA	$\hat{\sigma}_R / P_i$ Stress Function	$\hat{\sigma}_R / P_i$ Difference
Main Steam	67.5	1.045	2.79	2.86	2.48%
Hot Reheat	23.75	1.035	17.78	17.70	0.45%

Table 6.6: Results of interpolation study using both FEA and parametric equation methods for $n = 5$ (peak stresses are normalised with respect to internal pressure).

Pipe Type	$Th_{NOM}(\varphi = 0)$ (mm)	$In(\varphi = 0)$	$\hat{\sigma}_R / P_i$ FEA	$\hat{\sigma}_R / P_i$ Stress Function	Difference
Main Steam	67.5	1.045	3.37	3.14	7.07%
Hot Reheat	23.75	1.035	19.24	18.87	1.94%

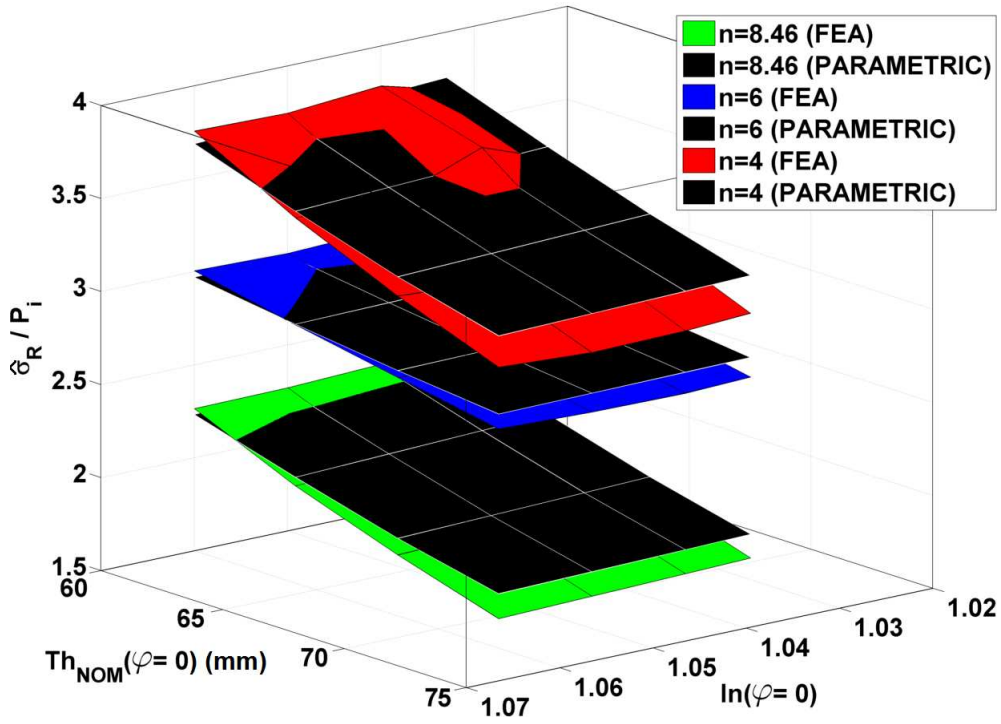

Figure 6.8: Peak rupture stress surfaces and associated parametric approximations for a Main Steam type pipe bend.

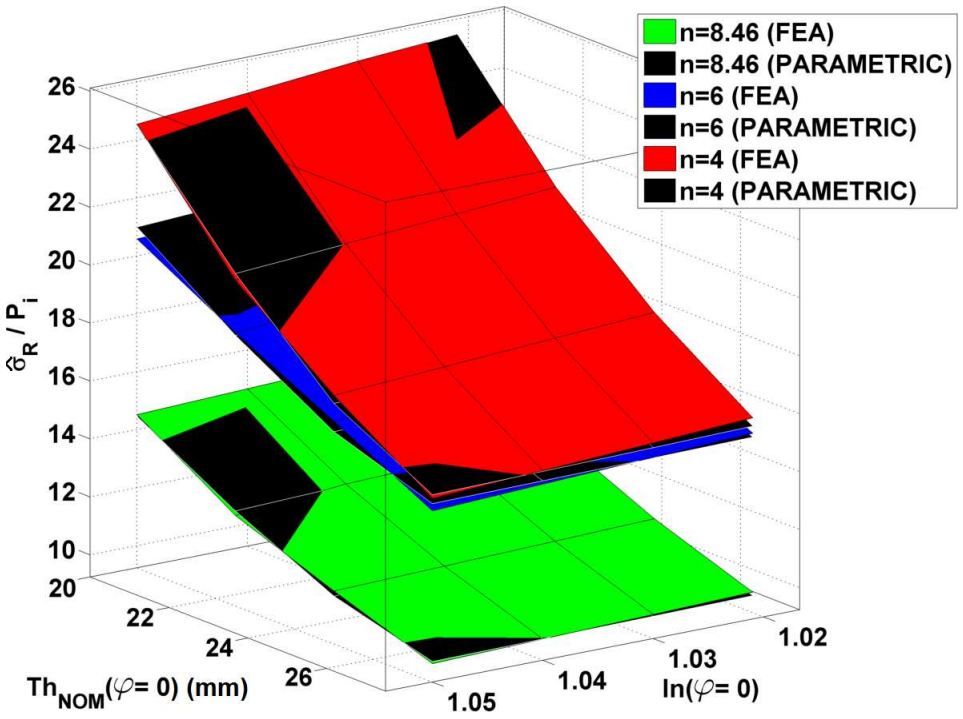

Figure 6.9: Peak rupture stress surfaces and associated parametric approximations for a Hot Reheat type pipe bend.

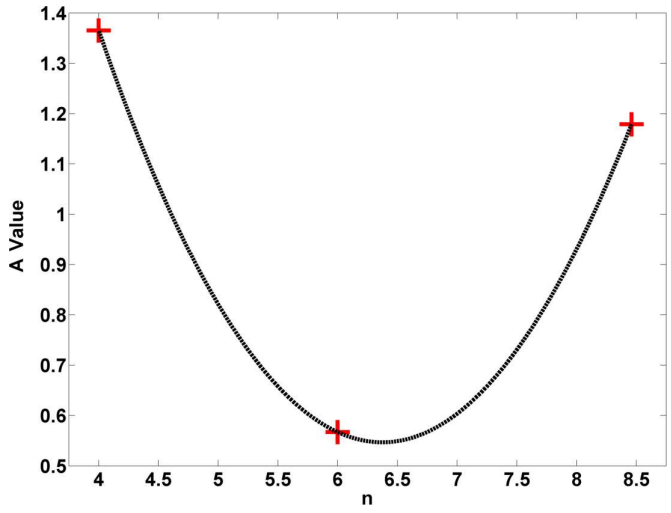

(a)

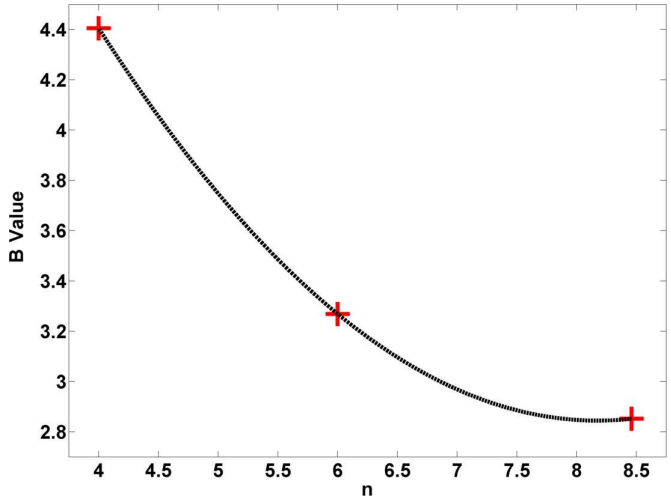

(b)

Figure 6.10: Variations of (a) the A coefficient value and (b) the B coefficient value, with stress exponent (n), for a Main Steam type of pipe bend.

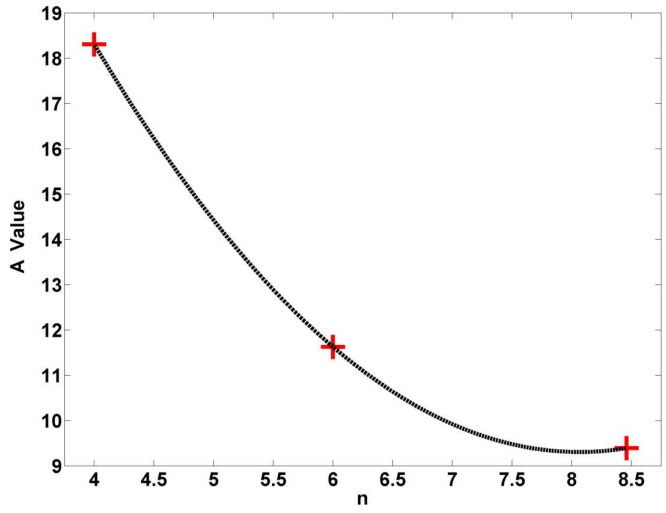

(a)

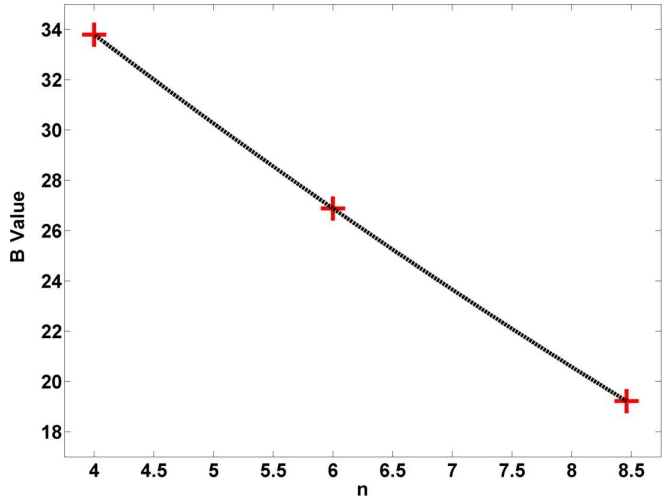

(b)

Figure 6.11: Variations of (a) the A coefficient value and (b) the B coefficient value, with stress exponent (n), for a Hot Reheat type of pipe bend.

6.7.3 Effect of α Value

As mentioned in the introduction, an α value of 0.3 was chosen for use to calculate σ_R as it is a typical value for commercial steels used in power plant. In practice however, users may wish to analyse pipe bends made from materials with alternative α values. Also, whereas other material constants may be determined from uniaxial testing, the determination of α requires multiaxial test data and FEA analysis[192] (see section 4.2.5). This can make α a difficult constant to determine, so users may wish to determine the upper and lower limits of a peak rupture stress for a practical α value range. To extend the scope of this research, a study into the effect of the α value on the predicted peak rupture stress was conducted for several of the meshes from the systematic studies (see tables 6.1 and 6.2). Models representing the limits of the geometry scales were chosen (MS_4, MS_13, HR_4 and HR_13) and along with the extreme stress exponent values,

($n = 4$ and $n = 8.46$). By using the upper and lower limit values, it is expected that the most extreme effects of varying α will be realised. The results of this study are presented in table 6.7, with plots showing the relationship between $\hat{\sigma}_R / P_i$ and α for the Main Steam and Hot Reheat pipe bend types in figures 6.12 and 6.13, respectively.

Table 6.7: Variations of normalised steady state peak rupture stress ($\hat{\sigma}_R / P_i$) with α.

α	0	0.3	0.7	1
MS_4 $n = 4$	3.18	3.01	2.82	2.69
MS_4 $n = 8.46$	1.87	1.70	1.80	1.88
MS_13 $n = 4$	3.90	3.76	3.61	3.52
MS_13 $n = 8.46$	2.47	2.26	2.45	2.48
HR_4 $n = 4$	15.82	16.17	16.74	17.22
HR_4 $n = 8.46$	6.69	10.15	10.41	10.97
HR_13 $n = 4$	23.86	24.54	25.61	26.49
HR_13 $n = 8.46$	14.23	14.51	15.04	16.44

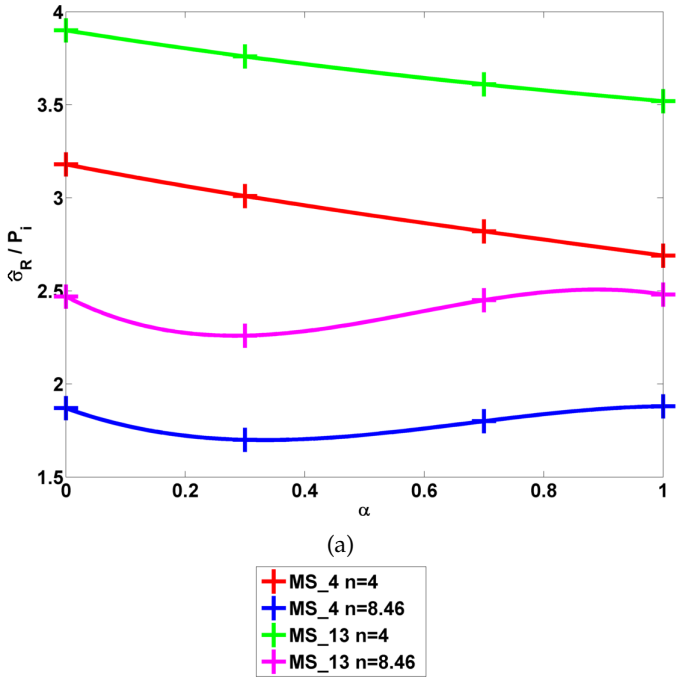

(a)

Figure 6.12: Variations of peak steady-state rupture stress with α for the Main Steam type of pipe bend geometry.

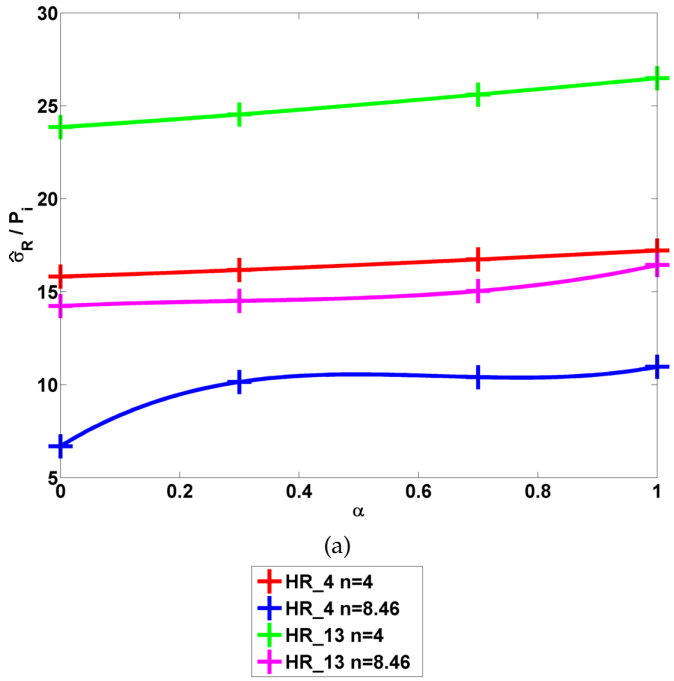

(a)

Figure 6.13: Variations of peak steady-state rupture stress with α for the Hot Reheat type of pipe bend geometry.

6.8 A Novel Pipe Bend Modelling Method

6.8.1 Requirement

The inclusion of variable wall thicknesses in 3D FEA pipe bend models can be complex and can require a great deal of time to create meshes manually. Additionally, 3D model analysis will take considerably longer to run than more simplistic 2D analyses. The more representative constraint imposed by the variable geometry case however allows for more accurate predictions of the stress state in these critical regions, complementing existing analysis methods. In the well-known R5 procedure for example, approximations of the elastic stress state in the structure to be analysed are often required to make preliminary evaluations of the likelihood of several failure mechanisms, such as creep fatigue interaction or crack initiation and growth[125,126,203]. In this section, given a bend centreline, 2D cross-sections are created that correspond to several planes of a 3D model. By analysing the 2D models individually, an averaging procedure can be implemented to allow for interpolation between the planes. In this way, the full 3D behaviour is "mapped" by the multiple 2D results. This clearly assumes a limited dependence on constraint between the considered planes but, if verified, this procedure would allow complex 3D models of pipe bends to be approximated quickly using 2D results. A description of the 2D axi-symmetric model can be seen in figure 4.10. Variable bend angles (30°, 60° and 90°) have also been analysed in the present section, extending the

work's applicability.

6.8.2 Interpolation Method

Procedure

An interpolation procedure based on 2D axi-symmetric models is illustrated in figure 6.14. Planes are drawn through the 3D model at defined bend position angles (φ). In the case of a 90° pipe bend, these bend position angles are equally spaced, at 0°, 11.25°, 22.5°, 33.75° and 45° (planes $\acute{A} - \acute{E}$, respectively, in figure 6.14). The cross sections intercepted by these planes are then recreated in 2D models, with planar variations in wall thickness values being represented in the 2D models. It is expected that, although the overall constraint of the pipe bend is not represented accurately in the 2D models, an approximation of the stress distribution can be achieved by interpolating over intermediate bend position angles between the 2D models. Note that all of the 2D meshes are constructed to ensure that their centrelines coincide with the centreline in the 3D model. The resolution (i.e. the spacing between planes used to construct the 2D meshes from the 3D model) is not considered in the present chapter. 5 planes have been assumed to be sufficient in order to describe the 3D pipe bend variation.

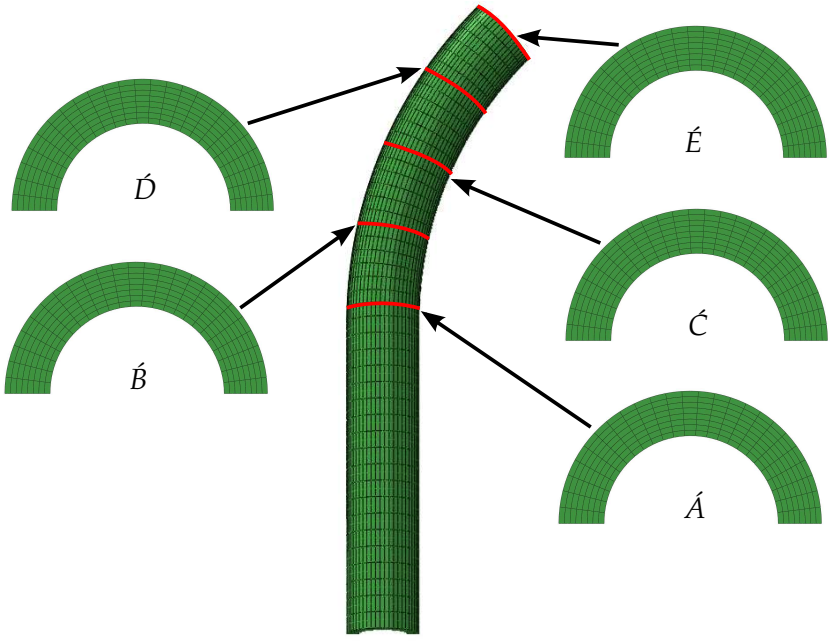

Figure 6.14: Illustration of 2D to 3D interpolation procedure, showing the 5 cross section locations ($\acute{A} - \acute{E}$) represented by 2D axi-symmetric models.

Dimensions of analysed pipe bends

Characteristic equations have been derived for Main Steam and Hot Reheat pipe bend types (shown in the previous sections). These take the general forms shown in equa-

tions (6.8) and (6.9). The coefficients for these equations (a_1, a_2, b_1 and b_2) are determined by observing trends in industrial data. In this sub-investigation, several pipe bends will be considered, therefore geometry factors ($In(\varphi = 0)$ and $Th_{NOM}(\varphi = 0)$, see section 6.3.3) have been chosen so that the resultant dimensions would be in a realistic range. Data on wall thickness variations at the pipe's intrados and extrados is limited. This data is used to determine the constants a_1 and a_2. Due to limited industrial data, values for a_1 and a_2 are preserved from equations (6.3) and (6.5). Alternative average wall thickness values ($Th_{NOM}(\varphi)$) are however available, therefore alternative b_1 and b_2 values may be calculated. This has been done to highlight the wider applicability of the characterisation method. A summary of the coefficients used to define the geometry for each bend model can be found in table 6.8. In any case, pipe bend geometries are realistic and exhibit dimension variation. Wall thicknesses (Th) for the Main Steam and Hot Reheat pipes are approximately $60mm$ and $20mm$, respectively. Outside diameters (D_O) for the Main Steam and Hot Reheat pipes are approximately $350mm$ and $490mm$, respectively. These approximate values have been assumed for any straight pipe section attached to the bend region in the 3D models.

$$In(\varphi) = a_1\varphi^2 + a_2\varphi + In(\varphi = 0) \tag{6.8}$$

$$Th_{NOM}(\varphi) = b_1\varphi^2 + b_2\varphi + Th_{NOM}(\varphi = 0) \tag{6.9}$$

Table 6.8: Summary of coefficients used to define the pipe bend geometry for the 2D stress interpolation investigation.

Identifier	a_1	a_2	b_1	b_2	$In(\varphi = 0)$	$Th_{NOM}(\varphi = 0)$ (mm)
HR_A	0.1649	-0.1172	0.0956	-0.1735	1	20.42
HR_B	0.1649	-0.1172	0.0956	-0.1735	1	21
HR_C	0.1649	-0.1172	0.0956	-0.1735	1.375	20.42
MS_A	0.1812	-0.1553	0.3748	-0.3	1	61.98
MS_B	0.1812	-0.1553	-0.0375	0.0239	1	61.98

6.8.3 Results

Uniform Cross Section Pipe Bends

Before investigating the effects of the proposed interpolation procedure when applied to detailed dimensioned pipe bends, it is important to verify that the idealized 2D axi-symmetric approximation has the capability to represent a 3D pipe bend with a uniform cross section. This was the original intention for the 2D approximation[139]. Analyses where conducted using a Norton's Law material model ($A = 6.599x10^{-16} MPa^{1/n}.hr$ and $n = 6.108$). Once a steady-state condition (i.e. after transient stress redistribution has completed) was achieved, the rupture stress for the structure (either the 2D or 3D pipe

bend model) could be calculated using $\hat{\sigma}_R = \alpha\sigma_1 + (1-\alpha)\sigma_{EQ}$. A value of 0.3 was chosen for α, the multiaxial material constant. This is typical of industrial steels used for power generation. Although the 2D axi-symmetric approximation was originally intended for use with 90° pipe bends (given that the bend/straight interface region makes up a minimum amount of the bend section, thus reducing its influence on the rest of the structure), comparisons have also been drawn to uniform pipe bends with 60° and 30° bend angles (see figures 6.15 and 6.16). Generally, the 2D axi-symmetric approximation predicts the stresses in the 3D model very well. Typical percentage differences in the middle section of the pipe bend are less than 1% (approximately 0.7% for the Main Steam type and 0.6% for the Hot Reheat type). Nearer the bend/straight interface, a discrepancy is observed (percentage differences are typically in the region of 2-3%). This is due to the difference in constraint conditions in the 2D and 3D models. In the centre region of the pipe bend, the uniform 2D model appears to estimate the 3D model well irrespective of bend angle. For the thin walled pipe bend (Hot Reheat type), percentage differences between the 2D and 3D method stress values increase with decreasing bend angle (an average percentage difference of 0.36% is observed for the 90° bend but this increases to 1.39% for the 30° bend). Percentage differences in the thick walled bend (Main Steam type) are consistent, irrespective of bend angle (approximately 0.77%). In any case, the difference between the stress fields predicted by the full 3D uniform pipe bend analysis and the idealised 2D axi-symmetric approximation is minimal.

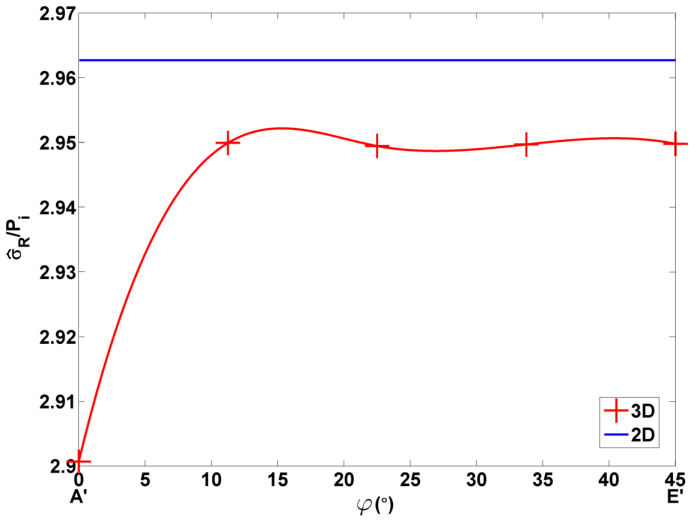

(a)

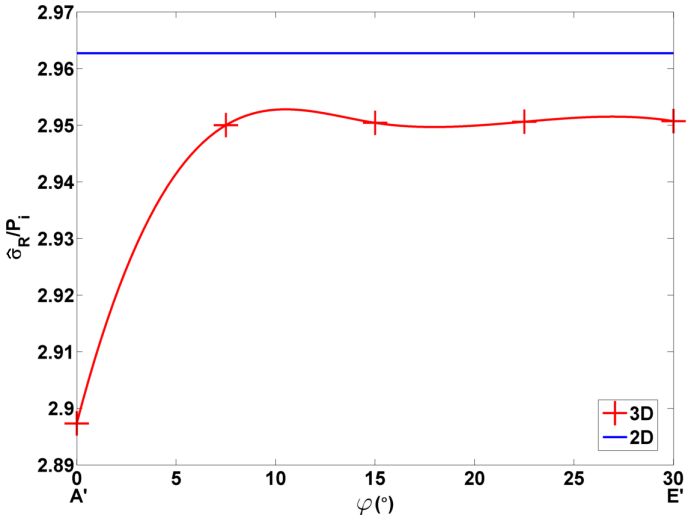

(b)

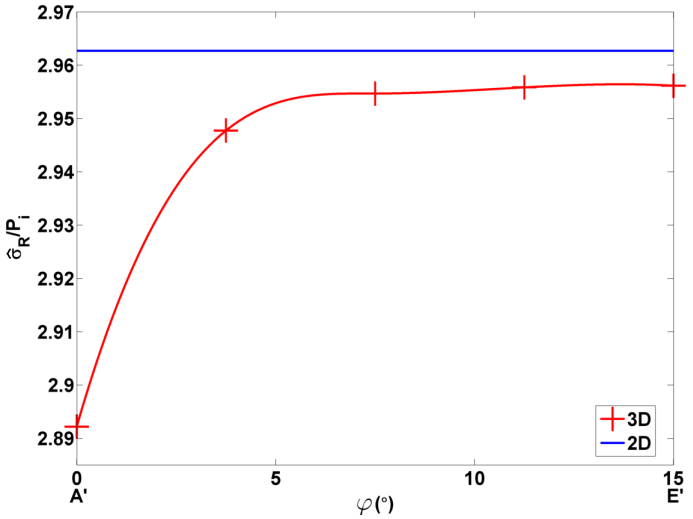

(c)

Figure 6.15: Plots of normalized local peak rupture stresses versus bend angle positions for (a) uniform 90° pipe bend, Main Steam type, (b) uniform 60° pipe bend, Main Steam type, (c) uniform 30° pipe bend, Main Steam type.

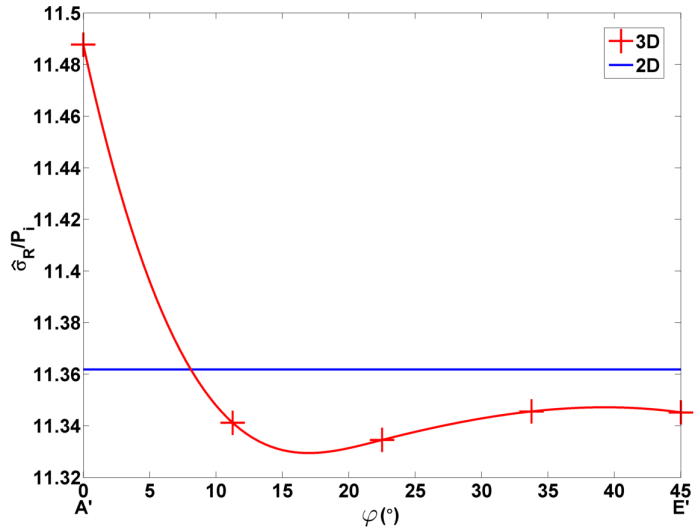

(a)

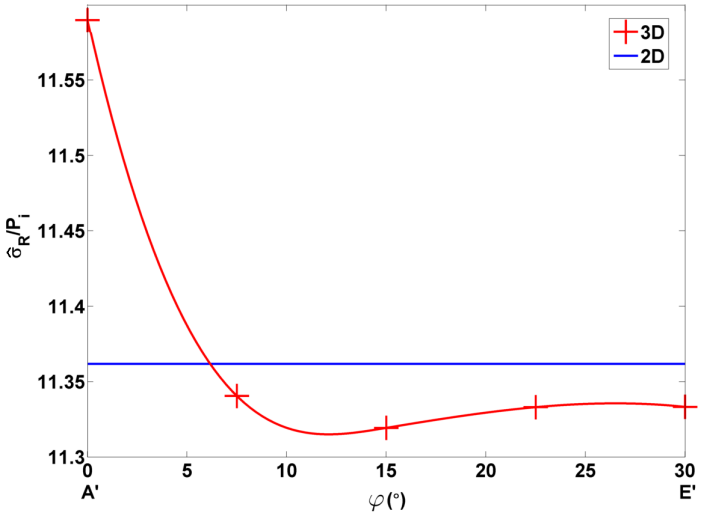

(b)

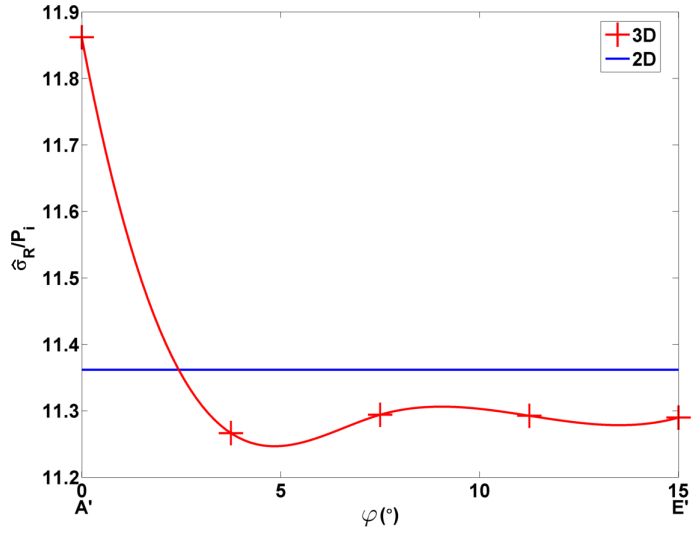

(c)

Figure 6.16: Plots of normalized local peak rupture stresses versus bend angle positions for (a) uniform 90° pipe bend, Hot Reheat type, (b) uniform 60° pipe bend, Hot Reheat type, (c) uniform 30° pipe bend, Hot Reheat type.

Variable Cross Section Dimension 90° Pipe Bends

The interpolation procedure has been applied to several 90° pipe bends with variable cross section geometry, representing the manufacturing induced dimension variation observed in industrial components. Analyses were conducted using the same material as the uniform study ($A = 6.599x10^{-16} MPa^{1/n}.hr$ and $n = 6.108$). Plots of the peak rupture stress ($\hat{\sigma}_R$, normalized to the internal pressure P_i) versus bend angle position are presented in figures 6.17 and 6.18 for the 5 pipe bend geometries. Peak rupture stress values for each of the 2D meshes are plotted against bend angle position (determined by the orientation of the plane used to construct the 2D mesh from the 3D model, see figure 6.14) under the data set "2D". Polynomial fitting is applied to these results. An interpolated maximum can then be found from the polynomial (data set "2D PEAK"). Using the 3D model, a peak rupture stress can be determined with associated bend position angle (data set "3D PEAK"). The planes used to create the 2D models can be applied to the 3D mesh and local, planar peak rupture stresses can be found. These localized peak rupture stresses can then be plotted verses bend angle position (data set "3D") and compared to the data set "2D". By considering the four data sets, the ability of the 2D axi-symmetric interpolation procedure to predict the peak and general rupture stress state (both in terms of magnitude and position) of a 3D model can be determined. An example of the contour plots, for both 3D and 2D meshes, used to verify the interpolation procedure for rupture stress determination can be seen in figure 6.19 for the thin walled model HR_A. The ability of the interpolation procedure to predict the stress state around the bend is verified for thick walled bends (MS_A) by comparison of the von Mises stress contour plots shown in figure 6.20.

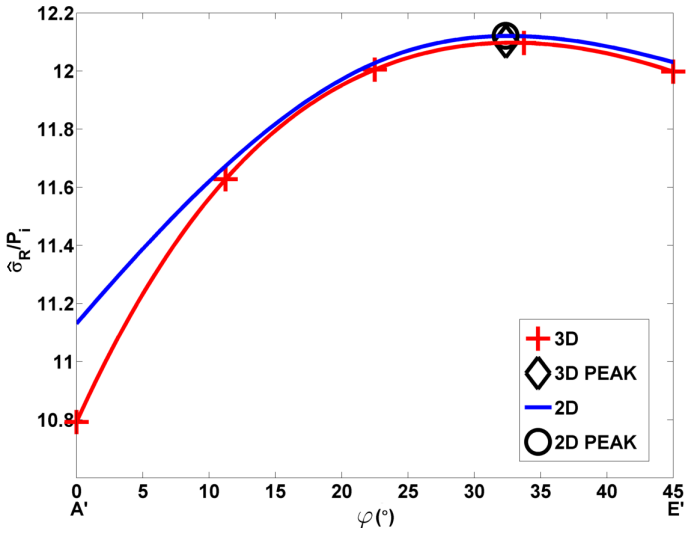

(a)

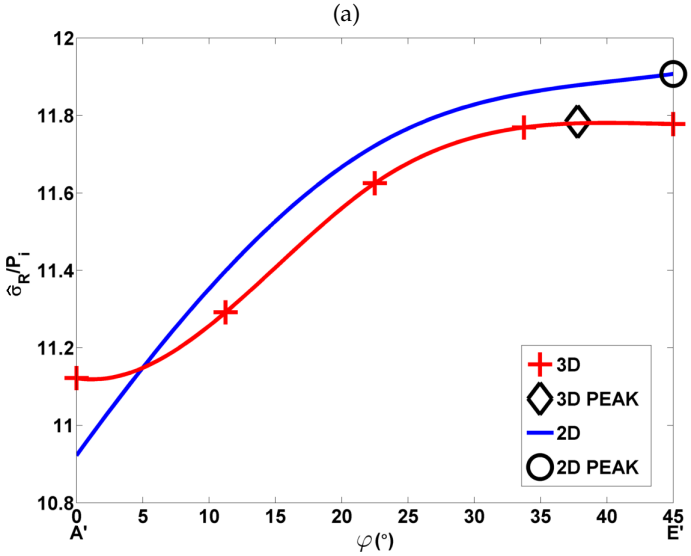

(b)

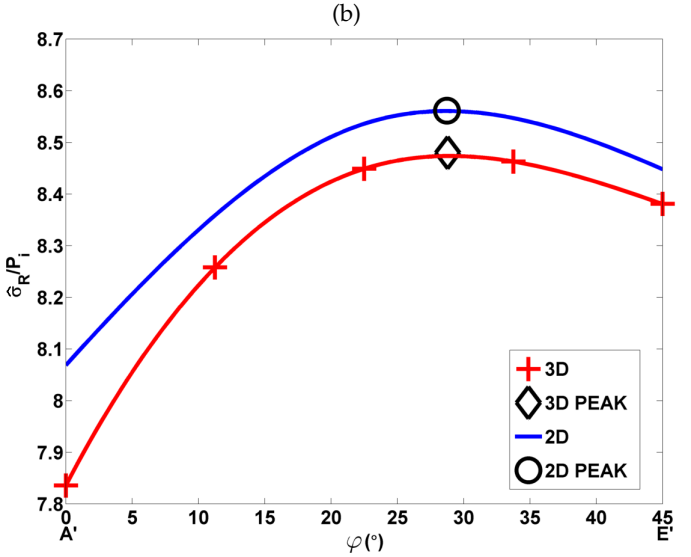

(c)

Figure 6.17: Plots of normalized local peak rupture stresses versus bend angle positions for the pipe bend models (a) HR_A, (b) HR_B, (c) HR_C.

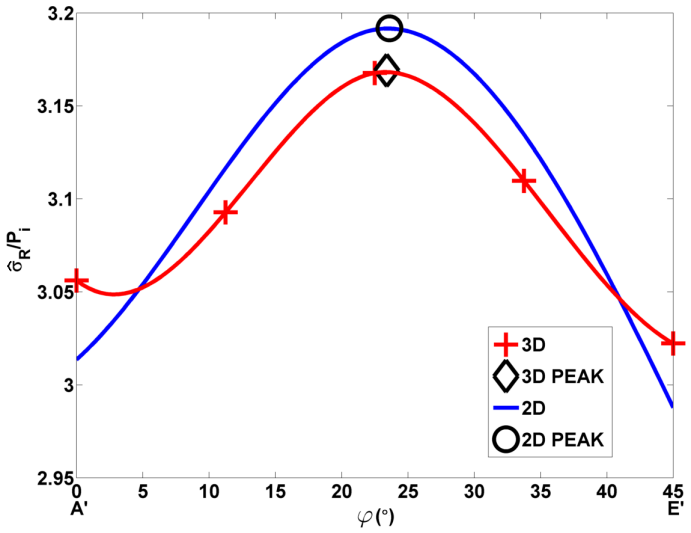

(a)

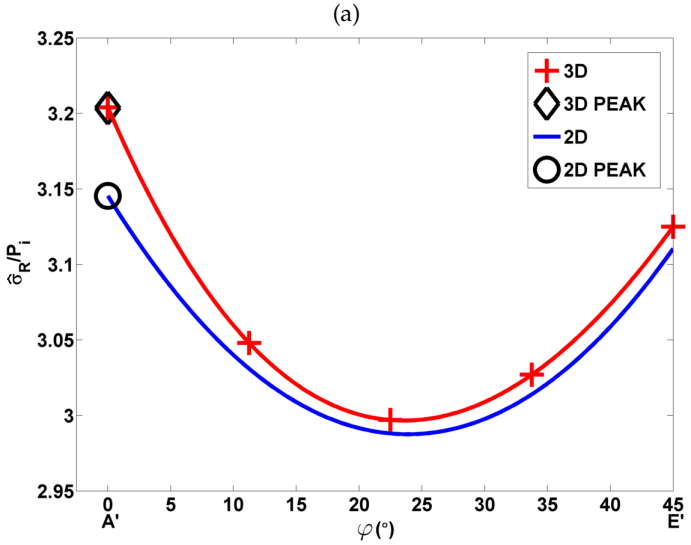

(b)

Figure 6.18: Plots of normalized local peak rupture stresses versus bend angle positions for the pipe bend models (a) MS_A and (b) MS_B.

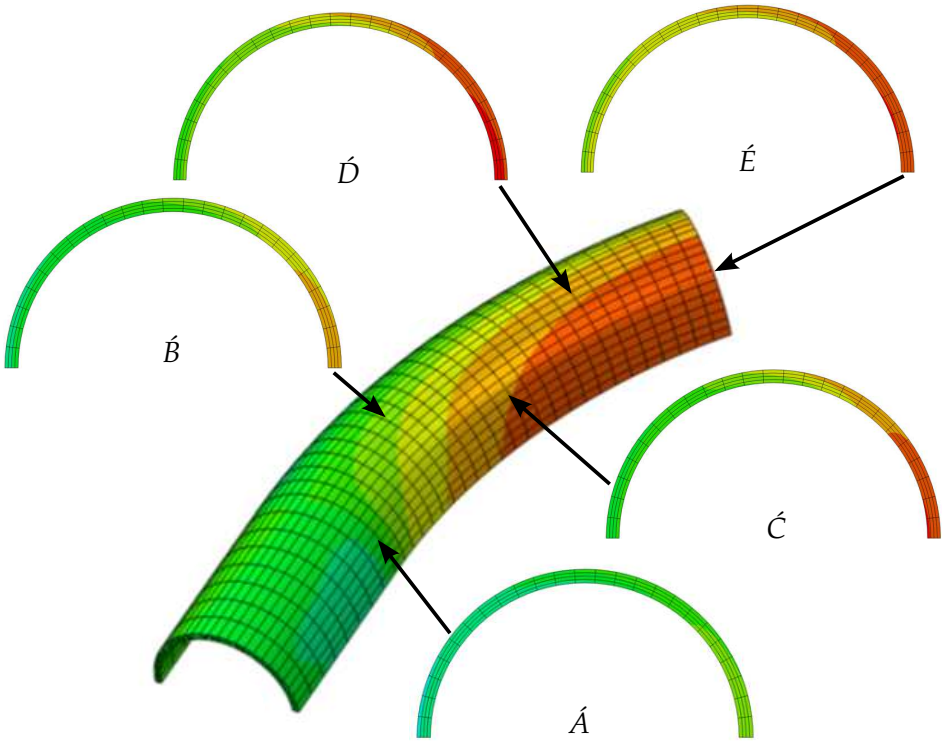

Figure 6.19: Example contour plots of normalized rupture stress the proposed 2D interpolation procedure (shown for the geometry HR_A, $\alpha = 0.3$, $n = 6.108$).

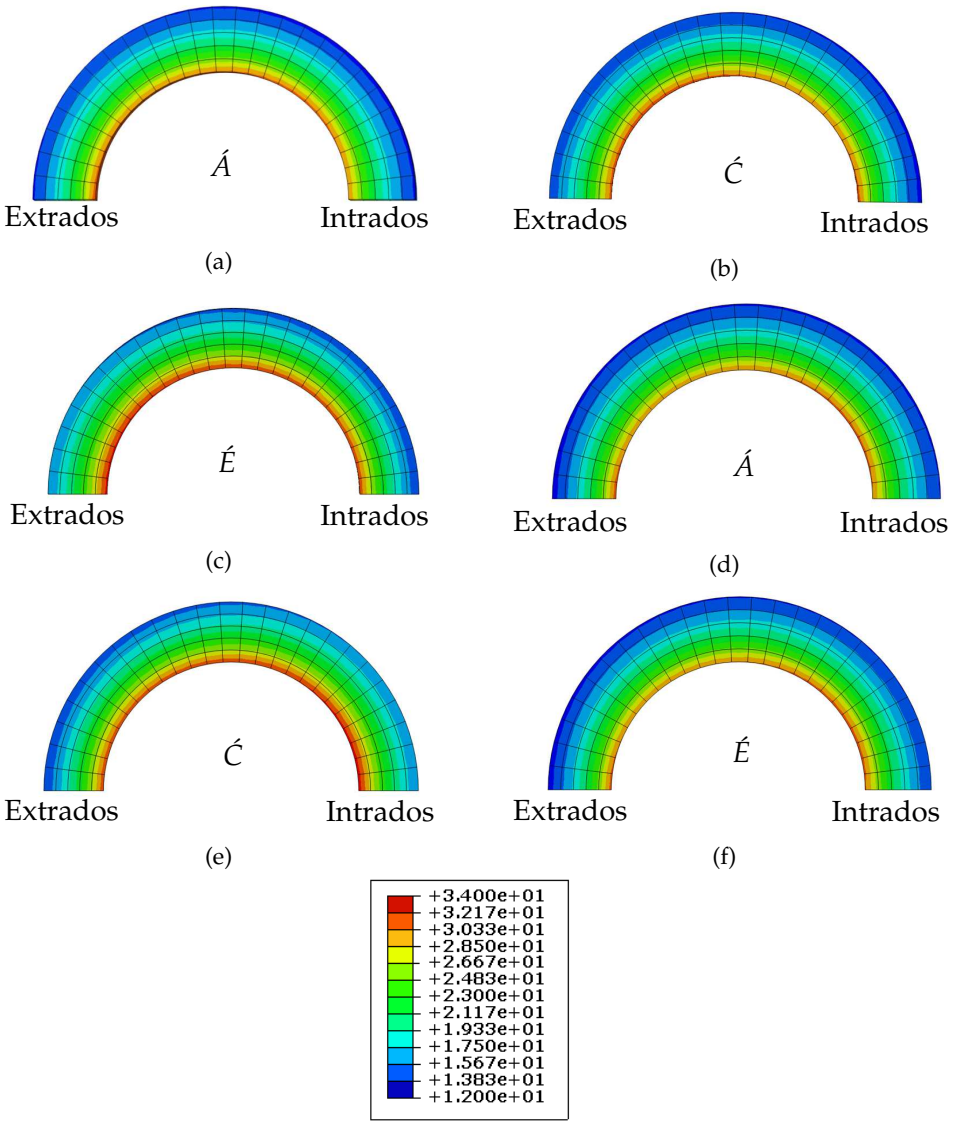

Figure 6.20: Equivalent von Mises stress (normalized to internal pressure) contour plots for the model MS_A ($\alpha = 0.3$, $n = 6.108$), taken at cross section planes defined in figure 6.14. Both 3D ((a), (b) and (c)) and 2D ((d), (e) and (f)) meshes are shown.

Several design codes are used in industry to account for the dimension variation, the relevant example used in the UK at present being BS EN 13480[128]. Tolerances for the intrados and extrados wall thicknesses ($e_{In/Ex}$) are derived based on the allowable wall thickness for a straight pipe section (e, see equation (6.10)). The correction of the straight pipe wall thickness is based on the mean bend radius (R_M) of the pipe bend and outside diameter of the pipe (D_O). Using the assumed straight pipe dimensions, tolerances can be established for the two bend types considered in the present chapter. 3D and 2D meshes can then be generated that represent a design case for the two pipe bend types considered. Clearly, equation (6.10) will not estimate any variation in intrados

and extrados wall thickness with bend angle position. This is observed in industrial data, as shown by equations (6.8) and (6.9). To generate FEA models from the design data therefore, it is assumed that the tolerance values for the intrados and extrados wall thicknesses ($e_{In/Ex}$) are applied around the pipe bend (i.e the wall thickness is consistent at the intrados and extrados but neither of these values are equal to the wall thickness in the straight pipe section). FEA conducted on the design case models (see figure 6.21) highlights the potential importance of accurately determining the dimensions around a pipe bend (as opposed to assuming design conditions). From the 3D models, it is clear that peak ruptures stress positions are predicted at the bend/straight interface for the design case. This is not always the case in the more realistic models. Rupture stress values are the same order of magnitude; however percentage differences vary between 5% and 25% for the Hot Reheat type and 1% and 7% for the Main Steam Type. Using the reference rupture stress method for life prediction[138,139,192], it is noted that the reference rupture stress is raised to the power χ (see equation (5.2)). Relatively small variations in the reference rupture stress can therefore result in large differences in predicted failure times. This study therefore highlights the importance of full dimension characterisation of pipe bends when more accurate life estimations are required.

$$e_{In/Ex} = e\frac{(R_M/D_O) \mp 0.25}{(R_M/D_O) \mp 0.5} \tag{6.10}$$

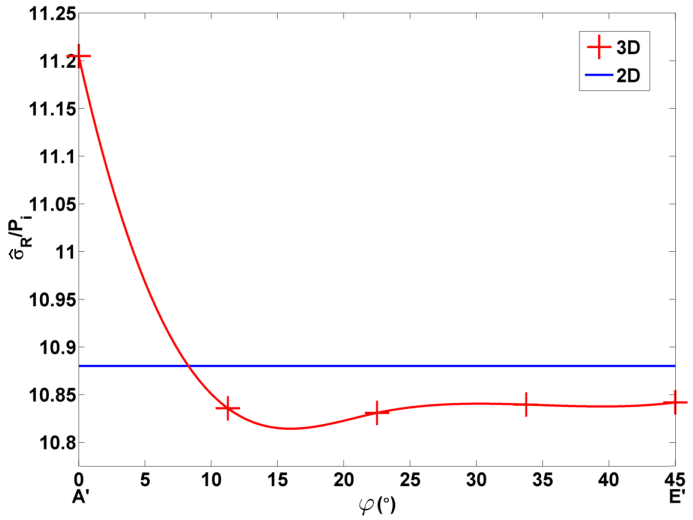

(a)

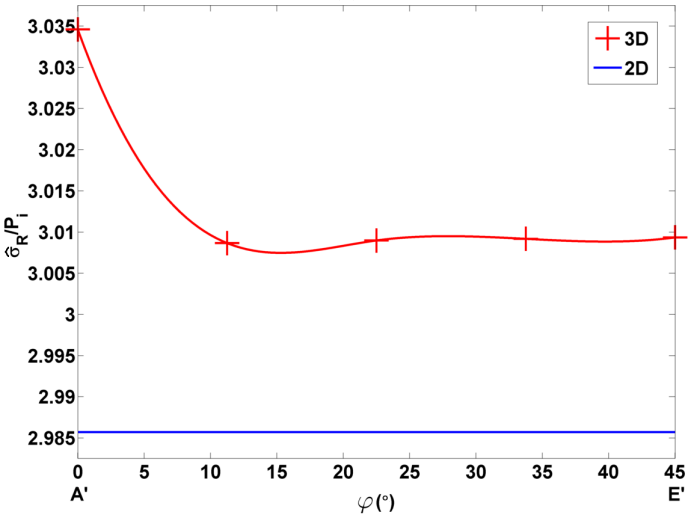

(b)

Figure 6.21: Plots of normalized local peak rupture stresses versus bend angle position for (a) Hot Reheat design bend and (b) Main Steam design bend.

Effect of Bend Angle

As mentioned previously a 90° pipe bend angle represents an upper limit for most industrial applications, displaying the greatest degree of dimensional variation. 90° pipe bends are also the most common in power plants. Despite this, it is important to verify that the method described above can be applied to bend angles less than 90°. To investigate this effect, 30° and 60° bend angle hot reheat pipe bends were considered. Characteristic equations were assumed that represent the variation of $Th_{NOM}(\varphi = 0)$ and $In(\varphi = 0)$ in the relevant bend angle range. For this study therefore, the characteristic equations and geometry factors for the bends HR_A and MS_A are maintained when creating any of the variable bend angle models. The geometry of a 30° model therefore is identical to the first 30°'s of the 60° and 90° models. This assumption

is required as there is no industrial data available at present for bend angles other than 90°. Given the suspected planar transfer of material during the bending process, this assumption is considered reasonable. The 5 planes used to construct the 2D models were equally spaced in all 3D models regardless of bend angle. As before, quarter 3D models were used. Plots of normalized rupture stress can be seen in figures 6.22 and 6.23. The same naming convention used in the previous result plots is applied. As with previous examples, the location and magnitude of the peak rupture stress in the complex 3D model is generally well predicted by the 2D axi-symmetric method. Away from the bend/straight interface region, the general stress state is also well approximated, with percentage differences typically less than 1% for both bend types.

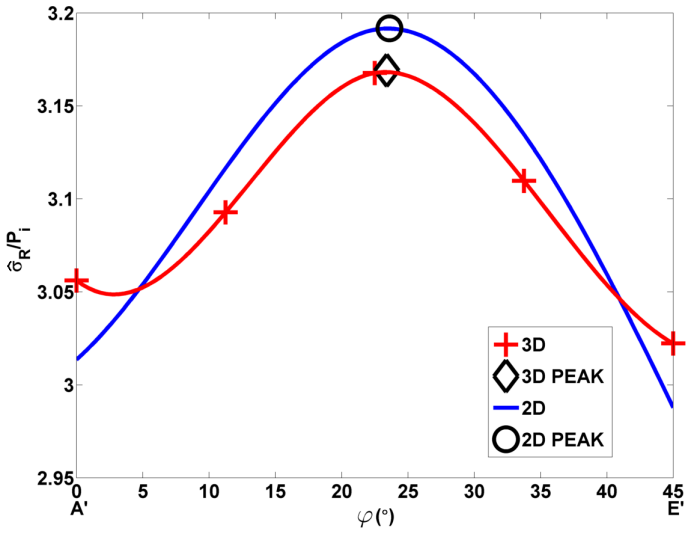

(a)

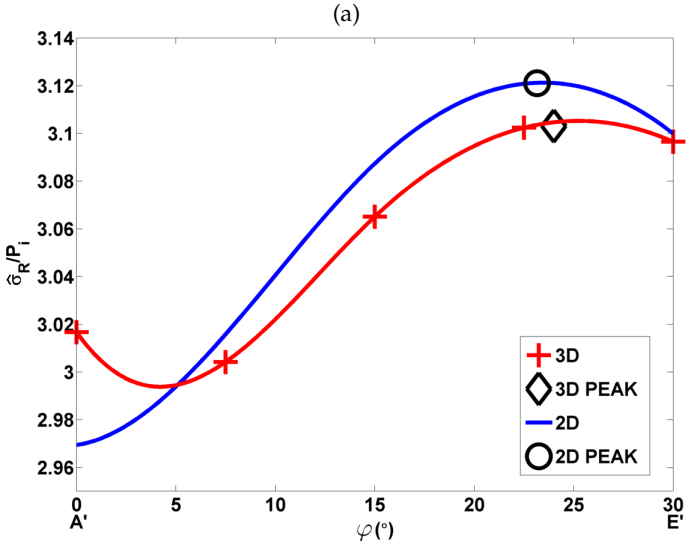

(b)

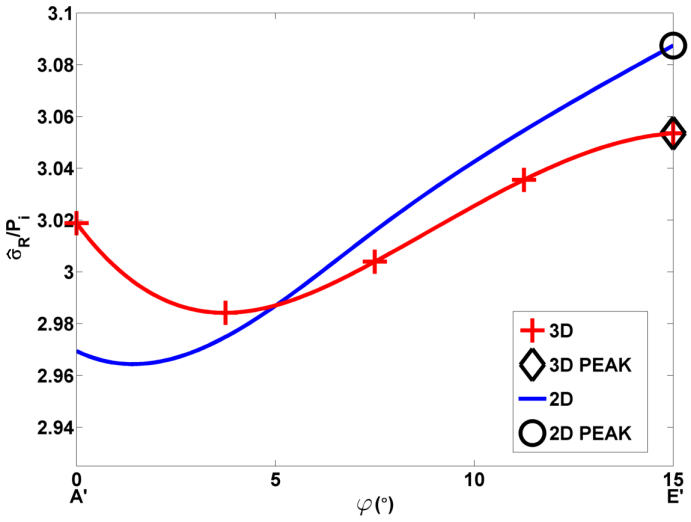

(c)

Figure 6.22: Plots of normalized local peak rupture stress versus bend angle position for the models (a) MS_A 90° pipe bend, (b) MS_A 60° pipe bend and (c) MS_A 30° pipe bend.

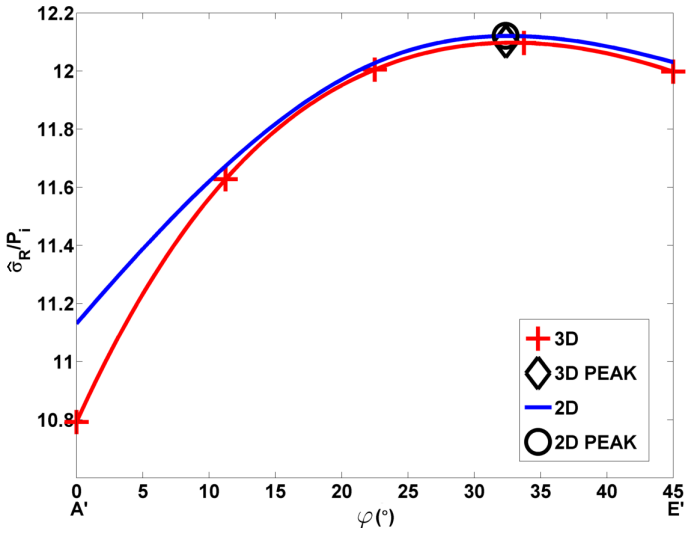

(a)

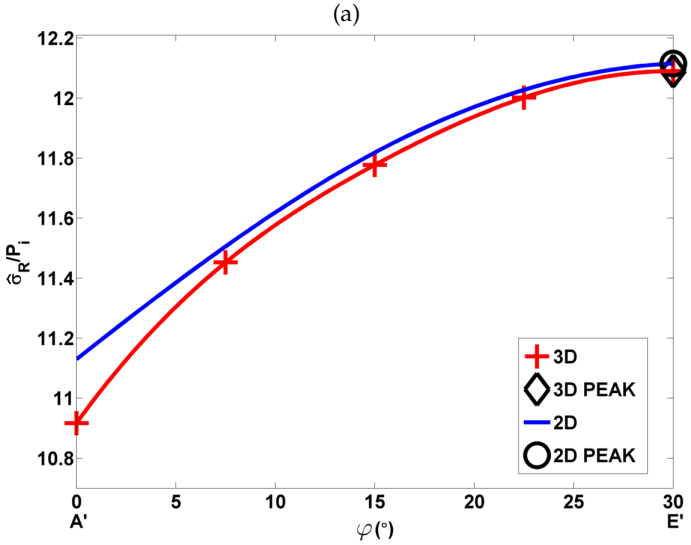

(b)

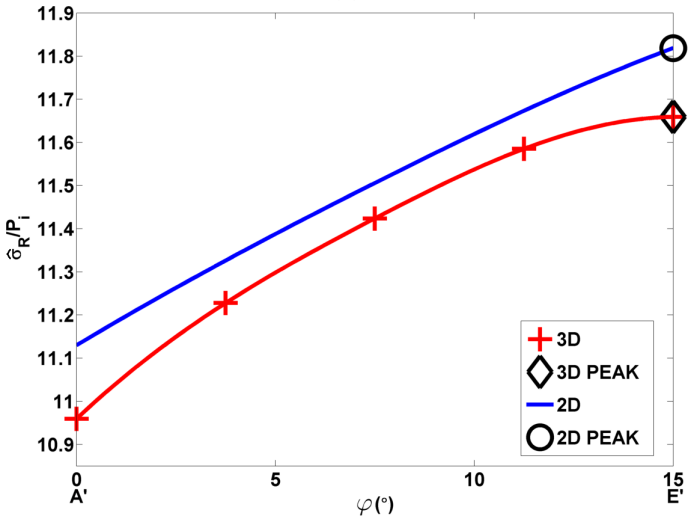

(c)

Figure 6.23: Plots of normalized local peak rupture stress versus bend angle position for the models (a) HR_A 90° pipe bend, (b) HR_A 60° pipe bend and (c) HR_A 30° pipe bend.

Effect of Stress Exponent (n) Value

The dependence of a steady-state stress value in a structure on the material's stress exponent value (n) has been proposed previously by Calladine[197]. For a point in a structure operating under steady-state creep, a linear relationship may be used between stress and the inverse of the stress exponent ($1/n$). The stress exponent is therefore a critical parameter in steady-state creep analysis. The ability of the 2D axi-symmetric interpolation method to predict the response of a 3D model should be verified therefore for a range of exponent values. The stress exponent will be dependent on material, stress range and operating temperature. The same material may exhibit a great variance in stress exponent values between heats[196]. Analysing a range of stress exponent values therefore gives confidence for the interpolation method to be extended to alternative materials. Stress exponents of 4, 6, 8 and 10 were applied to the models HR_A (figure 6.24) and MS_A (figure 6.25).

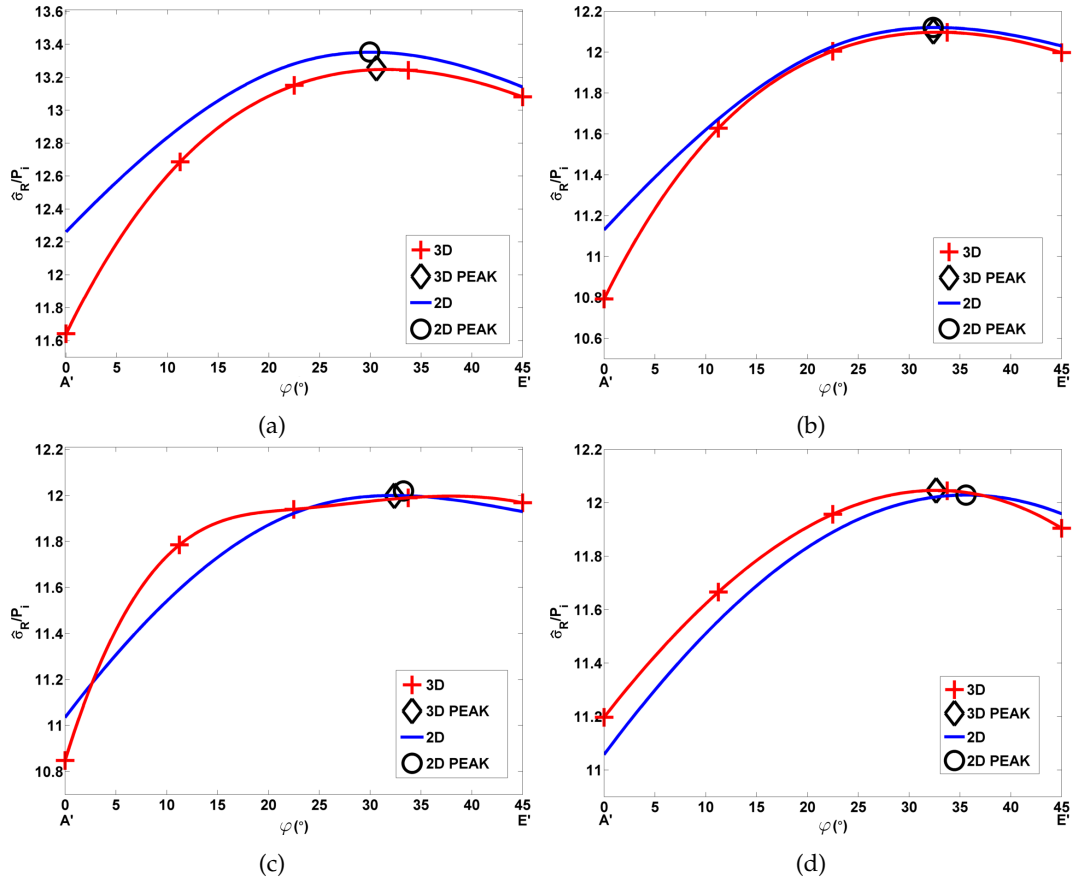

Figure 6.24: Comparison of rupture stresses predicted by 2D axi-symmetric and 3D models for a Hot Reheat type pipe bend (HR_A), with stress exponent values of (a) $n = 4$, (b) $n = 6.108$, (c) $n = 8$ and (d) $n = 10$.

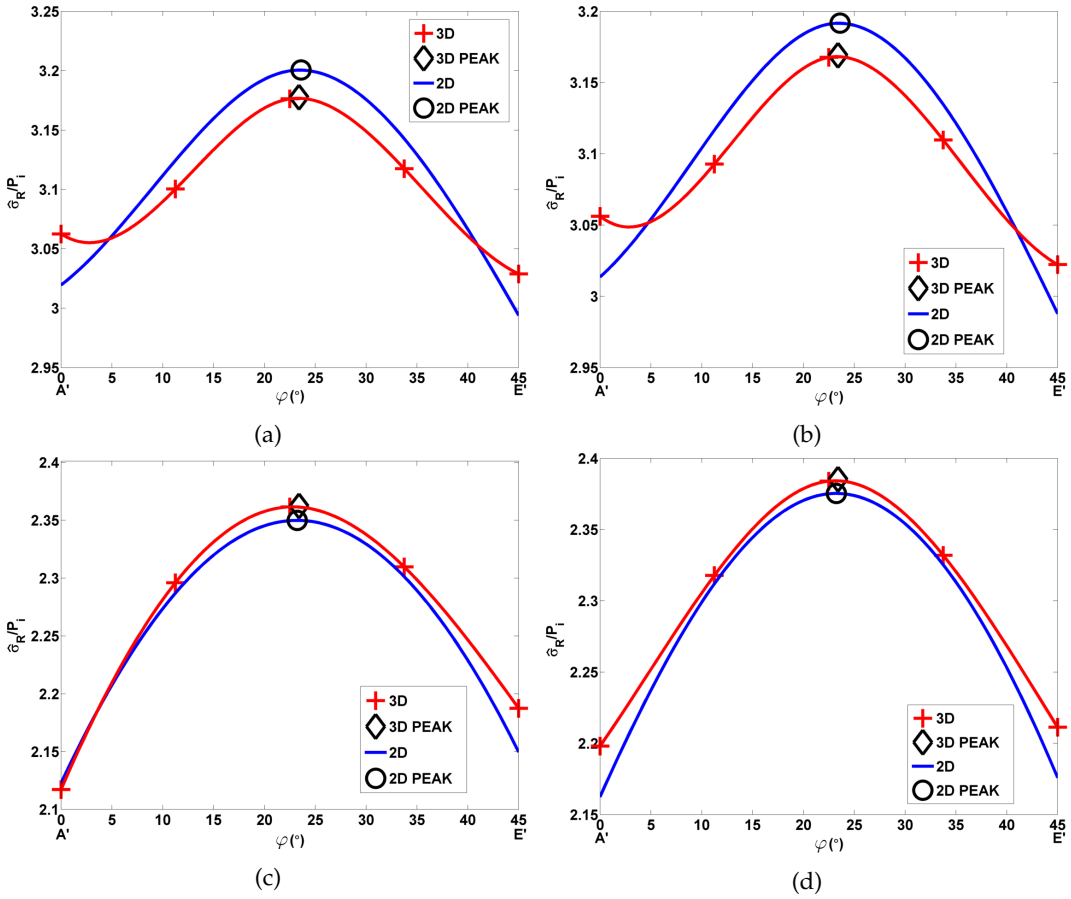

Figure 6.25: Comparison of rupture stresses predicted by 2D axi-symmetric and 3D models for a Main Steam type pipe bend (MS_A), with stress exponent values of (a) $n = 4$, (b) $n = 6.108$, (c) $n = 8$ and (d) $n = 10$.

Effect of Multiaxial Material Constant (α) Value

The contributions from the maximum principal stress and equivalent von Mises stress in the rupture stress is controlled by the multiaxial material constant (α). It is foreseeable therefore that the magnitude and location of the peak rupture stress could be influenced by the value of α. Two geometries that have a peak rupture stress in the bend section (as opposed to the bend/straight interface or the crown of the bend) for the previous case (where $\alpha = 0.3$) where analysed again using variable α values. Multiaxial material constant values of 0, 0.3, 0.7 and 1 were applied to the models HR_A (figure 6.26) and MS_A (figure 6.27).

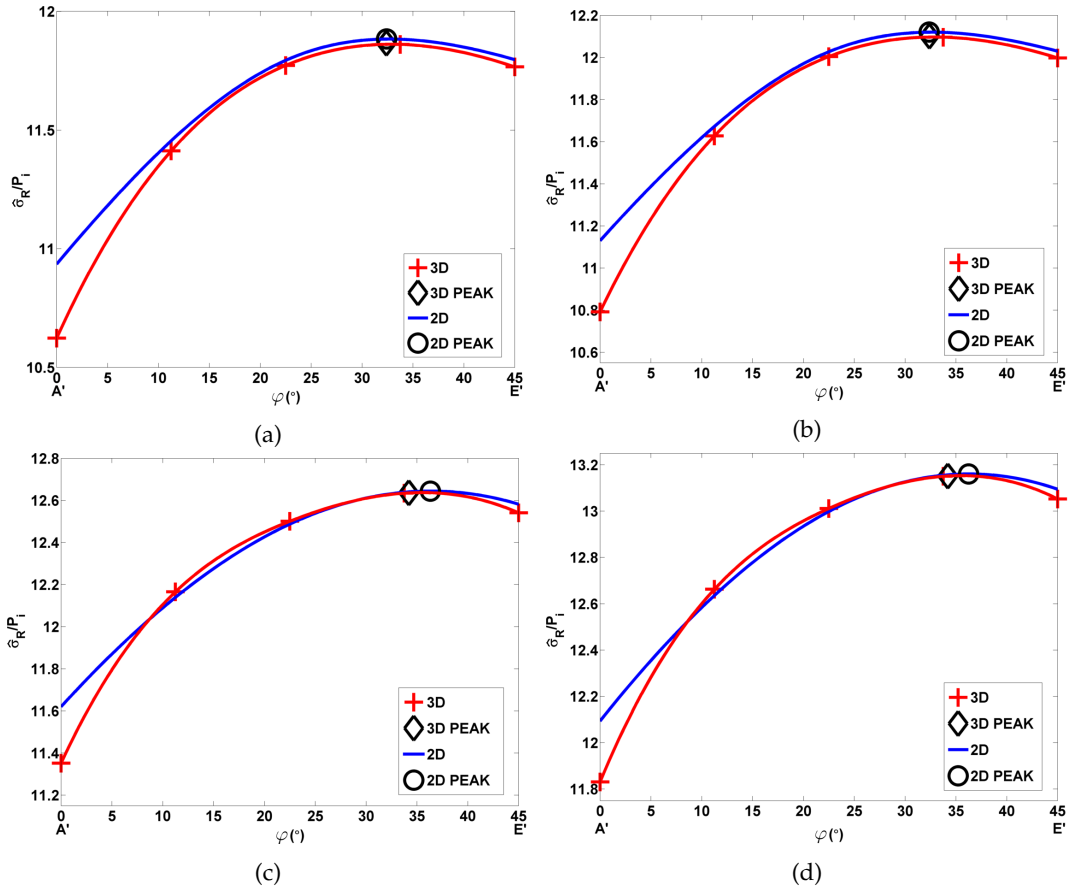

Figure 6.26: Comparison of rupture stresses predicted by 2D axi-symmetric and 3D models for a Hot Reheat type pipe bend (HR_A), with multiaxial material constant values of (a) $\alpha = 0$, (b) $\alpha = 0.3$, (c) $\alpha = 0.7$ and (d) $\alpha = 1$.

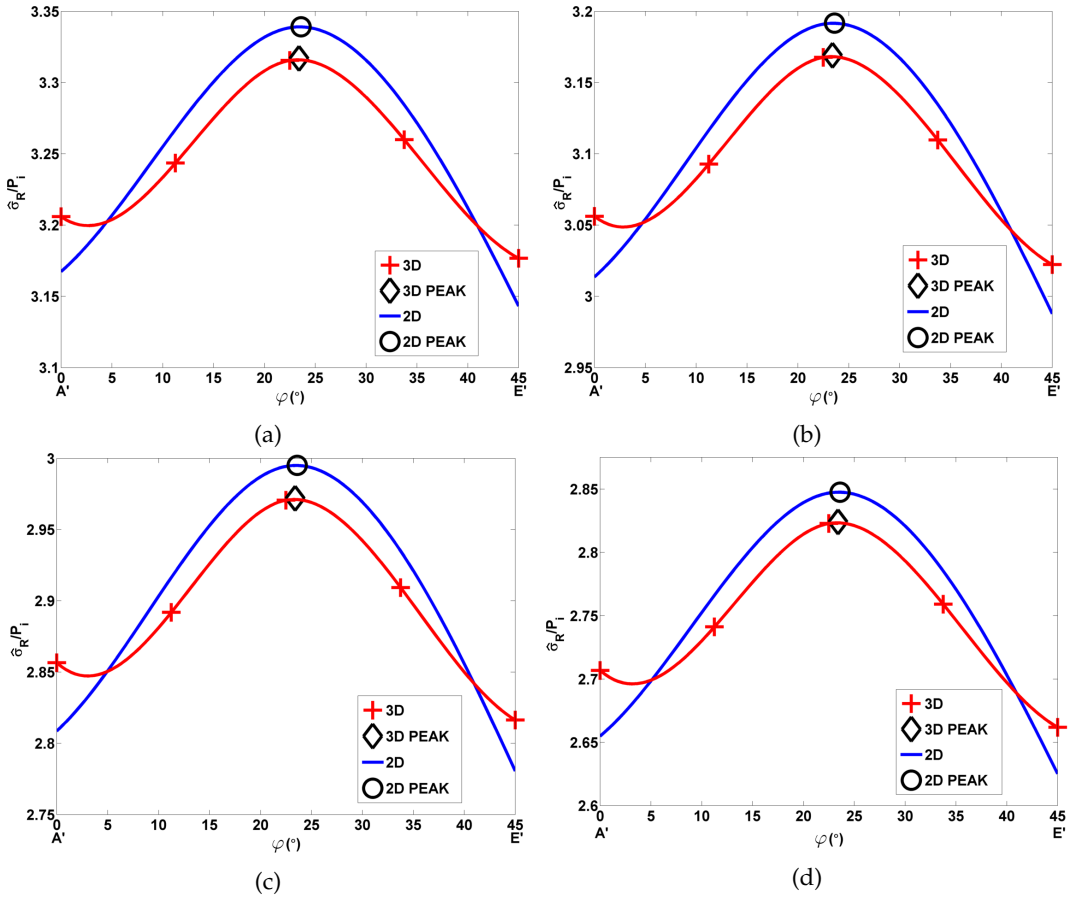

Figure 6.27: Comparison of rupture stresses predicted by 2D axi-symmetric and 3D models for a Main Steam type pipe bend (MS_A), with multiaxial material constant values of (a) $\alpha = 0$, (b) $\alpha = 0.3$, (c) $\alpha = 0.7$ and (d) $\alpha = 1$.

6.9 Discussion and Conclusions

Pipe bends exhibit significant variations in cross section dimensions (predominately induced during the manufacturing process). The wall thicknesses vary circumferentially at specific bend position angles; the degree of variation is dependent upon the bend angle. A parametric method has been developed which allows the complexity of a specific type of pipe bend (such as a Main Steam pipe bend with a $2m$ bend radius) to be represented by only two factors ($In(\varphi = 0)$ and $Th_{NOM}(\varphi = 0)$) and related characteristic equations. Other pipe bends of a similar type may also be characterised by these two factor values (i.e. using the same characteristic equations). For example, if one Main Steam pipe bend was fully characterised (geometry factors and characteristic equations), additional Main Steam pipe bends with a similar bend radii and outside diameters (as exist in industry) may also be defined using the same characteristic equations but with different factor ($In(\varphi = 0)$ and $Th_{NOM}(\varphi = 0)$) values. This procedure has been used for a systematic study of the peak steady-state rupture stresses in pipe bends under internal pressure loading only. Parametric equations were then

established using the afore mentioned geometry factors ($In(\varphi = 0)$ and $Th_{NOM}(\varphi = 0)$) to predict peak rupture stress magnitudes for a wide range of practical geometries and stress exponents (n). Although alternative parametric equation forms could be proposed to better fit the rupture stress surfaces shown in figures 6.8 and 6.9 and a greater number of levels could be considered for the factors $In(\varphi = 0)$ and $Th_{NOM}(\varphi = 0)$ in future systematic studies, the present chapter establishes the framework for the procedure.

Stress functions for Hot Reheat pipe bends (figure 6.9) are found to be generally smoother than those for their Main Steam counterparts (figure 6.8). In general the stress function predicts these smoother surfaces with a higher accuracy (as shown by the relative coefficient of determination, r^2, values in table 6.3 and in the interpolation study). In all cases however coefficients of determination are very high indicating a good quality of fit (the lowest value is actually noted for the Hot Reheat type pipe study when $n = 5$). If parametric equations similar to the ones derived in this work are to be used in industry, it is critical that interpolation between geometric factors ($In(\varphi = 0)$ and $Th_{NOM}(\varphi = 0)$) and between material parameters (n and α) should return accurate results. Even between different heats of the same material, stress exponent values may double in magnitude[196]. Clearly, surfaces for every stress exponent or geometry factor cannot be produced. Given the approximately linear relation which exists between the stress at a point in a structure and $1/n$ (identified by Calladine[197]), it is reasonable to expected that the stress surfaces shown in figures 6.8 and 6.9 for different (approximately equally spaced) stress exponent values would adhere to this linearity. However, for both Hot Reheat and Main Steam type pipe bend meshes, the distance in function space between the $n = 8.46$ and $n = 6.108$ surfaces is far greater than that between the $n = 6.108$ and $n = 4$ surfaces. This greater distance results in the reduced accuracy which occurs when stresses are predicted for $n = 7$ as opposed to $n = 5$ in the interpolation study (see table 6.4). Furthermore, it is noted that the surfaces in both pipe bend types for $n = 6.108$ and $n = 4$ converge as the factor $Th_{NOM}(\varphi = 0)$ is reduced. The constraint imposed by the varying pipe cross section dimensions around the pipe bend is complex. Variations in n cause different stress fields to be realised in the pipe bend. Given that the peak rupture stress is dependent on both the maximum principal stress (σ_1) and equivalent von Mises stress (σ_{EQ}), the variation in stress state may result in different peak rupture stress locations. The approximate linear relationship proposed by Calladine is only applicable to stresses at the same position, with the same α value. It is worth noting that, while the percentage differences in table 6.4 for $n = 7$ are high (most notably for the Main Steam pipe bend geometry), this is most likely due to the larger distance over which the parametric constants are interpolated. The relationships shown in figures 6.10 and 6.11 are estimated based on only three stress surfaces (shown in figures 6.8 and 6.9). The relationship in the high stress exponent (n) region could be improved with more stress surfaces in this region, thereby increasing the resolution.

Work by Sun et. al. suggests that (for straight pipe lengths at least) the peak rupture

stresses will increase with α. However, the degree with which it varies is dependent on the ratio of the wall thickness to the outside diameter[192]. Thin walled pipes generally experience greater changes in the steady-state peak rupture stress with variations in α than thick wall examples do. Similar behaviour can be seen in figure 6.13 for the Hot Reheat pipe bend type. Main Steam pipe peak rupture stresses however decrease with α (see figure 6.12). It can also be seen that in both of these figures, non-linear relationships are found to exist between α and the peak rupture stress for $n = 8.46$. Contributions from the maximum principal stress (σ_1) and from the equivalent von Mises stress (σ_{EQ}) are controlled by the material constant α when calculating the rupture stress (σ_R). The magnitude (and in the case of the maximum principal stress, the direction) of σ_1 and σ_{EQ} are controlled by the geometry of the structure being analysed. In the case of pipe bends, Hot Reheat type geometries give rise to greater σ_1 values than σ_{EQ}, resulting in increased rupture stress values with increased α values. The opposite may be true for Main Steam type pipe geometries. Furthermore, the expected linear relationship between peak rupture stress and α is only valid at the same point in a structure. In the FEA study used in section 6.7.3, variations were observed in the exact locations of peak rupture stresses for different α values (particularly in high n value cases). As such, the non-linear behaviour observed in figures 6.12 and 6.13 may be the result of a combination of multiple linear relationships for different points within the structure.

The present work requires a great deal of time to be invested in producing and analysing the detailed 3D meshes for the systematic study. A methodology has been established for creating the meshes in a consistent manner using a specially design program (see section 7.3), however it is important to note some of these modelling assumptions. In particular, great care is required when defining the inside surface of the pipe bend. Internal surfaces at specific cross sections, where wall thickness variations exist, may be created in CAE packages by defining the intrados and extrados wall thicknesses, along with the nominal thickness at the peak of the bend cross section (circumferential position 1 in figure 6.1 (b)). These points could then be connected using a spline, however if these three points alone are used a parabola will be produced, giving rise to sharp corners at the intrados and extrados, (plane XZ in figure 6.6). Clearly, this is incorrect and would lead to spurious stress concentrations. However, these concentrations can be removed by specifying the nominal thickness again at the circumferential position 9, thus giving 4 points to define the spline. In the quarter model, information at circumferential position 9 has no relevance. Therefore, once the spline is created it can be trimmed accordingly. While concentrations may still be present, they will not be sharp tips in the plane of symmetry. Modelling procedures should identify the correct number of points to be defined when creating the surfaces for a pipe bend model. Supposing that only the values at circumferential positions 1, 5, 9, 13 (see figure 6.1 (b)) can be directly derived using the parameter method described in this work, intermediate values (for example, at positions 3, 7, 11, 15) could be estimated

using, say, a linear approximation between adjacent values. This would no doubt lead to a smoother surface (with more points defined). However, care must be taken not to over constrain the problem, which would cause divergence from reality.

The complications arising from the use of 3D models has been addressed by using a novel 2D interpolation procedure. The cross section of the 3D model at specific bend angle positions (φ, in figure 6.1 (a)) can be used to define a 2D axi-symmetric model. Several different 2D models can then be created round the pipe bend. In this way, complex dimensions variation that may be present in the intrados and extrados of a pipe bend due to manufacturing or service can be represented with relative ease. Not only are 2D models simpler to produce, they will generally take substantially less time to complete than 3D counterparts (typically, 3D model completion times are 140 and 250 times greater than 2D models for thin walled and thick walled pipe bends, respectively). Even when multiple 2D models are used (as in the above interpolation procedure), completion times are usually noticeably shorter than a full 3D analysis. It can be seen from the results in section 6.8.3 that, for the majority of cases, when a peak rupture stress in a 3D pipe bend model occurs away from the bend/straight interface (due to internal pressure loading only), the location and magnitude of the peak rupture stress can be approximated using several 2D axi-symmetric models. Although the smaller b_1 and b_2 values (see equation (6.9)) used for models in this section result in smaller wall thickness variations than the models in section 6.6 (see table 6.8), significant stress variations are still observed and geometries are representative of real industrial cases. Errors are generally in the region of 1%. Furthermore, the general stress state across the pipe bend can be well approximated.

Typically, the stress state at the bend/straight interface is not predicted as accurately (compared to the other locations) by the 2D axi-symmetric interpolation method; see figure 6.18 (b). Percentage differences in this region are usually 2%-5% for both thick wall and thin wall pipe bends. Significant discrepancies in the prediction of the magnitude of peak rupture stress at crown (centre) of bend are also noted; see figure 6.22 (c) and figure 6.23 (c). Again, percentage differences are approximately 2%-5%. Both thin walled and thick walled pipe bends exhibit this discrepancy in the magnitude of peak rupture stress prediction. The location of peak rupture stress however is in general well approximated in these situations (an exception being shown for the pipe bend HR_A in figure 6.17 (a)). As the bend is pressurized, it will attempt to straighten[119]. This induces a bending moment in the 3D model, effectively resulting in redistributed loading in the bend section. The presence and effect of this induced bending moment will be partly dependent on the precise geometry of the pipe bend. It is suspected that for certain pipe bend dimensions, the stress state will be mainly dependent on the planar geometry. In this case, the 2D interpolation method should provide a reasonable approximation of the 3D model. Stress profiles predicted by the 2D models may map directly onto the 3D model (see figure 6.19). Alternatively, the constraint of the entire model may have a

significant effect. This could take the form of an induced bending moment in the bend or a complex interaction between the planar deformations in the bend (potentially to ensure continuity of volume). In these cases, the 2D models (which of course cannot account for the interaction between planes) may not be sufficient to estimate the 3D model.

In all cases in this chapter (both 2D and 3D models) peak rupture stresses were localized around the intrados of the pipe bend (circumferential position 13, see figure 6.1 (b)). The results of this study therefore agree with literature[104]. Using this information on circumferential failure position and the critical bend angle position from the 2D interpolation method, non-destructive testing could be applied to in service components in a precise way, increasing the likelihood of defect detection.

Several trends in the predicted rupture stresses have been noticed. A reduction in bend angle for example is commonly followed by a reduction in peak rupture stress. Variations in the stress exponent (n) or the multiaxial material constant (α) have little to no effect on the accuracy of peak rupture stress location predictions. When thin walled examples (the Hot Reheat type) are analysed, an increase in α often results in an increase in the rupture stresses calculated (see figure 6.26). The opposite (a reduction in computed rupture stresses for an increase in α) can be observed for the thick walled Main Steam type pipe bends, see figure 6.27. Increases in the stress exponent (n) values applied in the analyses commonly result in lower calculated rupture stresses for both pipe bend types (see figures 6.24 and 6.25), in agreement with Calladine[197,198].

Chapter 7

The Development of a Power Plant Pipe Bend Analysis Toolbox and Neural Network

7.1 Introduction

The work presented thus far has been completed in order to provide a foundation for the development of power plant component analysis toolbox. For example, in chapters 5 and 6 steady-state peak rupture stresses were calculated for power plant pipe sections (straight lengths with scoop excavations and pipe bends under internal pressure loading). These steady-state rupture stresses can be used with CDM equations (compared in chapter 4) to estimate component failure lives. In the present chapter, an analysis methodology (or "toolbox") is developed that combines these approximate techniques. This establishes a framework for the advanced analysis methods employed in academia to be implemented in industry. For example, FEA models of pipe bend sections with dimension variation and complex system loading conditions are difficult to define in computer aided engineering (CAE) packages. With a suitable routine however, these meshes could be generated quickly and consistently. These models could then be analysed without the user having to interact directly with commercial FEA packages (such as ABAQUS). Results could then be post processed in order for the most relevant outputs to be returned. All of the procedures described should be included in a graphical user interface (GUI) to encourage their use.

A neural network is also developed and trained in the present chapter. The described methodology includes two possible analysis streams for practising engineers. In one stream, full FEA models may be created with bespoke loading conditions and then analysed to determine complete stress states in creeping power plant components. Although the GUI greatly simplifies the modelling procedure, completing FEA calculations may represent a significant time investment. An approximate analysis stream

is therefore also suggested. This would utilise the empirical equations developed in several of the previous chapters. The neural network represents a potential generalised method for estimating peak rupture stresses in pipe bend sections with complex system loading patterns.

7.2 Overview of Methodology

The work described in this thesis has a common theme in that it all may be applied to a general component analysis methodology. This methodology could provide a formulaic approach for the analysis of components, making the analysis procedure straight forward and establishing an entry point for novel analysis techniques to be implemented into industry. A flowchart detailing the proposed methodology can be seen in figure 7.1. For clarity, a brief explanation of each module's role in component analysis will be given here.

A primary input required from the user is the definition of a component's geometry. Pipe bend sections have received a great deal of attention in the present thesis due to the relatively limited amount of research that has been dedicated to them, however in principal any component type (such as branch pipe sections or steam headers) may be incorporated. Material constants may be supplied directly from a user or, using optimisation strategies similar to those discussed in chapter 3, they may be found from experimental data. The automation of a robust and reliable optimisation procedure allows representative material constants to be determined from potentially novel experiments. If small specimen techniques (figure 2.39) could be implemented to determine local material constants, scoop sampling would become increasingly prevalent, thus highlighting the significance of the research conducted in chapter 5. Available material constants and the type of loading conditions to be used will determine the most suitable material model. For example, fatigue or cyclic loading conditions could potentially be modelled using a Chaboche type material model, whereas a pure creep condition may be approximated using CDM equations (such as Kachanov and Liu-Murakami models). At this point, two alternative analysis strategies may be employed. Full FEA analysis may be completed and results may be presented in their entirety (which would be of interest to users wishing to have a detailed understanding of a component) or post processed in order to determine quantities of interest (such as peak rupture stress, $\hat{\sigma}_R$). Alternatively, if a full FEA simulation is not required, approximate methods (such as empirically derived equations or neural networks) can be used to provide estimates of quantities of interest in a short period of time.

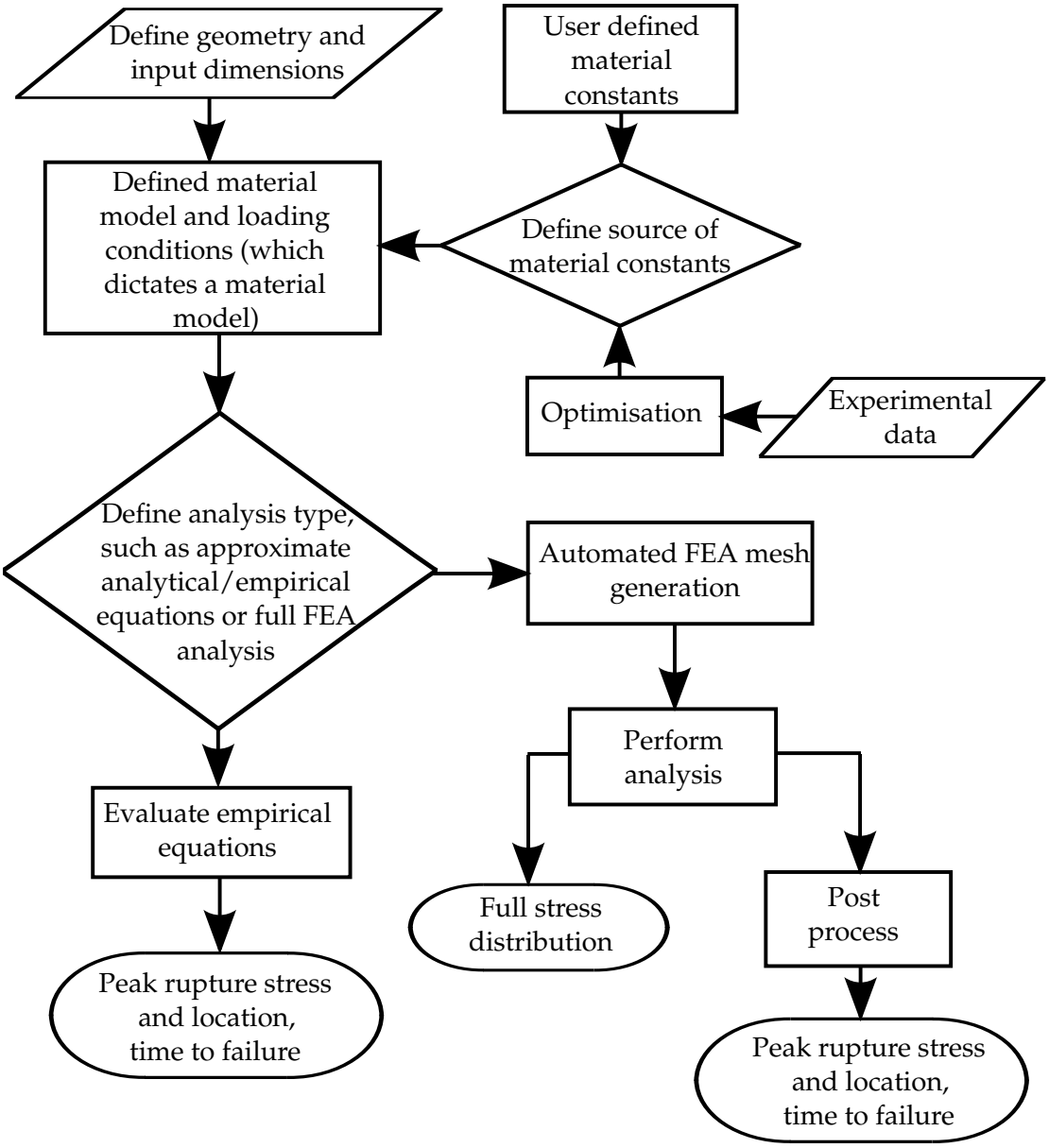

Figure 7.1: A flowchart detailing the proposed analysis methodology.

7.3 Graphical User Interface (GUI) Development

7.3.1 Requirement

Fundamentally, the incorporation of the analysis methodology into a GUI has been undertaken to promote its use by practising engineers. It allows complex FEA models to be generated quickly and consistently using data that would be collected in during common outage inspections. The GUI may be compiled as a stand alone executionable file, meaning that FEA input files can be generated by users that do not have access to the FEA solver (promoting cooperation between power plant departments). There

is however a secondary advantage to the GUI which is particular relevant to industry. In power plants, data may be generated through investigations carried out by several departments, which may be both internal and external to a particular site. Geometry data for power plant components may be collected by one department whereas material sampling and testing may be completed by another. In practice, this restricts how the data is used and commonly limits its implementation. A GUI encourages the formation of a central data base of component data. In this way, component analyses may be conducted with the greatest amount of information available.

7.3.2 GUI Features

Several features have been incorporated into the GUI that address concerns within industry and will therefore be summarised here. As mentioned previously, data relevant to component analysis may be collected by several different departments in a power plant. The GUI was therefore modularised as follows, with each module being accessed through the GUI's main menu (see figure 7.2):

- A component's geometry is described in a geometry file. Note that not only are the dimensions of a component detailed in this file but also the mesh (node and element definitions) information, which may also be controlled by a user. The degree of complexity of a mesh may also be defined. For example, in the presented GUI for pipe bends, meshes may be generated for 2D and 3D pipe bend models with or without manufacturing induced dimensions variation. An example may be seen in figure 7.3.

- Material constants are stored in a material file. This clearly dictates the material model to be used in an analysis (suitable error messages have been programmed in order to prevent the incorrect application of material model). The material file may be generated through a module in the GUI or by creating a text file using the correct format.

- Loading conditions (the internal pressure and system loads applied to a pipe bend section) are defined in a load file. When generated in the GUI (see figure 7.4), FEA models are created that remove unused loads and apply relevant boundary conditions.

- FEA input files and subroutines (used for analyses which implement more complex material models) are generated in the GUI by defining geometry, material and load files. As each file is generated separately, different combinations (for example, the same geometry and material under different load conditions) may be considered with the minimum amount of user effort.

- After the FEA simulation has been completed, post processing may be performed

in the GUI to determine peak rupture stress magnitudes and locations (see figure 7.5).

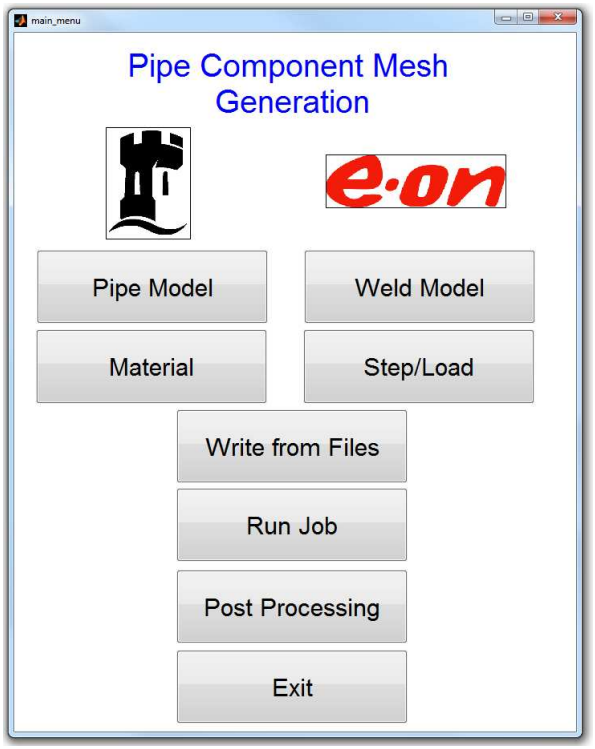

Figure 7.2: The GUI main menu, showing the modular nature of the of the GUI.

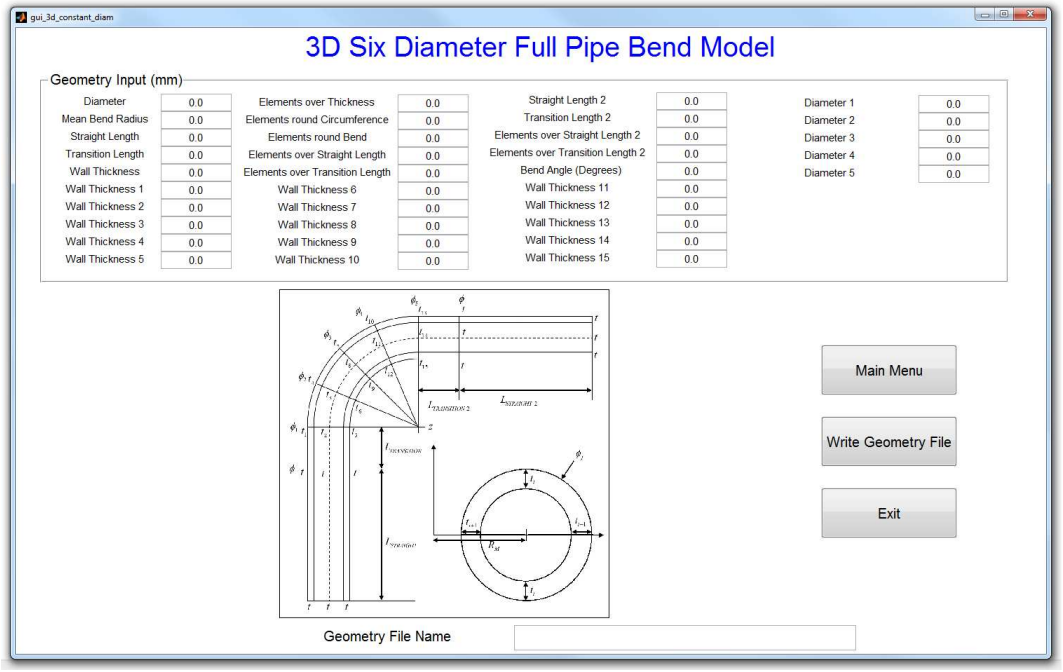

Figure 7.3: An example screen from the GUI that produces a geometry file for a 3D pipe bend. In this case, pipe external diameters may be varied around the pipe bend, along with variations in local wall thicknesses.

Figure 7.4: The GUI module to create load files. Several different system loads may be applied. Load step durations and parameters used in FEA analyses may also be defined here.

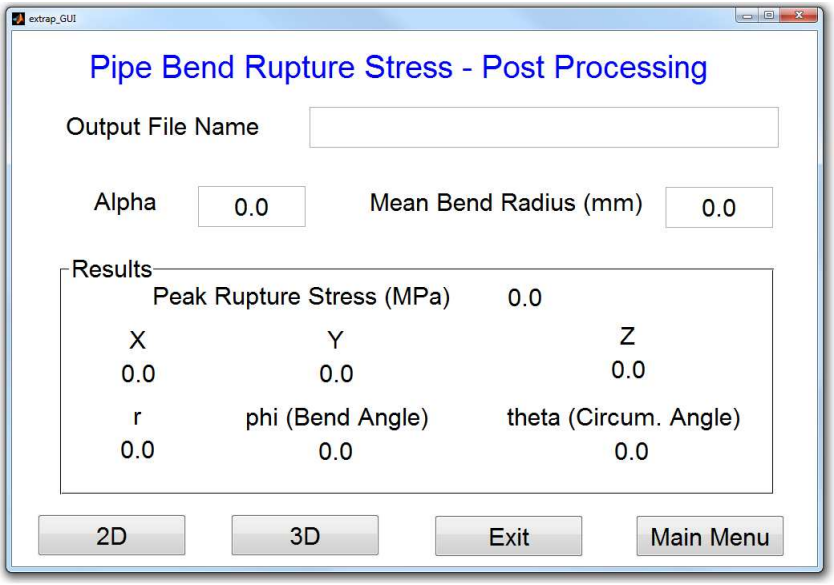

Figure 7.5: The post processing GUI module that can be used to estimate peak rupture stress locations and magnitudes in pipe bend models.

A great deal of geometry cases have been considered for the modelling of pipe bend sections. To extend the scope of the GUI a weld geometry module has been created (see figure 7.6). This allows a user to create an axi-symmetric approximation of a pipe weldment. Both similar and dis-similar welds (i.e. welds with matching and non-matching parent materials, respectively) may be modelled. Pipe welds are common place in power plant systems and have been the subject of several research projects. Indeed, weld sections will often be included to join pipe bend sections to straight lengths. Using the GUI, bespoke FEA models may be constructed for component analysis or fundamental research.

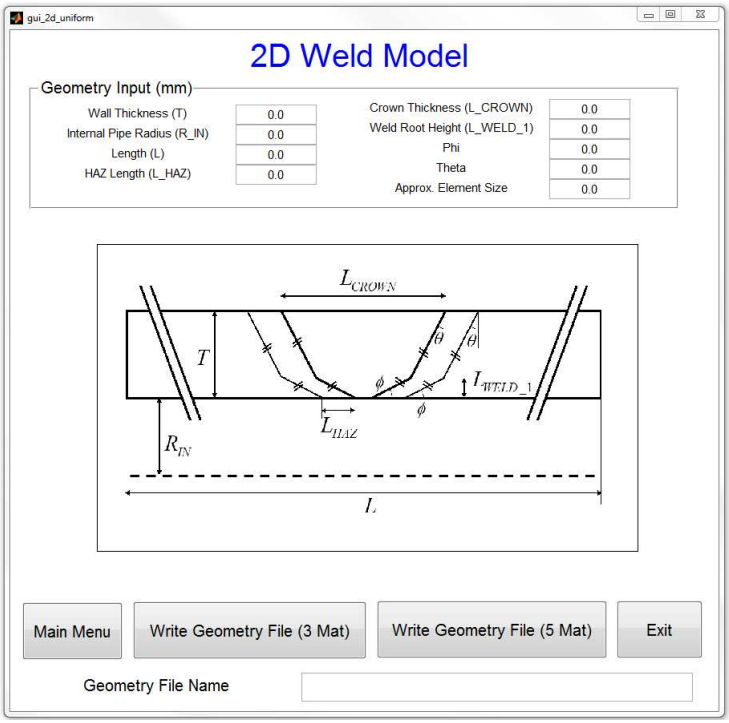

Figure 7.6: An example GUI module to create axi-symmetric pipe weld geometry files. Similar and dis-similar welds may be modelled and the user has control over over the weld metal and HAZ geometry.

7.3.3 Example Pipe Bend Results

To demonstrate the use of the GUI two example pipe bend models have been produced. Both use geometry taken from an in service 90° Main Steam type pipe bend (see section 6.2 for a description of pipe bend types). As the actual material properties of the bend material are unknown, a BAR 257 material was assumed (material constants for this material where determined in section 4.4.1 and can be found in table 4.3 for a Kachanov damage model) as this is a weaker reference version of P91 (a common power plant material), representing a degradation of material properties due to service exposure. The examples presented here are illustrative and in practice any material could be applied. A system loading condition was applied, designated B4-OP568 (this condition is specified in tables 7.3 and 7.4). A description of the loading condition convention applied in the present work may be found in section 7.4.3. The two FEA models are distinct from one another as different material behaviour models have been implemented in each. Norton's power law model (figure 7.7) was implemented in order to determine the steady-state stress state of the pipe bend and Kachanov's CDM model was used to investigate damage evolution in the same pipe bend (figure 7.8). It can be seen from figure 7.7 that the peak steady-state rupture stress ($\hat{\sigma}_R$ =37.20MPa) in this pipe bend under the B4-OP568 loading condition is found at the outside surface of the intrados. It is also noted that this peak stress region is located towards one end of the

bend section. This is in good agreement with the peak damage location for the CDM analysis (see figure 7.8), however the peak damage ($\hat{\omega}$) location is on the inside surface if the pipe bend (possibly due to the redistribution of stress after an accumulation of creep damage). A time to failure (t_f) may be calculated using the steady-state peak rupture stress, equation (5.2) and the material constants given in table 4.3. For the model shown in figure 7.7, t_f was estimated to be 73340hrs, which is in reasonable agreement with the time to failure predicted by the damage analysis (87300hrs). The example analyses presented in this section therefore not only demonstrate the applicability of the GUI but also verify the reference rupture stress lifing method for pipe bend sections (which has been referenced extensively in chapters 5 and 6).

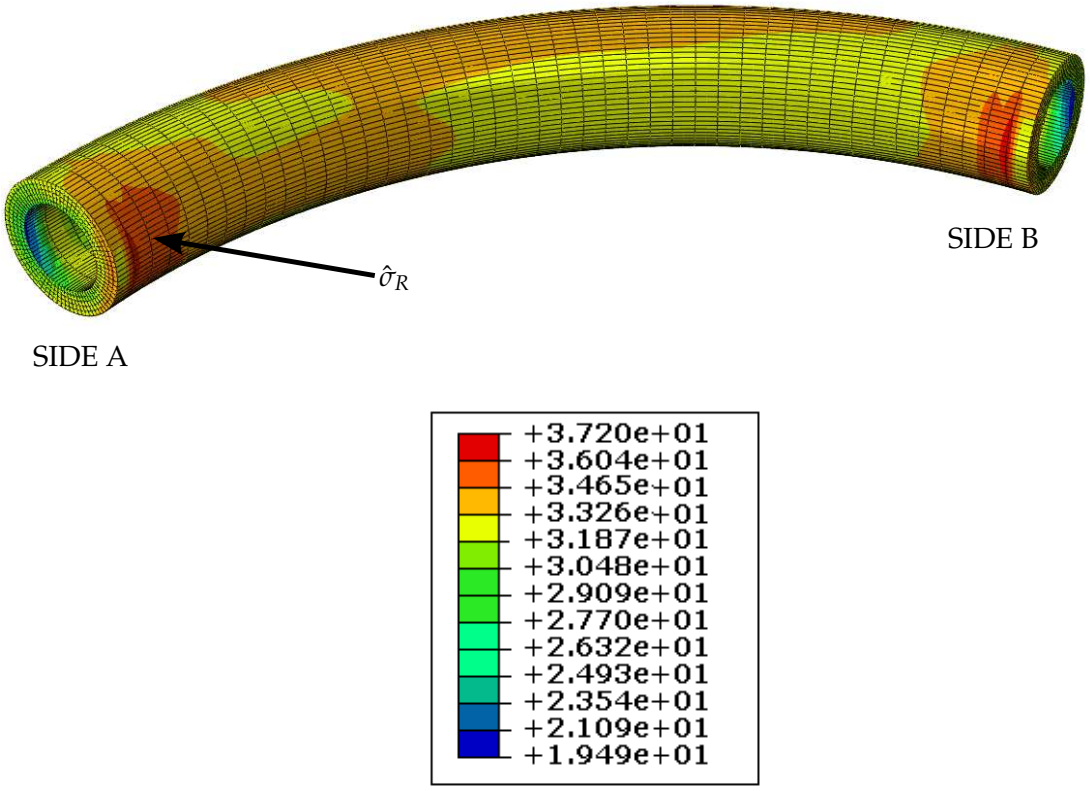

Figure 7.7: An example FEA contour plot showing steady state rupture stresses in a pipe bend model with manufacture induced dimension variation. This simulation was completed using a simple power law model (Norton's law).

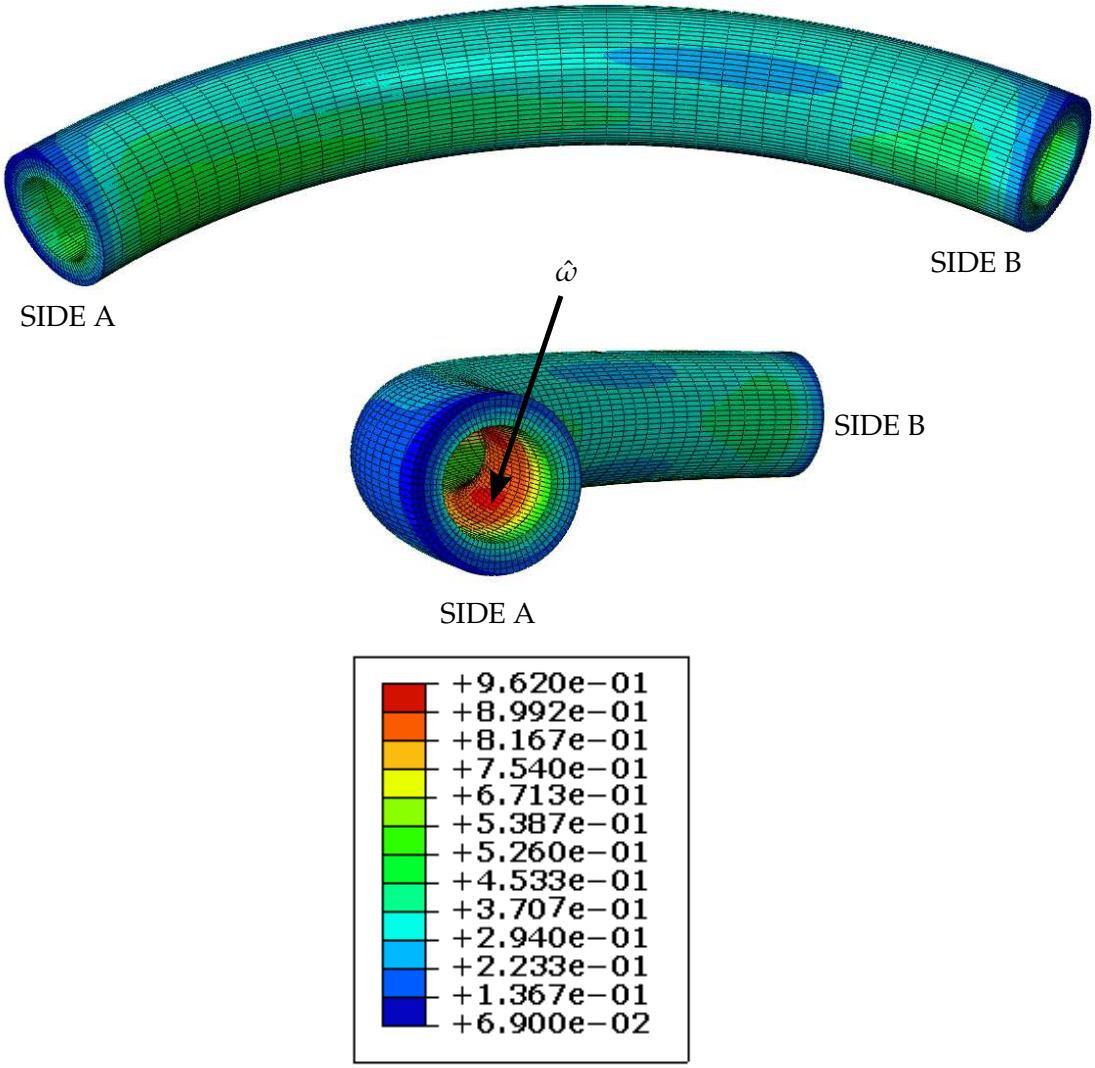

Figure 7.8: An example FEA contour plot of creep damage (ω) for a pipe bend model with manufacture induced dimension variation. The same geometry, material and loading conditions are used in this model and the model shown in figure 7.7. This simulation was completed using a creep CDM model (Kachanov's model).

7.4 Neural Network

7.4.1 Requirement

Pipe bend sections in power plants will be subjected to loads imposed by the piping system (system loads) as well as an internal pressure. System loads will be dependent on several factors, notably a piping system's design and the load (i.e. steam pressure and temperature) it is operating at. A system's load will itself be cycled as generation output is matched to market trends. Figure 7.9 shows that, over a one month period, a unit went through multiple start up and shut down cycles with prolonged operation at full ($\approx 500MW$) and partial generation load. It is noted that there is a strong correlation between

a unit's generated load (or power, in MW) and steam pressure and temperature. Given the range of operating conditions that a pipe component may act in and remembering that any modification to the piping system will also affect system loads, a procedure is needed in order to quantify the effect of system loads. In the present chapter, it is suggested that a neural network can be created which accommodates the complex dependencies that system loads have on peak steady-state rupture stresses ($\hat{\sigma}_R$) in pipe bend sections operating in creep conditions.

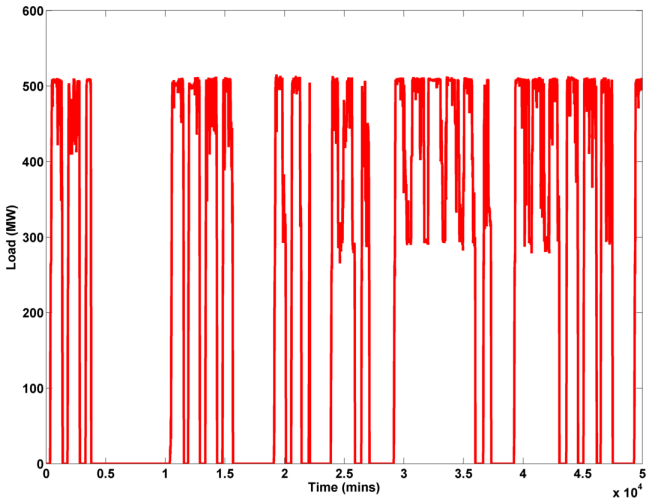

(a)

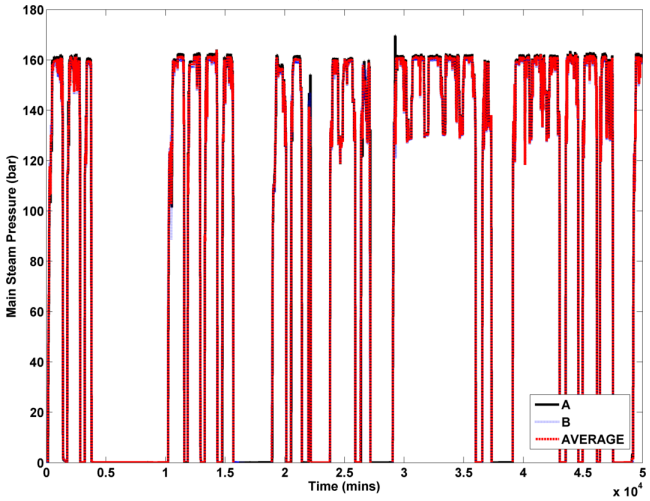

(b)

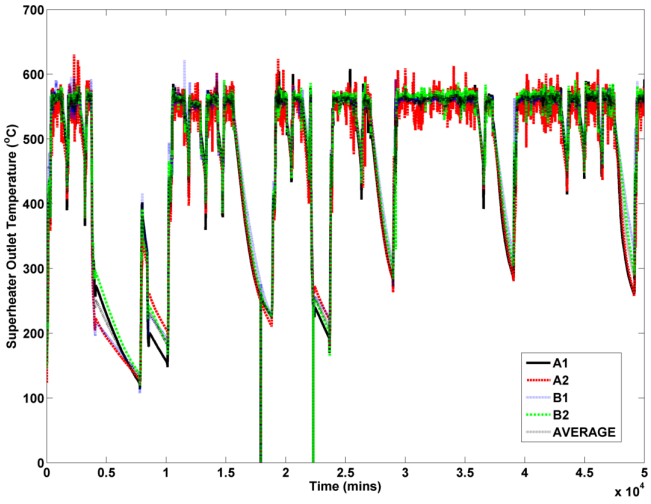

(c)

Figure 7.9: Example load profiles from a coal fired power plant unit, showing variations in (a) generated load (MW), (b) steam pressure in the unit's steam chests (MPa) and (c) superheated steam outlet temperatures (°C).

7.4.2 FEA Models

A neural network requires data so that it may be "trained" (whereby weights and biases are optimised to fit a target data set). Additional data points may then be used to verify the neural network's predictive capabilities. As the focus of the neural network here is steady-state peak rupture stresses, several FEA models of pipe bends under various loading conditions must be generated. An example FEA mesh can be seen in figure 7.10. In addition to an internal pressure load, system load induced displacements (shown in red) and rotations (shown in blue) are applied to each end of the pipe bend section (deemed "SIDE A" and "SIDE B"). As steady-state operation is the consideration of the present work Norton's power law (see equation (2.48)) has been applied to model creep behaviour. A sub-investigation verified that GNL effects are negligible, as suggested by Yaghi et. al.[104]. A mesh study determined that quadratic elements should be implemented (C3D20R in ABAQUS[191]), with 5 elements across the wall thickness of the pipe, 80 elements around its circumference and 45 around the bend section.

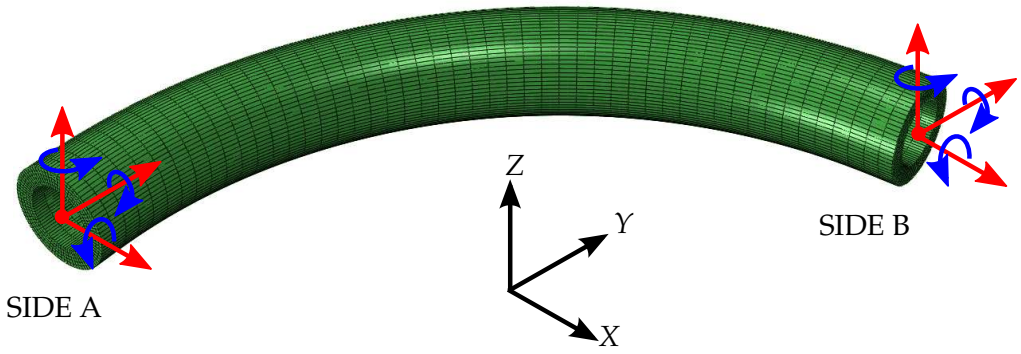

Figure 7.10: The load convention used when applying system loads to FEA pipe bend models.

7.4.3 Loading Conditions

In practice, pipe sections are supported by hangers which allow (or prevent) displacements in specific degrees of freedom. These hangers may be sprung loaded, allowing forces to be measured at these positions. Hanger readings may then be used in specialist software such as PSA5[115] to estimate displacements at points in a piping system (such as the beginning and end of a bend section). Multiple loading scenarios may be modelled as the system displacements during, for example, sustained operation may be different to those found during a "ramp-up" period. The load scenarios considered in the present chapter are identified by the labels "SUS", "RVFORCE", "TH568", "OP20", "OP568", "RVOP568" and "OP_SUPPS". The exact definition of each of these scenarios is not strictly relevant to the present work as the objective is to create a generalised analysis method. These labels are used to emphasise that a piping system may be subjected to a

range of loading conditions and that each of the loading conditions have been calculated for a real piping system.

Loading conditions (both internal pressure and system loads) are used as inputs in the neural network. While each load could be entered to its own input node, this could potentially lead to a very large neural network with 13 input nodes (one for each system load at either end of the pipe section, see figure 7.10). It is proposed here that an alternative input method may be used to reduce the number of input parameters required, namely the difference between the corresponding system loads at either end of the bend section. It is the relative motion between the two ends of the pipe that defines the effect of a system load on the pipe section. For example, rotational displacements around the Z axis at each end of the pipe section could cause the bend section to open or close, but the effect can be represented by the difference between the two loads. With this in mind, system load factors were determined for a range of load cases that were calculated using PSA5 and a real world main steam piping system. Displacement load factors in the x, y and z directions (factors X, Y and Z, respectively) for a variety of load cases can be seen in figure 7.11, with corresponding rotational factors about the x, y and z axes (factors R_x, R_y and R_z) shown in figure 7.12. It can be seen that there is a general relationship between displacement system load factors (X, Y and Z) and rotational system load factors (R_x, R_y and R_z), in so much as load cases types with relatively high displacement system load factors (such as "TH568", "OP20" and "OP_SUPPS" types) also tend to have high rotational system load factors. System load cases have been chosen so that a spectrum of displacement and rotation deflection combinations is considered in the training and validation steps. The neural network should therefore be equipped to predict peak rupture stresses for any load cases shown in the range of system load factors displayed in figures 7.11 and 7.12. Displacement and rotational system load factors used for training the neural network are summarised in tables 7.1 and 7.2, respectively. Validation inputs are given in tables 7.3 and 7.4.

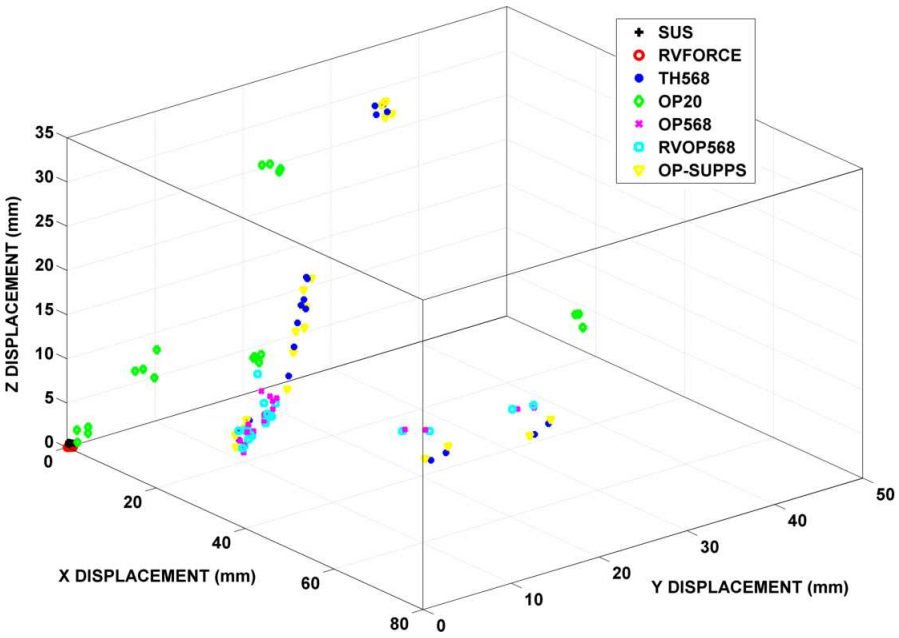

Figure 7.11: A comparison of several displacement loading conditions in the X, Y and Z directions (see figure 7.10).

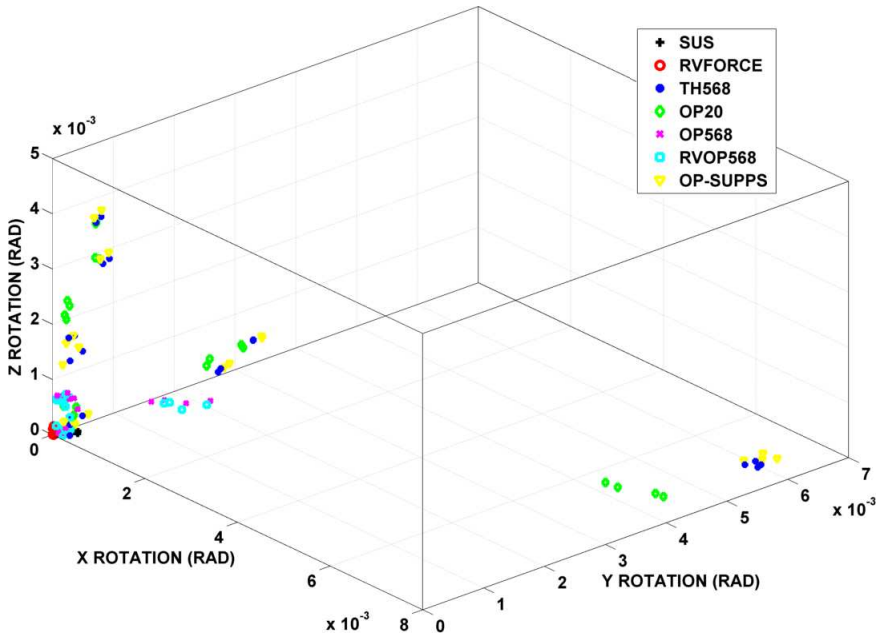

Figure 7.12: A comparison of several rotational loading conditions, given around the X, Y and Z axes (R_x, R_y and R_z, respectively, see figure 7.10).

Table 7.1: A summary of the displacement loading conditions used for the training of the neural network.

Identifier	$P_i\ (MPa)$	$X\ (mm)$	$Y\ (mm)$	$Z\ (mm)$
PRESS	16.49	0.00	0.00	0.00
A3-OP20	0.00	0.96	-0.68	-0.58
D5-OPSUPPS	16.49	-69.67	-19.72	13.28
C3-TH568	16.49	-11.94	14.68	-1.42
C3-HALF-TH568	8.25	-5.97	7.34	-0.71
B3-OP20	0.00	2.82	-0.92	-1.95
D5-OP20	0.00	35.26	40.80	-9.53
C5-TH568	16.49	44.72	-8.27	12.71
C1-TH568	16.49	-8.06	21.11	-3.64
D5-RVFORCE	16.49	$-1.93x10^{-1}$	$1.99x10^{-1}$	0.16
A2-HALF-RVFORCE	8.25	0.18	0.17	$1.50x10^{-3}$
A2-RVFORCE	16.49	0.36	0.33	$3.00x10^{-3}$
A4-OP568	16.49	-9.89	18.37	-1.11
B1-OP20	0.00	5.07	-6.08	-8.20
C1-RVOP568	16.49	-12.56	15.31	-6.63
D2-OP-SUPPS	16.49	-2.01	-26.12	-8.59
A4-HALF-OP568	8.25	-4.95	9.18	-0.56
D2-HALF-OP-SUPPS	8.25	-1.01	-13.06	-4.29
D1-TH568	16.49	-5.63	24.31	-9.73
D1-OP20	0.00	5.92	-6.93	7.17
D1-OP568	16.49	10.96	9.61	-2.53
D1-OP-SUPPS	16.49	-5.58	24.16	-7.63
TEST-P	15.00	0.00	0.00	0.00
C3-OP568	16.49	14.90	11.99	-1.19
C3-OP-SUPPS	16.49	-12.47	14.10	-1.76

Table 7.2: A summary of the rotation loading conditions used for the training of the neural network.

Identifier	$R_x\ (RAD)$	$R_y\ (RAD)$	$R_z\ (RAD)$
PRESS	0.00	0.00	0.00
A3-OP20	-7.85$x10^{-4}$	-1.75$x10^{-4}$	6.98$x10^{-5}$
D5-OPSUPPS	-7.47$x10^{-3}$	-5.99$x10^{-3}$	2.62$x10^{-4}$
C3-TH568	-8.03$x10^{-4}$	-1.05$x10^{-4}$	1.61$x10^{-3}$
C3-HALF-TH568	-4.01$x10^{-4}$	-5.24$x10^{-5}$	8.03$x10^{-4}$
B3-OP20	-7.16$x10^{-4}$	-1.75$x10^{-4}$	1.99$x10^{-3}$
D5-OP20	6.89$x10^{-3}$	3.85$x10^{-3}$	-3.49$x10^{-4}$
C5-TH568	-7.65$x10^{-3}$	-5.83$x10^{-3}$	1.92$x10^{-4}$
C1-TH568	-2.09$x10^{-4}$	-3.32$x10^{-4}$	2.97$x10^{-4}$
D5-RVFORCE	-7.70$x10^{-6}$	1.59$x10^{-5}$	0.00
A2-HALF-RVFORCE	0.00	-8.73$x10^{-6}$	-3.49$x10^{-5}$
A2-RVFORCE	0.00	-1.75$x10^{-5}$	-6.98$x10^{-5}$
A4-OP568	-8.73$x10^{-5}$	1.40$x10^{-4}$	1.05$x10^{-4}$
B1-OP20	-1.22$x10^{-4}$	1.40$x10^{-4}$	-2.09$x10^{-4}$
C1-RVOP568	-1.22$x10^{-4}$	-1.92$x10^{-4}$	6.46$x10^{-4}$
D2-OP-SUPPS	1.05$x10^{-4}$	8.73$x10^{-5}$	1.27$x10^{-3}$
A4-HALF-OP568	-4.36$x10^{-5}$	6.98$x10^{-5}$	5.24$x10^{-5}$
D2-HALF-OP-SUPPS	5.24$x10^{-5}$	4.36$x10^{-5}$	6.37$x10^{-4}$
D1-TH568	-1.75$x10^{-4}$	-1.57$x10^{-4}$	1.92$x10^{-4}$
D1-OP20	1.22$x10^{-4}$	2.97$x10^{-4}$	-4.36$x10^{-4}$
D1-OP568	-2.79$x10^{-4}$	-1.40$x10^{-4}$	7.16$x10^{-4}$
D1-OP-SUPPS	-1.22$x10^{-4}$	-2.79$x10^{-4}$	1.22$x10^{-4}$
TEST-P	0.00	0.00	0.00
C3-OP568	-6.98$x10^{-5}$	-3.49$x10^{-5}$	-8.73$x10^{-5}$
C3-OP-SUPPS	-8.38$x10^{-4}$	-5.24$x10^{-5}$	1.06$x10^{-3}$

Table 7.3: A summary of the displacement loading conditions used for the validation of the neural network.

Identifier	$P_i\ (MPa)$	$X\ (mm)$	$Y\ (mm)$	$Z\ (mm)$
A3-HALF-OP20	0.00	0.48	-0.34	-0.29
D5-HALF-OPSUPPS	8.25	-34.84	-9.86	6.64
A1-OP20	0.00	5.84	-7.22	-10.22
A5-OP568	16.49	18.55	-23.12	-3.09
B5-OP568	16.49	36.17	-34.81	-2.42
D4-OPSUPPS	16.49	-5.39	34.21	28.82
D3-OPSUPPS	16.49	-15.47	11.39	-0.17
A5-RVOP568	16.49	19.35	-23.50	-2.88
C4-RVOP568	16.49	-10.82	17.09	-1.02
B4-OP568	16.49	-11.17	16.74	0.57
B1-HALF-OP20	0.00	2.54	-3.04	-4.10
B4-HALF-OP568	8.25	-5.59	8.37	0.29
C1-HALF-RVOP568	8.25	-6.28	7.65	-3.31
D1-RVOP568	16.49	8.74	11.86	-0.85
C3-RVOP568	16.49	15.14	3.22	-0.77
C4-TH568	16.49	-4.31	32.99	28.80

Table 7.4: A summary of the rotational loading conditions used for the validation of the neural network.

Identifier	$R_x\ (RAD)$	$R_y\ (RAD)$	$R_z\ (RAD)$
A3-HALF-OP20	-3.93$x10^{-4}$	-8.73$x10^{-5}$	3.49$x10^{-5}$
D5-HALF-OPSUPPS	-3.74$x10^{-3}$	-3.00$x10^{-3}$	1.31$x10^{-4}$
A1-OP20	-3.49$x10^{-5}$	-1.57$x10^{-4}$	-4.71$x10^{-4}$
A5-OP568	4.97$x10^{-4}$	8.03$x10^{-4}$	-5.24$x10^{-5}$
B5-OP568	5.63$x10^{-5}$	1.13$x10^{-4}$	0.00
D4-OPSUPPS	-8.20$x10^{-4}$	2.29$x10^{-3}$	7.16$x10^{-4}$
D3-OPSUPPS	-9.42$x10^{-4}$	-6.98$x10^{-5}$	2.09$x10^{-3}$
A5-RVOP568	5.97$x10^{-4}$	1.08$x10^{-3}$	-3.49$x10^{-5}$
C4-RVOP568	1.05$x10^{-4}$	-1.92$x10^{-4}$	1.57$x10^{-4}$
B4-OP568	5.24$x10^{-5}$	1.92$x10^{-4}$	5.24$x10^{-5}$
B1-HALF-OP20	-6.11$x10^{-5}$	6.98$x10^{-5}$	-1.05$x10^{-4}$
B4-HALF-OP568	2.62$x10^{-5}$	9.60$x10^{-5}$	2.62$x10^{-5}$
C1-HALF-RVOP568	-6.11$x10^{-5}$	-9.60$x10^{-5}$	3.23$x10^{-4}$
D1-RVOP568	-1.92$x10^{-4}$	-3.49$x10^{-5}$	6.46$x10^{-4}$
C3-RVOP568	-1.05$x10^{-4}$	-1.22$x10^{-4}$	-1.22$x10^{-4}$
C4-TH568	-8.90$x10^{-4}$	2.62$x10^{-3}$	1.03$x10^{-3}$

7.4.4 Development and Validation of a Pipe Bend Neural Network

The concept of artificial neural networks has been introduced in section 2.5. Fundamentally, a neural network can be visualised as a modularised mathematical function. An output, in this case $\hat{\sigma}_R$ (see figure 7.13), is determined based on inputs (here representing an internal pressure load P_i and system load induced displacements and rotations, X, Y, Z and R_x, R_y, R_z, respectively). Prior to constructing the neural network, system loads and internal pressures (defined in tables 7.1 and 7.2 and tables 7.3 and 7.4 for training and validation, respectively) are used to construct FEA models for a given bend geometry (note that in the present network only a single variable cross section pipe bend geometry is considered). Peak steady-state rupture stresses ($\hat{\sigma}_R$) found from these simulations may be compared to the output from the neural network. During the training of the neural network, the results of this comparison are used to determine the weights and biases (w and θ in figure 7.13, respectively) though an optimisation procedure. A validation stage is used to guard against "over fitting", whereby a network accurately predicts the results for a training data set but exhibits poor approximations for data sets not included in the training set. Note in the presented examples two materials were considered, namely BAR 257 at 650°C and a $1/2Cr1/2Mo1/4V$ steel at 640°C. A power law (Norton's law, see equation (2.41)) was used to model the steady-state creep

response of the materials. Material constants for this model were derived for BAR 257 in section 4.4.1 ($A = 1.09x10^{-20} MPa^{1/n}.hr$ and $n = 8.46$). Material constants for the CMV steel ($A = 6.599x10^{-16} MPa^{1/n}.hr$ and $n = 6.108$) were taken from literature[139].

In the present chapter, a neural network architecture was constructed using MATLAB's neural network toolbox[163]. Determining the correct architecture (the combination and order of specific neurons with different activation functions) for a particular application is perhaps the most time consuming aspect of establishing a network. In the present work, only two types of activation function have been used (the logarithmic sigmoid function and the pure linear function[163], see figure 7.13). Symbols used for each of these functions in figure 7.13 may be seen in figure 7.14, along with a graphical representation of the relationship between input and output for each function. The pure linear function (see figure 7.14 (a)) can be considered to be an extension of the semi-linear limiting function shown in figure 2.42 (b). In short, there is a linear relationship between the input and the output. The logarithmic sigmoid function creates positive outputs between 0 and 1 and is defined by equation (7.1)[163] (see figure 7.14 (b)). Neurons are collected into layers (each neuron in a layer has the same activation function but potentially different weights and biases). In figure 7.13, layers are numbered in red and all layers comprise of 6 neurons. Inputs are fed into each of a layer's nodes and are modified by that node's weight and bias values (see figure 2.43 for an example with a vector input).

$$\text{logsig}(x) = \frac{1}{1 + e^{-x}} \tag{7.1}$$

Training of the network is accomplished using a gradient decent algorithm with momentum back propagation (in MATLAB this is defined by the in-built function TRAINDM[163]). The gradient descent optimisation method has been discussed in the literature review of this thesis (see section 2.6.3) and is easily visualised. For a given set of weights and biases (the parameters to be optimised), an error function can be defined by comparing the outputs of the neural network to the known true values[204]. The gradient of this error function is calculated and a direction is chosen to reduce the error. This direction (coupled with a step size) defines a new set of weights and biases for the network that will be analysed in the following optimisation procedure. If momentum is introduced, equation (2.114) (which defines the steepest gradient decent approach) becomes equation (7.2), where the term $P_0 d(\boldsymbol{x}^{n-1})$ is "momentum" (the previous change in $\boldsymbol{x}$ multiplied by a momentum parameter P_0). The introduction of a momentum term prevents solutions localising on small fluctuations in the error surface (local minima) and oscillating between similar values in certain topological regions (such as long narrow valleys in the error surface)[204]. P_0 is defined prior to training and lies in the range $0 \leq P_0 < 1$. In the presented network, a value of 0.9 was found to give a good convergence rate in training, suggesting that the momentum term makes a significant contribution in equation (7.2). Errors are calculated using the mean square error method, which is similar to the sum of squares method (see equation (2.110)) except that the sum

of error squared is divided by the total number of data points (or m in equation (2.110)).

$$d(\boldsymbol{x}^n) = -M_0 \nabla E\left(\boldsymbol{x}^n\right) + P_0 d(\boldsymbol{x}^{n-1}) \tag{7.2}$$

Initial values for the weights and biases used in the network must be found before the training procedure begins in order to provide a "starting point". For the majority of neuron layers, a zero initial value for the weights and biases was assumed (meaning that these neurons are not active). During the training procedure, non-zero values are quickly determined. For layers 1, 2 and 3 in figure 7.13 (which have neurons with logarithmic sigmoid activation functions), the Nguyen-Widrow initialisation algorithm[205] has been implemented. Using this method, initial values for weights and biases take a random value (generated between the limits -1 and 1). The factors β and $norm$ (equations (7.3) and (7.4), respectively) are then calculated and used to determine a revised weight and bias (based on the randomised value, see equation (7.5))[205]. Note that in equations (7.3) to (7.5), h is the number of hidden neurons for a particular layer, I is the total number of inputs to that layer, w_i is the i^{th} weight (or bias as the two are initiated simultaneously) determined by a random number generator and w_i' is the weight (or bias) w_i that has been adjusted by the Nguyen-Widrow algorithm. If the values of the weights and biases were plotted on a histogram for a suitably large network, a distribution would be observed with higher frequencies of weights and biases at certain values and very low frequencies at the limits of the range. During training, the high frequency regions may shift and redistribute, however by localising them to begin with a faster training rate is observed than if a "hard" (uniform) or Gaussian distribution had been implemented. After initialisation, the weights and biases may be optimised through training.

$$\beta = 0.7h^{1/I} \tag{7.3}$$

$$norm = \sqrt{\sum_{i=0}^{i=I} w_i^2} \tag{7.4}$$

$$w_i' = \frac{\beta w_i}{norm} \tag{7.5}$$

From experience, networks initialised with all zero values took substantially longer to train and were susceptible to locking (the convergence of a solution to a local minimum that results in poor network performance). Networks with fully randomised initial conditions were generally quicker to train, however convergence problems were still observed. As the initial values of the weights and biases are random, the initial condition of the network prior to training is different for each time a network is constructed. It was found that if a network began with a fully randomised set of initial conditions there could be significant differences between the performance of the network for repeated training procedures. The partial random initialisation used in the present

network appears to give a good network performance (predictions made using the network tend to be accurate) with consistent results between repeated training attempts. The training procedure has a non-zero starting position in optimisation space as a result of the randomised initialisation method used on some layers, however the weight and bias optimisation is still initially constrained in certain degrees of freedom by the zero initial values for some neuron layers.

A partially connected structure is used in the present network (see section 2.5). Through experience, it has been found that a fully connected neural network (similar to that shown in figure 2.43) required a great deal of computational effort to train. By creating a partially connected network, specific weights and biases may be applied to each input type (note that the internal pressure load P_i, the displacement loads X, Y and Z and the rotational loads R_x, R_y and R_z are applied to the neural network in different input nodes). This tends to lead to a better training rate (as changes to weights and biases can be made to modify certain input types individually) and more representative network outputs (as the output's dependency on specific inputs can be isolated and better represented).

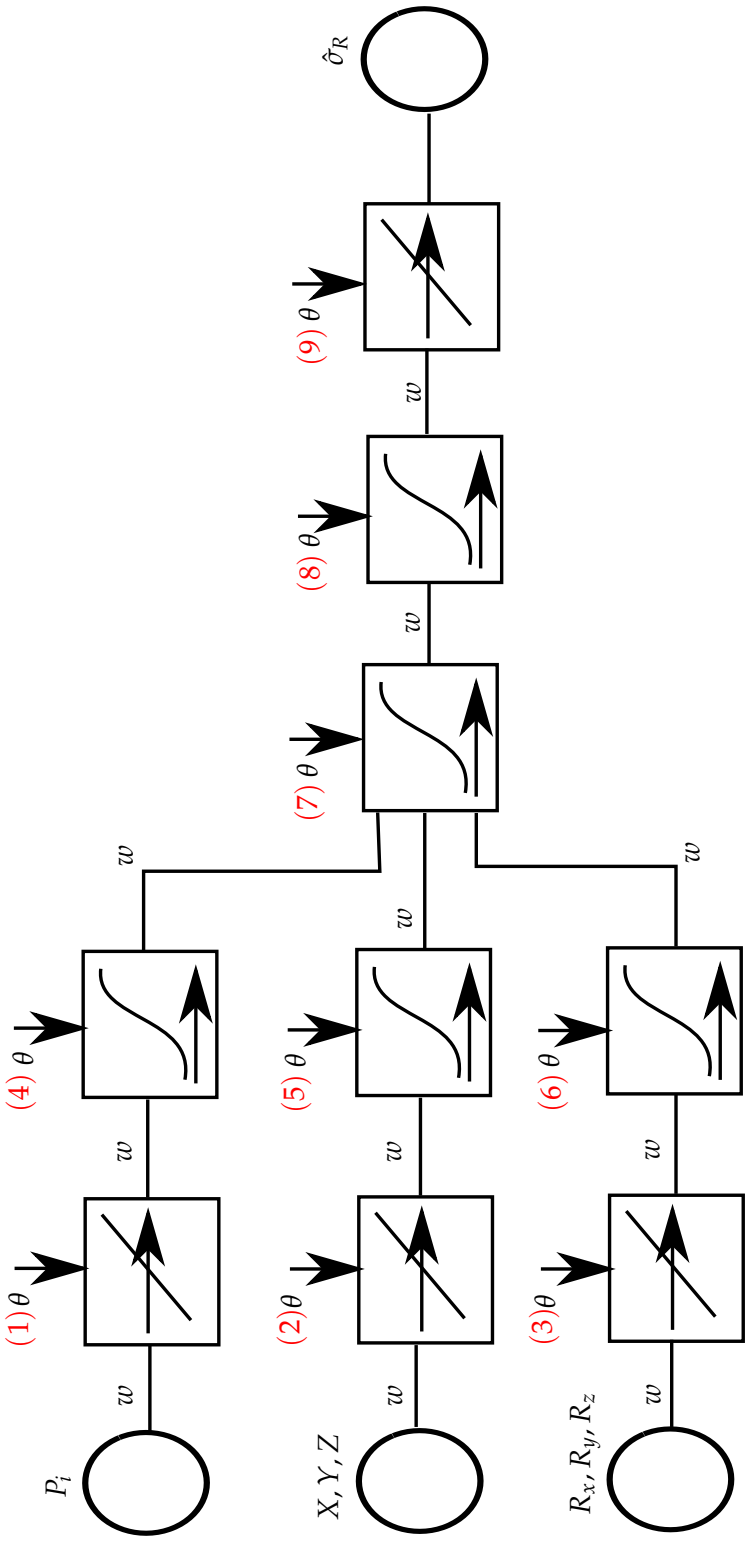

Figure 7.13: The developed partially connected neural network structure used to estimate peak steady-state rupture stresses ($\hat{\sigma}_R$) in pipe bends loaded by an internal pressure (P_i) and system loads (X, Y, Z, R_x, R_y and R_z).

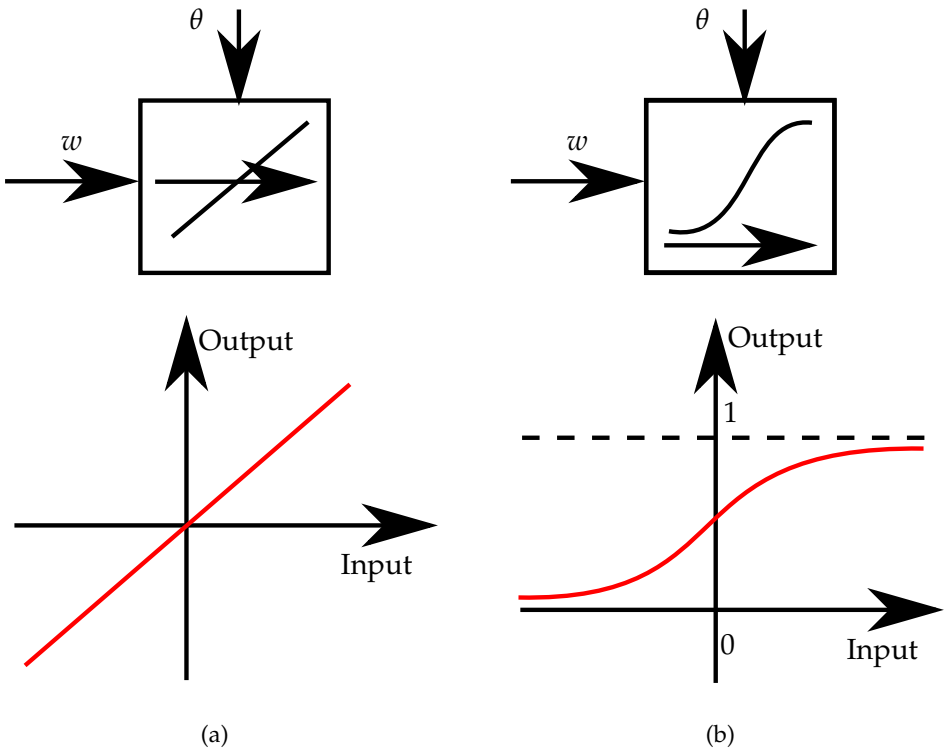

(a) (b)

Figure 7.14: Symbols that represent the activation functions used in neuron layers in figure 7.13 and graphical representations of these functions, showing (a) the pure linear activation function and (b) the logarithmic sigmoid activation functions. Note that w and θ are the weights and biases (respectively) that are optimised during training.

The network described in figure 7.13 has been trained using the results of FEA simulations on a pipe bend for two steels (BAR 257 at 650°C and a $1/2Cr1/2Mo1/4V$ steel at 640°C). As material dependencies are not included in the present form, the network was trained separately for each material (each network has the same architecture but different optimised weight and bias values). A comparison of the true $\hat{\sigma}_R$ values (determined from the FEA) and the stresses predicted by the trained networks can be seen for the two materials in figures 7.15 and 7.18 (raw data values are given in tables 7.5 and 7.7). To ensure that the networks could predict stresses for a range of load cases (and not only those used in the training data set), a validation data set was implemented. For each material, a comparison of the true and predicted stresses for the validation load cases (see tables 7.3 and 7.4) may be seen in figures 7.16 and 7.19 (results are presented in tables 7.6 and 7.8). For clarity, the error between the true (FEA) and neural network predicted peak steady-state rupture stresses are plotted for each load case in the validation set in figures 7.17 and 7.20.

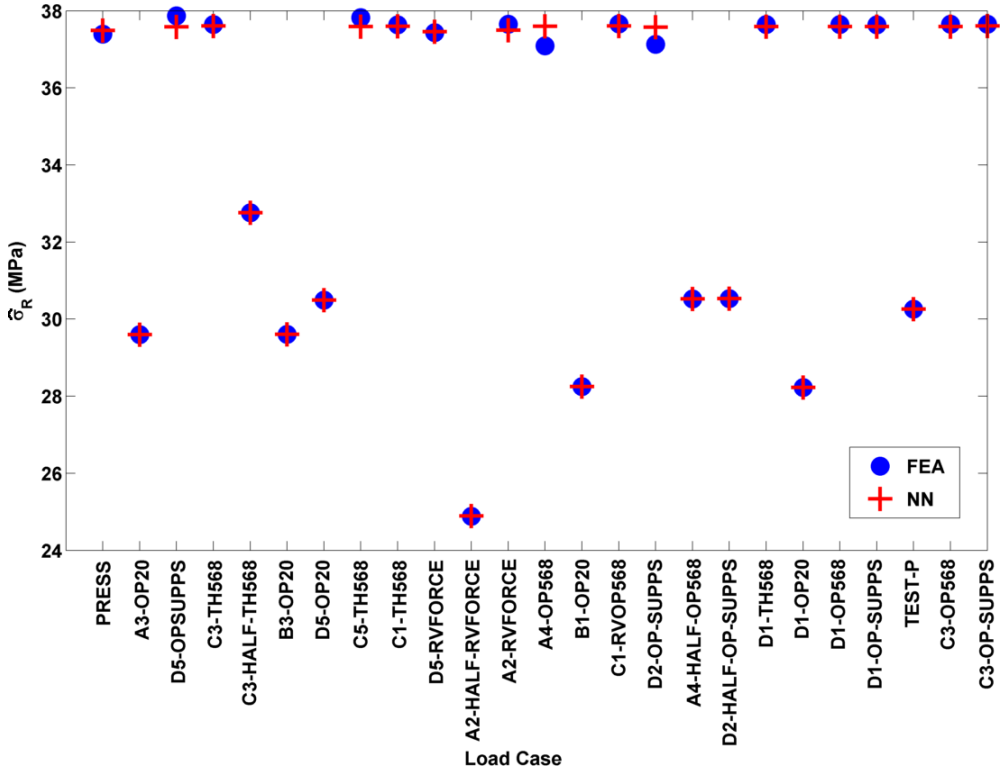

Figure 7.15: A comparison of the true (FEA) and predicted (NN) peak rupture stresses for a pipe bend made of BAR 257 steel at 650°C. The results are for a training data set (see tables 7.1 and 7.2) used in the development of a neural network.

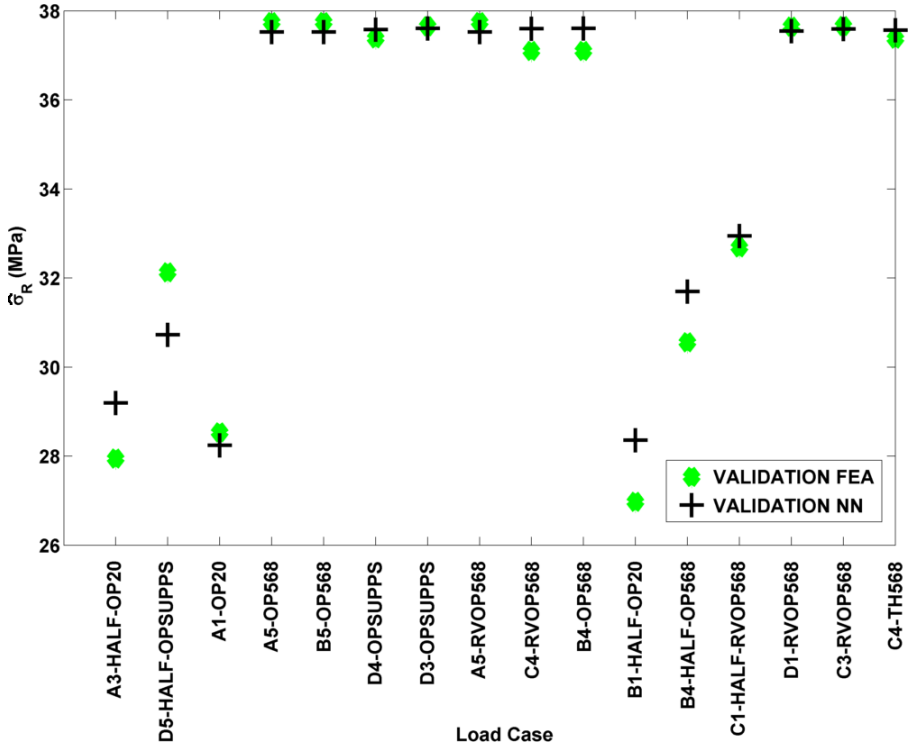

Figure 7.16: A comparison of the true (FEA) and predicted (NN) peak rupture stresses for a pipe bend made of BAR 257 steel at 650°C. The results are for a validation data set (see tables 7.3 and 7.4) used in the development of a neural network.

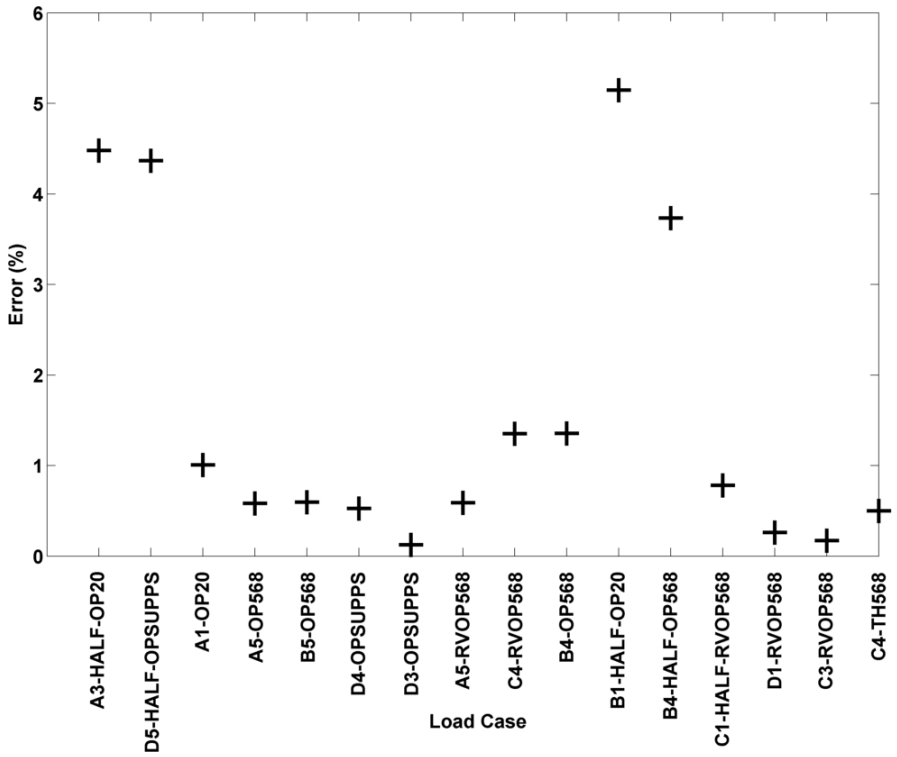

Figure 7.17: The errors between the true (FEA) and predicted (NN) peak rupture stresses for a pipe bend made of BAR 257 steel at 650°C. The results are for a validation data set (see tables 7.3 and 7.4).

Table 7.5: The results of a training procedure on a neural network, predicting peak rupture stresses for a pipe bend made of BAR 257 steel at 650°C. True (FEA) and predicted (NN) stress values are shown and the error has been calculated.

Identifier	$\hat{\sigma}_R$ (MPa) - FEA	$\hat{\sigma}_R$ (MPa) - NN	Error (%)
PRESS	37.39	37.49	0.27
A3-OP20	29.60	29.59	0.00
D5-OPSUPPS	37.87	37.58	0.77
C3-TH568	37.65	37.61	0.11
C3-HALF-TH568	32.76	32.76	0.00
B3-OP20	29.60	29.60	0.00
D5-OP20	30.49	30.49	0.00
C5-TH568	37.82	37.59	0.62
C1-TH568	37.64	37.60	0.11
D5-RVFORCE	37.44	37.46	0.06
A2-HALF-RVFORCE	24.89	24.89	0.00
A2-RVFORCE	37.65	37.50	0.40
A4-OP568	37.09	37.60	1.36
B1-OP20	28.25	28.25	0.00
C1-RVOP568	37.66	37.61	0.15
D2-OP-SUPPS	37.13	37.58	1.20
A4-HALF-OP568	30.53	30.53	0.00
D2-HALF-OP-SUPPS	30.53	30.53	0.00
D1-TH568	37.65	37.59	0.14
D1-OP20	28.22	28.22	0.00
D1-OP568	37.65	37.59	0.14
D1-OP-SUPPS	37.64	37.59	0.11
TEST-P	30.26	30.26	0.00
C3-OP568	37.66	37.59	0.17
C3-OP-SUPPS	37.65	37.61	0.12

Table 7.6: The results of a validation procedure on a neural network, predicting peak rupture stresses for a pipe bend made of BAR 257 steel at 650°C. True (FEA) and predicted (NN) stress values are shown and the error has been calculated.

Identifier	$\hat{\sigma}_R$ (MPa) - FEA	$\hat{\sigma}_R$ (MPa) - NN	Error (%)
A3-HALF-OP20	27.94	29.20	4.48
D5-HALF-OPSUPPS	32.13	30.72	4.37
A1-OP20	28.53	28.25	1.01
A5-OP568	37.74	37.52	0.58
B5-OP568	37.75	37.52	0.59
D4-OPSUPPS	37.38	37.58	0.52
D3-OPSUPPS	37.65	37.61	0.13
A5-RVOP568	37.75	37.52	0.59
C4-RVOP568	37.10	37.60	1.35
B4-OP568	37.10	37.60	1.36
B1-HALF-OP20	26.97	28.36	5.15
B4-HALF-OP568	30.56	31.70	3.73
C1-HALF-RVOP568	32.69	32.94	0.78
D1-RVOP568	37.65	37.55	0.26
C3-RVOP568	37.66	37.59	0.17
C4-TH568	37.38	37.56	0.50

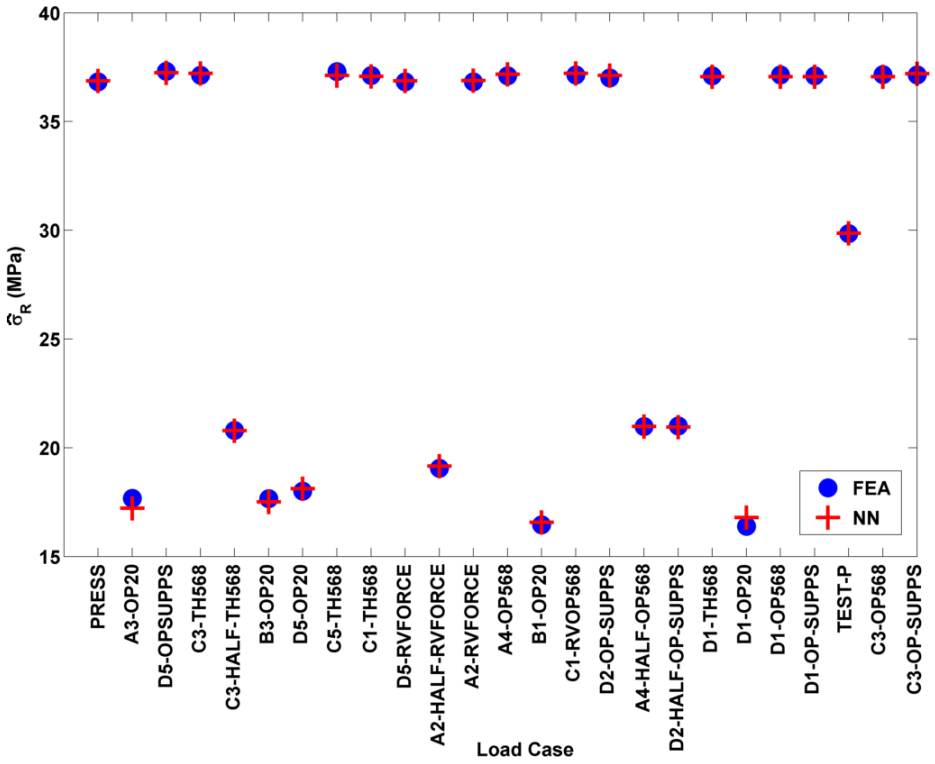

Figure 7.18: A comparison of the true (FEA) and predicted (NN) peak rupture stresses for a pipe bend made of $1/2Cr1/2Mo1/4V$ steel at 640°C. The results are for a training data set (see tables 7.1 and 7.2) used in the development of a neural network.

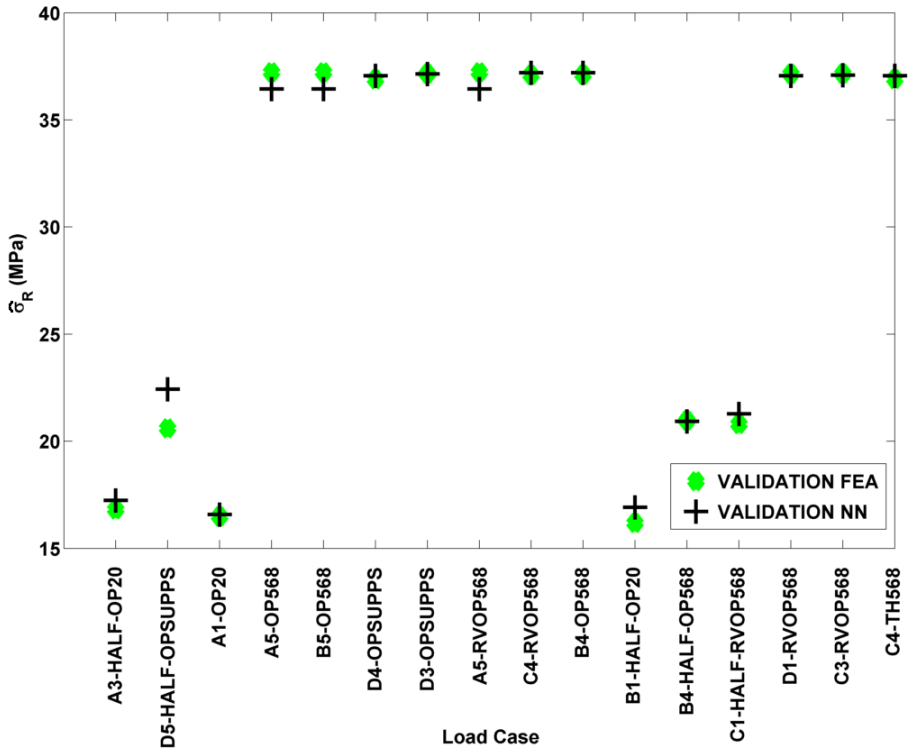

Figure 7.19: A comparison of the true (FEA) and predicted (NN) peak rupture stresses for a pipe bend made of $1/2Cr1/2Mo1/4V$ steel at 640°C. The results are for a validation data set (see tables 7.3 and 7.4) used in the development of a neural network.

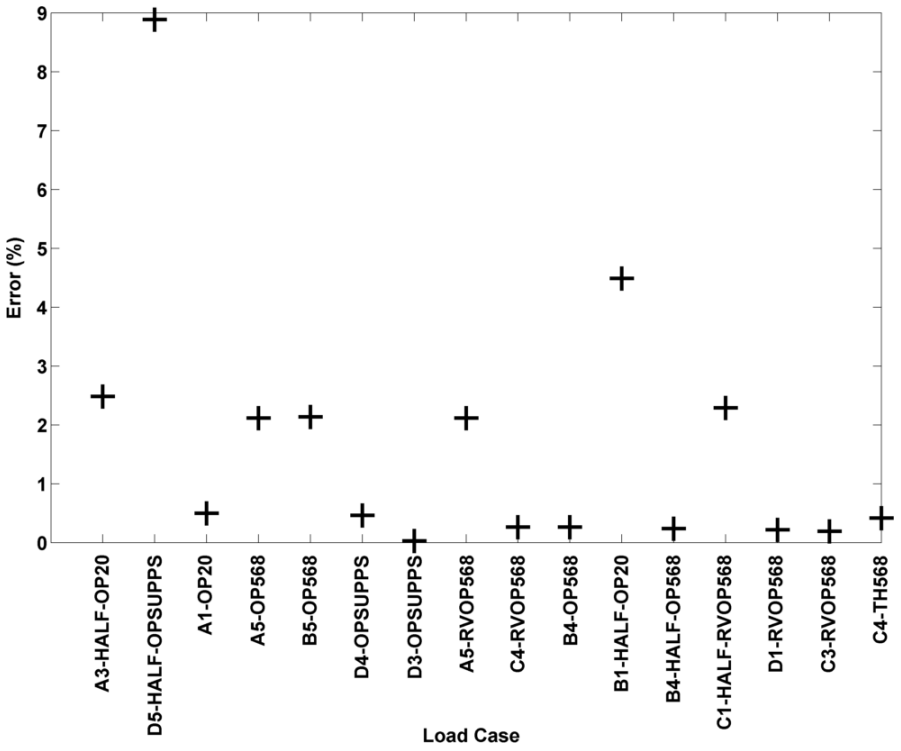

Figure 7.20: The errors between the true (FEA) and predicted (NN) peak rupture stresses for a pipe bend made of $1/2Cr1/2Mo1/4V$ steel at 640°C. The results are for a validation data set (see tables 7.3 and 7.4).

Table 7.7: The results of a training procedure on a neural network, predicting peak rupture stresses for a pipe bend made of $1/2Cr1/2Mo1/4V$ steel at 640°C. True (FEA) and predicted (NN) stress values are shown and the error has been calculated.

Identifier	$\hat{\sigma}_R$ (MPa) - FEA	$\hat{\sigma}_R$ (MPa) - NN	Error (%)
PRESS	36.83	36.87	0.11
A3-OP20	17.68	17.22	2.56
D5-OPSUPPS	37.31	37.24	0.19
C3-TH568	37.14	37.21	0.19
C3-HALF-TH568	20.80	20.78	0.09
B3-OP20	17.66	17.51	0.86
D5-OP20	18.01	18.11	0.56
C5-TH568	37.30	37.12	0.47
C1-TH568	37.12	37.08	0.10
D5-RVFORCE	36.82	36.87	0.13
A2-HALF-RVFORCE	19.06	19.16	0.51
A2-RVFORCE	36.83	36.88	0.16
A4-OP568	37.10	37.17	0.20
B1-OP20	16.46	16.57	0.68
C1-RVOP568	37.15	37.22	0.20
D2-OP-SUPPS	37.01	37.12	0.32
A4-HALF-OP568	20.97	20.97	0.00
D2-HALF-OP-SUPPS	21.00	20.96	0.22
D1-TH568	37.11	37.06	0.12
D1-OP20	16.39	16.79	2.43
D1-OP568	37.14	37.06	0.22
D1-OP-SUPPS	37.10	37.06	0.11
TEST-P	29.86	29.86	0.01
C3-OP568	37.16	37.06	0.27
C3-OP-SUPPS	37.14	37.20	0.17

Table 7.8: The results of a validation procedure on a neural network, predicting peak rupture stresses for a pipe bend made of $1/2Cr1/2Mo1/4V$ steel at 640°C. True (FEA) and predicted (NN) stress values are shown and the error has been calculated.

Identifier	$\hat{\sigma}_R$ (MPa) - FEA	$\hat{\sigma}_R$ (MPa) - NN	Error (%)
A3-HALF-OP20	16.82	17.24	2.48
D5-HALF-OPSUPPS	20.60	22.43	8.89
A1-OP20	16.49	16.57	0.50
A5-OP568	37.23	36.44	2.11
B5-OP568	37.23	36.44	2.13
D4-OPSUPPS	36.89	37.06	0.46
D3-OPSUPPS	37.16	37.15	0.03
A5-RVOP568	37.23	36.44	2.12
C4-RVOP568	37.11	37.21	0.26
B4-OP568	37.11	37.21	0.26
B1-HALF-OP20	16.18	16.91	4.49
B4-HALF-OP568	20.98	20.93	0.24
C1-HALF-RVOP568	20.81	21.28	2.29
D1-RVOP568	37.14	37.06	0.21
C3-RVOP568	37.16	37.09	0.19
C4-TH568	36.91	37.06	0.41

7.5 Conclusions

An analysis methodology has been presented in the current chapter for power plant components. This methodology combines several of the aspects that have been discussed and developed in the previous chapters. Such aspects include material constant determination (by optimising material constant values to experimental data) and approximate component analysis techniques (such as parametric equations to characterise pipe bend dimension variation). The implementation of the described methodology would promote information exchange between power plant departments (through a centralised database feeding the methodology) and would encourage the more effective use of collected data. Routines have also been written that allow FEA models to be created, tested and analysed automatically from only a handful of user defined parameters. In this way, bespoke FEA analyses may be conducted to support the methodology without the user requiring a working knowledge of the finite element method. FEA should not be treated as a "black box", but the ease with which models may be created and simulated allows users with the necessary background to spend their time processing results rather than constructing models (which is commonly tedious). To summarise, the methodology presented combines information on component's material, geometry

and the loading case which it experiences to construct and analyse FEA models. Results may be processed in order to obtain a tangible metric (such as peak rupture stress $\hat{\sigma}_R$) by which a particular scenario may be judged. This can be done using the parametric methods described and developed in this thesis or by conducting bespoke FEA models.

As an additional approximate method, an analysis neural network (figure 7.13) has been developed. Using this method for a particular pipe bend geometry and material, $\hat{\sigma}_R$ may be estimated based on the loading condition (internal pressure and system loads). Two materials have been implemented in the present chapter (BAR 257 at 650°C and a $1/2Cr1/2Mo1/4V$ steel at 640°C) to demonstrate that the network can be applied for a range of materials. For both materials, stresses for the training data set (tables 7.1 and 7.2) were predicted well with average errors less that 0.5% (0.23% for BAR 257 and 0.44% for $1/2Cr1/2Mo1/4V$). Stress distributions are plotted in figures 7.15 and 7.18. Low errors in this data set are to be expected as the weights and biases used in the network are optimised based on these results. The training procedure will commonly terminate when an error limit has been achieved. To ensure that the network may be used to predict results outside the training data set, a validation set (tables 7.3 and 7.4) was also tested using the trained networks. Although discrepancies between predicted and true stresses were higher for the validation than the training set, average errors were still low at approximately 1.60% for both materials. Peak errors were noted at 4.48% for the A3-HALF-OP20 load case in the BAR 257 results and at 8.89% for the D5-HALF-OPSUPPS in the $1/2Cr1/2Mo1/4V$ results. With the exception of the D5-HALF-OPSUPPS case in the $1/2Cr1/2Mo1/4V$ data, all errors in the validation data sets were below 5% for both materials (see figures 7.17 and 7.20). The network has been verified to give accurate predictions of the peak rupture stress for a wide range of load cases operating under steady-state creep conditions. As shown in section 7.3.3, peak rupture stress values may be used in CDM equations in order to estimate failure lives of the component (or the damage fraction due to a specific loading condition).

The presented network may be further developed in several ways in the future. Before implementation, a wider validation set should be tested in order to increase the confidence in the predictive capability of the network. The training set reported in tables 7.1 and 7.2 appears to be sufficient to allow the network to predict the validation load cases, however this may need to be revised to cover a wider range of system load combinations (this would potentially improve the validation set fitting). A single pipe bend geometry has been considered in the creation of the presented neural network. This geometry included dimension variation (as discussed in section 6.3). Chapter 6 also discusses how manufacturing induced geometry variation may be described by several key factors. Potentially these factors could be fed into a network as additional inputs, allowing the network to predict peak rupture stresses for a range of load cases and bend geometries. Similar additional inputs could also be created for material parameters (for example the constants A and n in Norton's power law for creep, see equation (2.47)[50]).

Stresses could then be determined for a range of materials without using Calladine's method[197]. Engineers will also most likely be interested in determining the location of $\hat{\sigma}_R$ as this will be an indication of a possible failure site. The failure location can be expressed as a bend position angle and a circumferential position angle (see figure 6.1). Future networks could have multiple output nodes to predict these quantities in addition to the peak rupture stress value. This would most likely be geometry dependent, therefore either one network would be trained per pipe bend or geometry factors would be required as inputs to the network. For the multiple output network, alternative training and validation data sets would of course be required. By adding additional input and output nodes, it may be necessary to increase the number of neurons or neuron layers, use different combinations of activation functions and implement an alternative architecture. Although this would be a major component of the future work, the presented research described in this chapter has demonstrated that a partially connected network using linear and logarithmic sigmoid activation functions can predict the dependency of system loads on peak steady-state rupture stress values.

Chapter 8

Conclusions and Future Work

Although the research presented in this thesis has been conducted in several different areas, it has had a common purpose. The loads that high temperature power plant components experience will be both greater and cycled in a more arduous fashion in the future. Components that are in service at present have been designed with large safety factors, meaning that when they are retired there is often a great deal of remnant life left. A component analysis methodology is required that can translate the advanced material models and techniques used in academia to industry. The focus of this thesis has been establishing a foundation for this methodology by producing a framework (see section 7.2) and developing several important aspects of the methodology. It is worth noting that, in addition to aiding in the analysis of components, constructing a methodology similar to this would promote the formation of databases of plant information with multiple departments collaborating. The analysis methodology would maximise the effectiveness of this data which may be collected on site as part of routine inspections.

Specific conclusions are drawn at the end of each chapter, however a brief summary of the findings of the thesis will be given here. The main conclusion of the present work is that a single component analysis suite (or methodology) is a possibility and will require the development of new material models, methods to determine material dependent parameters, geometry characterisation techniques and analysis methods. With these advanced methods and the increased accuracy with which a material's behaviour may be approximated, high temperature components can be operated safely for longer and in more arduous conditions. In addition to this statement, several conclusions in individual research areas have been outlined:

- When a single set of material constants should be adequate to predict multiple experiments, an optimisation procedure to determine these material parameters should use cleaned experimental data (to avoid numerical instabilities) and objective functions should be evaluated simultaneously for all experimental data sets (combined parallel optimisation).

- The Chaboche unified visco-plasticity model may be modified (in the drag stress equation) to include secondary hardening effects. Using the correct optimisation procedure, excellent qualities of fit may be achieved for cyclic experimental data (with coefficients of determination in the region of 0.99).
- The choice of creep damage model should be carefully considered prior to its use. If a power law model is used rather than a hyperbolic sine model and its material constants are determined for a higher stress range than that of interest, potentially larger discrepancies in estimated failure times can be observed, particularly in multiaxial load cases.
- The stress concentration effect of a scoop sample in a piping component may be approximated by a polynomial expression. This information may be used to determine the likelihood of failure due to the scoop sampling activity.
- The geometry of pipe bend sections showing manufacturing induced dimension variation may be accurately described by two characteristic equations and two geometry factors. Peak rupture stresses in pipe bend sections may be related to these factors by a polynomial expression.
- The stress state in a pressurised 3D pipe model with dimension variation can be approximated by using multiple 2D models that defined the cross section of the 3D model at critical locations.
- A partially connected neural network can be created that will predict the peak stress in a pipe bend section due to the application of system loads and an internal pressure.

At the end of each research chapter, comments have been made as to how the research in that particular area may develop in the future. In general, there are several directions which the analysis methodology could develop. Firstly, the full methodology should be incorporated into a user friendly GUI, similar to that used to construct FEA models in section 7.3.2. This GUI (along with a suitable user manual) would encourage the implementation of the advanced techniques that have been discussed. Additional component types could also be considered in future development and implementation of the methodology. Weld models have been included in the FEA model generation routines in section 7.3.2, however additional general models, such as steam chests, headers and branch pipe sections could also be produced and analysed.

In the majority of cases, steady-state peak rupture stresses have been used as a metric to judge the potential for a reduction in remnant life for a geometry/loading condition. It has often been assumed that these peak rupture stresses can give an indication of failure location as damage accumulation in creep damage models is largely controlled by this parameter. Indeed, in section 7.3.3, particularly in figures 7.7 and 7.8, a steady-state rupture stress distribution for a pipe bend under system loads was a good

approximation of the damage distribution in the same pipe. The time to failure predicted by the rupture stress was also a reasonable approximation of the damage time to failure. Additional research needs to be conducted to verify that peak rupture stresses may be used in all cases to approximate the damage accumulation in a component operating under creep conditions. Furthermore, due to the extrapolation discrepancies in power law models for reduced stress cases (see chapter 4), a method to relate the steady-state stresses in hyperbolic sine models to damage accumulation should be investigated.

Pipe bend geometry characterisation and analysis can be expanded in several areas. Some classification of ovality such as the out of roundness factor used in BS 806[129] could be included in parametric equations for example. While little ovality was observed in the industrial data in section 6.3.2, this may be due to the measurements being taken from in service pipe work (an internal pressure will act to reduce ovality[120]). System loads have been incorporated into a neural network, however their inclusion in a parametric equation may be possible using the combined primary and secondary loading reference stress used in the R6 procedure[126], for example. Parametric equations and the neural network may also be developed or modified to predict the location of the maximum rupture stress. This can be used to predict the possible failure location and may provide a starting point for inspections. Thermal loads inside the pipe bend sections have also not been considered in the present work. While system loads analysed in section 7.4.3 may be driven by the thermal expansion and distortion of a piping system, additional stresses in the pipe will be created by a temperature differential over the wall thickness. Future work should look to incorporate these effects as they may prove significant in the simulation of start up/shut down behaviour.

Material models that can accommodate the more complex (and realistic) fluctuations in loading and operational temperature could be used to establish more accurate failure time predictions. Typical start-up/shut down cycle profiles could be used to extrapolate loading conditions for a specific pipe bend geometry (similar to resolving the loading history in the R5 procedure[125]). Using a damage function in, say, the Chaboche model, failure times could be estimated by determining the number of cycles which a component could withstand before rupture. Methods to interpolate the behaviour predicted by the Chaboche model for fluctuations in temperature should also be considered (at present, only isothermal loading conditions are considered), as well as any loading rate dependencies that may exist.

Bibliography

[1] Smallman RE, Ngan AHW. Physical Metallurgy and Advanced Materials. 7th ed. Oxford, U.K.: Elsevier; 2007.

[2] Kelly A, Knowles KM. Crystallography and Crystal Defects. 2nd ed. Chichester, U.K.: Wiley; 2012.

[3] Dieter GE. Mechanical Metallurgy. 3rd ed. New York, U.S.A.: McGraw-Hill; 1986.

[4] ASM International. Phase Diagrams: Understanding the Basics. 1st ed. Campbell FC, editor. Materials Park, Ohio, U.S.A.: ASM International; 2012.

[5] Phillips R. Crystal, Defects and Microstructures: Modelling Across Scales. 1st ed. Cambridge, U.K.: Cambridge University Press; 2001.

[6] Thomason PF. Ductile Fracture of Metals. 1st ed. Oxford, U.K.: Pergamon Press; 1990.

[7] Morris DG, Harries DR. Recovery of a Creep-Deformed Type 316 Stainless Steel. Journal of Materials Science. 1979;14:2625–2636.

[8] Besson J. Damage of Ductile Materials Deforming Under Multiple Plastic or Viscoplastic Mechanisms. International Journal of Plasticity. 2009;25:2204–2221.

[9] Hutchinson JW, Tvergaard V. Softening due to Void Nucleation in Metals. In: Wei RP, Ganloff RP, editors. Fracture Mechanics: Perspectives and Directions (20th Symposium). American Society for Testing and Materials; 1989. p. 61–83.

[10] Freiman SW, Mecholsky Jr JJ. The Fracture of Brittle Materials: Testing and Analysis. 1st ed. Hoboken, New Jersey, U.S.A.: Wiley Publications; 2012.

[11] Kassner ME. Fundamentals of Creep in Metals and Alloys. 2nd ed. Oxford, U.K.: Elsevier; 2009.

[12] Zener C. The Micro-Mechanism of Fracture. In: Fracturing of Metals. American Society for Metals; 1948. p. 3–31.

[13] Stroh AN. The Formation of Cracks as a Result of Plastic Flow. Proceedings of the Royal Society of London A. 1954;223:404–414.

[14] Xiao ZM, Fan H, Sun YM. On the Contact Zone of a Sub-Interfacial Zener-Stroh Crack. Acta Mechanica. 2000;142:133–148.

[15] Bernasconi G, Piatti G, editors. Creep of Engineering Materials and Structures. 1st ed. London, U.K.: Applied Science Publishers Ltd.; 1978.

[16] Bathias C, Pineau A, editors. Fatigue of Materials and Structures: Fundamentals. Hoboken, New Jersey, U.S.A.: Wiley; 2010.

[17] Hertzberg RW, Vinci RP, Hertzberg JL. Deformation and Fracture Mechanics of Engineering Materials. 5th ed. Hoboken, New Jersey, U. S. A.: Wiley; 2013.

[18] Hibbler RC. Mechanics of Materials. 6th ed. Upper Saddle River, New Jersey, U.S.A.: Pearson/Prentice Hall; 2005.

[19] Poisson SD. Mémoire sur l'Équilibre et le Mouvement des Corps Élastiques; 1828.

[20] Betten J. Creep Mechanics. 3rd ed. Berlin, Germany: Springer; 2008.

[21] Landau LD, Lifshitz EM. Theory of Elasticity. 3rd ed. Oxford, U.K.: Pergamon Press; 1986.

[22] Hooke R. De Potentia Restitutiva; 1678.

[23] Dunne F, Petrinic N. Introduction to Computational Plasticity. 2nd ed. Oxford, U.K.: Oxford University Press; 2005.

[24] Melan E. Zur Plastizitat des Raumlichen Kontinumms. Ingenieur Archiv. 1938;9:116–125.

[25] Maugin GA. The Thermomechanics of Plasticity and Fracture. 1st ed. Cambridge, U.K.: Cambridge University Press; 1992.

[26] Prandtl LT. Spannungsverteilung in Plastischen Korpern. In: Proceedings of the First International Congregation for Applied Mechanics. Delft, Holland; 1924. p. 43–54.

[27] Rees DWA. Basic Engineering Plasticity: An Introduction with Engineering and Manufacturing Applications. 1st ed. Oxford, U.K.: Elsevier; 2006.

[28] Boresi AP, Schmidt RJ, Sidebottom OM. Advanced Mechanics of Materials. 5th ed. New York, U.S.A.: Wiley; 1993.

[29] Dowling NE. Mechanical Behaviour of Materials : Engineering Methods for Deformation, Fracture and Fatigue. 3rd ed. Upper Saddle River, New Jersey, U.S.A.: Pearson/Prentice Hall; 2007.

[30] Gong YP, Hyde CJ, Sun W, Hyde TH. Determination of Material Properties in the Chaboche Unified Viscoplasticity Model. Proceedings of the Institution of Mechanical Engineers Part L-Journal of Materials-Design and Applications. 2010;224:19–29.

[31] Hyde CJ, Sun W, Leen SB. Cyclic Thermo-Mechanical Material Modelling and Testing of 316 Stainless Steel. International Journal of Pressure Vessels and Piping. 2010;87:365–372.

[32] Mroz Z. On the Description of Anisotropic Workhardening. Journal of the Mechanics and Physics of Solids. 1967;15:163–175.

[33] Chaboche JL. A Review of Some Plasticity and Viscoplasticity Constitutive Theories. International Journal of Plasticity. 2008;24:1642–1693.

[34] Chaboche JL. Time-Independent Constitutive Theories for Cyclic Plasticity. International Journal of Plasticity. 1986;2:149–188.

[35] Chaboche JL, Cailletaud G. On the Calculation of Structures in Cyclic Plasticity or Viscoplasticity. Computers & Structures. 1986;23:23–31.

[36] Prager N. The Theory of Plasticity: A Survey of Recent Achievements. Proceedings of the Institute of Mechanical Engineers. 1955;169:41–57.

[37] Ziegler H. A Modification of Prager's Hardening Rule. Quarterly of Applied Mathematics. 1959;17:55–65.

[38] Armstrong PJ, Frederick CO. A Mathematical Representation of the Multiaxial Bauschinger Effect. Berkeley Nuclear Laboratories; 1966.

[39] Andrade E. The Viscous Flow in Metals and Allied Phenomena. Proceedings of the Royal Society of London A. 1910;84:1–12.

[40] Ashby MF. A First Report on Deformation Mechanism Maps. Acta Metallurgica. 1972;20:887–897.

[41] Hazzledine PM, Schneibel JH. Theory of Coble Creep for Irregular Grain Structures. Acta Metallurgica et Materialia. 1993;41:1252–1262.

[42] Raman V, Raj SV. An Analysis of Harper-Dorn Creep Based on Specimen Size Effects. Scripta Metallurgica. 1985;19:629–634.

[43] Yavari P, Miller DA, Langdon TG. An Investigation of Harper-Dorn Creep - 1. Mechanical and Microstructural Characteristics. Acta Materialia. 1982;30:871–879.

[44] Langdon TG, Mohamed FA. A Simple Method of Constructing an Ashby-Type Deformation Mechanism Map. Journal of Materials Science. 1978;13:1282–1290.

[45] Monkman FC, Grant NJ. An Empirical Relationship Between Rupture Life and Minimum Creep Rate in Creep-Rupture Tests. Proceedings of the American Society for Testing and Materials. 1956;56:593–620.

[46] Larson FR, Miller J. A Time-Temperature Relationship for Rupture and Creep Stresses. Transactions of the American Society of Mechanical Engineers. 1952;74:765–771.

[47] Bailey RW. The Utilization of Creep Test Data in Engineering Design. Proceedings of the Institution of Mechanical Engineers. 1935;131:131–349.

[48] Bailey RW. Creep of Steel Under Simple and Compound Stress and the use of High Initial Temperature in Steam Power Plants. In: The Transactions of the Tokyo Sectional Meeting, World Power Conference. Tokyo, Japan; 1929. .

[49] Vakili-Tahami F, Hayhurst DR, Wong MT. High-Temperature Creep Rupture of Low Alloy Ferritic Steel Butt-Welded Pipes Subjected to Combined Internal Pressure and End Loadings. Philosophical Transactions of the Royal Society a-Mathematical Physical and Engineering Sciences. 2005;363:2629–2661.

[50] Norton FH. The Creep of Steel at High Temperatures. 1st ed. New York, U.S.A.: McGraw-Hill Book Company; 1929.

[51] Odqvist FKG. Mathematical Theory of Creep and Creep Rupture. 2nd ed. Oxford, U.K.: Clarendon Press; 1974.

[52] Hyde CJ, Hyde TH, Sun W, Becker AA. Damage Mechanics Based Predictions of Creep Crack Growth in 316 Stainless Steel. Engineering Fracture Mechanics. 2010;77:2385–2402.

[53] Kachanov LM. The Theory of Creep. 1st ed. Kennedy AJ, editor. Boston Spa, Yorkshire, U.K.: National Lending Library for Science & Technology; 1967.

[54] Robotnov YN. Creep Problems in Structural Member. 1st ed. Amsterdam, Holland: North-Holland Publishing Company; 1969.

[55] Backhaus G. Yu. N. Robotnov, Creep Problems in Structural Members. ZAMM - Journal of Applied Mathematics and Mechanics. 1971;51:575–576.

[56] Leckie FA, Hayhurst DR. Creep-Rupture of Structures. Proceedings of the Royal Society of London Series A - Mathematical Physical and Engineering Sciences. 1974;340:323–347.

[57] Chaboche JL. Continuum Damage Mechanics: Part 1 - General Concepts. Journal of Applied Mechanics. 1988;55:59–64.

[58] Chaboche JL. Continuum Damage Mechanics: Part 2 - Damage Growth, Crack Initiation and Crack Growth. Journal of Applied Mechanics. 1988;55:65–72.

[59] Kang G, Liu Y, Ding J, Gao Q. Uniaxial Ratcheting and Fatigue Failure of Tempered 42CrMo Steel: Damage Evolution and Damage-Coupled Visco-Plastic Constitutive Model. International Journal of Plasticity. 1999;97:125–135.

[60] Murakami S, Liu Y, Mizuno M. Computational Methods for Creep Fracture Analysis by Damage Mechanics. Computer Methods in Applied Mechanics and Engineering. 2000;183:15–33.

[61] Liu Y, Murakami S, Kanagawa Y. Mesh-Dependence and Stress Singularity in Finite-Element Analysis of Creep Crack-Growth by Continuum Damage Mechanics Approach. European Journal of Mechanics A - Solids. 1994;13:395–417.

[62] Liu Y, Murakami S. Damage Localization of Conventional Creep Damage Models and Proposition of a New Model for Creep Damage Analysis. JSME International Journal Series A - Solid Mechanics and Material Engineering. 1998;41:57–65.

[63] Murakami S, Kawai M, Rong H. Finite-Element Analysis of Creep Crack-Growth by a Local Approach. International Journal of Mechanical Sciences. 1988;30:491–502.

[64] Hyde TH, Sun W, Becker AA, Williams JA. Creep Properties and Failure Assessment of New and Fully Repaired P91 Pipe Welds at 923K. Proceedings of the Institute of Mechanical Engineers. 2004;218:211–222.

[65] Dyson B. Use of CDM in Materials Modelling and Component Creep Life Prediction. Journal of Pressure Vessel Technology - Transactions of the ASME. 2000;122:281–296.

[66] Kowalewski ZL, Hayhurst DR, Dyson BF. Mechanisms Based Creep Constitutive Equations for an Aluminium Alloy. Journal of Strain Analysis for Engineering Design. 1994;29:309–316.

[67] Hyde TH, Becker AA, Sun W, Williams JA. Finite-Element Creep Damage Analyses of P91 Pipes. International Journal of Pressure Vessels and Piping. 2006;83:853–863.

[68] Evans RW, Wilshire B. Creep of Metals and Alloys. 1st ed. London, U.K.: Institute of Materials; 1987.

[69] Ule B, Sustar T, Dobes F, Milicka K, Bicego V, Tettamanti S, et al. Small Punch Test Method Assessment for the Determination of the Residual Creep Life of Service Exposed Components: Outcomes from an Interlaboratory Exercise. Nuclear Engineering and Design. 1999;192:1–11.

[70] Evans M, Wang D. Stochastic Modelling of the Small Disc Creep Test. Materials Science and Technology. 2007;23:883–892.

[71] Evans M, Wang D. Optimizing the Sensitivity of the Small-Disc Creep Test to Damage and Test Conditions. Journal of Strain Analysis for Engineering Design. 2007;42:389–413.

[72] Evans RW, Evans M. Numerical Modelling of Small Disc Creep Test. Materials Science and Technology. 2006;22:1155–1162.

[73] Albert WAJ. Uber Treibseile am Haqrz. Archive fur Mineralogie, Geognosie, Bergbau und Huttenkunde. 1838;10:215–234.

[74] Rankine WJM. On the Causes of Unexpected Breakage of the Journals of Railway Axles and the means of Preventing such Accidents by Observing the Law of Continuity in their Construction. Proceedings of the Institute of Civil Engineers. 1843;2:105–108.

[75] Hodgkinson EA. Report of the Commissioners Appointed to Enquire into the Application of Iron to Railway Structures. London, U.K.: Command Paper 1123; 1849.

[76] Wholer A. Versuche uber die Festigkiet der Eisenbahnwagenachen. Zeitschrift fur Bauwesen. 1860;4:160–161.

[77] Suresh S. Fatigue of Materials. 2nd ed. Cambridge, U.K.: Cambridge University Press; 1998.

[78] Gerber H. Bestimmung der Zulassigen Spannungen in Eisenknostructionen. Zeitschrift des Bayerischen Architeckten und Ingenieur-Vereins. 1874;6:101–110.

[79] Goodman J. Mechanics Applied to Engineering. London, U.K.: Longmans Green; 1908.

[80] Soderberg CR. Factor of Safety and Working Stress. Transactions of the American Society of Mechanical Engineers. 1939;52:13–28.

[81] Ince A, Glinka G. A Modification of Morrow and Smith-Watson-Topper Mean Stress Correction Models. Fatigue and Fracture of Engineering Materials and Structures. 2011;34:854–867.

[82] Smith KN, Watson P, Topper TH. A Stress-Strain Function for the Fatigue of Materials. Journal of Materials. 1970;5:767–778.

[83] Walker K. The Effect of Stress Ratio During Crack Propagation and Fatigue for 2024-T3 and 7075-T6 Aluminum. In: Effects of Environment and Complex Load History on Fatigue Life. 1st ed. West Conshohocken, Pennsylvania, U. S. A.: American Society for Testing and Materials; 1970. p. 1–14.

[84] Basquin OH. The Exponential Law of Endurance Tests. Proceedings of the American Society for Testing and Materials. 1910;10:625–630.

[85] Coffin LF. A Study of the Effects of Cyclic Thermal Stresses on a Ductile Metal. Transactions of the American Society of Mechanical Engineers. 1954;76:931–950.

[86] Bernhart G, Moulinier G, Brucelle O, Delagnes D. High Temperature Low Cycle Fatigue Behaviour of a Martensitic Forging Tool Steel. International Journal of Fatigue. 1999;21:179–186.

[87] Dafalias YF, Popov EP. Plastic Internal Variables Formalism of Cyclic Plasticity. Journal of Applied Mechanics. 1976;43:645–651.

[88] Tavassoli AAF, Fournier B, Sauzay M. High Temperature Creep-Fatigue Design. Transactions of the Indian Institute of Metals. 2010;63:235–244.

[89] Gorash Y, Chen H. Creep-Fatigue Life Assessment of Cruciform Weldments Using the Linear Matching Method. International Journal of Pressure Vessels and Piping. 2013;104:1–13.

[90] Manson SS, Halford GR, Hirschberg MH. Creep-Fatigue Analysis by Strain-Range Partitioning. In: Zamrik SY, editor. Design for Elevated Temperature Environment. 1st ed. San Francisco, California, U.S.A.: American Society of Mechanical Engineers; 1971. p. 12–24.

[91] Kichenin J, Van KD, Boytard K. Finite-Element Simulation of a New Two-Dissipative Mechanisms Model for Bulk Medium-Density Polyethylene. Journal of Materials Science. 1996;31:1653–1661.

[92] Figiel L, Gunther B. Modelling the High-Temperature Longitudinal Fatigue Behaviour of Metal Matrix Composites (SiC/Ti-6242): Nonlinear Time-Dependent Matrix Behaviour. International Journal of Fatigue. 2008;30:268–276.

[93] Leen SB, Deshpande A, Hyde TH. Experimental and Numerical Characterization of the Cyclic Thermomechanical Behaviour of a High Temperature Forming Tool Alloy. Journal of Manufacturing Science and Engineering. 2010;132:1–12.

[94] Chaboche JL, Rousselier G. On the Plastic and Viscoplastic Constitutive-Equations - Part 1: Rules Developed with Internal Variable Concept. Journal of Pressure Vessel Technology - Transactions of the ASME. 1983;105:153–158.

[95] Chaboche JL, Rousselier G. On the Plastic and Viscoplastic Constitutive-Equations - Part 2: Application of Internal Variable Concepts to the 316 Stainless-Steel. Journal of Pressure Vessel Technology - Transactions of the ASME. 1983;105:159–164.

[96] Lavender DA, Hayhurst DR. The Prediction of Fatigue Lifetimes in a Model Structure Using a Non-Linear Kinematic Hardening Model with Continuum Damage. International Journal of Mechanical Sciences. 1989;31:537–548.

[97] Ambroziak A, Klosowski P. The Elasto-Viscoplastic Chaboche Model. Task Quarterly. 2006;10:49–61.

[98] Ganczarski A, Cegielski M. Continuous Damage Deactivation in Modelling of Cycle Fatigue of Engineering Materials. Procedia Engineering. 2010;2:1057–1066.

[99] Gharad AE, Zedira H, Azari Z, Pluvinage G. A Synergistic Creep Fatigue Failure Model Damage (Case of the Alloy Z5NCTA at 550C). Engineering Fracture Mechanics. 2006;73:750–770.

[100] Tong J, Vermeulen B. The Description of Cyclic Plasticity and Viscoplasticity of Waspaloy Using Unified Constitutive Equations. International Journal of Fatigue. 2003;25:413–420.

[101] Tong J, Zhan JL, Vermeulen B. Modelling of Cyclic Plasticity and Viscoplasticity of a Nickel-Based Alloy Using Chaboche Constitutive Equations. International Journal of Fatigue. 2004;26:829–837.

[102] Zhan ZL, Tong J. A Study of Cyclic Plasticity and Viscoplasticity in a New Nickel-Based Superalloy Using Unified Constitutive Equations. - Part 1: Evaluation and Determination of Material Parameters. Mechanics of Materials. 2007;39:64–72.

[103] Zhan ZL, Tong J. A Study of Cyclic Plasticity and Viscoplasticity in a New Nickel-Based Superalloy Using Unified Constitutive Equations - Part 2: Simulation of Cyclic Stress Relaxation. Mechanics of Materials. 2007;39:73–80.

[104] Yaghi AH, Hyde TH, Becker AA, Sun W. Parametric Peak Stress Functions of 90 Degrees Pipe Bends with Ovality Under Steady-State Creep Conditions. International Journal of Pressure Vessels and Piping. 2009;86:684–692.

[105] Maharaj C, Dear JP, Morris A. A Review of Methods to Estimate Creep Damage in Low-Alloy Steel Power Station Steam Pipes. Strain. 2009;45:316–331.

[106] Cicero S, Guiterrez-Solana F, Alvarez JA. Structural Integrity Assessment of Different Components of a Power Plant. Engineering Failure Analysis. 2007;14:301–309.

[107] Weber J, Klenk A, Rieke A. A New Method of Strength Calculation and Lifetime Prediction of Pipe Bends Operating in the Creep Range. International Journal of Pressure Vessels and Piping. 2005;82:77–84.

[108] Carmichael GDT. An Assessment of Primary System Stresses on the Creep-Behaviour of High-Temperature Steam Piping Systems. Proceedings of the Institution of Mechanical Engineers Part A - Journal of Power and Energy. 1986;200:197–204.

[109] Hyde TH, Sun W. Effect of Bending Load on the Creep Failure Behaviour of a Pressurised Thick Walled CrMoV Pipe Weldment. International Journal of Pressure Vessels and Piping. 2002;79:331–339.

[110] Hayhurst DR, Wong MT, Tahami FV. The use of CDM Analysis Techniques in High Temperature Creep Failure of Welded Structures. JSME International Journal Series A - Solid Mechanics and Material Engineering. 2002;45:90–97.

[111] Hyde TH, Sun W. Some Issues on Creep Damage Modelling of Welds with Heterogeneous Structures. International Journal of Mechanics and Materials in Design. 2009;5:327–335.

[112] Yaghi AH, Hyde TH, Becker AA, Williams JA, Sun W. Residual Stress Simulation in Welded Sections of P91 Pipes. Journal of Materials Processing Technology. 2005;167:480–487.

[113] Yaghi A, Hyde TH, Becker AA, Sun W, Williams JA. Residual Stress Simulation in Thin and Thick-Walled Stainless Steel Pipe Welds Including Pipe Diameter Effects. International Journal of Pressure Vessels and Piping. 2006;83:864–874.

[114] Zhang G, Zhou C, Wang Z, Xue F, Zhao Y, Zhang L, et al. Numerical Simulation of Creep Damage for Low Alloy Steel Welded Joints Considering as-Welding Residual Stress. Nuclear Engineering and Design. 2012;242:26–33.

[115] Whessoe Computing Systems. Product Overview: PSA5 Pipe Stress Analysis and Design Code Compliance Checking. Whessoe Oil & Gas Ltd; 2010.

[116] Induction Pipe Bending UK Ltd . http://www.inductionbending.co.uk.; 2008.

[117] Kale AV, Thorat HT. Effect of Pre-Compression on Ovality of Pipe After Bending. Journal of Pressure Vessel Technology - Transactions of the ASME. 2009;131:1–7.

[118] Veerappan AR, Shanmugam S. Stress Analysis of Pipe Bends Subjected to Internal Fluid Pressure Using the Finite Element Technique. Journal of Strain Analysis for Engineering Design. 2006;41:561–573.

[119] Robertson A, Li HJ, Mackenzie D. Plastic Collapse of Pipe Bends Under Combined Internal Pressure and in-Plane Bending. International Journal of Pressure Vessels and Piping. 2005;82:407–416.

[120] Chattopadhyay J, Kushwaha HS, Roos E. Improved Integrity Assessment Equations of Pipe Bends. International Journal of Pressure Vessels and Piping. 2009;86:454–473.

[121] Samal MK, Dutta BK, Guin S, Kushwaha HS. A Finite Element Program for on-Line Life Assessment of Critical Plant Components. Engineering Failure Analysis. 2009;16:85–111.

[122] Mukhopadhyay NK, Dutta BK, Kushwaha HS. On-Line Fatigue-Creep Monitoring System for High-Temperature Components of Power Plants. International Journal of Fatigue. 2001;23:549–560.

[123] Paterson IR, Wilson JD. Use of Damage Monitoring Systems for Component Life Optimisation in Power Plant. International Journal of Pressure Vessels and Piping. 2002;79:541–547.

[124] Ainsworth RA, Booth SE. Use of R5 in Plant Defect Assessment. Materials at High Temperatures. 1998;15:299–302.

[125] Ainsworth RA. R5 Procedures for Assessing Structural Integrity of Components Under Creep and Creep-Fatigue Conditions. International Materials Reviews. 2006;51:107–126.

[126] Ainsworth RA, Hooton DG. R6 and R5 Procedures: The Way Forward. International Journal of Pressure Vessels and Piping. 2008;85:175–182.

[127] British Standards Institution. PD 5500:2012 Specification for Unfired Fusion Welded Pressure Vessels; 2012.

[128] British Standards Institution. BS EN 13480-3:2002+A4:2010 Metallic Industrial Piping: Design and Calculation; 2002.

[129] British Standards Institution. BS 806:1993 Specification for Design and Construction of Ferrous Piping Installations for and in Connection with Land Boilers; 1993.

[130] Kraus H. Creep Analysis. Hoboken, New Jersey, U.S.A.: Wiley; 1980.

[131] Hong SP, An JH, Kin YJ, Nikbin K, Budden PJ. Approximate Elastic Stress Estimate for Elbows Under Internal Pressure. Sciences. 2011;53:526.

[132] Kim YJ, Je JH, Oh CS, Han JJ, Budden PJ. Plastic Loads for 90 Degrees Thick-Walled Elbows Under Combined Pressure and Bending. Journal of Strain Analysis for Engineering Design. 2010;45:115–127.

[133] Veerappan AR, Shanmugam S, Soundrapandian S. The Accepting of Pipe Bends with Ovality and Thinning Using Finite Element Method. Journal of Pressure Vessel Technology - Transactions of the ASME. 2010;132:1–9.

[134] Weiss E, Lietzmann A, Rudolph J. Linear and Nonlinear Finite-Element Analyses of Pipe Bends. International Journal of Pressure Vessels and Piping. 1996;67:211–217.

[135] Oh CS, Kim YJ, Park CY. Plastic Loads of Elbows with Local Wall Thinning Under in-Plane Bending. International Journal of Fracture. 2007;145:63–79.

[136] Kim B, Lim B. Local Creep Evaluation of P92 Steel Weldment by Small Punch Creep Test. Acta Mechanica Solida Sinica. 2008;21:312–317.

[137] Kochekseraii SB. Finite Element Modelling of Plastic Collapse of Metallic Single Mitred Pipe Bends Subject to in-Plane Bending Moments. International Journal of Pressure Vessels and Piping. 2004;81:75–81.

[138] Hyde TH, Yaghi A, Proctor M. Use of the Reference Stress Method in Estimating the Life of Pipe Bends Under Creep Conditions. International Journal of Pressure Vessels and Piping. 1998;75:161–169.

[139] Hyde TH, Sun W, Williams JA. Life Estimation of Pressurised Pipe Bends Using Steady-State Creep Reference Rupture Stresses. International Journal of Pressure Vessels and Piping. 2002;79:799–805.

[140] Gyekenyesi AL, Kautz HE, Shannon RE. Quantifying Creep Damage in a Metallic Alloy Using Acousto-Ultrasonics. Journal of Materials Engineering and Performance. 2002;11:205–210.

[141] Somieski B, Krause-Rehberg R. Creep-Damaged Pipe Steels Probed with Positron Spectroscopy. Fatigue & Fracture of Engineering Materials & Structures. 2001;24:267–274.

[142] Gao H, Guers MJ, Rose JL, Zhao GX, Kwan C. Ultrasonic Guide Wave Annular Array Transducers for Structural Health Monitoring. Review of Quantitative Nondescructive Evaluation. 2006;25:1680–1686.

[143] Gandossi L, Summers SA, Taylor NG, Hurst RC, Hulm BJ, Parker JD. The Potential Drop Method for Monitoring Crack Growth in Real Components Subjected to Combined Fatigue and Creep Conditions: Application of FE Technique for Deriving Calibration Curves. International Journal of Pressure Vessels and Piping. 2001;78:881–891.

[144] Sposito G, Cawley P, Nagy PB. An Approximate Model for Three-Dimensional Alternating Current Potential Drop Analyses Using a Commercial Finite Element Code. Non Destructive Testing and Evaluation International. 2010;43:134–140.

[145] Furtado HC, de Almeida LH, Dille J, Le May I. Correlation Between Hardness Measurements and Remaining Life Prediction for 2.25Cr-1MO Steel used in Power Plants. Journal of Materials Engineering and Performance. 2010;19:558–561.

[146] Morris A, Maharaj C, Palmer I, Puri A, Dear J. Developments in Combined ARCMAC and Strain Mapping Systems for Creep Measurement. In: ASME Pressure Vessels and Piping Division Conference. Chicago, Illinois, U. S. A.; 2008. .

[147] Morris A, Maharaj C, Puri A, Kourmpetis M, Dear J. Recent Developments in Methods to Study Creep Strain Variations in Power Station Steam Plant. In: ASME Pressure Vessels and Piping Division Conference. Chicago, Illinois, U. S. A.; 2008. .

[148] Lee YJ, Muddle BC. Creep Damage of Weldments in 1Cr-0.5Mo Steels During Long Term Service at Elevated Temperature. Scripta Metallurgica et Materialia. 1995;33:355–362.

[149] Corwin WR, Lucas GE. The use of Small-Scale Specimens for Testing Irradiated Material: A Symposium Sponsored by ASTM Committee E-10 on Nuclear Technology and Applications, Albuquerque, N.M., 23 Sept. 1983. Philadelphia, Pennsylvania, U.S.A.: ASTM; 1986.

[150] Klueh RL. Miniature Tensile Test Specimens for Fusion-Reactor Irradiation Studies. Nuclear Engineering and Design-Fusion. 1985;2:407–416.

[151] Rolls-Royce Power Engineering Plc . Scoop Sampling - Extraction of Material Samples for Examination and Analysis. http://www.rolls-royce.com/Images/ScoopRolls-Royce, Derby, UK; 2010.

[152] ETD. http://www.etd-consulting.com/our-services/engineering-services/advanced-nondestructive-evaluation/;.

[153] Hyde TH, Sun W, Becker AA. Analysis of the Impression Creep Test Method Using a Rectangular Indenter for Determining the Creep Properties in Welds. International Journal of Mechanical Sciences. 1996;38:1089–1102.

[154] Hyde TH, Yehia KA, Becker AA. Application of the Reference Stress Method for Interpreting Impression Creep Test Data. Materials at High Temperatures. 1995;13:133–138.

[155] Hyde TH, Sun W. A Novel, High-Sensitivity, Small Specimen Creep Test. Journal of Strain Analysis for Engineering Design. 2009;44:171–185.

[156] Hyde TH, Sun W, Williams JA. Requirements for and use of Miniature Test Specimens to Provide Mechanical and Creep Properties of Materials: A Review. International Materials Reviews. 2007;52:213–255.

[157] European Committee for Standardisation. Workshop Agreement: Small Punch Test Method for Metallic Materials. CEN; 2006.

[158] Hyde TH, Sun W, Balhassn SMA. A Small Creep Test Specimen for use in Determining Uniaxial Creep Rupture Data. In: 2nd International Conference on Small Specimen Testing Techniques. Ostrava, Czech Republic; 2012. .

[159] Cowan JD. Discussion: McCulloch-Pitts and Related Neural Networks from 1943 to 1989. Bulletin of Mathematical Biology. 1990;52:73–97.

[160] Alavala CR. Fuzzy Logic and Neural Networks : Basic Concepts and Application. Daryaganj, Delhi, India: New Age International; 2008.

[161] Adeli H, Jiang X. Intelligent Infrastructure: Neural Networks, Wavelets, and Chaos Theory for Intelligent Transportation Systems and Smart Structures. 1st ed. Boca Raton, Florida, U.S.A.: CRC Press; 2009.

[162] Chapra SC, Canale RP. Numerical Methods for Engineers. 6th ed. Boston, Massachusetts, U.S.A.: McGraw-Hill Higher Education; 2010.

[163] MATLAB. Neural Network Toolbox TM 4 User's Guide. T. M. Inc; 2008.

[164] Canning A, Gardner E. Partially Connected Models of Neural Networks. Journal of Physics A: Mathematical and General. 1988;21:3275–3284.

[165] Cao J, Lin J. A Study on Formulation of Objective Functions for Determining Material Models. International Journal of Mechanical Sciences. 2008;50:193–204.

[166] Chaparro BM, Thuillier S, Menezes LF, Manach PY, Fernandes JV. Material Parameters Identification: Gradient-Based, Genetic and Hybrid Optimization Algorithms. Computational Materials Science. 2008;44:339–346.

[167] Pan W, Boyle J, Ramlan M, Dun C, Ismail M, Hakoda K. Material Plastic Properties Characterization Using a Genetic Algorithm and Finite Element Method Modelling of the Plane Strain Small Punch Test. In: 1st Annual International Conference SSTT (Small Sample Test Techniques). vol. 63. Ostrava, Czech Republic: Metallurgical Journal; 2010. p. 174–179.

[168] Li B, Lin J, Yao X. A Novel Evolutionary Algorithm for Determining Unified Creep Damage Constitutive Equations. International Journal of Mechanical Sciences. 2002;44:987–1002.

[169] Peauelas I, Cuesta II, Betegan CC, Rodriguez C, Belzunce FJ. Inverse Determination of the Elastoplastic and Damage Parameters on Small Punch Tests. Fatigue & Fracture of Engineering Materials & Structures. 2009;32:872–885.

[170] Guler O. Foundations of Optimisation. 1st ed. New York, U.S.A.: Springer; 2010.

[171] Joshi MC, Moudgalya KM. Optimisation: Theory and Practice. 1st ed. Harrow, U. K.: Alpha Science; 2004.

[172] Pflugfelder D, Wilkens JJ, Nill S, Oelfke U. A Comparison of Three Optimization Algorithms for Intensity Modulated Radiation Therapy. Zeitschrift far Medizinische Physik. 2008;18:111 – 119.

[173] Nocedal J, Wright SJ. Numerical Optimisation. 2nd ed. New York, U.S.A.: Springer; 2006.

[174] Guillaume P, Pintelon R. A Gauss-Newton like Optimisation Algorithm for "Weighted" Nonlinear Least-Squares Problems. IEEE Transactions on Signal Processing. 1996;44:2222–2228.

[175] Levenberg K. A Method for the Solution of Certain Problems in Least Squares. Quarterly of Applied Mathematics. 1944;2:164–168.

[176] Marquardt D. An Algorithm for Least Squares Estimation of Nonlinear Parameters. Journal of Applied Mathematics. 1963;11:431–441.

[177] Salomon R. Evolutionary Algorithm and Gradient Search: Similarities and Differences. IEEE Transactions on Evolutionary Computation. 1998;2:45–55.

[178] Egan P, Whelan MP, Lakestani F, Connelly MJ. Small Punch Test: An Approach to Solve the Inverse Problem by Deformation Shape and Finite Element Optimization. Computational Materials Science. 2007;40:33–39.

[179] Zidan AA, Brookfield DJ. A Technique for the Determination of Post-Yield Material Properties from the Small Punch Test. Journal of Strain Analysis for Engineering Design. 2003;38:367–376.

[180] Hyde TH, Sun W, Tang A. Determination of Material Constants in Creep Continuum Damage Constitutive Equations. Strain. 1998;34:83–90.

[181] Saad AA. Cyclic Plasticity and Creep of Power Plant Materials. University of Nottingham; March 2012.

[182] Hyde CJ. Thermo-Mechanical Fatigue and Creep of High Temperature Materials. University of Nottingham; August 2010.

[183] Farragher TP, Scully S, O'Dowd NP, Leen SB. Development of Life Assessment Procedures for Power Plant Headers Operated under Flexible Loading Scenarios. International Journal of Fatigue. 2013;49:50–61.

[184] Lemaitre J, Chaboche JL. Mechanics of Solid Materials. 1st ed. Cambridge, U.K.: Cambridge University Press; 1990.

[185] Ramberg W, Osgood WR. Description of Stress-Strain Curves by Three Parameters. Washington D.C., U.S.A.: National Advisory Committee For Aeronautics; 1943. 902.

[186] Rasmussen KJR. Full-Range Stress-Strain Curves for Stainless Steel Alloys. Journal of Constructional Steel Research. 2003;59:47–61.

[187] MATLAB 7 Mathematics. T. M. Inc; 2008.

[188] Venkataraman P. Applied Optimization with MATLAB Programming. 2nd ed. Hoboken, New Jersey, U.S.A.: John Wiley & Sons; 2009.

[189] Lin J, Dunne FPE, Hayhurst DR. Aspects of Testpiece Design Responsible for Errors in Cyclic Plasticity Experiments. International Journal of Damage Mechanics. 1999;8:109–137.

[190] Lin J, Hayhurst DR, Dunne FPE. Errors in Creep-Cyclic Plasticity Testing: Their Quantification and Correction for Obtaining Accurate Constitutive Equations. International Journal of Mechanical Sciences. 2001;43:1387–1403.

[191] ABAQUS 6.9 Online Documentation. Dassault Syste'mes; 2009.

[192] Sun W, Hyde TH, Becker AA, Williams JA. Steady-State Creep Reference Rupture Stresses for Internally Pressurised Pipes for use in Life Prediction. International Journal of Pressure Vessels and Piping. 2002;79:135–143.

[193] Hyde TH, Becker AA, Sun W, Williams JA. Influence of Geometry Change on Creep Failure Life of 90 Degrees Pressurised Pipe Bends with no Initial Ovality. International Journal of Pressure Vessels and Piping. 2005;82:509–516.

[194] Orr J, Burton D. Experience in Data Collection and Assessment for Material Standards. In: CEC ECSC Information Day on the Manufacture and Properties of Steel 91 for the Power Plant and Process Industries. Dusseldorf, Germany; 1992. .

[195] European Creep Collaborative Committee. ECCC Data Sheet; 2005. Issue 2. AC/MC/94.

[196] Harlow DG, Delph TJ. Creep Deformation and Failure: Effects of Randomness and Scatter. Journal of Engineering Materials and Technology - Transactions of the ASME. 2000;122:342–347.

[197] Calladine CR. A Rapid Method for Estimating the Greatest Stress in a Structure Subject to Creep. Proceedings of the Institution of Mechanical Engineers, Part 3L. 1964;178:198–206.

[198] Hyde TH, Sabesan R, Leen SB. Approximate Prediction Methods for Notch Stresses and Strains Under Elastic-Plastic and Creep Conditions. Journal of Strain Analysis for Engineering Design. 2004;39:515–527.

[199] Chen HF, Ponter ARS, Ainsworth RA. The Application of the Linear Matching Method to the Life Assessment Method R5: A Comparison. Proceedings of the ASME Pressure Vessels and Piping Conference 2005, Vol 2. 2005;2:241–251.

[200] Yoshikawa M, Katoh A, Sasaki K. A Failure Assessment Method for a Pipe Bend Subjected to both a Bending Moment and Internal Pressure. Journal of Pressure Vessel Technology-Transactions of the ASME. 2006;128:605–617.

[201] Iost A. The Correlation Between the Power-Law Coefficients in Creep: The Temperature Dependence. Journal of Materials Science. 1998;33:3201–3206.

[202] Optimisation Toolbox TM 4 User's Guide. T. M. Inc; 2008.

[203] Ainsworth RA, Budden PJ. R5 and British Standards Defect Assessment Procedures. Materials at High Temperatures. 1998;15:291–297.

[204] Qian N. On the Momentum Term in Gradient Descent Learning Algorithms. Neural Networks. 1999;12:145–151.

[205] Nguyen D, Widrow B. Improving the Learning Speed of 2-Layer Neural Networks by Choosing Initial Values of the Adaptive Weights. In: Proceedings of the International Joint Conference on Neural Networks. vol. 3. Washington, D. C., U.S.A.; 1990. p. 21–26.